



저작자표시-비영리-변경금지 2.0 대한민국

이용자는 아래의 조건을 따르는 경우에 한하여 자유롭게

- 이 저작물을 복제, 배포, 전송, 전시, 공연 및 방송할 수 있습니다.

다음과 같은 조건을 따라야 합니다:



저작자표시. 귀하는 원저작자를 표시하여야 합니다.



비영리. 귀하는 이 저작물을 영리 목적으로 이용할 수 없습니다.



변경금지. 귀하는 이 저작물을 개작, 변형 또는 가공할 수 없습니다.

- 귀하는, 이 저작물의 재이용이나 배포의 경우, 이 저작물에 적용된 이용허락조건을 명확하게 나타내어야 합니다.
- 저작권자로부터 별도의 허가를 받으면 이러한 조건들은 적용되지 않습니다.

저작권법에 따른 이용자의 권리는 위의 내용에 의하여 영향을 받지 않습니다.

이것은 [이용허락규약\(Legal Code\)](#)을 이해하기 쉽게 요약한 것입니다.

[Disclaimer](#)

공학박사학위논문

**Prediction of rock cutting performance  
and abrasiveness considering dynamic  
properties at intermediate strain rate**

중간변형률속도에서의 동적 물성을 고려한 암석  
절삭성능 및 마모율 예측

2020 년 2 월

서울대학교 대학원  
에너지시스템공학부  
Yudhidya Wicaksana

## **ABSTRACT**

# **Prediction of rock cutting performance and abrasiveness considering dynamic properties at intermediate strain rate**

Yudhidya Wicaksana

Department of Energy Systems Engineering

The Graduate School

Seoul National University

The application of mechanized excavation has been widely used in various civil and mining projects. It has significant advantages over the drill-and-blast method concerning continuity, safety, stability, and environmental friendliness. With the global increase of safety and environmental awareness, the demand for mechanized excavation has been increasing steadily, especially in urban tunneling.

Rock mechanical excavation involves a dynamic process where the rock experiences dynamics loading induced by cutting tools. And, many previous studies showed that the strength of rock under dynamic loading is higher than those under static loading. However, the dynamic properties of rock have not been considered in the existing mechanical excavation prediction models. This issue will potentially cause

misleading results in performance prediction and machine selection in a project.

In this study, the mechanical cutting problem from a dynamic perspective was investigated. First of all, it was shown that the loading rate of mechanical cutting falls in the intermediate strain rate (ISR), which is higher than the quasi-static rate and lower than the high strain rate (HSR). Accordingly, a series of tests were carried out to obtain dynamic mechanical properties by using a non-explosive powder reaction loading apparatus that was able to generate loading in the ISR range. The results of the dynamic mechanical properties at the ISR range are discussed.

Further, a laboratory linear cutting test was carried out with several cutting conditions. Besides, numerical simulations using the finite element method, considering static and dynamic property sets, were performed. The cutter forces and specific energy from the numerical simulation were validated against laboratory linear cutting tests. It was found that numerical simulation using dynamic input parameters fit better with the laboratory experiment than the simulation using quasi-static input parameters. Additionally, prediction models involving dynamic properties based on multiple linear regression were also derived. The performance of the models was tested in a given database, and it shows that the proposed models performed better than some theoretical models.

Finally, the abrasiveness test under the dynamic mode, called the Gouging abrasiveness test, was also considered. The test allows the pin to interact with the rock surface in a high-speed impact, which imitates the process that is experienced by cutting tools in the field. A comparison

with Cerchar abrasiveness test was discussed covering several aspects, including their relationship with geomechanical properties and groove profiles.

***Keywords:* Rock cutting performance, Dynamic properties, Intermediate strain rate loading, Non-explosive reaction-based loading apparatus, Linear cutting test, FEM, Gouging abrasiveness test**

Student ID: 2014-31439

# TABLE OF CONTENTS

Abstract.....	i
Table of Contents .....	iv
List of Figures.....	viii
List of Tables .....	xv
1. Introduction.....	1
1.1 Background.....	1
1.2 Objectives of the Study.....	5
1.3 Scope of the Study .....	6
2. Literature Review .....	8
2.1 Rock Breakage Mechanism by a Rock Cutting Tool .....	8
2.2 Theoretical and Empirical Models for Rock Cutting .....	10
2.3 Loading Classification over Strain Rate .....	13
2.4 Intermediate Strain Rate (ISR) Loading .....	14
2.4.1 Intermediate Strain Rate Loading Techniques .....	15
2.4.2 Dynamic Rock Behavior under Compression in Intermediate Strain Rate.....	23
2.4.3 Dynamic Rock Behavior under Tension in Intermediate Strain Rate.....	29
2.4.4 Rock Fragmentation on Dynamic Loading Condition.....	35
2.5 Rock Abrasiveness Test.....	37
2.6 Explicit Dynamic Simulation using ANSYS AUTODYN® .....	41
2.6.1 Explicit Transient Dynamics.....	42
2.6.2 Explicit Time Integration .....	43
3. Dynamic Test of Rock .....	45
3.1 Introduction to Dynamic Rock Test .....	45
3.2 Non-Explosive Reaction-Driven Loading Apparatus.....	45

3.3	Test Setup .....	49
3.3.1	Test Type.....	49
3.3.2	Rock Specimen.....	50
3.3.3	Test Scenario .....	52
3.4	Test and Results .....	53
3.4.1	Uniaxial Compression .....	53
3.4.2	Brazilian Tension .....	56
3.4.3	Mode-I Fracture Toughness .....	60
3.4.4	Punch Shear.....	64
3.5	Numerical Modeling of Dynamic Rock Test.....	68
3.5.1	Material Model of Dynamic Rock Test.....	68
3.5.2	Geometry and Boundary Conditions of the Dynamic Rock Test Model .....	70
3.5.3	Results of Dynamic Rock Test Modeling .....	74
3.6	Discussion on Dynamic Rock Properties .....	79
3.6.1	Rock Failure Under Dynamic Loading .....	79
3.6.2	Effect of Strain Rate on Mechanical Properties of Rock .....	81
3.6.3	Critical Strain Rate .....	94
3.6.4	Effect of Strain Rate on Elastic Properties.....	96
4.	Rock Cutting Test .....	99
4.1	Introduction to Rock Cutting Test .....	99
4.2	Small-Scale Linear Cutting Machine.....	99
4.3	Linear Cutting Test.....	101
4.3.1	Test Specimen for Linear Cutting Test .....	101
4.3.2	Procedure of Linear Cutting Test .....	102
4.3.3	Results of Linear Cutting Test .....	103
4.4	Numerical Modeling of Linear Cutting Test .....	110
4.4.1	Material Model of Linear Cutting Test .....	110

4.4.2	Geometry and Boundary Conditions of Linear Cutting Test Model.....	112
4.4.3	Results of Linear Cutting Test Modeling.....	112
4.5	Discussion on the Linear Cutting Test: Laboratory vs. FEM Simulation .....	116
4.6	Cutting Force Prediction Model .....	123
4.6.1	Database and the Conversion to Dynamic Strength of Rock .....	123
4.6.2	Multiple Linear Regression Analysis .....	124
4.6.3	Performance of the Proposed Prediction Models .....	129
4.7	Strain Rate Determination During Cutting Process .....	137
4.7.1	Calculation from the Technical Data Sheet of the Machine .....	137
4.7.2	Direct Measurement from Linear Cutting Test .....	139
4.7.3	Numerical Modeling of Linear Cutting Test.....	147
4.7.4	Recapitulation of the Strain Rate Determination in Cutting Process.....	151
5.	Abrasiveness Test .....	153
5.1	Introduction to Abrasiveness Test .....	153
5.2	Preparation of the Testing Apparatus .....	154
5.2.1	Strain Rate Determination in the Charpy Test .....	154
5.2.2	Impact Testing Machine Modification .....	157
5.3	Rock Sample .....	158
5.4	Wear Tool (Pin) .....	162
5.5	Test Procedure .....	162
5.5.1	Gouging Abrasiveness Test.....	162
5.5.2	Cerchar Abrasiveness Test .....	165
5.6	Results and Discussion .....	167
5.6.1	Equivalent Quartz Content .....	167
5.6.2	Effect of Geomechanical Properties of Rock .....	172
5.6.3	Relationship Between CAI and $G_i$ .....	180

5.6.4 Groove Profile .....	182
5.6.5 Gouging and Cerchar Tests in an Identical Scratch Distance.....	185
6. Conclusions.....	188
Reference .....	192
초록 (Abstract in Korean).....	205
Acknowledgment.....	207

## LIST OF FIGURES

Figure 2.1. Idealized tensile breakage under constant-cross-section disc cutter (Adapted from Rostami and Ozdemir (1993)) .....	9
Figure 2.2. Schematic diagram of the intermediate strain rate machine with a fully gas-driven operation (Green & Perkins, 1968) .....	16
Figure 2.3. (a) Working principle of the pneumatic-hydraulic loading system; (b) schematic layout of the machine and the data acquisition system (Zhao et al., 1999) .....	18
Figure 2.4. Schematic diagram of pneumatic-hydraulic loading machine (Tarigopula et al., 2009) .....	19
Figure 2.5. The drop weight test device (Reddish et al., 2005) .....	21
Figure 2.6. Schematic view of pendulum hammer-driven split Hopkinson pressure bar (Zhu et al., 2015) .....	22
Figure 2.7. Uniaxial compressive strength over strain rate collected from various references (Blanton, 1981; Chen et al., 2017; Doan & Gary, 2009; Frew et al., 2001; Kimberley & Ramesh, 2011; Li et al., 2005; Lindholm et al., 1974; Liu et al., 2015; Olsson, 1991; Perkins et al., 1970; Wang & Tonon, 2011; Wicaksana & Jeon, 2016; Xia et al., 2008; Zhang & Zhao, 2013). The shaded area indicates the ISR range .....	27
Figure 2.8. Dynamic increase factor (DIF) over strain rate in compression loading collected from various references (Blanton, 1981; Chen et al., 2017; Doan & Gary, 2009; Frew et al., 2001; Kimberley & Ramesh, 2011; Li et al., 2005; Lindholm et al., 1974; Liu et al., 2015; Olsson, 1991; Perkins et al., 1970; Wang et al., 2016; Wang & Tonon, 2011; Wicaksana & Jeon, 2016; Xia et al., 2008; Zhang & Zhao, 2013). The shaded area indicates the ISR range .....	28
Figure 2.9. Dynamic increase factor (DIF) over loading rate in compression (Kumar, 1968; Zhao et al., 1999; Zhou et al., 2015) .....	29
Figure 2.10. Dynamic increase factor (DIF) over strain rate in tension collected from various references (Asprone et al., 2009; Cadoni, 2010; Cho et al., 2003; Dutta & Kim, 1993;	

Kubota et al., 2008; Wang et al., 2009). The shaded area indicates the ISR range. ....	33
Figure 2.11. Dynamic increase factor over loading rate in tension (Dai et al., 2010a; Dai et al., 2010b; Huang et al., 2010a; Xia et al., 2017; Yan et al., 2012; Zhang & Zhao, 2013; Zhao & Li, 2000) .....	33
Figure 2.12. Strain rate effect on (a) changing in fragment size for Ibbenbüren sandstone, and (b) number of micro-fractures (Whittles et al., 2006) .....	37
Figure 2.13. Basic mechanisms of the Cerchar abrasiveness test. Left: type 1, the original design proposed by (Valantin, 1973) and, right: type 2, the modified design reported by (West, 1989). Index: (1) mass/deadweight, (2) pin chuck/guide, (3) pin/stylus, (4) rock specimen, (5) vice, (6) lever/hand crank (Alber et al., 2014) .....	39
Figure 2.14. Gouging abrasiveness test setup. Index: (1) sample holder, (2) transmission screw, (3) spring-loaded mechanism, (4) wear tool, (5) wear tool holder, and (6) pendulum arm (Golovanevskiy & Bearman, 2008) .....	40
Figure 2.15. The computational cycle of the explicit dynamic solution in ANSYS AUTODYN® (ANSYS, 2010).....	42
Figure 3.1. Dynamic testing components. a) loading frame; b) NRC powder and initiator; c) non-explosive powder charge; d) oscilloscope; and e) electric discharge controller. ....	48
Figure 3.2. Dynamic testing using the non-explosive reaction-driven loading device and its connectivity with other devices. Upper: schematic diagram; lower: actual test.....	48
Figure 3.3. Calibration of the dynamic load cell. (a) output voltage – time history; (b) static load – output voltage (Min et al., 2017) .....	49
Figure 3.4. Schematic diagram of each of the dynamic tests .....	50
Figure 3.5. The actual condition of the quasi-static test using a hydraulic servo-controlled loading machine .....	50
Figure 3.6. The location where the block samples were taken.....	51
Figure 3.7. Uniaxial compressive strength over strain rate .....	55

Figure 3.8. Crack evolution in Brazilian tensile test captured by the high-speed camera. Upper: Hwangdeung granite, lower: Linyi sandstone .....	57
Figure 3.9. Brazilian tensile strength over strain rate .....	59
Figure 3.10. Crack evolution in mode-I dynamic fracture toughness test captured by the high-speed camera. Upper: Hwangdeung granite, lower: Linyi sandstone.....	61
Figure 3.11. Mode-I fracture toughness ( $K_{IC}$ ) over loading rate .....	63
Figure 3.12. Detailed schematic view of the specimen holder (unit: mm).....	64
Figure 3.13. Punch shear test. a) Specimen holder; b) setup; c) specimen after quasi-static test; and d) specimen after the dynamic test .....	65
Figure 3.14. Shear strength over strain rate .....	67
Figure 3.15. Uniaxial compression FEM model and boundary condition .....	70
Figure 3.16. Brazilian tension FEM model and boundary condition ...	71
Figure 3.17. Mode-I NSCB fracture toughness FEM model and boundary condition .....	72
Figure 3.18. Punch shear FEM model and boundary condition .....	74
Figure 3.19. Uniaxial compressive strength over strain rate: the laboratory test and the FEM simulation.....	75
Figure 3.20. Tensile strength over strain rate: the laboratory test and the FEM simulation .....	76
Figure 3.21. Mode-I fracture toughness over loading rate: the laboratory test and the FEM simulation.....	76
Figure 3.22. Shear strength over strain rate: the laboratory test and the FEM simulation .....	77
Figure 3.23. Typical modeling result for various tests at high rate loading .....	78
Figure 3.24. Relationship between DIF of uniaxial compressive strength and strain/loading rate for (a)-(b) granite; and (c) sandstone.....	83
Figure 3.25. DIF of uniaxial compressive strength for various rock related to (a) strain rate, and (b) loading rate.....	84

Figure 3.26. Relationship between DIF of tensile strength and strain/loading rate for (a)-(b) granite; and (c)-(d) sandstone ....	86
Figure 3.27. DIF of tensile strength for various rock related to (a) strain rate, and (b) loading rate .....	88
Figure 3.28. Relationship between $K_{IC}$ and loading rate for (a) granite and (b) sandstone .....	89
Figure 3.29. Relationship between DIF of shear strength and loading rate for granite and sandstone .....	90
Figure 3.30. Experimental variation of compressive strength with strain rate from Kobayashi (1970) (after Blanton (1981)).....	91
Figure 3.31. The trend of rate dependency under (a) compressive and (b) tensile fracture mechanisms .....	93
Figure 3.32. The critical strain rate of uniaxial compressive strength for (a) granite and (b) sandstone .....	95
Figure 3.33. The critical strain rate of tensile strength for (a) granite and (b) sandstone .....	96
Figure 4.1. Small-scale linear cutting machine. a) the whole SLCM system; b) 3D load cell; c) cutting tool and its holder; d) control panel; and e) sample box .....	100
Figure 4.2. Schematic diagram and picture of the conical pick cutter (Jeong, 2017) .....	101
Figure 4.3. Rock sample (a) Typical rock block; (b) rock surface after preconditioning.....	102
Figure 4.4. Typical of three orthogonal cutter forces history from a single linear cutting test (example: the case of $p = 5$ mm, $s = 30$ mm, 1st line) .....	105
Figure 4.5. Mean cutting force associated with s/p ratio for all cutting conditions.....	106
Figure 4.6. Mean normal force associated with s/p ratio for all cutting conditions.....	106
Figure 4.7. Mean side force associated with s/p ratio for all cutting conditions.....	107
Figure 4.8. Specific energy with s/p ratio for all cutting conditions ..	108
Figure 4.9. The relationship between specific energy and penetration depth at the optimum cutting condition .....	109

Figure 4.10. Numerical modeling of linear cutting test.....	113
Figure 4.11. Representative cutter forces graph of the two-pick cutter model .....	114
Figure 4.12. The cut volume of the rock model over the cutting process .....	115
Figure 4.13. Cutting groove pattern of rock specimen at various cut spacing cases.....	116
Figure 4.14. Mean cutting force comparison between experimental test and numerical simulation .....	117
Figure 4.15. Mean normal force comparison between experimental test and numerical simulation .....	118
Figure 4.16. Mean side force comparison between experimental test and numerical simulation.....	118
Figure 4.17. Specific energy comparison between experimental test and numerical simulation.....	119
Figure 4.18. Dynamic increase factor (DIF) of UCS and BTS within the intermediate strain rate loading range and their representative averaged values .....	124
Figure 4.19. Relationship between measured and predicted mean cutting force of different models .....	135
Figure 4.20. Relationship between measured and predicted peak cutting force of different models .....	136
Figure 4.21. (a) Relationship between strain rates occurred on the sandstone surface and loading speed of the piston in uniaxial compression test, (b) the typical axial strain history plot .....	139
Figure 4.22. Strain rate determination during cutting by a disc cutter on a granitic rock. (a) strain gauge position, and (b) penetration depth scenarios.....	141
Figure 4.23. Example of strain rate calculation (cut 3, strain gauge #1, parallel to the cutting line).....	142
Figure 4.24. Strain rate determination in cutting by a pick cutter on a sandstone rock .....	143
Figure 4.25. (a) Typical strain history plot; (b) the relationship between strain rate and monitoring distance during cutting by a pick cutter on a sandstone .....	144

Figure 4.26. Strain rate determination in cutting by a disc cutter on a cement-gravel mixed ground .....	146
Figure 4.27. Configuration of the strain rate measurement calibration process between laboratory and FEM simulation.....	148
Figure 4.28. Model configuration for strain rate level detection during cutting.....	150
Figure 4.29. Averaged strain rates values recorded in various distance from cutting tip using FEM simulation .....	150
Figure 4.30. Determination of strain rate level in cutting process .....	152
Figure 5.1. Charpy impact test. a) primary mechanism; b) specimen dimension; c) test on granite; and d) test on PMMA.....	155
Figure 5.2. Machine modification. (a) schematic design of sample holder; the real picture of (b) sample holder; and (c) pin holder .....	158
Figure 5.3. Representative specimen for (a) Gouging and (b) Cerchar abrasiveness tests .....	161
Figure 5.4. The wear tool (Pin); (a) schematic design and (b) real picture .....	162
Figure 5.5. Testing procedure showing rock and pin interaction during scratching .....	164
Figure 5.6. The pin under the microscope; (a) before, and (b) after the Gouging abrasiveness test.....	165
Figure 5.7. (a) Calibration ruler, and (b) calibration process under microscope .....	165
Figure 5.8. Cerchar abrasiveness test; (a) testing apparatus, and (b) typical rock specimen .....	166
Figure 5.9. The pin under the microscope; (a) before, and (b) after the Cerchar abrasiveness test .....	167
Figure 5.10. Relationship between Mohs hardness and Rosiwal hardness (Thuro & Plinninger, 2003) .....	168
Figure 5.11. Relationship between the abrasiveness indexes and rock density.....	173
Figure 5.12. Relationship between the abrasiveness indexes and porosity .....	173

Figure 5.13. Relationship between the abrasiveness indexes and Young's modulus.....	174
Figure 5.14. Relationship between the abrasiveness indexes and Poisson's ratio.....	174
Figure 5.15. Relationship between the abrasiveness indexes and uniaxial compressive strength.....	175
Figure 5.16. Relationship between the abrasiveness indexes and tensile strength.....	175
Figure 5.17. Relationship between the abrasiveness indexes and shore hardness.....	176
Figure 5.18. Relationship between the abrasiveness indexes and Schmidt hammer rebound value.....	176
Figure 5.19. Relationship between the abrasiveness indexes and quartz content.....	177
Figure 5.20. Relationship between the abrasiveness indexes and equivalent quartz content.....	177
Figure 5.21. Relationship between the measured index and predicted index based on model 1: (a) CAI and (b) Gi.....	180
Figure 5.22. Relationship between the measured index and predicted index based on model 2: (a) CAI and (b) Gi.....	180
Figure 5.23. Relationship between CAI and Gi of tested rocks.....	181
Figure 5.24. Groove profile of Gouging test for low abrasive rock. (a) picture; (b) color-contoured map; (c) representative (A-A') cross-sectional profile.....	183
Figure 5.25. Groove profile of Gouging test for high abrasive rock. (a) picture; (b) color-contoured map; (c) representative (A-A') cross-sectional profile.....	184
Figure 5.26. Groove profile of Cerchar test for low abrasive rock. (a) picture; (b) color-contoured map; (c) representative (A-A') cross-sectional profile.....	184
Figure 5.27. Scratch test under an identical scratch length. (a) Gouging test; (b) Cerchar test.....	186
Figure 5.28. Comparison between the Gouging and Cerchar tests. (a) wear diameter vs. scratch length; (b) wear diameter of Gouging vs. Cerchar tests.....	187

## LIST OF TABLES

Table 2.1. Prediction models to estimate cutter forces.....	12
Table 2.2. Classification of loading techniques over a wide range of strain rates (Modified from Zhang and Zhao (2014b)).....	13
Table 2.3. Dynamic compression and tension experiments covering intermediate strain rate range.....	34
Table 3.1. The mineral contents of the rock samples .....	51
Table 3.2. Uniaxial compression test results .....	54
Table 3.3. Descriptive statistics on uniaxial compressive strength of tested rock types under three testing groups.....	56
Table 3.4. Brazilian tension test results.....	58
Table 3.5 Descriptive statistics on Brazilian tensile strength of tested rock types under three testing groups .....	59
Table 3.6. Mode-I fracture toughness test results.....	62
Table 3.7. Descriptive statistics on mode-I fracture toughness of tested rock types under three testing groups.....	63
Table 3.8. Punch shear test results.....	66
Table 3.9. Descriptive statistics on shear strength of tested rock types under three testing groups.....	67
Table 3.10. Parameters of the RHT model for rock material model ....	69
Table 3.11. Parameter of the referenced steel material used in this study.....	69
Table 3.12. DIF tested mechanical properties at ISR range for granite and sandstone tested in this study.....	81
Table 4.1. Linear cutting test results.....	104
Table 4.2. Input parameters for Drucker Prager strength criterion in AUTODYN® simulation.....	111
Table 4.3. Results FEM linear cutting simulation with quasi-static and dynamic strength input properties.....	115

Table 4.4. The results of FEM simulation with quasi-static and dynamic strength input properties compared to laboratory LCM test with their mean absolute errors .....	120
Table 4.5. Summary of the selected results of the MLR analysis in predicting mean and peak cutting forces from three independent variables from the SPSS statistical program .....	125
Table 4.6. Summary of the selected results of the MLR analysis in predicting mean and peak cutting forces from two independent variables from the SPSS statistical program (DV: dependent variable and IV: independent variable).....	127
Table 4.7. Summary of mechanical properties, cutting configuration, and cutting forces from various estimations .....	132
Table 4.8. Statistical analysis of the theoretical and prediction models.....	135
Table 4.9. Strain rate estimation from operational data of several cutting machines .....	139
Table 4.10. Results of strain rate estimation of disc cutting on granite rock .....	141
Table 4.11. Strain rate measured at 2 cm and 4 cm from the cutting line resulted by laboratory LCM test and FEM simulation ....	148
Table 4.12. Averaged strain rate from FEM cutting simulation.....	150
Table 5.1. Charpy impact test results including strain rate information .....	156
Table 5.2. Type, location, and mineral composition of rock samples used in the Gougging and Cerchar abrasiveness tests .....	159
Table 5.3. Mineral composition and its equivalent quartz content.....	169
Table 5.4. The result of CAI, Gi, and physical and mechanical properties of tested rocks .....	171
Table 5.5. Recapitulation of coefficient of determination ( $R^2$ ) and p-value of all independent variables .....	178
Table 5.6. Results of multiple linear regression of model 1 and model 2 .....	179
Table 5.7. Results wear diameter of Gougging and Cerchar abrasiveness tests under an identical scratch length .....	186

# 1. INTRODUCTION

## 1.1 Background

Mining and civil projects, whether carried out on surface or in underground, consist of excavation of rock material. The increasing trend towards modern mechanized methods has made a significant contribution to the rock excavation industry with the opportunity to replace the traditional drill-and-blast method in the long run. Furthermore, with the increase of safety and environmental awareness, in general, mechanized excavation offers fewer consequences than the drill-and-blast method in both aspects (Vogt, 2016).

Mechanized excavation provides considerable advantages over the drill-and-blast method (Hood et al., 1989):

1. It is a continuous process that can break, load, and transport the broken rock from the working area to the stockpile. Unlike, the blasting process requires a cyclic process that is not easy to automate.
2. It results in minimum overbreak that may lead to the reduction of operational costs. In blasting operation, special care should be carried out to minimize overbreak in the rock surface.
3. It produces a relatively uniform rock fragment size that eases the transportation of rock debris by conveyor. In drill-and-blast, it is rather challenging to control the outcome of fragmented rock.
4. It potentially has the capability for selective mining, which allows the operator of the machine to control the cutter head to

mine the ore separately from the waste material, while in blasting, the excavation should be advanced entirely towards rock mass.

Due to its considerable advantages, the demand and application of mechanical excavation have been steadily increasing in many civil and mining projects (Jeong, 2017). Thus, the prediction of the performance of mechanical cutting is one of the main concerns in determining the economy of a mechanical excavation project, especially in the feasibility stage (Bilgin et al., 2014). The performance prediction will inform engineers to select a proper machine to be used in operation. An inaccurate performance prediction will affect the cost and time overruns in the entire project. A lesson learned can be taken out from Korea's Busan metro railway project line-2 section-230 in 2002. A slurry pressure balanced (SPB) TBM is employed to cut 840 m (418 m outbound + 422 m inbound) with 7.1 m diameter of the tunnel. It required 11 months to excavate the outbound tunnel due to frequent replacement of the 14-inch disk cutters. In contrast, after replacing the cutter head and the disk cutters to the size of 17-inch, it took only four months to finish the inbound tunnel (Kim et al., 2002). The other example can be studied from Gwangju metro railway project line-1 section-TK-1. Korea Agency for Infrastructure Technology Advancement, KAIA (2010) reported that the earth pressure balanced (EPB) TBM was unable to advance according to the plan, given the advance rate as low as 0.6 m/day. The cutter head was replaced due to severe damage; thus, the project experienced unexpected delays and substantial cost overruns. These examples teach us the importance of machine performance prediction, particularly in the mechanical excavation project.

Most methods used in rock fragmentation are based on dynamic transient loading (Lundberg, 1976), involving high-speed rotation, percussion, as well as thermal loading (Lindholm et al., 1974). Rock breakage based on explosion and percussion involves dynamic fracture that induces the rock into tension, initiating fracture, and fragmentation (Grady & Kipp, 1979). Additionally, in mechanized excavation, high-intensity vibration and torque fluctuation are produced. The vibration will damage machine components, including tools and gearboxes, and may ultimately lead to the premature failure of the machine (Fowell et al., 1988). In rock fragmentation by cutting, the interaction between the cutting tool and rock surface, both for dragging and indenting mechanisms, is a dynamic process. In drag cutting, for example, in pick cutting of a roadheader, the tool attacks the rock in a rapid motion. The fast-moving pick creates an impact on the rock surface. Also, due to the irregularity of the excavated surface, the tool-rock interactions perform multiple dynamic events during the cutting process. Similarly, in indenting cutting such as disc cutter cutting of a TBM, slow-motion video evidently shows that it is a dynamic process. Furthermore, in a mixed ground condition; with the appearance of strength contrast of rock, non-uniformity of grain size, the existence of significant fragments such as cobbles; the cutting tools experience more dynamic process than in a uniform ground condition due to the work face variability during the cutting process.

The existing theoretical and experimental studies on rock cutting performance primarily concentrated on cutting parameters and static mechanical properties of rock (Bilgin et al., 2006; Evans, 1984a, 1984b; Goktan, 1997; Nishimatsu, 1972; Roxborough & Liu, 1995; Yilmaz et al., 2007). Although rock cutting is a dynamic process, none of the existing prediction models considers the dynamic rock properties. It is

doubtful that the static strength of fracture criteria will be sufficient to describe the dynamic process (Lindholm et al., 1974). Various studies reported that the strength in the dynamic condition would increase significantly compared with the static strength (Dai & Xia, 2013; Kubota et al., 2008; Li et al., 2005; Xia et al., 2017; Zhao et al., 1999). Therefore, this condition will potentially cause misleading results in performance prediction and machine selection in an excavation project.

Mechanical tools excavate the hard rock at a slower rate than in blasting fragmentation (Zhou et al., 2015), but it is faster than the quasi-static loading regime. Thus, in this study, the range between quasi-static and high strain rate (HSR) loading, namely the intermediate strain rate (ISR) loading, is considered. This loading involves a relatively narrow range of strain rates from  $10^{-1}$  to  $10^1$   $s^{-1}$ . Simple calculations based on the specification of some excavation machines show that cutting by roadheaders will generate loading at the strain rate of about  $0.76 - 1.03$   $s^{-1}$ , while TBM will cut the rock at the rate of roughly  $0.43 - 0.91$   $s^{-1}$  (the detailed calculation is presented in Chapter 4.7.1). Those typical rates fall in the ISR loading range.

Assessment of rock abrasiveness is also crucial when dealing with mechanical excavation works. The abrasiveness of rock controls the wear amount of cutting tools; therefore, it has a significant impact on the service life and efficiency of the tools. Cutting tools are subjected to a dynamic load in which the tools interact with the rock at high-speed velocity and unpredictable angle of occurrence. To address the issue, an abrasiveness test under dynamic mode should be considered. One of the available methods is called the Gouging test (Golovanevskiy & Bearman, 2008). The method and testing apparatus allow the pin/stylus to interact with the rock surface in high-speed gouging/sliding impact abrasiveness

mode, which imitates the process that is experienced by cutting tools in the field.

This study highlights the importance of dynamic rock properties in the application of mechanical excavation. First, a comprehensive review of the mechanical properties of rock at the ISR loading is discussed. Then, laboratory tests to obtain the ISR rock strength under various modes are conducted. Also, laboratory tests and numerical simulations on the linear cutting test are carried out, and the results are discussed. Furthermore, simple prediction models based on the laboratory data from various references considering dynamic properties are developed and compared with some theoretical models. Finally, the abrasiveness test under dynamic mode is carried out, and the results are compared with the well-know Cerchar abrasiveness test. In general, this study contributes to the field of rock engineering in viewing the rock cutting phenomenon from a dynamic perspective.

## **1.2 Objectives of the Study**

The aims of this study can be summarized as follows.

1. To gain more understanding of the dynamic behavior of rock, especially under the intermediate strain rate loading that is presumed as the dynamic range of the rock cutting process
2. To investigate the rate dependency of rock strength and toughness through various testing modes and suggest the representative dynamic increase factor under intermediate strain rate loading

3. To develop the numerical model to simulate the linear cutting test using multiple input properties and compare the results with the laboratory works
4. To develop a simple prediction model based on multiple linear regression that includes dynamic properties of rock
5. To estimate the dynamic level of the rock cutting process through literature surveys, laboratory works, and numerical simulations
6. To discuss the Gouging abrasiveness test that considers dynamic features in its procedure and compare it with the well-known Cerchar abrasiveness test

### **1.3 Scope of the Study**

The scope of this study is presented as follows.

- Chapter 1 introduces the background and the specific objectives that need to be addressed in the study.
- Chapter 2 presents the literature reviews, including the rock breakage process induced by mechanical cutting as well as some well-known rock cutting theories. Past studies on dynamic rock experimentation, particularly in the intermediate strain rate loading and some features related to it, are also reviewed in this chapter. Finally, brief reviews on rock abrasiveness tests and numerical simulation concepts using explicit dynamic simulation are addressed.
- Chapter 3 demonstrates the use of non-explosive reaction-driven loading apparatus for dynamic testing. The testing procedures, testing types, and the results of quasi-static and dynamic tests are

presented. Numerical simulations, discussions, and comparisons with other references are also described.

- Chapter 4 covers the linear cutting test experimentation, both laboratory and numerical simulation methods. Extensive discussions are also made comparing both methods. Prediction models based on a statistical approach are derived, and finally, the strain rate level during the cutting process is estimated through several approaches.
- Chapter 5 highlights the Gouging abrasiveness test that includes dynamic features in its procedure. The results from the Gouging test are compared with the ones from Cerchar abrasiveness test. Correlations between those abrasiveness tests and some geomechanical properties are also derived.
- Chapter 6 summarizes the main ideas and conclusions of this study.

## **2. LITERATURE REVIEW**

### **2.1 Rock Breakage Mechanism by a Rock Cutting Tool**

In general, the rock cutting mechanism by a mechanical tool can be classified into two groups: indentation and dragging. The difference between these two methods is that, in the indentation, an indenter attacks the rock by applying a force that is primarily in the normal direction to the rock surface. On the other hand, the main force applied by a drag bit is mainly parallel to the rock surface. Disc cutters, percussion drill bits, impactors are the example of tools that induce rock breakage by indentation process. Radial cutters (wedge and chisel cutters) and conical cutters break the rock by applying the main force over the rock surface in a parallel direction. Drag bits, or often mentioned as picks, attack the rock to initiate a tensile fracture in a relatively direct manner while indenters generate tensile stress by crushing the rock mass underneath the tools.

There are numerous theoretical explanations of rock breakage mechanisms by cutting (Evans, 1962; Paul & Sikarskie, 1965; Potts & Shuttleworth, 1958; Reichmuth, 1963). Moreover, a comprehensive review of the physical mechanisms of hard rock fragmentation under mechanical loading has been published by Mishnaevsky (1995). The rock breakage mechanisms are similar in all cutter shapes (Bilgin et al., 2014). In general, the breakage process starts when the tool indents the rock surface, as the stress increases, a crushed zone takes place beneath the tool due to the high concentration of compressive stress induced by the tool. This compressive stress concentration induces a tangential tensile stress field and then generates tensile fractures. As the process

continues, a median crack starts to develop into the rock and is followed by secondary tensile cracks that are developed radially away from the crushed zone. The tensile cracks then propagate to the free surface or connect to adjacent tensile cracks to form, commonly called rock cutting chips. The typical rock breakage mechanism by a rock cutting tool can be seen in Figure 2.1.

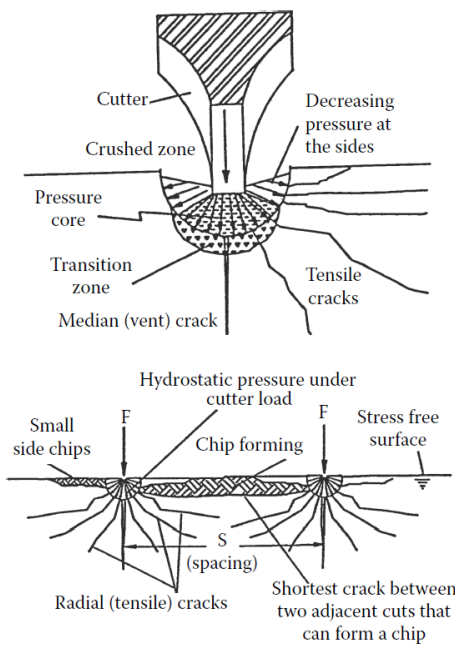


Figure 2.1. Idealized tensile breakage under constant-cross-section disc cutter (Adapted from Rostami and Ozdemir (1993))

The cut spacing between picks is an important parameter to achieve efficient cutting. If the picks are well-positioned (at optimum cut spacing), it is an excellent condition to cut the rock efficiently, i.e., producing material in desirable fragment size, with economical use of power, and minimum fine particles (Evans, 1982). Depending on the

penetration depth of the cutting tool, the optimum cut spacing may vary, so the ratio between cut spacing to the penetration depth ( $s/p$ ) is often used when determining the optimum cutting condition. In practice, the optimum condition of  $s/p$  ratio is achieved when a scenario of  $s/p$  gives a minimum value of specific energy that is the minimum required work to cut a unit volume of rock.

During the rock breakage process by cutting, three forces acting on the tip of the cutting tool, i.e., cutting, normal, and side forces, and they are perpendicular to each other. The cutting force acts parallel to the cutting line while the normal force acts perpendicularly, and the side force acts laterally. They are essential parameters in the machine selection process since they define the thrust, torque, as well as the balance of the cutting machine (Jeong, 2017).

## **2.2 Theoretical and Empirical Models for Rock Cutting**

Numerous formulations have been published by many scientists to explain the rock cutting mechanism induced by a cutting tool. The majority of them are developed from rock properties while simplifying geometrical parameters. One of the pioneers in rock cutting study is Evans (1962, 1965, 1972, 1982, 1984a, 1984b). Evans performed some works on rock cutting in coal and established a fundamental principle of rock cutting that has been widely used in the designing process of excavation machines such as roadheaders, shearers, and continuous miners. Evans developed the theoretical model based on tensile fracturing and claimed that, in addition to some geometrical features, tensile strength and compressive strength of rock are the affecting parameters to the cutting force of chisel and conical picks.

Goktan (1997) modified Evans' cutting theory by considering the friction angle between a rock and a cutting tool to the equation. A similar modification was made by Roxborough and Liu (1995) with their experiment on Grindelford sandstone. They suggested that the friction angle between rock and tool was  $16^\circ$ , based on the friction angle between a steel block and a natural flat rock surface.

Nishimatsu (1972) developed a prediction model by introducing shear fracturing. Nishimatsu applied a similar principle as the established formula in metal cutting (Merchant, 1944). He used the Mohr-Coulomb failure criterion and suggested that shear strength is the parameter driving the formation of the chip. Additionally, the internal friction angle and the friction angle between a rock and a tool were also introduced in the formula.

An empirical study on the effect of dominant rock properties on cutting performance has been done, specifically for 22 different rocks from Turkey (Bilgin et al., 2006; Copur et al., 2003). They found out that uniaxial compressive strength, tensile strength, and Schmidt hammer rebound value were the most dominant parameters affecting the cutting force obtained from the linear cutting test. The proposed empirical model was statistically reliable with the theoretical models. However, they suggested that a correction factor on the tip angle calculation must be made to improve the rock cutting theory.

Yilmaz et al. (2007) derived an equation including six independent variables to predict cutting force a radial bit. The equation included shear strength, depth of cut, bit width, the friction angle between a rock and a tool, rake angle, and uniaxial compressive strength. The experiment was subjected to four different rock types, and it was shown that the

prediction model was superior to other models within a given range of applications. The theoretical and empirical models explained above are listed in Table 2.1.

Table 2.1. Prediction models to estimate cutter forces

Reference	Normal Force (N)	Cutting Force (N)	Tool
Merchant (1944)	-	$FC = 2 \cdot d \cdot \sigma_s \cdot \tan^{\frac{1}{2}}(90 - \alpha - \psi)$	Chisel
Evans (1962, 1965, 1972, 1982, 1984a, 1984b)	-	$FC = \frac{2 \cdot \sigma_t \cdot d \cdot w \cdot \sin \frac{1}{2}(\frac{\pi}{2} - \alpha)}{1 - \sin \frac{1}{2}(\frac{\pi}{2} - \alpha)}$	Chisel
	-	$FC = \frac{16 \cdot \pi \cdot \sigma_t^2 \cdot d^2}{\cos^2(\frac{\phi}{2}) \cdot \sigma_c}$	Conical
Nishimatsu (1972)	-	$FC = \frac{2 \cdot \sigma_s \cdot d \cdot w \cdot \cos(\psi - \alpha) \cdot \cos(i)}{(n + 1) \cdot [1 - \sin(i + \psi - \alpha)]}$	Chisel
Goktan (1997)	-	$FC = \frac{4 \cdot \pi \cdot d^2 \cdot \sigma_t \cdot \sin^2(\frac{\phi}{2} + \psi)}{\cos(\frac{\phi}{2} + \psi)}$	Conical
Roxborough and Liu (1995)	-	$FC = \frac{16 \cdot \pi \cdot d^2 \cdot \sigma_t^2 \cdot \sigma_c}{\left[2 \cdot \sigma_t + \left(\sigma_c \cdot \cos\left(\frac{\phi}{2}\right)\right) \left(\frac{1 + \tan\psi}{\tan(\phi/2)}\right)\right]^2}$	Conical
Bilgin et al. (2006)	$FN = 1.217\sigma_c^{1.104} \times d$	$FC = 0.826\sigma_c + 21.76$	Conical
Yilmaz et al. (2007)	-	$FC = -24.504 + 0.513\sigma_s + 1.873d + 0.249\psi + 0.227w + 0.154\alpha - 0.047\sigma_c$	Chisel

Symbols remark:

$\sigma_s$ : Shear strength  
 $\sigma_c$ : Compressive strength  
 $\sigma_t$ : Tensile strength  
 $\alpha$ : Rake angle of the cutting tool  
 $\psi$ : Rock and tool friction angle

$d$ : Depth of cut  
 $w$ : Width of the cutting tool  
 $i$ : Angle of internal friction  
 $n$ : Stress distribution factor  
 $\phi$ : Tip angle of the conical cutter

### 2.3 Loading Classification over Strain Rate

In general, the loading level based on its strain rate is classified into five classifications (Zhang & Zhao, 2014b), as shown in Table 2.2. The first classification is the creep loading with the strain rate level ranging from  $10^{-8}$  to  $10^{-5} \text{ s}^{-1}$ . To produce a creep loading, a specialized machine that performs a constant load with a prolonged time interval is used. The creep law is primarily considered to explain the time-dependent mechanical behavior of rock. The second classification is the quasi-static loading condition. The range of quasi-static loading conditions is from  $10^{-5}$  to  $10^{-1} \text{ s}^{-1}$ . This loading can be produced by a standard hydraulic servo-controlled testing machine. This loading condition is usually used by most of the standard testing methods such as the International Society for Rock Mechanics and Rock Engineering (ISRM) Suggested Method and American Society for Testing and Materials (ASTM) to obtain stress-strain curve and to determine elastic properties of rock material.

Table 2.2. Classification of loading techniques over a wide range of strain rates (Modified from Zhang and Zhao (2014b))

Classification	Strain rate ( $\text{s}^{-1}$ )	Loading technique
Creep	$10^{-8} - 10^{-5}$	Specialized hydraulic machine
Quasi-static	$10^{-5} - 10^{-1}$	Servo-controlled hydraulic machine
Intermediate strain rate	$10^{-1} - 10^0$	Pneumatic-hydraulic machine
	$10^0 - 10^1$	Drop weight machine
High strain rate	$10^1 - 10^4$	Split Hopkinson pressure bar
Very high strain rate	$10^4 - 10^6$	Plate impact technique

The third classification is the intermediate strain rate (ISR) loading condition. This loading condition is ranging from  $10^{-1}$  to  $10^1 \text{ s}^{-1}$ . This loading can be generated by a pneumatic machine, a combined hydro-

pneumatic machine, a drop weight, a pendulum hammer, and a slow rate version of a split-Hopkinson pressure bar (SHPB). A more detailed description of some of the machines is presented later in this document.

The fourth classification is the high strain rate (HSR) loading condition. The most successful loading technique that has been widely used is the one using an SHPB. The standard strain rate level that can be achieved by SHPB is ranging from  $10^1$  to  $10^4 \text{ s}^{-1}$ . Strain rate level of  $10^4 \text{ s}^{-1}$  or higher, the fifth classification, is classified as a very high strain rate (VHSR). The loading technique that has been used for this classification is a plate impact technique.

#### **2.4 Intermediate Strain Rate (ISR) Loading**

The ISR loading condition has a relatively narrow range of strain rates. According to Zhang and Zhao (2014b), it lies between  $10^{-1}$  and  $10^1$  per second. These strain rates are not reachable with either conventional split-Hopkinson pressure bar (SHPB) or ordinary hydraulic servo-controlled loading machine. The data in the ISR range is limited; thus, experimental data have always been necessary to be filled so that the full range of rate-dependent material model can be established over the entire strain rate range. The fact is that less attention was put on the ISR range. One of the possible reasons is the difficulty of experimenting. ISR has been associated with specialized machines, e.g., pneumatic-hydraulic-driven compression machine and modified split-Hopkinson pressure bar, which require extra efforts in manufacturing the devices.

However, it should be noted that this range is crucial. In real engineering practices, this range of strain rate needs to be properly considered. For example, in tunnel construction, the excavation includes a high-speed

rotary and percussion bits in drilling and also an impact of the cutting tool to the rock in mechanical excavation. The impact loading rate belongs to the ISR and is presumed to be far lower than the strain rate generated by an explosive wave of blasting process and higher than the quasi-static loading regime.

#### **2.4.1 Intermediate Strain Rate Loading Techniques**

A few studies can be found dealing with ISR loading conditions. To produce the ISR loading, dynamic loading equipments have been used for laboratory experiment, i.e., fully gas-driven (Green & Perkins, 1968; Logan & Handin, 1970), pneumatic-hydraulic-driven (Tarigopula et al., 2009; Zhao et al., 1999), drop weight (Hogan et al., 2012; Reddish et al., 2005; Whittles et al., 2006), and modified SHPB (Li et al., 2005; Zhu et al., 2015). The working principles of those devices are briefly described in this chapter.

##### *2.4.1.1 Fully Gas-Driven Loading Machine*

The device used a few decades ago by Green and Perkins (1968) was entirely driven by gas. A lightweight movable piston can travel in one direction for compression and the other direction for tension testing. The piston velocity, and hence the loading rate, is driven by the size of the discharge orifice, the gas used, the pressure in the reservoirs, and the test specimen (see Figure 2.2). By proper selection of gas, pressure, and orifice size, the desired constant strain (or loading) rate can be obtained for any specimen. An upper limit based on stress wave propagation might be as low as  $10\text{-}20\text{ s}^{-1}$  (Green & Perkins, 1968).

Using a similar principle as SHPB but in the vertical direction, the load applied to the specimen is measured by strain gauges attached to the elastic load bar located precisely above the tested specimen. Specimen strain is obtained by measuring piston displacement, by using strain gauges glued on the specimen, or by using an optical extensometer which looks at marks placed on the specimen.

A substantially similar machine was also manufactured by Logan and Handin (1970) to conduct a series of triaxial tests at the rates between  $10^{-2}$  and  $1 \text{ s}^{-1}$ , with the confining pressures of 7 and 3 kilobar, respectively.

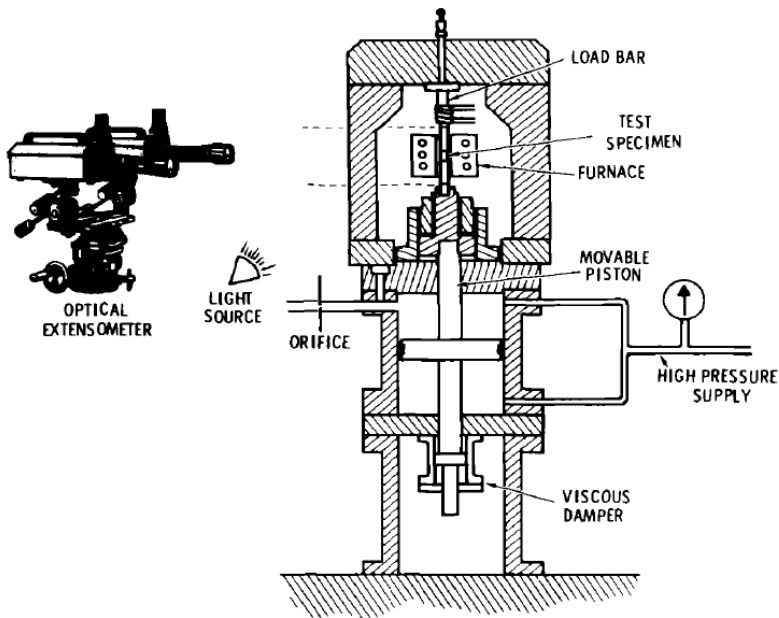


Figure 2.2. Schematic diagram of the intermediate strain rate machine with a fully gas-driven operation (Green & Perkins, 1968)

#### *2.4.1.2 Pneumatic-Hydraulic Loading Machine*

Zhao et al. (1999) explained clearly how the pneumatic-hydraulic loading machine works. According to them, the loading machine consists of two gas cylinders (A and B), a connecting piston, a release valve, a regulating valve, an oil cylinder, and a loading piston, as presented in Figure 2.3(a). Initially, the pressure in the gas cylinders A and B are increased to a preferred value, to produce stress that can break the tested specimen. When the release valve is opened, gas in the cylinder B escapes and the pressure quickly drops to zero. At the same time, the gas from the cylinder A pushes down the connecting piston. The movement of the connecting piston generates pressure in the oil cylinder and pushes the loading piston to apply a dynamic load to the tested rock. The regulating valve controls the oil flow between the upper and lower parts of the cylinder, which means controlling the loading rate of the loading piston. Axial dynamic load, axial strains, and lateral strains are measured and recorded to plot the stress-strain curve. The axial load is measured by a load cell consisting of a strain-gauged high strength steel block. Axial and lateral strain gauges are attached to the rock specimen at a proper position. Stress and strain histories are recorded by a data acquisition system (see Figure 2.3(b)).

The other type of pneumatic-hydraulic loading machine has been used to test metallic materials (Tarigopula et al., 2009) and rock material (Cadoni, 2010) in direct tension mode. The machine is driven by gas and water with a lightweight movable piston. The motion of the piston is controlled by the pressure gap between the two chambers. Both chambers are initially set to equal pressure by injecting nitrogen gas into one chamber and water in the other chamber at the end of the piston, thus creating an equilibrium pressure. The pressure gap is created by a fast

opening of valve 6 (see Figure 2.4) to allow quick transfer of water through the orifice. As a result, the piston moves and stresses the specimen to fracture. The force exerted by the constant gas pressure on the piston is then equilibrated by the resistance of the specimen, by the friction of the piston movement and by the resistance of the water flow, which results in a constant speed of the piston. The size of the orifice opening controls piston velocity. The load resisted by the specimen is measured with strain gauges on the elastic bars in which the specimen is fixed. The specimen elongation is measured using a laser type displacement transducer, which senses the displacement of a metallic strip connected to the piston shaft. The illustration is given in Figure 2.4.

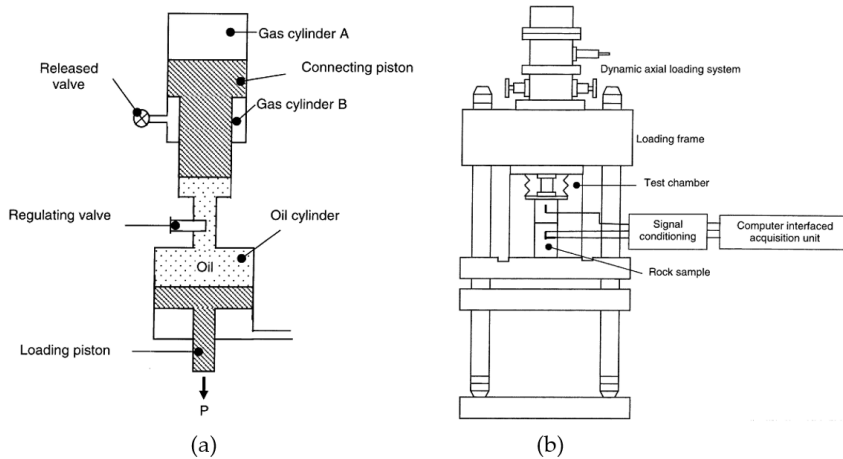


Figure 2.3. (a) Working principle of the pneumatic-hydraulic loading system; (b) schematic layout of the machine and the data acquisition system (Zhao et al., 1999)

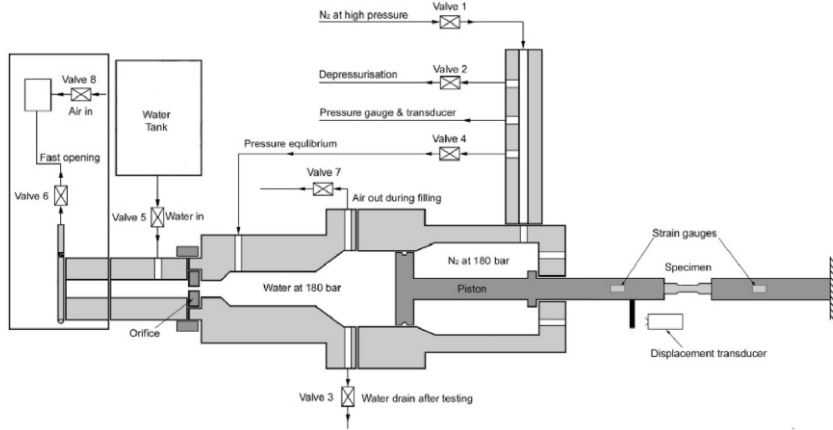


Figure 2.4. Schematic diagram of pneumatic-hydraulic loading machine (Tarigopula et al., 2009)

### 2.4.1.3 Drop Weight Loading Machine

Most of the investigators used a drop weight machine to study rock fragmentation employing impact loading in rock comminution (Hogan et al., 2012; Reddish et al., 2005; Whittles et al., 2006). However, some of them use this technique to study fracture toughness behavior (Islam & Bindiganavile, 2012).

The drop-weight machine uses a simple mechanism to break the rock specimen. The only principle used is gravitational potential energy which is determined from the mass of the drop weight and the distance through which it falls prior to impacting the specimen ( $E = mgs$ , where  $E$  = energy in joules,  $m$  = mass of the drop weight in kilogram,  $g$  = gravitational acceleration =  $9.81 \text{ m/s}^2$  and  $s$  = drop height in meter). Energy calculation is based on the momentum acting on the falling weight and calculating the resultant temporal impact velocity. Drop weight machine has been used for strain rate up to  $10^1 \text{ s}^{-1}$ . The example

of the drop weight testing machine that was used by Reddish et al. (2005) is shown in Figure 2.5.

According to Zhang and Zhao (2014b), there are some limitations on using a drop-weight machine:

- the technique is passive, and the testing conditions are determined by trial and error from empirical parameters,
- the rate and form of the compressive loading depend on both the specimen and machine compliance, as well as the average energy of the falling weight,
- great care should be taken in interpreting experimental data because of coupling effects between machine vibration and wave propagation,
- the calculated displacement might be inaccurate because the deformation in the system could be higher than the specimen deflection, and
- the loading rate cannot be controlled, and thus multiaxial tests are unreliable.

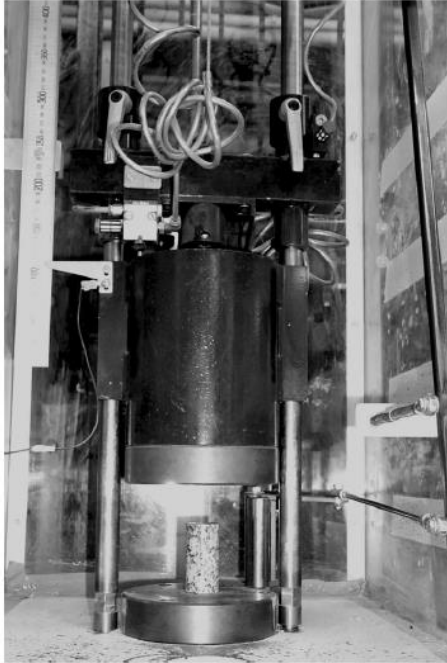


Figure 2.5. The drop weight test device (Reddish et al., 2005)

#### *2.4.1.4 Modified Split-Hopkinson Pressure Bar*

An SHPB driven by a pendulum hammer apparatus was used by Zhu et al. (2015) to conduct a set of Brazilian tension test in the intermediate strain rate loading condition. Pendulum hammer is used as a loading device. Pendulum hammer impacts an incident bar to produce the impact stress wave. A Brazilian disc is placed in between the incident and the transmission bars. A momentum trap device is placed on the other end of the transmission bar. Both bars have a length of 2.0 m. Data acquisition and a recording device that consists of a preamplifier, a digital oscilloscope, and a computer are used to monitor and collect the data from the test. Strain gauges are glued parallel to the bar axis on both incident and transmission bars to measure the strain on the bars that will be used to calculate the forces that occur at both ends of the test specimen.

The impact velocity is controlled by adjusting the swing angle of the pendulum hammer. The range of strain rate that can be achieved by this apparatus is up to  $10^2 \text{ s}^{-1}$ . They claimed that the pendulum hammer-driven SHPB is an excellent choice to test the rock behavior at intermediate strain rate. The reason is that the incident wave excited by the pendulum hammer is triangular, featuring a long rising time, and it is considered to be an ideal pulse for achieving a constant strain and maintaining the stress equilibrium (Zhu et al., 2015). They claimed that it is not necessary to utilize the pulse-shaping technique for obtaining a triangular incident pulse. A schematic view of the pendulum hammer-driven split Hopkinson pressure bar is shown in Figure 2.6.

A modification of SHPB was also done by Li et al. (2005) by increasing the diameter of the bars to 75 mm. The application of the machine has been successfully tested on granitic sandstone at the strain rate of about  $10^1 \text{ s}^{-1}$ .

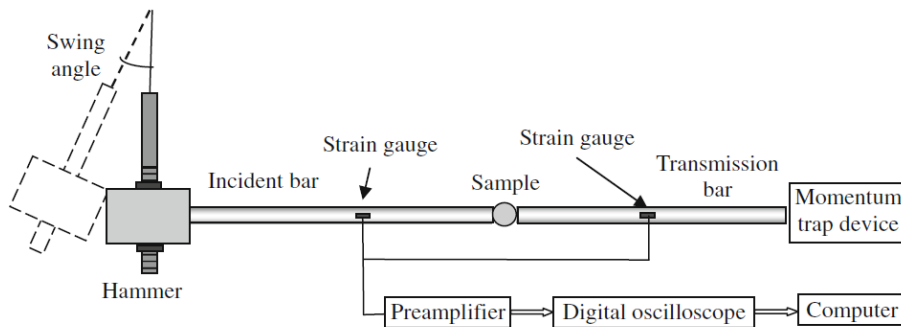


Figure 2.6. Schematic view of pendulum hammer-driven split Hopkinson pressure bar (Zhu et al., 2015)

## 2.4.2 Dynamic Rock Behavior under Compression in Intermediate Strain Rate

For the past decades, many investigators had put their effort into understanding the dynamic behavior of compressed rock. However, only a few of them covered the rates that belong to an intermediate strain rate range. One of the pioneers conducting a dynamic uniaxial compression test on the geologic materials that cover the intermediate strain rate was (Green & Perkins, 1968). They conducted a series of compression tests on three types of rock, namely Solenhofen limestone, Westerly granite, and volcanic tuff. The range of strain rate was from  $10^{-4}$  to  $10^3$  employing a fully gas-driven compression machine for the low and intermediate strain rate and a split Hopkinson pressure bar for a high strain rate. A notable result was found in the Solenhofen limestone. Limestone shows the sensitivity of failure stress to strain rate, particularly at the strain rate above  $10^2$  per second with a dramatic increase while at the strain rate below  $10^2$  per second, the failure stress is less sensitive to the strain rate increases. They assumed that the increased failure stress is affected by the thermal activation mechanism, analogous to the plastic behavior of metal.

To see the heat effect on the dynamic failure stress, Lindholm et al. (1974) conducted a series of tests on Dresser Basalt subjected to triaxial compression. The relationship between principal stresses ( $\sigma_1$ ,  $\sigma_2$ ,  $\sigma_3$ ), temperature, and strain rate were derived. The strain rate covered in the test was  $10^{-4}$  to  $10^3$ , with the maximum confining pressure and temperature of 100,000 psi ( $\approx 690$  MPa) and 1,400 °K ( $\approx 1,127$  °C). They claimed that at the high strain rate, there is no sufficient time available for the thermal activation process. Lankford's investigation (Lankford, 1981) on ceramic material supports the previous statement that a

dramatic increase of material strength in a high strain rate (above  $10^2$  per second) does not involve the change of temperature in the failure process. Lankford (1982) claimed that material inertia controls the strength of the ceramic material in the high strain rate loading ( $10^2$  to  $10^4$  per second). Blanton (1981) carried out a set of experiments on three rock types, i.e., Charcoal granodiorite, Berea sandstone, and Indiana Limestone subjected triaxial compression. In the strain rate ranging from  $10^{-2}$  to  $10^1$  per second, he found that there are three different types of behavior observed with increasing strain rate, precisely (1) either a constant strength or a constant rate of increase in strength; (2) a sudden increase in strength above specific rate; (3) apparent fluctuations in strength above a certain rate. However, he argued that the dramatic increase in failure stress is due to machine inertial effect and does not exhibit a real increase in rock strength.

Zhao et al. (1999) studied the effect of loading rate on Bukit Timah granite of Singapore. A pneumatic-hydraulic loading machine was used to load with the range of  $10^0 - 10^5$  MPa/s. Fracture stress increases by about 15% with increasing loading rate. In the higher loading rates, the number of microcracks increased with the rates. As the number of microcracks increased, the number of failure surfaces also increased (Swan et al., 1989). Bukit Timah granite was also used by Li et al. (2005) to observe rock behavior in dynamic loading. A large diameter of SHPB with a tapered striker bar was developed. The new shape of the striker bar controlled the loading so that a half-sine waveform can be generated on the input bar. They claimed that the half-sine waveform provides a relatively stable strain rate and smooth stress-strain relationship. They found that the strength increases with increasing strain rate. Growth in rock strength with the strain rate is related to high energy absorption

attributed to a larger number of small fragments and higher fracture surface at high strain rates. The fragment size distribution is strain rate dependent (Wang & Tonon, 2011). The higher the applied strain rate is, the smaller the average fragment size is. By using the discrete element method (DEM), however, the fragment size distribution cannot be well predicted (Wang & Tonon, 2011).

The investigation of strain rate dependency on oil shale material has been done by Lankford (1976). He tested ninety-eight specimens at various confining pressures (0, 35, 69, and 138 MPa) and various strain rates ( $10^{-4}$  to  $10^3$  per second). The slow intermediate strain rates were performed with a servo-controlled hydraulic ram, while the high strain rate was carried out by SHPB. From 18 unconfined tests, Lankford concluded that failure strength increased with strain rate. The actual failure stress of the oil shale approximately tripled, going from about 62 MPa to 165 MPa within the testing range of strain rate. Chong et al. (1980) did similar experiments for different oil shale specimens. They observed three distinct grades of the oil shale, namely lean, medium, and rich. The relationship between strength, organic content, and strain rate was derived. The monotonic increase in strength is different from Lankford's exponential rise at a certain level.

Strain rate dependence was discovered not only for geologic material but also for a stony meteorite called MacAlpine Hills chondrite that was studied by Kimberley and Ramesh (2011) under uniaxial compressive loading. They found a slight increase in compressive strength as the strain rate is increased from  $10^{-3}$  to  $10^{-1}$  per second. However, a vivid rate of dependency was observed in the range of  $10^2$  to  $10^3$  per second. The dynamic strength is nearly four times its static strength, which is

unusual for terrestrial material that has approximately two to three times of increasing.

Recently, to see the effect of bedding direction of coal specimens under compression, a series of static and dynamic tests were carried out (Liu et al., 2015). The range of strain rate observed was from  $10^{-5}$  to  $10^2$  per second. The specimens were tested in two directions of the bedding plane, i.e., parallel and perpendicular to the bedding directions. They found that the compressive strength, Young's modulus, and energy consumption increase with increasing strain rates, and the bedding effect of coal is not observable as the strain rate increases. The bedding direction no longer affects the coal behavior beyond a certain level of strain rates (demarcation points) both in static and dynamic loading conditions.

The uniaxial compressive strength of various rocks obtained from various strain rates are depicted in Figure 2.7. The plot shows the strength of the rocks instead of the increase. In this case, the compressive strength of rocks will vary depending on the rock types. So, no relationship could be seen from it.

To indicate the increased of the strength under various strain rates, the results of dynamic strength are normalized in terms of dynamic increase factor (DIF), which is defined as the ratio of the dynamic values of the compressive failure stress to the static one. Figure 2.8 shows the DIF over the full range of strain rates from various references. For both quasi-static (left side) and high strain rate range (right side), the tendencies are clear. In quasi-static, ranging from  $10^{-5}$  to  $10^{-1}$ , the DIF tends to increase gently. Most of the tests in this range were performed by a hydraulic servo-controlled loading machine. On the other hand, in a high strain rate ranging from  $10^1$  to  $10^5$ , the DIF increases significantly up to two to three

times for geologic rock and four times for meteorite rock. All of the works in the high strain rate range were carried out by SHPB.

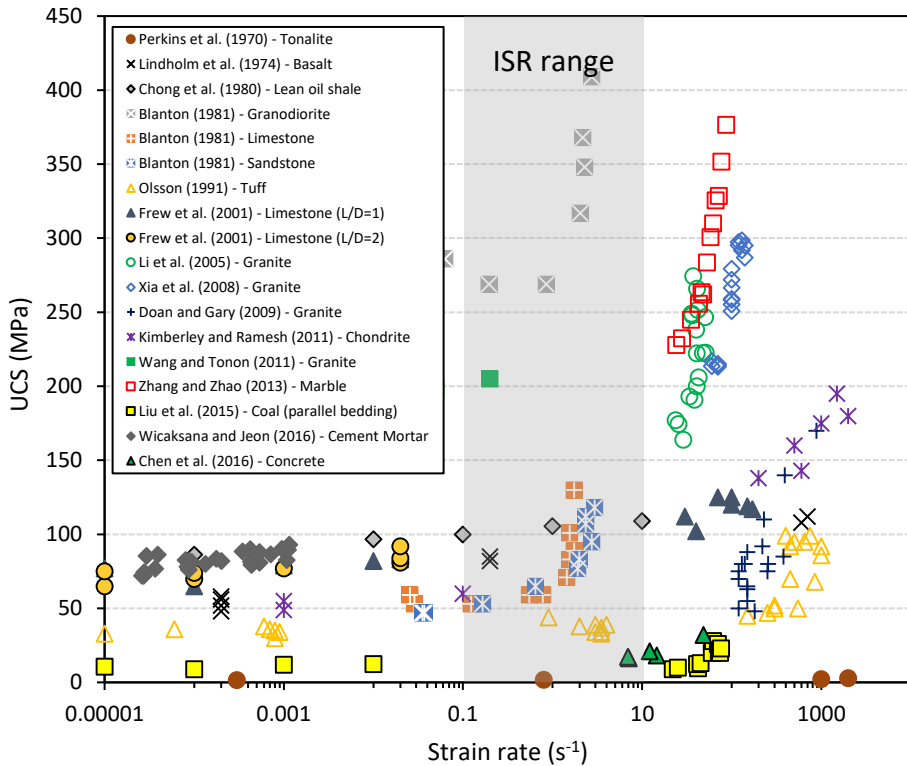


Figure 2.7. Uniaxial compressive strength over strain rate collected from various references (Blanton, 1981; Chen et al., 2017; Doan & Gary, 2009; Frew et al., 2001; Kimberley & Ramesh, 2011; Li et al., 2005; Lindholm et al., 1974; Liu et al., 2015; Olsson, 1991; Perkins et al., 1970; Wang & Tonon, 2011; Wicaksana & Jeon, 2016; Xia et al., 2008; Zhang & Zhao, 2013). The shaded area indicates the ISR range

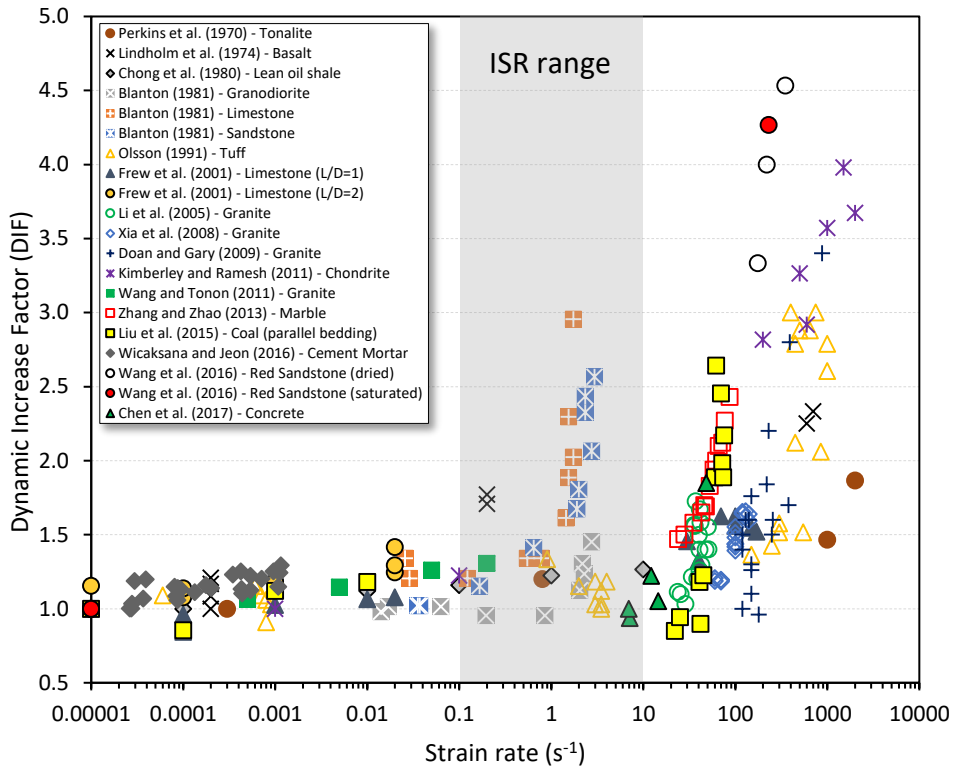


Figure 2.8. Dynamic increase factor (DIF) over strain rate in compression loading collected from various references (Blanton, 1981; Chen et al., 2017; Doan & Gary, 2009; Frew et al., 2001; Kimberley & Ramesh, 2011; Li et al., 2005; Lindholm et al., 1974; Liu et al., 2015; Olsson, 1991; Perkins et al., 1970; Wang et al., 2016; Wang & Tonon, 2011; Wicaksana & Jeon, 2016; Xia et al., 2008; Zhang & Zhao, 2013). The shaded area indicates the ISR range

The shaded area in Figure 2.8 indicates the ISR range. It is clearly shown that only a few data available in that range. From those few data, the tendency is not understandable. On the one hand, some investigators found a slight increase in strength in this range. On the contrary, some of them found a dramatic increase in this range. For example, Blanton (1981) made an observation on Indiana limestone and Berea sandstone that appear to have a vivid increase in this range. Even though he claimed

that the increase was due to machine inertial effect, the results are the facts that he obtained them from the actual experimental work.

Some investigators have plotted the strength increase, referring to the loading rate, as shown in Figure 2.9. Their result cannot be directly compared to others in terms of strain rate. The data taken from granite, basalt, and marble indicates that the DIF increases with loading rate increasing (Kumar, 1968; Zhao et al., 1999; Zhou et al., 2015). Detailed experimental data are summarized in Table 2.3.

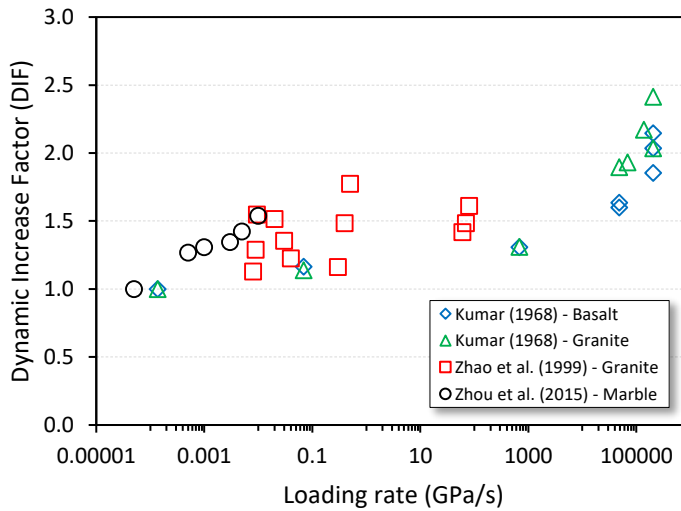


Figure 2.9. Dynamic increase factor (DIF) over loading rate in compression (Kumar, 1968; Zhao et al., 1999; Zhou et al., 2015)

### 2.4.3 Dynamic Rock Behavior under Tension in Intermediate Strain Rate

It is well known that the tensile strength of a brittle material is usually only a fraction of its compressive strength. The indirect tension method is commonly used in practice due to its simple instrumentation and high

repeatability. However, despite its complexity, it is believed that results obtained from the direct tension method give a better approach to the actual tensile strength of the rock specimen.

The dynamic tensile behavior of the rock is essential to study since the breakage of the rock is mainly controlled by its tensile strength. Asprone et al. (2009) studied the dynamic tensile behavior of Neapolitan yellow tuff, which is used in most of the historical structures in Mediterranean cities. Their direct tension experiments covered the strain rate ranging from  $10^{-5}$  to 50 per second, which is classified into three stages, i.e., quasi-static ( $10^{-5}$  per second), medium strain rate ( $10^{-1}$  to 5 per second), and high strain rate (20 and 50 per second). A hydraulic servo-controlled loading machine, hydro-pneumatic machine, and split Hopkinson tension bar (SHTB) were used to conduct quasi-static, medium, and high strain rate tests, respectively. From those three test stages, it was found that the ultimate failure stress (or load) increases as the increasing of strain rate with the maximum DIF of 2.90 at 50 per second. The DIF dependency on strain rate levels seems to be divided into two general slopes for medium and high strain rates. At the medium strain rate, the trend looks gentle, while at the high strain rate, the trend seems to increase significantly. The intersection (“knee”) between these two trends is located at the strain rate of 2.2 per second.

A similar test with Asprone et al. (2009) was conducted by Cadoni (2010) for moderate and high strain rate (0.1, 10, 100 per second) using hydro-pneumatic and SHTB, respectively. The author tried to figure out the strain rate dependence as well as the direction of the schistosity ( $\theta$ ) of Onsernone orthogneiss at  $0^\circ$ ,  $45^\circ$ , and  $90^\circ$  to the loading direction. The author observed that at lower strain rates, the strength increase is gradual above a specific strain rate, while this increase is dramatic for higher

strain rates. A notable effect can only be found at  $\theta = 0^\circ$ , while in the case of  $\theta = 45^\circ$  and  $90^\circ$ , the data appear to be dispersed.

Zhao and Li (2000) conducted a series of dynamic tension tests on Bukit Timah granite. The Brazilian and 3-point flexural tensile tests were used with the loading rate ranging from  $10^{-1}$  to  $10^4$  MPa/s. The results indicate that the tensile strength obtained from both methods increases by about 10% with increasing loading rate. They found that tensile strengths obtained from 3-point flexural bending are relatively higher than those obtained from the Brazilian method. Young's modulus has a small change within the studied loading range.

A detailed description on how to quantify dynamic tensile parameters using a modified Kolsky tension bar in direct tension mode was reported by Huang et al. (2010a). Subsequently, they indicated that the Laurentian granite in dumbbell-shaped is rate dependent. The tensile strength linearly increases with the loading rate within the range of 100-600 GPa/s. A similar phenomenon was also found by Dai et al. (2010a) in indirect tension mode (i.e., Brazilian test) for the same rock type. The observed phenomenon was attributed to the interaction of microcracks in rocks by Grady and Kipp (1980). In a static test, the main crack dominates the failure of a rock specimen while in dynamic, a single crack is not sufficient to cause the specimen to fail; additional microcracks must participate, leading to the high tensile strength at dynamic loads.

The strain rate dependence of tensile strength and failure patterns of Brazilian disc specimens of granite under the intermediate strain rate ( $10^0$  to  $10^2$ ) are numerically simulated (Zhu et al., 2015). The RFPA-Dynamic software was used and validated by a series of Brazilian test using a pendulum hammer-driven SHPB. They claimed that the pendulum

hammer-driven SHPB is an excellent choice to test the rock behavior at intermediate strain rate. Tensile strength increases with increasing strain rates in both laboratory and numerical experiments. The strain rate dependency may be caused by rock inhomogeneity.

Rock inhomogeneity was also one of the reasons for the rate dependency of the dynamic strength of Inada granite and Tage tuff (Cho et al., 2003). The rock inhomogeneity was represented by the uniformity coefficient. The higher uniformity coefficient means that the rock specimen is less heterogeneous. Cho et al. (2003) reported that the increase in the uniformity coefficient resulted in a reduction in the strain rate dependency. Accordingly, the strain rate dependency of the dynamic strength was caused by the inhomogeneity of the rock.

Figures 2.10 and 2.11 show the DIF over the full range of strain rate and loading rate, respectively. It can be seen from both graphs that there are two trends: a gradual increase at the lower rate and a significant at the higher rate. In Figure 2.10, it seems like the critical strain rates are located inside the shaded rectangle, which belongs to the ISR. Some investigators reported that the “knee,” intersection between two trends, is located at the strain rate of 2.2 per second (Asprone et al., 2009). In other words, in the ISR itself, there are two different rock behaviors. It is an indication that extensive study must be done in the ISR range. However, it should be noted that the trend transition may be dependent on rock type and loading generation.

For the data presented in the loading rate (Figure 2.11), the corresponding strain rate cannot be identified; thus, the loading classification based on the strain rate is undefined. Detailed experimental data are summarized in Table 2.3.

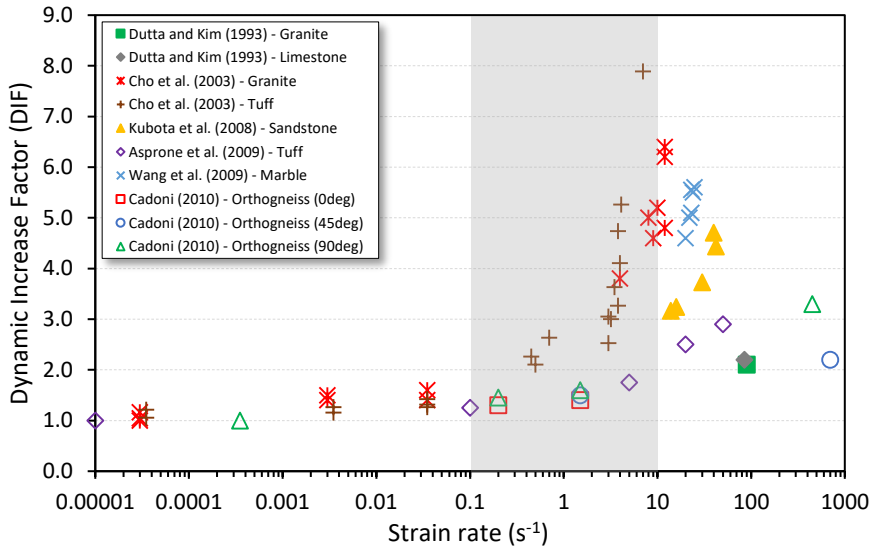


Figure 2.10. Dynamic increase factor (DIF) over strain rate in tension collected from various references (Asprone et al., 2009; Cadoni, 2010; Cho et al., 2003; Dutta & Kim, 1993; Kubota et al., 2008; Wang et al., 2009). The shaded area indicates the ISR range.

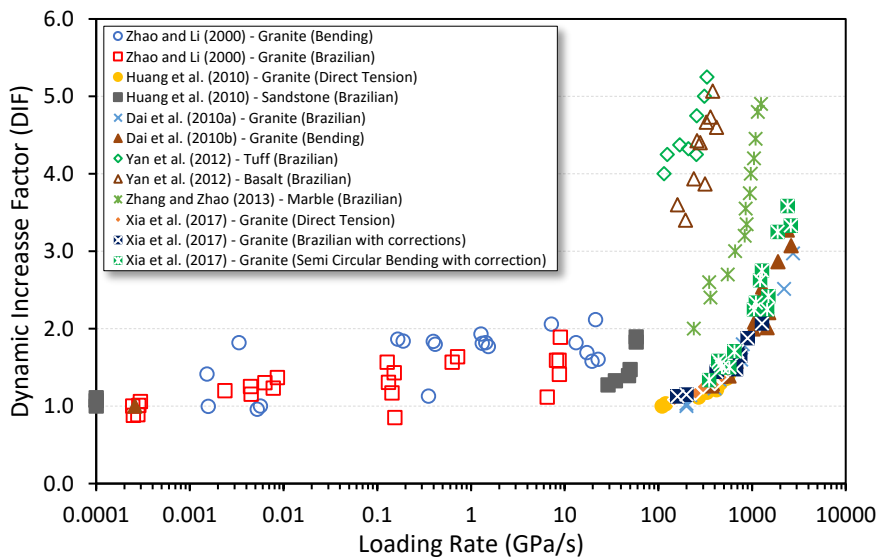


Figure 2.11. Dynamic increase factor over loading rate in tension (Dai et al., 2010a; Dai et al., 2010b; Huang et al., 2010a; Xia et al., 2017; Yan et al., 2012; Zhang & Zhao, 2013; Zhao & Li, 2000)

Table 2.3. Dynamic compression and tension experiments covering intermediate strain rate range

Reference	Testing type	Material	Strain/load rate	Apparatus	Key issue
Green and Perkins (1968)	Uniaxial compression	Solenhofen limestone, Westerly granite, volcanic tuff	$10^{-4} - 10^3 \text{ s}^{-1}$	Fully gas-driven loading machine and SHPB	Thermal activation; critical strain rate
Lindholm et al. (1974)	Triaxial compression	Dresser basalt	$10^{-4} - 10^3 \text{ s}^{-1}$	Hydraulic loading machine and SHPB	The relationship between strength, temperature, confining pressure, and strain rate
Chong et al. (1980)	Uniaxial compression	Oil shale	$10^{-4} - 10^1 \text{ s}^{-1}$	Hydraulic loading machine	The relationship between strength, organic content and strain rate
Blanton (1981)	Triaxial compression	Charcoal granodiorite, Berea sandstone, Indiana limestone	$10^{-2} - 10 \text{ s}^{-1}$	Gas-operated loading machine	Mathematical model of dynamic loading; inertial effect; critical strain rate
Olsson (1991)	Uniaxial compression	Tuff	$10^{-6} - 10^3 \text{ s}^{-1}$	Hydraulic loading machine and SHPB	Normalized dynamic strength by bulk density; critical strain rate
Zhao et al. (1999)	Uniaxial compression	Bukit Timah granite	$10^0 - 10^5 \text{ MPa/s}$	Pneumatic-hydraulic loading machine	Loading rate dependence on rock strength
Zhao and Li (2000)	Indirect tension	Bukit Timah granite	$10^{-1} - 10^4 \text{ MPa/s}$	Pneumatic-hydraulic loading machine	Loading rate dependence on rock strength
Frew et al. (2001)	Uniaxial compression	Indiana limestone	$10^{-5} - 300 \text{ s}^{-1}$	Hydraulic loading machine and SHPB	The copper disk pulse shaper
Cho et al. (2003)	Indirect tension	Inada granite, Tage tuff	$10^{-6} - 10^1 \text{ s}^{-1}$	SHPB	Rock inhomogeneity, FEM modeling
Li et al. (2005)	Uniaxial compression	Bukit Timah granite	$10^1 - 10^2 \text{ s}^{-1}$ (*)	SHPB	Shaped striker bar; half-sine waveform; repeated loading
Asprone et al. (2009)	Direct tension	Neapolitan yellow tuff	$10^{-5} - 50 \text{ s}^{-1}$	Hydraulic loading machine, hydro-pneumatic machine, SHTB	“Knee” between two trends at a strain rate of 2.2/s.
Cadoni (2010)	Direct tension	Onsernone orthogneiss	$10^{-1} - 10^2 \text{ s}^{-1}$	Hydro-pneumatic machine, SHTB	Effect of schistosity and strain rates on rock strength
Huang et al. (2010a)	Direct tension	Laurentian granite	100 – 600 GPa/s	Modified Kolsky tension bar	Loading rate dependence on rock strength

Reference	Testing type	Material	Strain/load rate	Apparatus	Key issue
Wang and Tonon (2011)	Uniaxial compression	Lac du Bonnet granite	$10^{-6} - 10^2 \text{ s}^{-1}$	Hydraulic loading machine and SHPB	DEM simulation; rock fragmentation; Weibull distribution; critical strain rate
Kimberley and Ramesh (2011)	Uniaxial compression	MacAlpine Hills chondrite (stony meteorite)	$10^{-3} - 10^3 \text{ s}^{-1}$	Hydraulic loading machine and SHPB	High normalized dynamic strength for stony meteorite
Zhou et al. (2015)	Uniaxial compression and tensile	Jinping marble	0.05 – 10 MPa/s (compression) $10^{-3} - 10^1$ kN/s (tensile)	Hydraulic loading machine	Strain rate dependence on rock strength
Zhu et al. (2015)	Indirect tension	Granite	$10^0 - 10^2 \text{ s}^{-1}$	Pendulum hammer-driven SHPB	Numerical simulation; strain rate dependence on rock strength
Liu et al. (2015)	Uniaxial compression	Coal	$10^{-5} - 100 \text{ s}^{-1}$	Hydraulic loading machine	Bedding directivity; fractal dimension

(\*) The authors classified their experiment range as ISR even though it is outside the ISR classified by Zhang and Zhao (2014)

#### 2.4.4 Rock Fragmentation on Dynamic Loading Condition

Observation by many investigators on fracture processes and failure patterns show a general trend where dynamic fracture changes from relatively single fracture to multiple fragmentations with increasing strain rates (Doan & Gary, 2009; Hogan et al., 2012; Liu et al., 2015). During dynamic fracturing, the primarily absorbed energy contributes to the generation of new surfaces, the number and size of fragments, and the kinetic energy of moving fragments (Zhang & Zhao, 2014b).

Doan and Gary (2009) conducted dynamic tests to study rock fragmentation of granite taken from San Andreas Fault. The experiments carried out at a strain rate higher than  $150 \text{ s}^{-1}$  produced finely broken samples, whereas those performed below  $100 \text{ s}^{-1}$  gave samples broken into two or three fragments. Rock fragmentation of coal was quantified

by using fractal dimension (Liu et al., 2015). It can be inferred that under a relative lower strain rate, the single block dominates, while with increasing strain rate, more pieces of rock specimen are destroyed.

Dynamic experiments using drop weight devices have been conducted to study rock fragmentation through impact loading (Hogan et al., 2012; Reddish et al., 2005; Whittles et al., 2006). Hogan et al. (2012) statistically concluded that rock fragmentation depends on the mineral composition of the rock material, i.e., quartz content. Rocks with higher quartz content have larger fragment sizes and smaller aspect ratios in the fragmentation probability distributions.

Reddish et al. (2005) compared the laboratory and numerical experiments on granite specimens under various impact energy, i.e., different configurations of mass weight/height in drop weight loading device. Results from both methods indicate that, with increasing energy of impact, a higher degree of fragmentation of granite specimen occurs. The degree of fragmentation showed an inversely linear relationship to impact energy that means the higher the impact energy, the smaller the fragmentation size is (Reddish et al., 2005; Vanichkobchinda, 2005).

Likewise, Whittles et al. (2006) claimed that both required energy to break rock specimens and the degree of fragmentation increase with the fast loading in compression. They conducted a series of compression tests using a hydraulic compression machine and drop weight device in order to investigate the effect of strain rate on the rock fragmentation in three different materials, i.e., Ibbenbüren sandstone, Caldon Low limestone, and Humberside chalk. Increasing strain rate shows an increase in the number of fragments; the tests undertaken at the highest strain rate show the most significant fragmentation (Figure 2.12(a)). By

numerical simulation, it can be observed in Figure 2.12(b) that the higher strain rate tests are associated with a more significant number of micro-fractures.

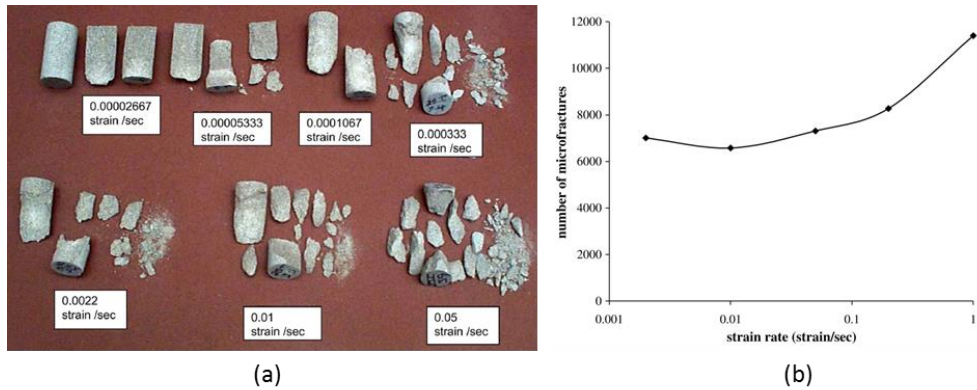


Figure 2.12. Strain rate effect on (a) changing in fragment size for Ibbenbüren sandstone, and (b) number of micro-fractures (Whittles et al., 2006)

## 2.5 Rock Abrasiveness Test

Rock abrasiveness plays a significant contribution in characterizing rock material in the mechanical excavation industry. Abrasiveness can be described as the wearing of particles from the surface that causing removal or displacement of material at a solid surface; lead to wear, especially on tools that are used in mining, drilling, and tunneling application (Alber et al., 2014). Thus, the increased production rate in the mechanical cutting project requires excellent knowledge of rock abrasiveness.

In general, rock abrasiveness can be measured in three different methods (Golovanevskiy & Bearman, 2008):

- Indirect method: assessment through a combination of hardness, compressive strength, and other fundamental rock properties.
- Direct method: assessment where there is relative movement of rock sample and a wear tool in contact under standard controlled test conditions.
- Holistic approach: assessment via a combination of fundamental rock properties and many varied process parameters and environmental conditions.

The indirect method assesses the abrasiveness via rock indices such as Schmidt hammer rebound value, shore scleroscope, and cone indenter (Atkinson et al., 1986) without any consideration of interaction aspects with a specific machine tool as well as some other essential rock parameters (Nilsen et al., 2006). On the other hand, the holistic method comprehensively combines some of the rock parameters with a specific mechanical machine setting; thus, the outcome is instead limited to a specific purpose. Meanwhile, in the direct method, the testing environment is standardized to a specific mode of wear in assessing the rock abrasiveness. The test usually examines the effect of relative movement of a tool to a rock sample under a controlled condition, so generally the test can be applied in various purposes.

Cerchar abrasiveness test is one of the most widely used abrasiveness tests in research and practices, and it is classified as a direct method. It was first proposed by the Laboratoire du Centre d'Etudes et Recherches des Charbonnages (CERCHAR) de France Institute in France in the 70s. There are two types of test procedures in the Cerchar test. They are different by the way a metal pin scratches the rock surface. The original Cerchar test (type I) was published by (Valantin, 1973) and the modified

one (type II) was proposed by (West, 1989). In type I, the pin together with a deadweight is moved by a lever to scratch a fixed specimen, while in type II, the rock specimen is moved by a lead screw beneath a stationary pin. The schematic diagram of the Cerchar abrasiveness test for both methods can be seen in Figure 2.13.

Cerchar test is performed relatively in a static environment with a constant load, a short scratch length, and a slow linear pin movement. In practice, however, cutting tools are subjected to a dynamic load in which the tools interact with the rock at high-speed velocity and unpredictable angle of occurrence. Those conditions are somehow not replicated by Cerchar abrasiveness test.

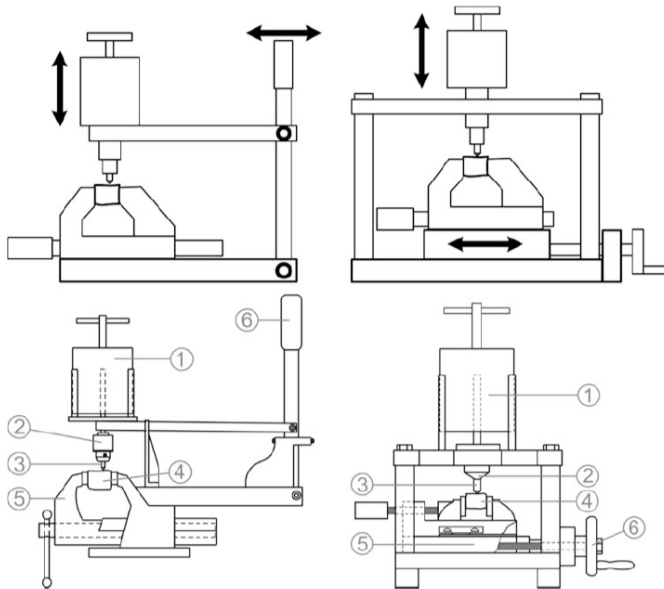


Figure 2.13. Basic mechanisms of the Cerchar abrasiveness test. Left: type 1, the original design proposed by (Valantin, 1973) and, right: type 2, the modified design reported by (West, 1989). Index: (1) mass/deadweight, (2) pin chuck/guide, (3) pin/stylus, (4) rock specimen, (5) vice, (6) lever/hand crank (Alber et al., 2014)

To address the issue mentioned above, the other abrasiveness test that incorporates a high-speed scratching was published by Golovanevskiy and Bearman (2008), called Gouging abrasiveness test. The gouging mode of wear was also studied earlier in various terminologies such as gouging (Budinski, 1988), sliding impact (Blau, 1989), or grooving wear (Zum Gahr, 1987). The Gouging abrasiveness test simulates a high-speed abrasiveness under a high energy impact condition by using a steel wear tool that is attached to a swing pendulum. The test is illustrated in Figure 2.14. The detailed procedure of the test is discussed later in Chapter 5.

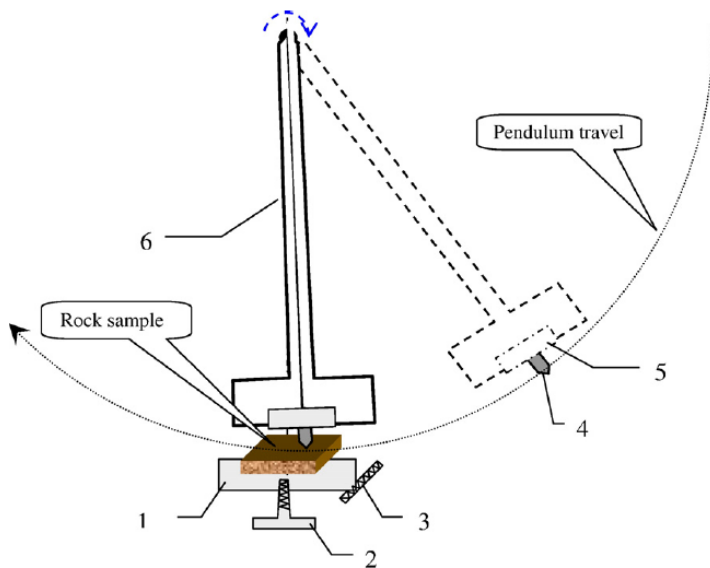


Figure 2.14. Gouging abrasiveness test setup. Index: (1) sample holder, (2) transmission screw, (3) spring-loaded mechanism, (4) wear tool, (5) wear tool holder, and (6) pendulum arm (Golovanevskiy & Bearman, 2008)

## **2.6 Explicit Dynamic Simulation using ANSYS AUTODYN®**

In this study, the explicit dynamic simulation is performed using ANSYS AUTODYN®. The explicit dynamic system is designed to enable the user to simulate non-linear structural mechanics in various applications, including impact behavior (roughly from 1 m/s to 5000 m/s), stress wave propagation, high-frequency dynamic response, massive deformation, and other structural mechanics phenomena. Explicit dynamic is most suited to events that take place over a short period of time, a few milliseconds, or less. Events that last more than a second can also be modeled; however, it will require a significantly long computation time during the process.

The calculation procedure of the explicit dynamic solution can be described as follow. The motion of the node points produces deformation in the element of mesh, and the deformation results in a change in volume of the material in each element. The rate of deformation is used to derive material strain rates using various element formulations. Then, constitutive laws take material strain rates and derive resultant material stresses. The material stresses are transformed back into nodal forces using various element formulations. External nodal forces are computed from boundary conditions, loads, and body interactions. The nodal forces are divided by nodal mass to produce nodal accelerations. The accelerations are integrated explicitly in time to produce new nodal velocities. Finally, the nodal velocities are integrated explicitly in time to produce new nodal positions. The cycle is repeated until the user-defined time limit is reached (ANSYS, 2010). The diagram of the computational cycle is presented in Figure 2.15.

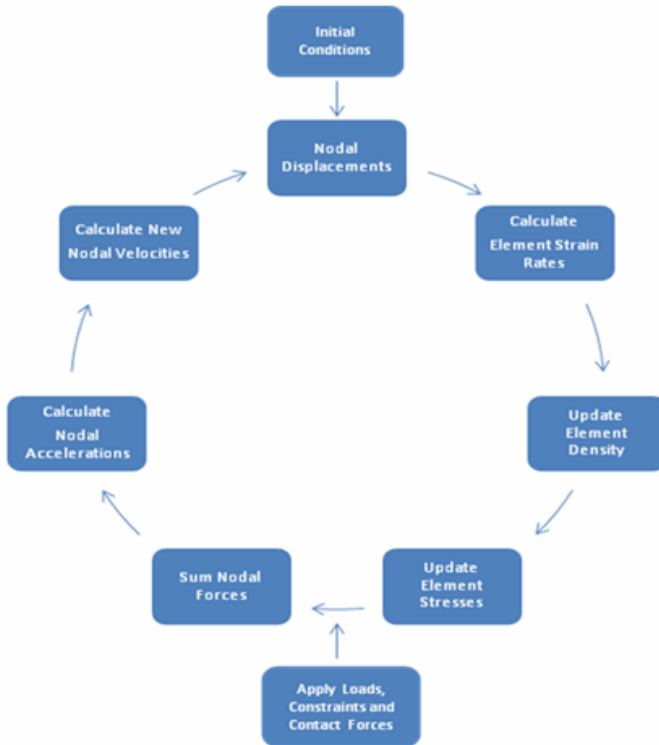


Figure 2.15. The computational cycle of the explicit dynamic solution in ANSYS AUTODYN® (ANSYS, 2010)

### 2.6.1 Explicit Transient Dynamics

The partial differential equations to be solved in an explicit dynamic analysis express the conservation of mass, momentum, and energy in Lagrangian coordinates. Those equations, together with a material model and a set of initial and boundary conditions, define the complete solution of the problem. For the Lagrangian formulations currently available in the explicit dynamic system, the mesh moves and distorts with the model, and conservation of mass is automatically satisfied. The density at any time can be determined from the current volume and its initial mass (Eq. 2.1):

$$\frac{\rho_0 V_0}{V} = \frac{m}{V} \quad (2.1)$$

The partial differential equations that express the conservation of momentum relate the acceleration to the stress tensor  $\sigma_{ij}$  (Eq. 2.2-2.4):

$$\rho \ddot{x} = b_x + \frac{\delta \sigma_{xx}}{\delta x} + \frac{\delta \sigma_{xy}}{\delta y} + \frac{\delta \sigma_{xz}}{\delta z} \quad (2.2)$$

$$\rho \ddot{y} = b_y + \frac{\delta \sigma_{yx}}{\delta x} + \frac{\delta \sigma_{yy}}{\delta y} + \frac{\delta \sigma_{yz}}{\delta z} \quad (2.3)$$

$$\rho \ddot{z} = b_z + \frac{\delta \sigma_{zx}}{\delta x} + \frac{\delta \sigma_{zy}}{\delta y} + \frac{\delta \sigma_{zz}}{\delta z} \quad (2.4)$$

The conservation of energy is expressed as (Eq. 2.5):

$$\dot{e} = \frac{1}{\rho} \left( \sigma_{xx} \dot{\epsilon}_{xx} + \sigma_{yy} \dot{\epsilon}_{yy} + \sigma_{zz} \dot{\epsilon}_{zz} + 2\sigma_{xy} \dot{\epsilon}_{xy} + 2\sigma_{yz} \dot{\epsilon}_{yz} + 2\sigma_{zx} \dot{\epsilon}_{zx} \right) \quad (2.5)$$

These equations are solved explicitly for each element in the model, based on input values at the end of the earlier time step. Small-time increments are used to ensure the stability and accuracy of the solution. Note that explicit dynamic does not seek any form of equilibrium; instead, it takes the results from the previous time point to predict results at the next time point.

## 2.6.2 Explicit Time Integration

The explicit dynamic solver uses a central difference time integration scheme (leapfrog method). After forces have been computed at the nodes of the mesh (resulting from internal stress, contact, or boundary

conditions), the nodal accelerations are derived by equating acceleration to force divided by mass. Therefore, the accelerations are (Eq. 2.6):

$$\ddot{x}_i = \frac{F_i}{m} + b_i \quad (2.6)$$

Where  $\ddot{x}_i$  is the component of nodal acceleration ( $i=1, 2, 3$ ),  $F_i$  is the force acting on the nodal points,  $b_i$  is the component of body acceleration, and  $m$  is the mass attributed to the node.

With the accelerations at time  $n$  determined, the velocities at time  $n + 1/2$  are found from (Eq. 2.7):

$$\dot{x}_i^{n+1/2} = \dot{x}_i^{n-1/2} + \ddot{x}_i^n \Delta t^n \quad (2.7)$$

Then finally, the positions are updated to time  $n + 1$  by integrating the velocities (Eq. 2.8):

$$x_i^{n+1} = x_i^n + \dot{x}_i^{n+1/2} \Delta t^{n+1/2} \quad (2.8)$$

### **3. DYNAMIC TEST OF ROCK**

#### **3.1 Introduction to Dynamic Rock Test**

As explained earlier in Chapter 1, the interaction between the tool and rock in rock mechanical excavation is a dynamic process, but the rate of the interaction is not as high as the one of blasting operation. Thus, the mechanical properties of rock under a relatively similar loading range should be obtained, which is presumed to be in the intermediate strain rate (ISR) range. To obtain dynamic mechanical properties of rock, we set up a series of laboratory tests, including sets of quasi-static tests as a benchmark. Dynamic and quasi-static tests were separately conducted in two laboratories, i.e., Rock Fracture Dynamic Laboratory at Chonbuk National University and Rock Mechanics and Rock Engineering Laboratory at Seoul National University, respectively. The detailed experiment is described in the following sections.

#### **3.2 Non-Explosive Reaction-Driven Loading Apparatus**

A specialized loading apparatus is prepared to perform the laboratory test under intermediate dynamic loading, as an alternative to several methods mentioned in Chapter 2.4.1. The use of the machine has been adopted for various testing modes (Min et al., 2017; Wicaksana et al., 2018a; Wicaksana et al., 2018b).

The system was designed initially by Nakamura et al. (2012), who used it to study the tensile fracture behavior of mortar specimen under a fast loading. In his study, Nakamura used an electric detonator as the prime mover of the piston to generate a high strain rate dynamic load. One

should be pointed out from the original apparatus that there is a restriction to work with an electric detonator. The electric detonator is classified as an explosive and, to work with such sensitive material, it is required to have a proper license and valid permission from the authority.

In this study, the use of an electric detonator was replaced by NRC powder. The NRC stands for “non-explosive rock cracker,” which basically performs like the industrial explosive but provides a lower velocity of detonation and less explosive energy. It is classified as a non-explosive material, so practically, it does not require any special permission to use it.

The NRC composes of metal powder and magnesium sulfate-hydrate mixture that is reacted exothermically when it is ignited by heat. From the technical data sheet, the NRC generates 409 kcal/kg of explosive energy with the velocity of detonation of 200-300 m/s (Powerking, n.d.). In contrast, ANFO, which is the most common industrial explosive used in mining, produces around 880 kcal/kg of explosive energy and velocity of detonation about 3900 m/s (Dyno Nobel, n.d.). This non-explosive powder is usually applied to crack quasi-brittle material such as rock and concrete in vibration and noise-sensitive areas. In mining industry, it can be used as a secondary blaster to break boulder fragments from an unsuccessful primary blasting fragmentation. Since the NRC produces a lower level of energy, it is more suitable for this study; in fact, this study needed lower explosive energy in order to achieve the ISR loading level.

The apparatus consists of a two-column frame, a dynamic load cell, and a loading piston that is paired to a reaction chamber. The working procedure of the loading apparatus can be explained as follows. The NRC powder was set together with an initiator in a sealed synthetic bag

and then placed inside the reaction chamber. The initiator was connected to an electric discharge controller (EDC). The EDC discharged an electrical pulse to trigger the initiator as well as the NRC powder. The reaction created heat and gas expansion pressure inside the reaction chamber and subsequently pushed the loading piston down to impact the rock sample. Data was measured and recorded by a system consisting of a dynamic load cell, a signal amplifier, and an oscilloscope. Voltage-time curves were recorded in the oscilloscope. Before the test, the dynamic load cell was calibrated with a servo-controlled loading machine, which resulted in the conversion factor that can transform the voltage to force output (Min et al., 2017). A high-speed camera was adopted to capture images during the test. All information from the load cell and the high-speed camera were transferred to a personal computer. A dedicated container with thick acrylic on one of its sides was designed to protect investigators and all supporting devices from rockburst and flying objects.

The loading apparatus components, the schematic diagram of the working procedure, and the actual testing condition are depicted in Figures 3.1 and 3.2. The calibration of the dynamic load cell is provided in Figure 3.3.

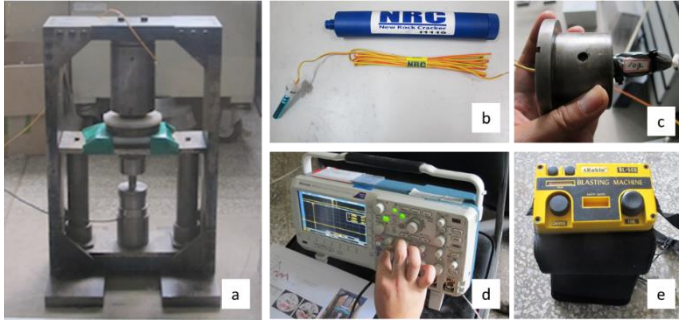


Figure 3.1. Dynamic testing components. a) loading frame; b) NRC powder and initiator; c) non-explosive powder charge; d) oscilloscope; and e) electric discharge controller.

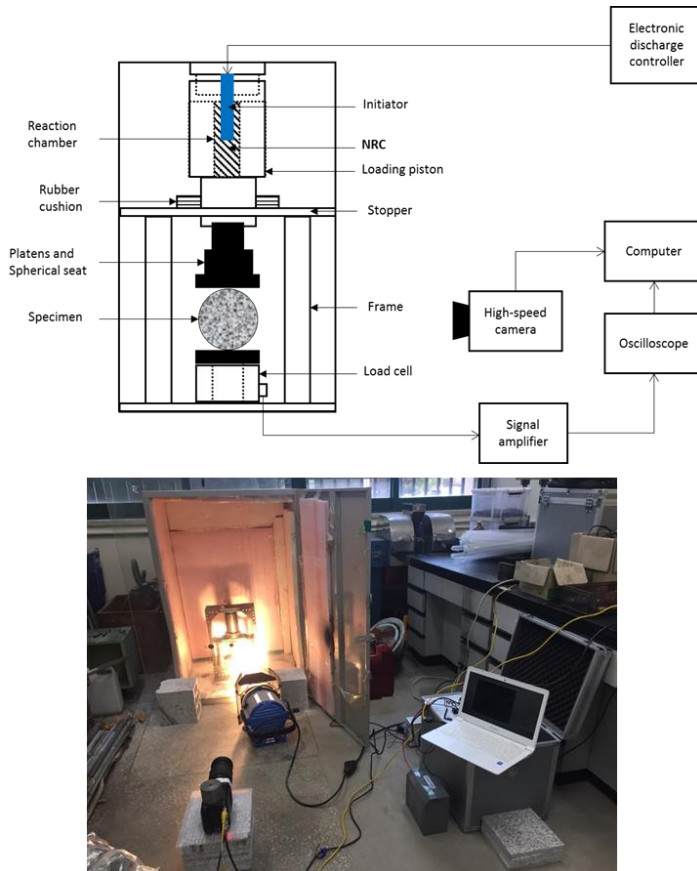


Figure 3.2. Dynamic testing using the non-explosive reaction-driven loading device and its connectivity with other devices. Upper: schematic diagram; lower: actual test

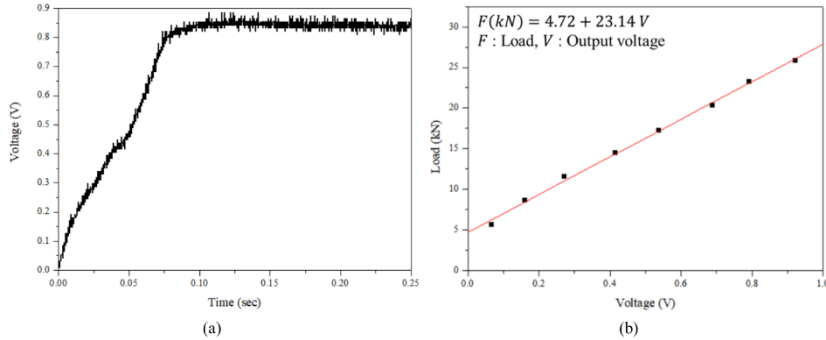


Figure 3.3. Calibration of the dynamic load cell. (a) output voltage – time history; (b) static load – output voltage (Min et al., 2017)

### 3.3 Test Setup

#### 3.3.1 Test Type

Four test modes were performed, namely, uniaxial compression, indirect Brazilian tension, mode-I fracture toughness, and punch shear tests. From those four test modes, we determined uniaxial compressive strength, tensile strength, mode-I fracture toughness, and shear strength of the rock, respectively. The schematic diagrams of those four test modes are depicted in Figure 3.4.

To set a benchmark for those dynamic experimentations, a series of quasi-static tests were carried out using an MTS 816 Rock Mechanics Testing System. The machine is generated by a hydraulic motor and equipped by a servo-controlled system with a capacity of 200 tons. A high-speed camera captured images during the tests. The system records the entire force and displacement histories during the test. The actual quasi-static test condition can be seen in Figure 3.5.

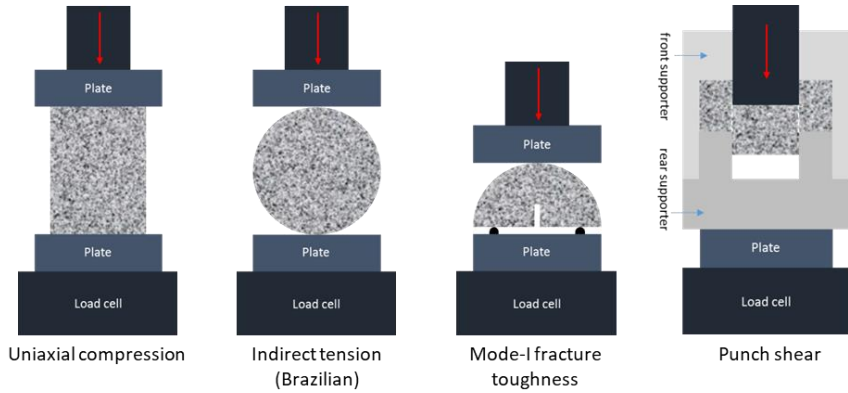


Figure 3.4. Schematic diagram of each of the dynamic tests

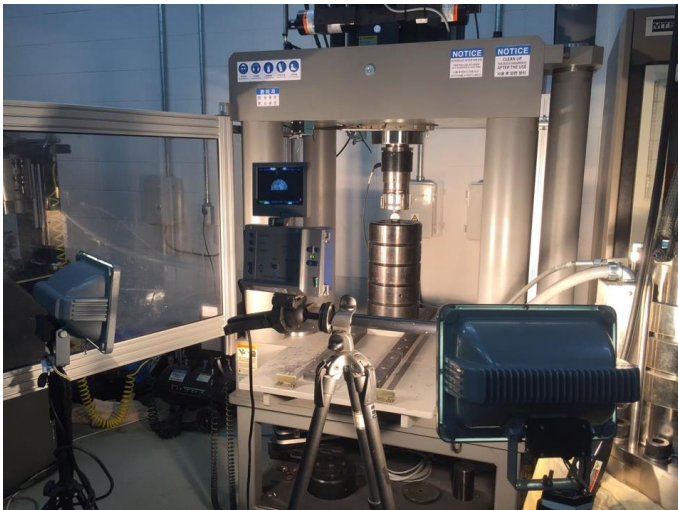


Figure 3.5. The actual condition of the quasi-static test using a hydraulic servo-controlled loading machine

### 3.3.2 Rock Specimen

Two types of rock samples were collected to conduct the tests: granite and sandstone. The granite and sandstone blocks used in this study were taken from the Hwangdeung area in Korea and the Linyi area in China, respectively (see Figure 3.6). They are called as Hwangdeung granite

and Linyi sandstone in this entire document. The specimen shape and size were prepared according to each test standard procedure and would be explained individually for each test later in this document. The typical mineral content of those rocks is provided in Table 3.1.



Figure 3.6. The location where the block samples were taken

Table 3.1. The mineral contents of the rock samples

No	Rock type	Location	Mineral content
1	Granite	Hwangdeung, Jeollabuk-do, Korea	Quartz: 48.8 %
			Albite: 35.4 %
			Microcline: 17.8 %
			Biotite: 7.1 %
			Magnetite: 2 %
2	Sandstone	Linyi, China	Albite: 42.2 %
			Quartz: 38.3 %
			Orthoclase: 10.7 %
			Hematite: 3.3 %
			Laumonite: 3 %
			Calcite: 1.7 %
	Montmorillonite: 0.7 %		

### 3.3.3 Test Scenario

There were three scenarios applied for each test and rock type. Two scenarios for the quasi-static and one scenario for the dynamic test were set as follows:

- Quasi-static 1 (regarded as  $QS_1$ )
  - Device: Hydraulic servo-controlled loading machine
  - Displacement rate: 0.01 mm/s
- Quasi-static 2 (regarded as  $QS_2$ )
  - Device: Hydraulic servo-controlled loading machine
  - Displacement rate: 10 mm/s
- Intermediate dynamic loading (regarded as  $D$ )
  - Device: Non-explosive reaction-driven loading apparatus
  - Powder charge: 20 gr of NRC

For the dynamic test, the amount of NRC powder used in the dynamic test was based on several trial and error attempts with the configuration of less and more than 20 grams of NRC. As a result, it was decided that a 20-gram of NRC charge was the optimum amount considering the strain rate target and safety and environment issues such as loading frame capacity, noise, and vibration caused by the test.

In this study, each specimen was named according to the following system: *test\_type-rock\_type-scenario-specimen\_number*. For instance:

- *UCS-HG-QS1-1* stands for the uniaxial compression test of Hwangdeung granite specimen number one with the scenario of  $QS_1$ .
- *FT-HG-D-5* stands for the fracture toughness (mode-I) of Hwangdeung granite specimen number 5 with the scenario of  $D$ .

### 3.4 Test and Results

#### 3.4.1 Uniaxial Compression

The granite and sandstone blocks were cored with a 15 mm inner diameter core bit and then cut with a length of around 30 mm to form cylindrical specimens ( $L/D \approx 2$ ). It should be noted that the specimen size in this study was smaller than the requirement proposed by ISRM (Fairhurst & Hudson, 1999) due to limitations in the loading capacity of the dynamic loading apparatus.

The uniaxial compressive strength of the specimen was calculated by dividing the maximum load carried by the rock specimen during the test by the original cross-sectional area. Corresponding strain rates for the  $QS_1$  and  $QS_2$  were calculated based on Eq.3.1, and for the  $D$  were calculated based on Eq.3.2.

$$\varepsilon = \frac{\Delta h}{h}, \dot{\varepsilon} = \frac{\Delta \varepsilon}{\Delta t} \quad (3.1)$$

$$\dot{\sigma}_c = \frac{\Delta \sigma_c}{\Delta t}, \dot{\varepsilon} = \frac{\dot{\sigma}_c}{E} \quad (3.2)$$

where  $\varepsilon$  is strain,  $h$  is the specimen height,  $\Delta h$  is the change of height,  $\dot{\varepsilon}$  is strain rate,  $\Delta \varepsilon$  is the change of strain,  $\Delta t$  is time duration,  $\dot{\sigma}_c$  stress rate,  $\Delta \sigma_c$  is the change of stress, and  $E$  is Young's modulus.

A total of 40 specimens were tested that consist of 19 granite and 21 sandstone specimens. The uniaxial compressive strength, its strain rate, and other detailed information for all testing scenarios and rock types can be seen in Table 3.2, and descriptive statistics of the UCS value is summarized in Table 3.3. The strain rate resulted from this experiment was ranging from  $3.2 \times 10^{-4} \text{ s}^{-1}$  to  $6.9 \times 10^1 \text{ s}^{-1}$ . The averaged compressive

strength of  $QS_1$ ,  $QS_2$ , and  $D$  for Hwangdeung granite were 100.64 MPa, 121.63 MPa, and 137.75 MPa while for Linyi sandstone were 57.10 MPa, 76.51 MPa, and 115.89 MPa. Overall, the result showed that compressive strength increased with increasing strain rate for both rock types. Figure 3.7 shows the relationship between uniaxial compressive strength and strain rate.

Table 3.2. Uniaxial compression test results

Specimen ID	Loading Rate (GPa/s)	Strain Rate ( $s^{-1}$ )	$D$ (mm)	$L$ (mm)	Peak Load (kN)	$\sigma_c$ (MPa)	DIF
UCS-HG-QS1-1	$3.1 \times 10^{-3}$	$3.4 \times 10^{-4}$	15.00	29.60	16.70	94.50	0.94
UCS-HG-QS1-2	$4.6 \times 10^{-3}$	$3.4 \times 10^{-4}$	15.00	29.70	18.24	103.20	1.03
UCS-HG-QS1-3	$8.1 \times 10^{-3}$	$3.4 \times 10^{-4}$	15.00	29.70	17.72	100.25	1.00
UCS-HG-QS1-4	$3.2 \times 10^{-3}$	$3.2 \times 10^{-4}$	15.00	31.20	15.90	90.00	0.89
UCS-HG-QS1-5	$4.4 \times 10^{-3}$	$3.2 \times 10^{-4}$	15.00	31.20	17.87	101.14	1.01
UCS-HG-QS1-6	$8.1 \times 10^{-3}$	$3.2 \times 10^{-4}$	15.05	31.30	20.28	114.74	1.14
UCS-HG-QS2-1	$3.3 \times 10^0$	$1.6 \times 10^{-1}$	15.10	30.30	20.39	115.38	1.15
UCS-HG-QS2-2	$3.9 \times 10^0$	$1.7 \times 10^{-1}$	15.00	29.80	22.69	128.42	1.28
UCS-HG-QS2-3	$1.8 \times 10^0$	$1.6 \times 10^{-1}$	15.00	30.40	20.05	113.48	1.13
UCS-HG-QS2-4	$2.4 \times 10^0$	$1.7 \times 10^{-1}$	15.10	29.80	22.04	124.71	1.24
UCS-HG-QS2-5	$2.3 \times 10^0$	$1.7 \times 10^{-1}$	15.05	29.70	22.31	126.23	1.25
UCS-HG-QS2-6	$2.4 \times 10^0$	$1.6 \times 10^{-1}$	15.10	29.80	21.48	121.54	1.21
UCS-HG-D-1	$4.1 \times 10^2$	$7.6 \times 10^0$	15.30	30.60	27.20	153.92	1.53
UCS-HG-D-2	$1.5 \times 10^2$	$2.8 \times 10^0$	15.35	30.00	24.80	140.34	1.39
UCS-HG-D-3	$2.6 \times 10^2$	$4.9 \times 10^0$	15.30	29.90	23.20	131.29	1.30
UCS-HG-D-4	$1.7 \times 10^2$	$2.8 \times 10^0$	15.35	29.90	26.40	149.39	1.48
UCS-HG-D-5	$1.7 \times 10^2$	$3.2 \times 10^0$	15.30	3.10	24.00	135.81	1.35
UCS-HG-D-6	$1.8 \times 10^2$	$3.3 \times 10^0$	15.30	30.70	22.40	126.76	1.26
UCS-HG-D-7	$8.1 \times 10^1$	$1.5 \times 10^0$	15.30	30.10	22.40	126.76	1.26
UCS-LS-QS1-1	$3.0 \times 10^{-3}$	$3.4 \times 10^{-4}$	14.80	29.90	11.56	65.40	1.15
UCS-LS-QS1-2	$1.5 \times 10^{-3}$	$3.7 \times 10^{-4}$	14.70	27.00	7.28	41.19	0.72
UCS-LS-QS1-3	$2.2 \times 10^{-3}$	$3.3 \times 10^{-4}$	14.90	30.10	9.44	53.41	0.94
UCS-LS-QS1-4	$2.9 \times 10^{-3}$	$3.3 \times 10^{-4}$	14.80	30.10	11.13	62.99	1.10
UCS-LS-QS1-5	$2.9 \times 10^{-3}$	$3.7 \times 10^{-4}$	14.70	27.00	11.16	63.13	1.11
UCS-LS-QS1-6	$3.3 \times 10^{-3}$	$3.3 \times 10^{-4}$	14.80	30.10	11.04	62.50	1.09

Specimen ID	Loading Rate (GPa/s)	Strain Rate ( $s^{-1}$ )	$D$ (mm)	$L$ (mm)	Peak Load (kN)	$\sigma_c$ (MPa)	DIF
UCS-LS-QS1-7	$2.1 \times 10^{-3}$	$3.3 \times 10^{-4}$	14.90	30.20	8.48	47.99	0.84
UCS-LS-QS1-8	$3.1 \times 10^{-3}$	$3.5 \times 10^{-4}$	14.80	29.00	10.63	60.18	1.05
UCS-LS-QS2-1	$7.9 \times 10^{-1}$	$1.8 \times 10^{-1}$	14.90	27.00	11.13	63.00	1.10
UCS-LS-QS2-2	$9.8 \times 10^{-1}$	$1.8 \times 10^{-1}$	16.65	27.10	13.25	75.00	1.31
UCS-LS-QS2-3	$1.6 \times 10^0$	$1.6 \times 10^{-1}$	14.80	30.10	15.55	88.00	1.54
UCS-LS-QS2-4	$1.5 \times 10^0$	$1.6 \times 10^{-1}$	14.80	30.00	16.62	94.05	1.65
UCS-LS-QS2-5	$1.6 \times 10^0$	$1.6 \times 10^{-1}$	14.65	30.00	15.02	85.00	1.49
UCS-LS-QS2-6	$7.6 \times 10^{-1}$	$1.6 \times 10^{-1}$	14.80	30.20	10.85	61.40	1.08
UCS-LS-QS2-7	$1.1 \times 10^0$	$1.7 \times 10^{-1}$	14.90	29.30	11.49	65.00	1.14
UCS-LS-QS2-8	$1.5 \times 10^0$	$1.6 \times 10^{-1}$	14.85	30.10	14.25	80.61	1.41
UCS-LS-D-1	$3.2 \times 10^2$	$2.0 \times 10^1$	15.10	31.25	22.00	124.49	2.18
UCS-LS-D-2	$1.5 \times 10^2$	$9.7 \times 10^0$	15.10	31.25	18.00	101.86	1.78
UCS-LS-D-3	$1.5 \times 10^2$	$9.3 \times 10^0$	15.10	31.10	20.80	117.70	2.06
UCS-LS-D-4	$1.1 \times 10^3$	$6.9 \times 10^1$	15.10	30.40	24.00	135.81	2.38
UCS-LS-D-5	$1.4 \times 10^2$	$8.9 \times 10^0$	15.20	30.40	17.60	99.60	1.74

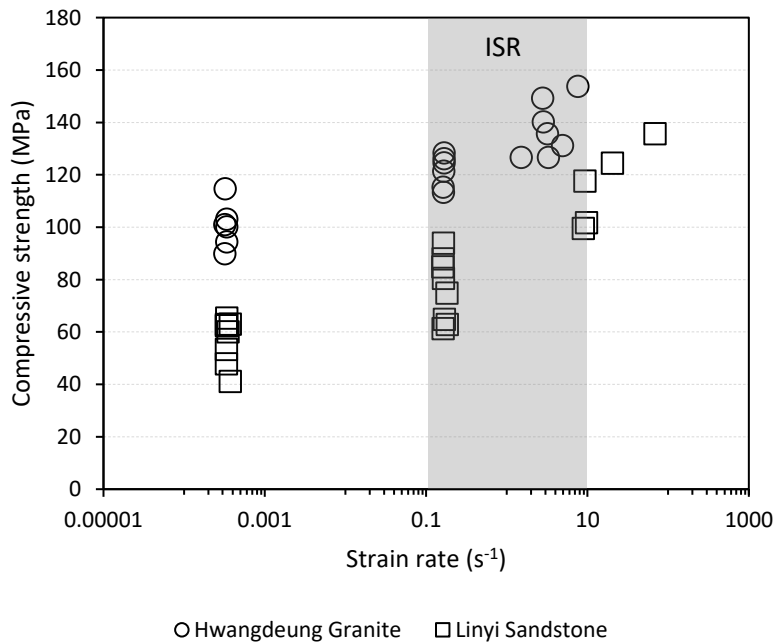


Figure 3.7. Uniaxial compressive strength over strain rate

Table 3.3. Descriptive statistics on uniaxial compressive strength of tested rock types under three testing groups

Parameters	Hwangdeung Granite			Linyi Sandstone		
	$QS_1$	$QS_2$	$D$	$QS_1$	$QS_2$	$D$
Mean	100.64	121.63	137.75	57.10	76.51	115.89
Standard Error	3.45	2.46	4.06	3.07	4.38	6.84
Median	100.70	123.13	135.81	61.34	77.81	117.70
Standard Deviation	8.45	6.04	10.73	8.69	12.39	15.30
Range	24.74	14.94	27.16	24.21	32.65	36.22
Minimum	90.00	113.48	126.76	41.19	61.40	99.60
Maximum	114.74	128.42	153.92	65.40	94.05	135.81
Sum	603.83	729.76	964.26	456.79	612.06	579.47
Count	6	6	7	8	8	5
Confidence Lev. (95.0%)	8.86	6.34	9.92	7.26	10.36	19.00

### 3.4.2 Brazilian Tension

The granite and sandstone blocks were cored with a 54 mm inner diameter core bit and then cut with a thickness of around 27 mm to form disc-shaped specimens ( $L/D \approx 0.5$ ).

Failure force was determined from the force history curve. The peak force value was used to calculate tensile strength, as mentioned in Eq. 3.3.

$$\sigma_t = \frac{2P}{\pi DT} \quad (3.3)$$

where  $\sigma_t$  is tensile strength,  $P$  is peak load,  $D$  is specimen diameter, and  $T$  is specimen thickness.

Corresponding strain rate was calculated by dividing the stress rate with the specimen Young's modulus, as shown in Eq. 3.4.

$$\dot{\sigma}_t = \frac{\Delta\sigma_t}{\Delta t}, \dot{\varepsilon} = \frac{\dot{\sigma}_t}{E} \quad (3.4)$$

where  $\dot{\sigma}_t$  stress rate,  $\Delta t$  is time duration until failure,  $\dot{\varepsilon}$  is strain rate, and  $E$  is Young's modulus.

A total of 33 specimens were tested that consist of 13 granite specimens and 20 sandstone specimens. The Brazilian tensile strength, its strain rate, and other detailed information for all testing scenarios and rock types are listed in Table 3.4, and descriptive statistics of the tensile strength value is summarized in Table 3.5. The range of strain rate resulted from this experiment was ranging from  $4.9 \times 10^{-6} \text{ s}^{-1}$  to  $5.7 \times 10^{-1} \text{ s}^{-1}$ . The averaged tensile strength of  $QS_1$ ,  $QS_2$ , and  $D$  for Hwangdeung granite were 9.15 MPa, 11.66 MPa, and 26.44 MPa while for Linyi sandstone were 4.00 MPa, 5.34 MPa, and 10.23 MPa. Overall, the result showed that tensile strength increased with increasing strain rate for both rock types. Figure 3.8 shows the crack evolution during dynamic tensile tests, and Figure 3.9 presents the relationship between Brazilian tensile strength and strain rate.

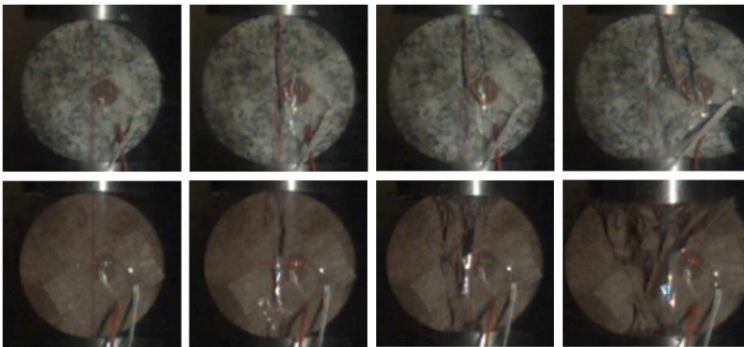


Figure 3.8. Crack evolution in Brazilian tensile test captured by the high-speed camera. Upper: Hwangdeung granite, lower: Linyi sandstone

Table 3.4. Brazilian tension test results

Specimen ID	Loading Rate (GPa/s)	Strain Rate (s <sup>-1</sup> )	<i>D</i> (mm)	<i>T</i> (mm)	Peak Load (kN)	$\sigma_t$ (MPa)	DIF
BTS-HG-QS1-1	2.5x10 <sup>-4</sup>	5.7x10 <sup>-6</sup>	53.60	26.60	24.36	10.87	1.19
BTS-HG-QS1-2	3.2x10 <sup>-4</sup>	5.9x10 <sup>-6</sup>	53.70	25.80	22.10	10.15	1.11
BTS-HG-QS1-3	3.7x10 <sup>-4</sup>	7.0x10 <sup>-6</sup>	53.65	25.80	20.94	9.62	1.05
BTS-HG-QS1-4	2.5x10 <sup>-4</sup>	4.9x10 <sup>-6</sup>	53.60	24.60	13.66	6.59	0.72
BTS-HG-QS1-5	3.4x10 <sup>-4</sup>	6.4x10 <sup>-6</sup>	53.55	25.50	18.34	8.54	0.93
BTS-HG-QS2-1	1.7x10 <sup>-1</sup>	3.3x10 <sup>-3</sup>	53.60	24.00	25.25	12.48	1.36
BTS-HG-QS2-2	1.1x10 <sup>-1</sup>	2.4x10 <sup>-3</sup>	53.55	25.80	21.21	9.76	1.07
BTS-HG-QS2-3	1.6x10 <sup>-1</sup>	3.6x10 <sup>-3</sup>	53.60	24.70	25.11	12.06	1.32
BTS-HG-QS2-4	1.6x10 <sup>-1</sup>	3.3x10 <sup>-3</sup>	53.60	24.40	26.45	12.86	1.41
BTS-HG-QS2-5	1.6x10 <sup>-1</sup>	3.1x10 <sup>-3</sup>	53.70	24.60	23.16	11.15	1.22
BTS-HG-D-1	1.3x10 <sup>1</sup>	4.6x10 <sup>-1</sup>	53.80	26.20	51.71	23.33	2.55
BTS-HG-D-2	3.2x10 <sup>1</sup>	4.5x10 <sup>-1</sup>	53.60	26.10	65.42	29.74	3.25
BTS-HG-D-3	2.3x10 <sup>1</sup>	4.2x10 <sup>-1</sup>	53.60	26.75	59.19	26.25	2.87
BTS-LS-QS1-1	1.4x10 <sup>-4</sup>	9.4x10 <sup>-6</sup>	53.25	26.40	8.28	3.75	0.94
BTS-LS-QS1-2	1.7x10 <sup>-4</sup>	9.9x10 <sup>-6</sup>	53.40	23.50	8.02	4.06	1.02
BTS-LS-QS1-3	1.6x10 <sup>-4</sup>	9.5x10 <sup>-6</sup>	53.40	25.60	8.32	3.87	0.97
BTS-LS-QS1-4	1.9x10 <sup>-4</sup>	1.2x10 <sup>-6</sup>	53.20	25.65	9.34	4.35	1.09
BTS-LS-QS1-5	1.3x10 <sup>-4</sup>	8.3x10 <sup>-6</sup>	53.35	23.50	7.50	3.81	0.95
BTS-LS-QS1-6	1.5x10 <sup>-4</sup>	1.0x10 <sup>-5</sup>	53.50	25.60	8.30	3.86	0.96
BTS-LS-QS1-7	1.8x10 <sup>-4</sup>	1.1x10 <sup>-5</sup>	53.20	26.45	9.20	4.16	1.04
BTS-LS-QS1-8	1.7x10 <sup>-4</sup>	1.0x10 <sup>-5</sup>	53.40	29.50	10.20	4.12	1.03
BTS-LS-QS2-1	7.6x10 <sup>-2</sup>	2.0x10 <sup>-3</sup>	53.20	26.40	11.05	5.00	1.25
BTS-LS-QS2-2	6.0x10 <sup>-2</sup>	2.8x10 <sup>-3</sup>	53.50	26.50	12.80	5.74	1.44
BTS-LS-QS2-3	7.5x10 <sup>-2</sup>	3.0x10 <sup>-3</sup>	53.30	26.40	10.63	4.80	1.20
BTS-LS-QS2-4	6.9x10 <sup>-2</sup>	2.4x10 <sup>-3</sup>	53.20	24.60	9.73	4.73	1.18
BTS-LS-QS2-5	7.6x10 <sup>-2</sup>	5.0x10 <sup>-3</sup>	53.35	24.70	12.56	6.06	1.52
BTS-LS-QS2-6	7.4x10 <sup>-2</sup>	5.1x10 <sup>-3</sup>	53.40	24.50	12.27	5.97	1.49
BTS-LS-QS2-7	8.8x10 <sup>-2</sup>	3.3x10 <sup>-3</sup>	53.30	26.10	12.28	5.61	1.40
BTS-LS-QS2-8	7.0x10 <sup>-2</sup>	4.0x10 <sup>-3</sup>	53.20	27.85	10.96	4.70	1.18
BTS-LS-QS2-9	8.0x10 <sup>-2</sup>	5.2x10 <sup>-3</sup>	53.20	26.40	12.59	5.40	1.35
BTS-LS-D-1	4.6x10 <sup>0</sup>	5.7x10 <sup>-1</sup>	53.50	28.75	25.53	10.56	2.64
BTS-LS-D-2	4.4x10 <sup>0</sup>	3.2x10 <sup>-1</sup>	53.45	28.60	26.15	10.88	2.72
BTS-LS-D-3	5.1x10 <sup>0</sup>	4.5x10 <sup>-1</sup>	53.10	29.00	22.41	9.26	2.32

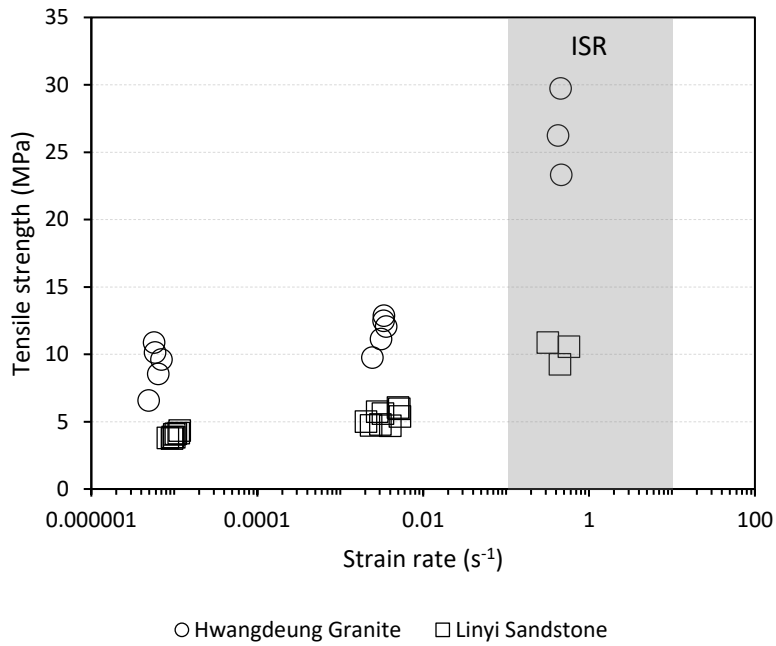


Figure 3.9. Brazilian tensile strength over strain rate

Table 3.5 Descriptive statistics on Brazilian tensile strength of tested rock types under three testing groups

Parameters	Hwangdeung Granite			Linyi Sandstone		
	$QS_1$	$QS_2$	$D$	$QS_1$	$QS_2$	$D$
Mean	9.15	11.66	26.44	4.00	5.34	10.23
Standard Error	0.74	0.55	1.85	0.07	0.18	0.50
Median	9.62	12.06	26.25	3.97	5.40	10.56
Standard Deviation	1.67	1.24	3.21	0.21	0.54	0.86
Range	4.28	3.10	6.41	0.61	1.36	1.62
Minimum	6.59	9.76	23.33	3.75	4.70	9.26
Maximum	10.87	12.86	29.74	4.35	6.06	10.88
Sum	45.76	58.32	79.32	31.97	48.02	30.70
Count	5	5	3	8	9	3
Confidence Lev. (95.0%)	2.07	1.54	7.97	0.18	0.42	2.13

### 3.4.3 Mode-I Fracture Toughness

To obtain mode-I fracture toughness, notched semi-circular bend specimens (NSCB) (Kuruppu et al., 2014) were prepared. The rock blocks were cored with a 38 mm inner diameter core bit and then sliced to form a disc-shaped specimen with a thickness of about 20 mm. Each disc-shaped specimen was then cut into two halves. The calculation of fracture toughness referred to the ISRM Suggested Method for Determining the Mode-I Static Fracture Toughness Using Semi-Circular Bend Specimen (Kuruppu et al., 2014). Mode-I fracture toughness ( $K_{IC}$ ) is determined using the peak load ( $P_{max}$ ) as shown in Eqs. 3.5 and 3.6.

$$K_{IC} = Y' \frac{P_{max} \sqrt{\pi a}}{2RB} \quad (3.5)$$

where,

$$Y' = -1.297 + 9.516 \left( \frac{s}{2R} \right) - \left[ 0.47 + 16.457 \left( \frac{s}{2R} \right) \right] \beta + \left[ 1.071 + 34.401 \left( \frac{s}{2R} \right) \right] \beta^2 \quad (3.6)$$

Geometrical terms used in the equations above are described as follows:  $R$  is the radius of the specimen,  $B$  is the thickness,  $a$  is the notch length,  $s$  is the distance between the two supporting rollers at the lower jig, and  $\beta = a/R$ . The non-dimensional stress intensity factor ( $Y'$ ) is proved to be valid for  $\beta \geq 0.2$ , and the recommended range for  $s/2R$  is  $0.5 \leq s/2R \leq 0.8$ . In this study, all  $\beta$  and  $s/2R$  values were maintained to meet the criteria. Separately, the loading rate was determined from the slope of the load history curve recorded from each test.

A total of 22 specimens were tested that consist of 11 specimens for each rock type. A comprehensive result of all test scenarios is provided in

Table 3.6, and descriptive statistics of the  $K_{IC}$  value is summarized in Table 3.7. For granite,  $K_{IC}$  value in  $QS_1$  ranged from 0.74 to 0.90 MPa.m<sup>0.5</sup> while in  $QS_2$ , the value was from 1.53 to 2.01 MPa.m<sup>0.5</sup>. The averaged loading rates for those two quasi-static scenarios varied from  $1.5 \times 10^{-5}$  to  $2.6 \times 10^{-2}$  GPa.m<sup>0.5</sup> s<sup>-1</sup>, respectively. In dynamic mode,  $K_{IC}$  value stretched from 4.26 to 5.33 MPa.m<sup>0.5</sup> with the loading rates varied between  $6.8 \times 10^0$  and  $7.1 \times 10^1$  GPa.m<sup>0.5</sup> s<sup>-1</sup>. The result showed that  $K_{IC}$  increases with loading rate and, in the dynamic state,  $K_{IC}$  rose for about six times from its static value.

A similar fact was also found in the sandstone case. The averaged  $K_{IC}$  and loading rate for  $QS_1$ ,  $QS_2$ , and  $D$  are 0.36, 0.57, 2.44 MPa.m<sup>0.5</sup> and  $5.7 \times 10^{-6}$ ,  $1.7 \times 10^{-2}$ ,  $2.9 \times 10^1$  GPa.m<sup>0.5</sup> s<sup>-1</sup>, respectively. Dynamic  $K_{IC}$  increased about seven times from the static ones. Figure 3.10 shows crack evolution during the test in dynamic mode, and Figure 3.11 presents the relationship between  $K_{IC}$  and loading rate.

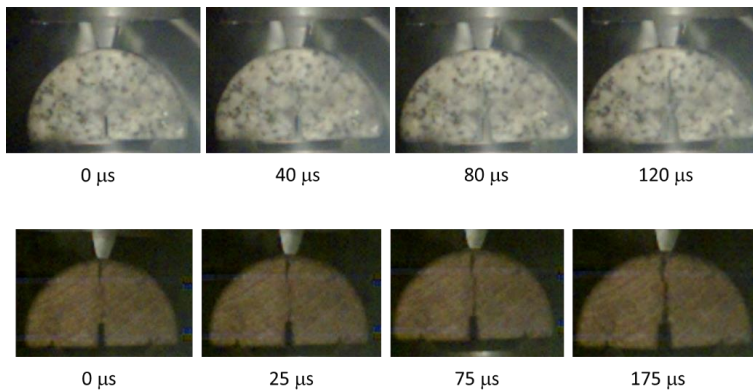


Figure 3.10. Crack evolution in mode-I dynamic fracture toughness test captured by the high-speed camera. Upper: Hwangdeung granite, lower: Linyi sandstone

Table 3.6. Mode-I fracture toughness test results

Specimen ID	Loading Rate		$B$ (mm)	$R$ (mm)	$P_{max}$ (kN)	$Y'$	$K_{IC}$ (MPa.m <sup>0.5</sup> )
	kN.s <sup>-1</sup>	GPa.m <sup>0.5</sup> .s <sup>-1</sup>					
FT-HG-QS <sub>1</sub> -1	2.6x10 <sup>-2</sup>	1.1x10 <sup>-5</sup>	19.95	22.33	1.76	2.73	0.74
FT-HG-QS <sub>1</sub> -2	5.9x10 <sup>-2</sup>	2.1x10 <sup>-5</sup>	21.46	21.51	1.99	2.90	0.85
FT-HG-QS <sub>1</sub> -3	2.9x10 <sup>-2</sup>	1.3x10 <sup>-5</sup>	19.90	22.17	2.09	2.76	0.90
FT-HG-QS <sub>2</sub> -1	3.4x10 <sup>1</sup>	2.7x10 <sup>-2</sup>	19.00	18.70	2.85	3.65	2.01
FT-HG-QS <sub>2</sub> -2	3.6x10 <sup>1</sup>	3.2x10 <sup>-2</sup>	19.50	19.85	2.61	3.30	1.53
FT-HG-QS <sub>2</sub> -3	3.9x10 <sup>1</sup>	1.8x10 <sup>-2</sup>	20.10	19.52	3.21	3.40	1.91
FT-HG-D-1	1.2x10 <sup>6</sup>	1.2x10 <sup>1</sup>	15.93	21.68	8.58	2.86	4.87
FT-HG-D-2	7.5x10 <sup>4</sup>	6.8x10 <sup>0</sup>	15.55	21.82	7.45	2.83	4.26
FT-HG-D-3	1.2x10 <sup>5</sup>	2.6x10 <sup>1</sup>	16.15	18.49	6.23	3.72	5.33
FT-HG-D-4	3.3x10 <sup>4</sup>	5.6x10 <sup>1</sup>	18.51	22.44	10.05	2.70	4.49
FT-HG-D-5	4.1x10 <sup>4</sup>	7.1x10 <sup>1</sup>	19.55	19.00	7.80	3.56	5.12
FT-LS-QS <sub>1</sub> -1	9.2x10 <sup>-3</sup>	4.2x10 <sup>-6</sup>	18.61	21.17	0.70	2.97	0.36
FT-LS-QS <sub>1</sub> -2	1.3x10 <sup>-2</sup>	6.7x10 <sup>-6</sup>	18.77	21.68	0.78	2.86	0.37
FT-LS-QS <sub>1</sub> -3	1.2x10 <sup>-2</sup>	6.3x10 <sup>-6</sup>	18.88	21.11	0.68	2.99	0.35
FT-LS-QS <sub>2</sub> -1	4.0x10 <sup>1</sup>	1.7x10 <sup>-2</sup>	19.50	22.00	1.25	2.79	0.56
FT-LS-QS <sub>2</sub> -2	3.8x10 <sup>1</sup>	1.4x10 <sup>-2</sup>	19.60	22.10	1.28	2.77	0.56
FT-LS-QS <sub>2</sub> -3	3.9x10 <sup>1</sup>	1.8x10 <sup>-2</sup>	18.50	22.00	1.27	2.79	0.60
FT-LS-D-1	1.2x10 <sup>6</sup>	5.8x10 <sup>1</sup>	18.38	21.61	3.56	2.87	1.77
FT-LS-D-2	7.5x10 <sup>4</sup>	3.5x10 <sup>1</sup>	18.51	21.69	5.10	2.86	2.49
FT-LS-D-3	1.2x10 <sup>5</sup>	2.7x10 <sup>1</sup>	18.30	21.93	6.23	2.81	2.99
FT-LS-D-4	3.3x10 <sup>4</sup>	4.3x10 <sup>0</sup>	18.70	22.30	5.60	2.73	2.52
FT-LS-D-5	3.0x10 <sup>4</sup>	2.0x10 <sup>1</sup>	18.60	21.75	5.03	2.84	2.43

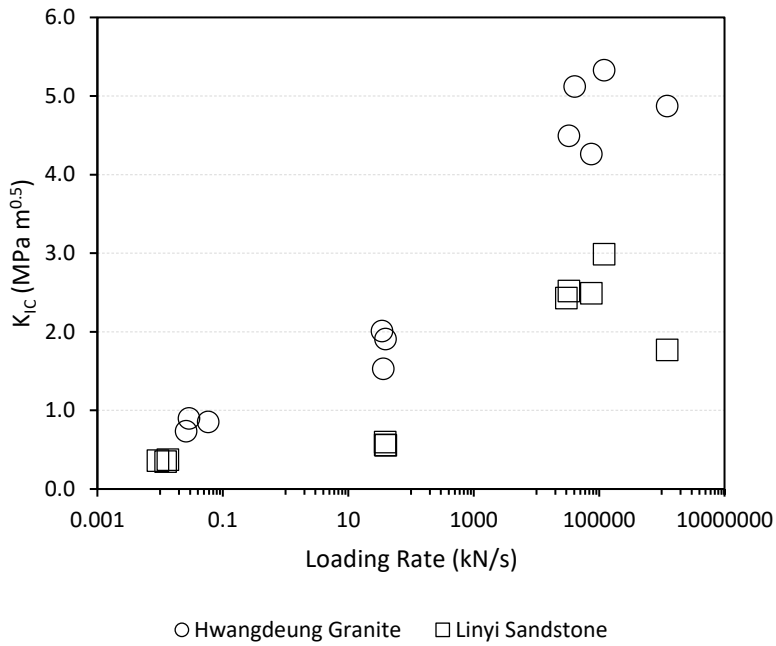


Figure 3.11. Mode-I fracture toughness ( $K_{IC}$ ) over loading rate

Table 3.7. Descriptive statistics on mode-I fracture toughness of tested rock types under three testing groups

Parameters	Hwangdeung Granite			Linyi Sandstone		
	$QS_1$	$QS_2$	$D$	$QS_1$	$QS_2$	$D$
Mean	0.83	1.82	4.82	0.36	0.57	2.44
Standard Error	0.05	0.15	0.20	0.01	0.01	0.19
Median	0.85	1.91	4.87	0.36	0.56	2.49
Standard Deviation	0.08	0.25	0.44	0.01	0.02	0.44
Range	0.16	0.48	1.07	0.02	0.04	1.22
Minimum	0.74	1.53	4.26	0.35	0.56	1.77
Maximum	0.90	2.01	5.33	0.37	0.60	2.99
Sum	2.49	5.45	24.08	1.09	1.72	12.20
Count	3	3	5	3	3	5
Confidence Lev. (95.0%)	0.21	0.63	0.54	0.03	0.06	0.54

### 3.4.4 Punch Shear

The rock blocks were cored with a 54 mm inner diameter core bit and then cut with a thickness of around 27 mm to form disc-shaped specimens ( $L/D \approx 0.24$ ). A unique holder was manufactured to hold the specimen during punch shear testing. An annular steel holder consists of a front and a rear supporter, which were joined by a screw to hold the disc specimen (see Figure 3.12). The purpose of the front supporter is to minimize bending force and secondary damage on the sample during and after the test. The inner diameter of the rear supporter was 25.4 mm, 0.4 mm larger than the diameter of the puncher to accommodate shear deformation (Huang et al., 2011). Representative images on the punch shear test can be seen in Figure 3.13.

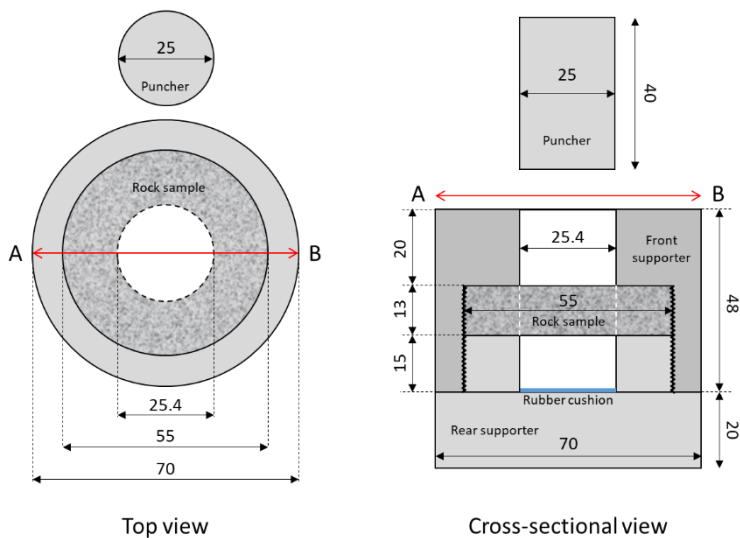


Figure 3.12. Detailed schematic view of the specimen holder (unit: mm)

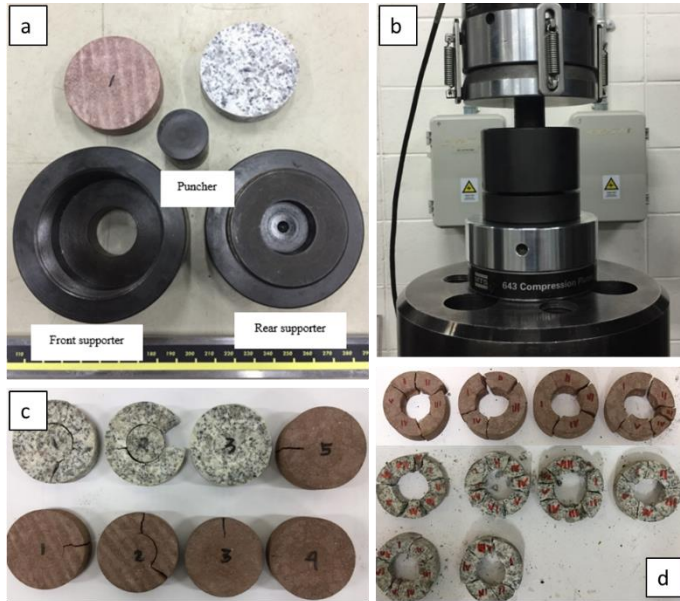


Figure 3.13. Punch shear test. a) Specimen holder; b) setup; c) specimen after quasi-static test; and d) specimen after the dynamic test

The shear strength of the specimen was calculated by dividing the maximum load carried by the specimen during the test by the shearing area that was measured from the lateral surface area of the plug resulted from the punching.

A total of 30 specimens were tested that consist of 15 specimens for each rock type. The shear strength, its strain rate, and other detailed information for all testing scenarios and rock types can be seen in Table 3.8, and descriptive statistics of the shear strength value is summarized in Table 3.9. The range of strain rate resulted from this experiment was ranging from  $1.0 \times 10^{-6} \text{ s}^{-1}$  to  $4.5 \times 10^2 \text{ s}^{-1}$ . The averaged shear strength of  $QS_1$ ,  $QS_2$ , and  $D$  for Hwangdeung granite were 15.17 MPa, 21.54 MPa, and 44.57 MPa while for Linyi sandstone were 11.27 MPa, 12.47 MPa, and 33.34 MPa. Overall, the result showed that shear strength increased

with increasing strain rate for both rock types. Figure 3.14 shows the relationship between shear strength and strain rate.

Table 3.8. Punch shear test results

Specimen ID	Loading Rate (GPa/s)	Strain Rate ( $s^{-1}$ )	D (mm)	T (mm)	Peak Load (kN)	Plug's Lateral Area ( $mm^2$ )	$\tau$ (MPa)	DIF
PS-HG-QS1-1	$6.6 \times 10^{-5}$	$2.5 \times 10^{-6}$	53.79	13.80	30.57	2167.70	14.10	0.93
PS-HG-QS1-2	$9.8 \times 10^{-5}$	$3.6 \times 10^{-6}$	53.79	13.96	42.50	2192.83	19.38	1.28
PS-HG-QS1-3	$7.8 \times 10^{-5}$	$2.9 \times 10^{-6}$	53.50	13.10	32.55	2057.74	15.82	1.04
PS-HG-QS1-4	$2.7 \times 10^{-5}$	$1.0 \times 10^{-6}$	53.30	13.30	23.81	2089.16	11.40	0.75
PS-HG-QS2-1	$2.4 \times 10^{-1}$	$8.6 \times 10^{-3}$	53.60	14.20	33.72	2230.53	15.12	1.00
PS-HG-QS2-2	$4.1 \times 10^{-1}$	$1.6 \times 10^{-2}$	53.50	13.15	51.08	2065.60	24.73	1.63
PS-HG-QS2-3	$4.2 \times 10^{-1}$	$1.6 \times 10^{-2}$	53.30	13.45	49.97	2112.72	23.65	1.56
PS-HG-QS2-4	$3.9 \times 10^{-1}$	$1.4 \times 10^{-2}$	53.50	13.50	50.00	2120.58	23.58	1.55
PS-HG-QS2-5	$3.1 \times 10^{-1}$	$1.2 \times 10^{-2}$	53.50	13.35	43.27	2097.01	20.64	1.36
PS-HG-D-1	$3.2 \times 10^2$	$1.7 \times 10^1$	53.90	13.55	100.80	2128.43	47.36	3.12
PS-HG-D-2	$3.2 \times 10^2$	$7.0 \times 10^0$	53.81	13.70	98.00	2151.99	45.54	3.00
PS-HG-D-3	$5.1 \times 10^1$	$1.8 \times 10^1$	53.78	13.20	96.80	2073.45	46.69	3.08
PS-HG-D-4	$3.7 \times 10^1$	$1.4 \times 10^0$	53.88	14.10	92.40	2214.82	41.72	2.75
PS-HG-D-5	$1.2 \times 10^3$	$4.6 \times 10^1$	53.95	14.40	115.33	2261.95	50.99	3.36
PS-HG-D-6	$4.6 \times 10^1$	$2.1 \times 10^0$	53.84	13.40	74.00	2104.87	35.16	2.32
PS-LS-QS1-1	$4.5 \times 10^{-5}$	$5.7 \times 10^{-6}$	53.45	15.31	23.58	2404.89	9.81	0.87
PS-LS-QS1-2	$6.0 \times 10^{-5}$	$7.4 \times 10^{-6}$	53.38	13.30	25.92	2089.16	12.41	1.10
PS-LS-QS1-3	$3.5 \times 10^{-5}$	$4.4 \times 10^{-6}$	53.24	21.00	34.07	3298.67	10.33	0.92
PS-LS-QS1-4	$4.6 \times 10^{-5}$	$5.8 \times 10^{-6}$	53.33	20.92	41.24	3286.11	12.55	1.11
PS-LS-QS2-1	$1.5 \times 10^{-1}$	$1.9 \times 10^{-2}$	53.35	13.70	20.30	2151.99	9.43	0.84
PS-LS-QS2-2	$2.5 \times 10^{-1}$	$3.1 \times 10^{-2}$	53.40	14.05	28.80	2206.97	13.05	1.16
PS-LS-QS2-3	$1.7 \times 10^{-1}$	$2.1 \times 10^{-2}$	53.35	13.50	32.20	2120.58	15.18	1.35
PS-LS-QS2-4	$1.7 \times 10^{-1}$	$3.8 \times 10^{-3}$	53.40	14.00	26.90	2199.11	12.23	1.09
PS-LS-D-1	$2.4 \times 10^2$	$4.5 \times 10^1$	53.70	14.10	70.40	2214.82	31.79	2.82
PS-LS-D-2	$2.0 \times 10^1$	$4.1 \times 10^1$	53.71	14.20	66.40	2230.53	29.77	2.64
PS-LS-D-3	$2.1 \times 10^2$	$6.4 \times 10^0$	53.65	14.60	71.20	2293.36	31.05	2.75
PS-LS-D-4	$2.3 \times 10^2$	$2.7 \times 10^1$	53.72	14.40	77.60	2261.95	34.31	3.04
PS-LS-D-5	$1.8 \times 10^1$	$1.2 \times 10^0$	53.54	14.60	76.40	2293.36	33.31	2.96
PS-LS-D-6	$6.4 \times 10^1$	$8.1 \times 10^0$	53.51	13.70	71.60	2151.99	33.27	2.95
PS-LS-D-7	$6.9 \times 10^2$	$7.5 \times 10^0$	53.66	13.70	85.78	2151.99	39.86	3.54

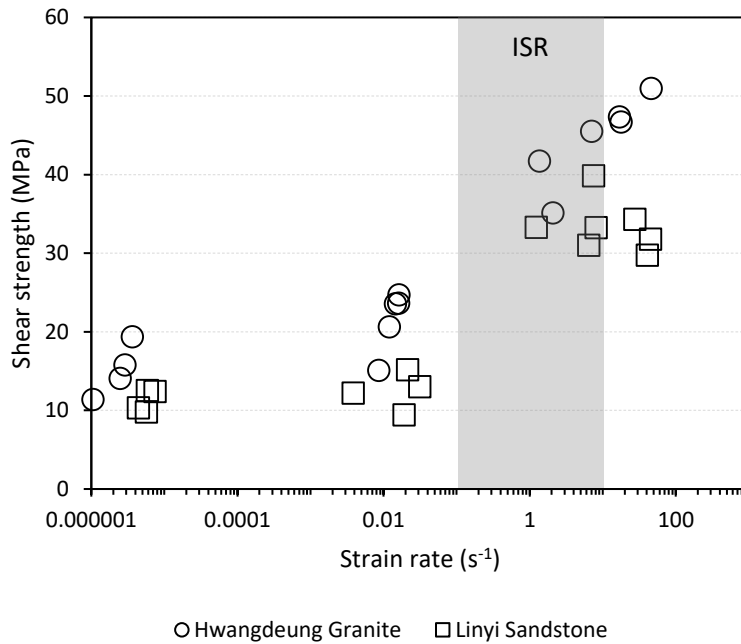


Figure 3.14. Shear strength over strain rate

Table 3.9. Descriptive statistics on shear strength of tested rock types under three testing groups

Parameters	Hwangdeung Granite			Linyi Sandstone		
	$QS_1$	$QS_2$	$D$	$QS_1$	$QS_2$	$D$
Mean	15.17	21.54	44.57	11.27	12.47	33.34
Standard Error	1.67	1.74	2.24	0.70	1.19	1.23
Median	14.96	23.58	46.11	11.37	12.64	33.27
Standard Deviation	3.34	3.90	5.50	1.41	2.38	3.26
Range	7.98	9.61	15.83	2.74	5.75	10.09
Minimum	11.40	15.12	35.16	9.81	9.43	29.77
Maximum	19.38	24.73	50.99	12.55	15.18	39.86
Sum	60.70	107.71	267.45	45.09	49.90	233.35
Count	4	5	6	4	4	7
Confidence Lev. (95.0%)	5.32	4.84	5.77	2.24	3.79	3.02

### 3.5 Numerical Modeling of Dynamic Rock Test

#### 3.5.1 Material Model of Dynamic Rock Test

In this study, the RHT (Riedel, Hiermaier, and Thoma) model was used to model the rock. The RHT model was initially developed for modeling the behavior of concrete under dynamic loading. In application, it can also be useful to model other brittle materials such as rock and ceramic (Riedel et al., 1999).

The uniaxial compressive strength used in the RHT model refers to the strength of a cubic-shaped specimen, known as cube strength. The model is formulated such that the input could be scaled with the cube strength, so by changing the cube strength value; the remaining terms would be scaled proportionally (ANSYS, 2010; Park & Jeon, 2010). In the material library of the program, there are two options for the RHT model: 35 MPa and 140 MPa of concrete strength. In this study, the 140 MPa option was chosen since it is relatively quite close to the strength of the rock model.

The uniaxial compressive strength of a cylindrical specimen obtained from this study was converted to the uniaxial compressive strength of a cubic specimen by the following empirical relationship (Eq. 3.7) (Griffiths & Thom, 2007):

$$f_{cube} = \frac{f_{cylinder}}{CF_s} \quad (3.7)$$

where  $f_{cube}$  is the uniaxial compressive strength of a cubic specimen,  $f_{cylinder}$  is the uniaxial compressive strength of a cylindrical specimen, and  $CF_s$  is the conversion factor for cubic vs. cylindrical specimen ( $CF_s = 0.8$ ). The tensile strength and shear strength were obtained from the

laboratory test and the ratio of  $f_t/f_c$  and  $f_s/f_c$  were calculated concerning the cube strength. The parameters of the RHT model for rock material used in this study are listed in Table 3.10.

The loading plate model was assumed to be steel, and the material model of the steel was adopted directly from the material library available in the software. The referenced parameter of the steel model is provided in Table 3.11.

Table 3.10. Parameters of the RHT model for rock material model

Parameter	Value	
	Granite	Sandstone
Density (gr/cm <sup>3</sup> )	2.94	2.75
Young's modulus (GPa)	53.83	15.85
Bulk modulus (GPa)	25.63	7.55
Shear modulus (GPa)	23.40	6.89
Uniaxial compressive strength (MPa)	137.75	115.89
Cube strength, $f_c$ (MPa)	172.19	144.86
Tensile strength, $f_t$ (MPa)	26.44	10.23
$f_t/f_c$ ratio	0.15	0.07
Shear strength, $f_s$ (MPa)	44.57	33.34
$f_s/f_c$ ratio	0.26	0.23
Erosion type	Geometric strain	Geometric strain
Erosion strain	0.009	0.01

Table 3.11. Parameter of the referenced steel material used in this study

Parameter	Value	Parameter	Value
Material	Steel S-7	Hardening constant (MPa)	477
Density (gr/cm <sup>3</sup> )	7.75	Strain rate constant	0.012
Material strength	Johnson Cook	Thermal softening exponent	1.00
Shear modulus (GPa)	81.8	Melting temperature (K)	1,763
Yield stress (MPa)	1,539	Ref. strain rate (/s)	1.00

### 3.5.2 Geometry and Boundary Conditions of the Dynamic Rock Test Model

#### 3.5.2.1 Uniaxial Compression Model

A 3-D cylinder model was made with a diameter of 15 mm and a height of 30 mm ( $L/D = 2$ ). The total element number of the cylinder model was 384,000 elements. On the top and the bottom of the cylinder, steel plate models were placed. A vertical load was applied from the top direction downward, through the movement of the top plate with predetermined velocities (0.1, 0.5, 1.0, 5.0, 10 m/s). The bottom plate is set to a fixed boundary, and the lateral surface of the cylinder model was to a free condition (see Figure 3.15).

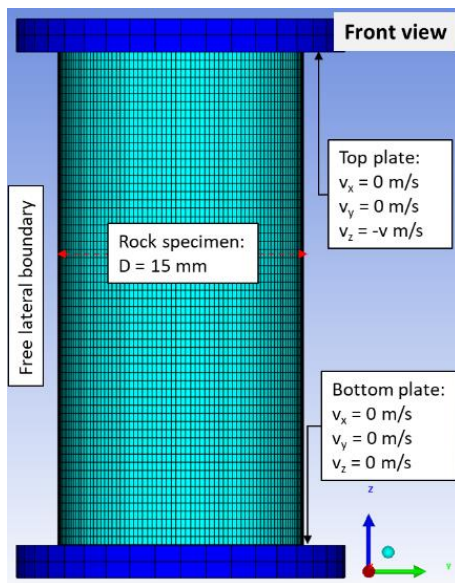


Figure 3.15. Uniaxial compression FEM model and boundary condition

### 3.5.2.2 Brazilian Tension Model

A 3-D disc-shaped model was developed with a 54 mm diameter and 27 mm thickness ( $L/D = 0.5$ ). The total element number of the disc model was 500,000 elements. Two plates were positioned on the upper and lower relative to the specimen. Dynamic loading was applied to the specimen downward from the top plate parallel to the z-axis, and the bottom view plate was left unmoved (see Figure 3.16). The contact force in the z-direction was monitored on the upper plate, then the maximum value of the contact force was taken for tensile strength calculation.

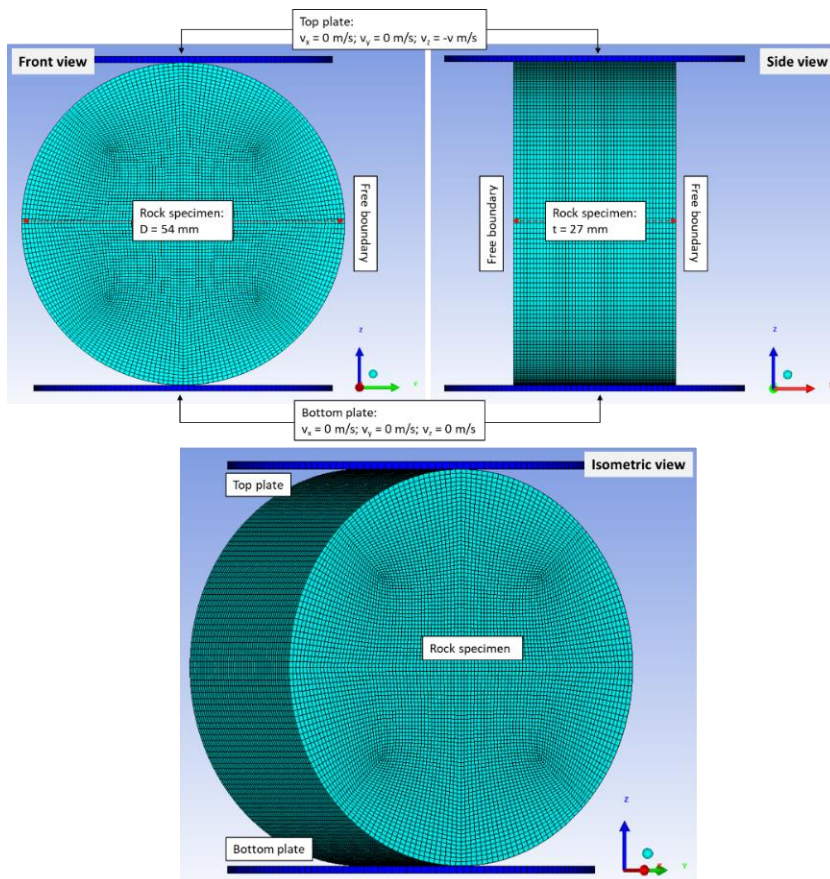


Figure 3.16. Brazilian tension FEM model and boundary condition

### 3.5.2.3 Mode-I Fracture Toughness Model

A 3-D notched semi-circular bending (NSCB) model was designed with a 38 mm of diameter, 19 mm of thickness, and 1 mm wide of notch located in the middle of the flat segment of the specimen model with a 6 mm of notch depth. The total element number for an NSCB specimen was one million elements.

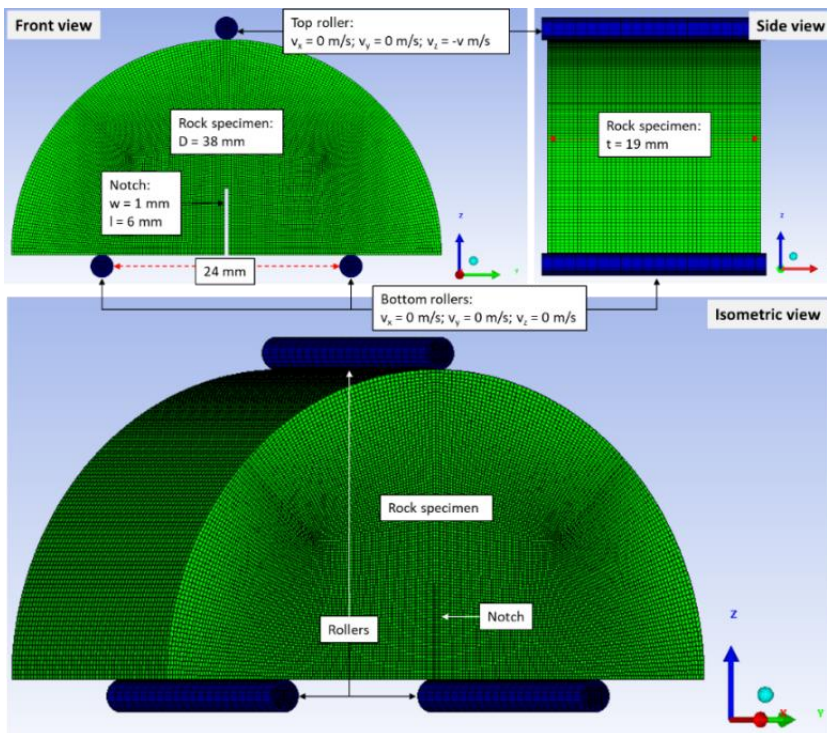


Figure 3.17. Mode-I NSCB fracture toughness FEM model and boundary condition

Figure 3.17 depicted the NSCB model. A roller was positioned on top of the sample, and two rollers were placed on the bottom. The distance between the two bottom rollers was 24 mm, which was corresponded to

the laboratory test configuration. Dynamic loading was applied to the specimen downward from the top roller parallel to the z-axis. Two rollers at the bottom were set to a fixed condition. Contact force in z-direction was monitored on the top roller then the maximum value of the contact force was taken for fracture toughness calculation.

#### 3.5.2.4 *Punch Shear Model*

A 3-D disc-shaped model was developed with a 54 mm of diameter and 12.5 mm of the thickness ( $L/D = 0.23$ ). The total element number of the disc model was 300,000 elements. The disc was placed inside the outer model called supporters. The supporter was divided into three parts: top, bottom, and radial supporters. The supporters restricted the disc model to deform to their respective directions. There is a hole in each of the top and bottom supporters with a diameter of 25.4 mm.

A cylinder type of puncher, 25 mm of diameter, vertically pushed the disc specimen with a defined velocity through the hole on the top supporter. This load would create a plug, and the plug would pass through the hole on the bottom supporter. Figure 3.18 shows the punch shear model.

The contact force in z-direction was monitored on the puncher, and then the maximum value of the contact force was taken for the shear strength calculation. The shearing area was calculated from the lateral surface area of the plug resulted from the punching.

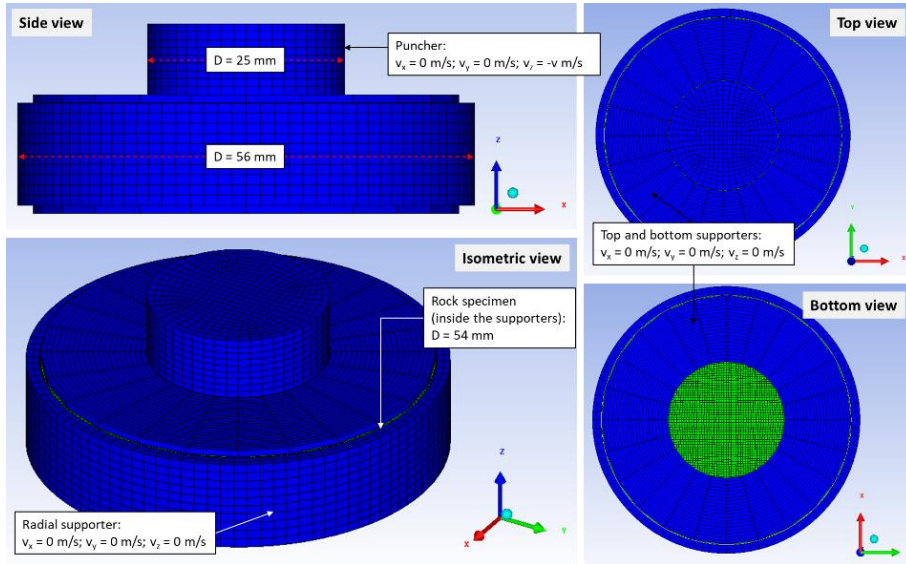


Figure 3.18. Punch shear FEM model and boundary condition

### 3.5.3 Results of Dynamic Rock Test Modeling

It should be noted that the simulation did not cover the entire span of strain rate level tested in the laboratory, specifically the quasi-static domain. The AUTODYN<sup>®</sup> program is a tool known for dynamic simulation. It means that it deals with a rapid process and, therefore, covering only a small fraction of time in each of its computation cycles. Thus, performing a quasi-static speed of simulation will require an extremely long computation time. That is why in Figures 3.19 – 3.22, the simulation results for the lower strain rate were not obtained. Consequently, in this study, the FEM simulation serves as the extended information of the laboratory works to a higher strain rate zone.

The results of FEM simulation for all tests are provided in Figures 3.19 – 3.22. The FEM results are plotted together with the laboratory test results correspondingly. The graphs show that, at the higher strain rate,

FEM simulation results show a more significant increase in strength compared to the laboratory works in all cases. This result corresponds to the idea that, at a higher rate, the increasing slope tends to be steeper than at the lower rate (Olsson, 1991; Wang & Tonon, 2011; Wicaksana et al., 2018a).

Representative damage distribution and its corresponding force-time graph are presented in Figure 3.23.

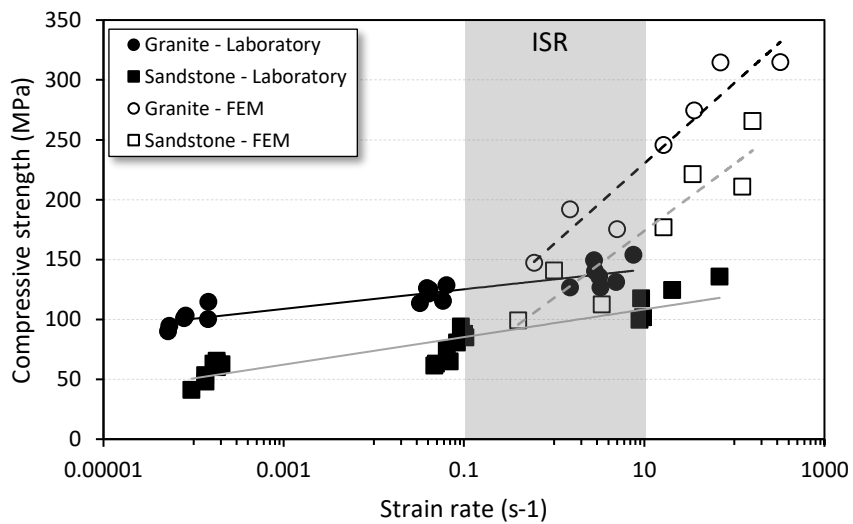


Figure 3.19. Uniaxial compressive strength over strain rate: the laboratory test and the FEM simulation

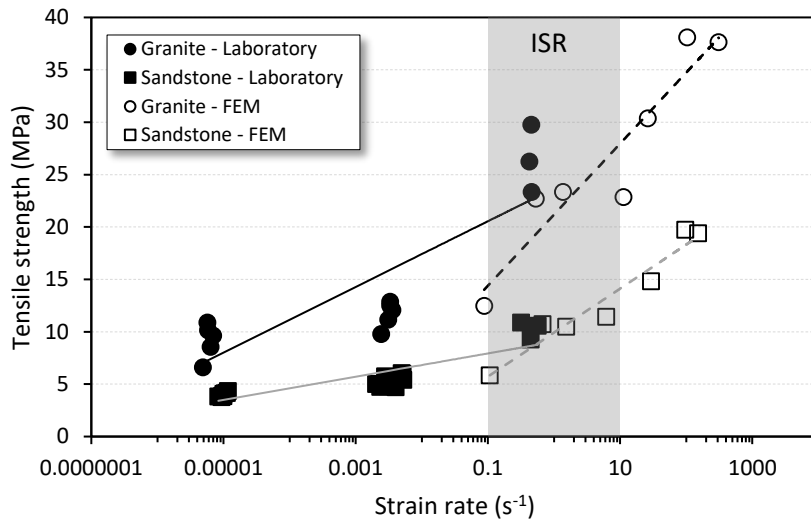


Figure 3.20. Tensile strength over strain rate: the laboratory test and the FEM simulation

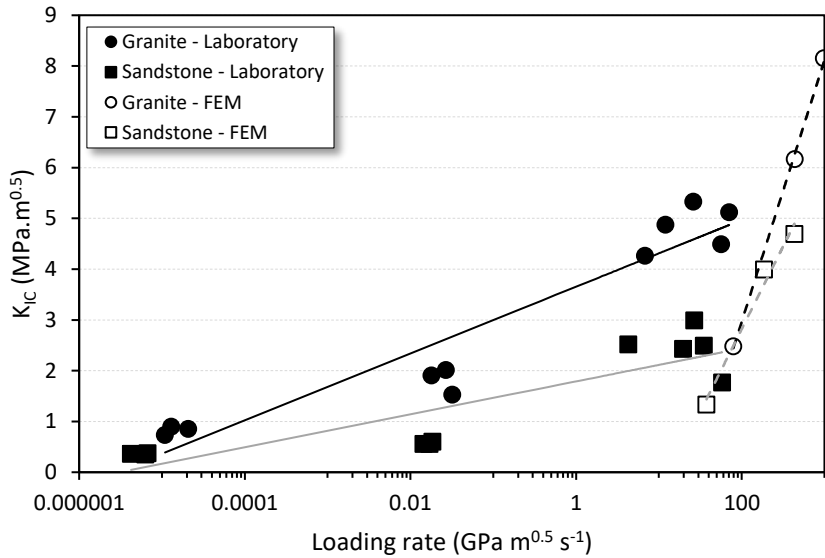


Figure 3.21. Mode-I fracture toughness over loading rate: the laboratory test and the FEM simulation

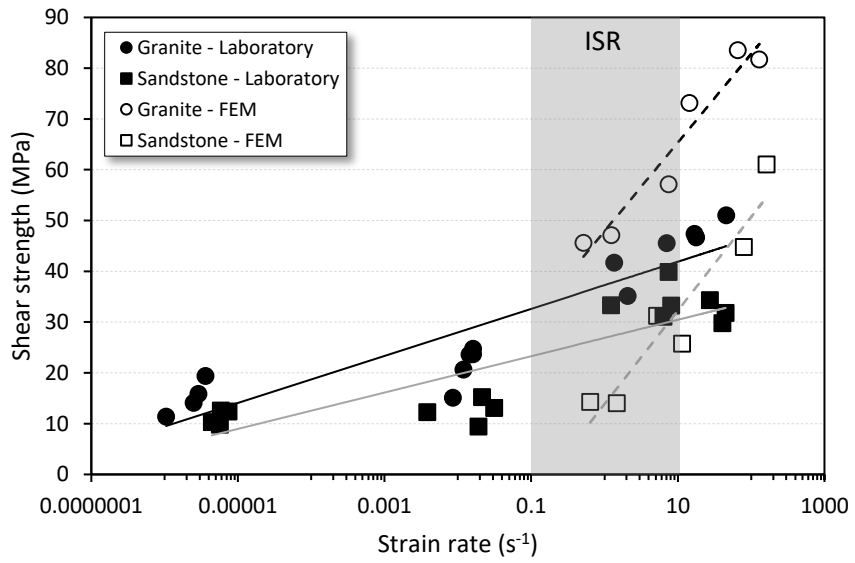
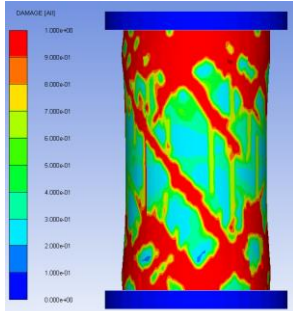
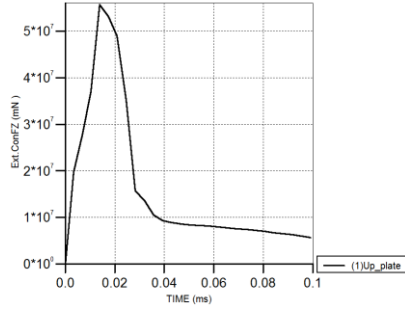


Figure 3.22. Shear strength over strain rate: the laboratory test and the FEM simulation

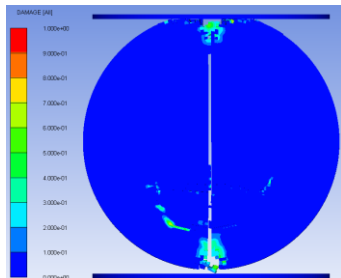


Damage distribution at cycle 1000, elapsed time 0.073 ms

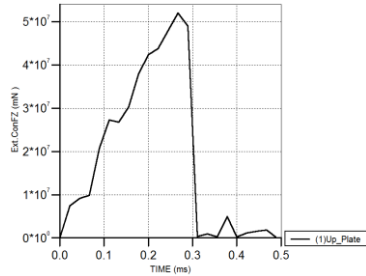


External contact force in z-direction over time

(a) UCS of granite at 10 m/s of loading speed

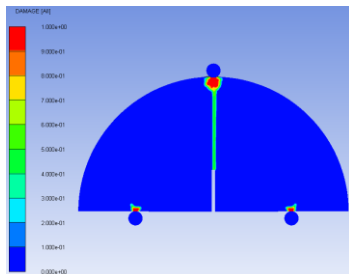


Damage distribution at cycle 25000, elapsed time 0.56 ms

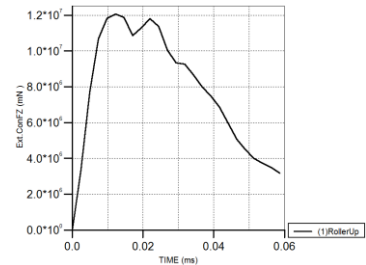


External contact force in z-direction over time

(b) BTS of granite at 1 m/s of loading speed

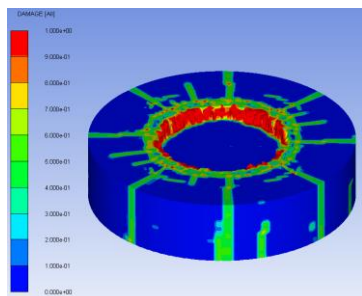


Damage distribution at cycle 20000, elapsed time 0.024 ms

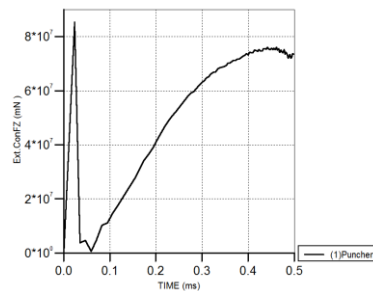


External contact force in z-direction over time

(c) Mode-I fracture toughness of granite at 10 m/s of loading speed



Damage distribution at cycle 62500, elapsed time 0.56 ms



External contact force in z-direction over time

(d) Punch shear of granite at 5 m/s of loading speed

Figure 3.23. Typical modeling result for various tests at high rate loading

## **3.6 Discussion on Dynamic Rock Properties**

### **3.6.1 Rock Failure Under Dynamic Loading**

Behavioral change of rock in dynamic loading conditions has been demonstrated by many investigators through laboratory experiments as well as by numerical simulations. The reason why it happens is not clearly identified. This phenomenon might be seen from the thermal activation approach, which is usually associated with the plastic behavior of metallic materials (Green & Perkins, 1968; Kumar, 1968; Lindholm et al., 1974). The thermal activation assumption is that the effect of increased strength at increased strain rate at room temperature is similar to an increased strength at a low temperature at a low strain rate (Kumar, 1968).

In ISR, the thermal activation mechanism can be logically accepted as suggested by Lankford (1982), on the ceramic material at the strain rate below  $10^2$  per second. However, at the microscopic view, the grain size of the rock is large compared to the scale of grain dislocation motion associated with the thermal activation process (Green & Perkins, 1968). Furthermore, the high strain rate is associated with a very rapid loading where no sufficient time is available for thermal activation of the fracture process (Lindholm et al., 1974).

The effect of material inertia can also describe the physical mechanism of dynamic rock fracture (Asprone et al., 2009; Lankford, 1982; Wang & Tonon, 2011). Inertia controls the strain rate dependent behavior because the crack extension is restricted by material inertia (Wang & Tonon, 2011). Typically, rock fails at the stress level corresponding to the beginning of the micro-crack initiation process, and material inertia inhibits crack growth. In the conclusion of a dynamic experiment on

ceramic material, Lankford (1982) also stated that material inertia controls the strength of the ceramic material, specifically suppresses the extension of micro-cracks, thus leads to the higher strength.

It has been discussed that rock fragmentation is also rate-dependent. A higher strain rate develops a higher number of micro-cracks and fragments of the specimen (Cho et al., 2003; Zhao et al., 1999). As the number of micro-cracks increases, the number of failure surfaces also increases (Swan et al., 1989). The more substantial fracture surface results in higher cumulative energy absorption (Li et al., 2005). It can be inferred that in the higher strain rate, energy absorption is also significant, that means numerous small fractures absorb energy from the load source. Therefore, the strength is correspondently improved at a high strain rate. Conversely, at the lower strain rate, a few fractures are responsible for the rock breaking process and are incapable of absorbing more energy, thus can lead to the lower strength of the rock.

The relation between fragment size and strain rate was visually recognizable, even though the fragment sizes were not analyzed in this study. Taking an example from the UCS test, at the lower strain rate, the sample was broken into larger fragments plus some fine particles. At the ISR rate, about 1/s, the samples were completely crushed into fine dust plus some particles not larger than three millimeters. From this observation, it can be inferred that a dynamic test involves a more significant number of micro-cracks in its breaking process that leads to the significant reduction of fragment sizes and higher fracture energy absorption.

The strength differences can also be associated with rock inhomogeneity (Cho et al., 2003; Zhu, 2008). The effect of the strain rate is less for the

material that has a high uniformity index (Cho et al., 2003). In other words, the dynamic strength of rock specimens does not change significantly with the uniformity index, while in the static case, the strength increases with increasing homogeneity index (Zhu, 2008). Hence, rock inhomogeneity controls the strain rate dependence on rock strength.

### 3.6.2 Effect of Strain Rate on Mechanical Properties of Rock

To indicate the increased strength under dynamic loading state, some of the results of dynamic strength are processed in terms of dynamic increase factor (DIF), which is defined as the ratio of the dynamic strength to the static one that has already been used in the earlier part of this document. In general, the DIF value at the ISR range for all tests is provided in Table 3.12.

Table 3.12. DIF tested mechanical properties at ISR range for granite and sandstone tested in this study

Mechanical property	Averaged DIF at ISR	
	Granite	Sandstone
Uniaxial compressive strength, $\sigma_c$	$1.37 \pm 0.11$	$2.03 \pm 0.27$
Tensile strength, $\sigma_t$	$2.89 \pm 0.35$	$2.56 \pm 0.21$
Mode-I fracture toughness, $K_{IC}$	$5.80 \pm 0.53$	$6.73 \pm 1.20$
Shear strength, $\tau$	$2.94 \pm 0.36$	$2.96 \pm 0.29$

The relationship between the mechanical properties of rock tested in this study and strain/loading rate for granite and sandstone is shown in Figure 3.24 – 3.29. The results from this study are plotted with other data from similar rock types. Although the data is considerably scatter at all rates, it is seen, however, that the strength is a weak function of strain rate at

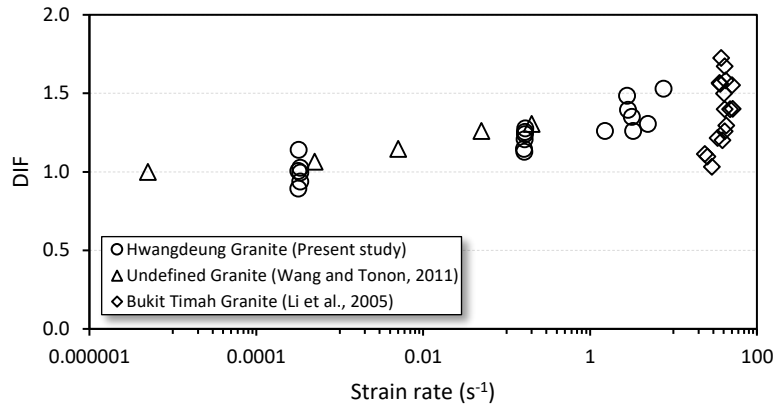
lower rates and that for higher rates, the strength increases rapidly with the increasing rate for all cases. Further discussion on each test is presented subsequently.

### *3.6.2.1 Effect of Strain Rate on Uniaxial Compressive Strength*

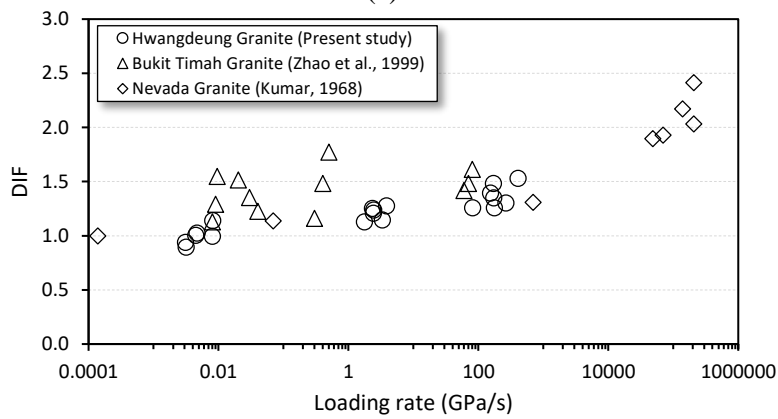
In the compression test, the strength for both granite and sandstone increases with the increasing rate; however, the increased magnitude is less in granite case. At the ISR range, the DIF of granite is about 1.37, while in sandstone, it reaches up to two (compared the DIF of granite in Figure 3.24(a) and sandstone in Figure 3.24(c)).

The results are supported by the tests on Nevada granite and Berea sandstone. Figure 3.24(b) shows that at 690 GPa/s (approximately at ISR range, presented by loading rate), the DIF of Nevada granite is about 1.32 (Kumar, 1968), quite close to 1.37 obtained at 260 GPa/s in this study. For sandstone, Berea sandstone tested by Blanton (1981) at the rate of 0.1/s to 10/s exhibits the DIF about two, which is comparable with the test on Linyi sandstone in this study (see Figure 3.24(c)).

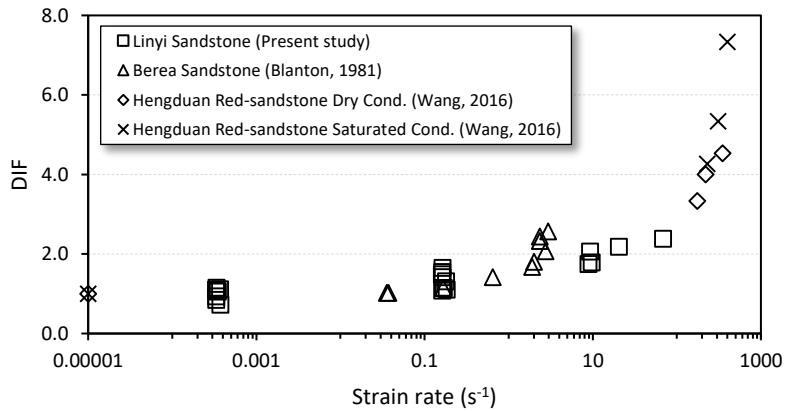
The UCS value from this study are plotted together in terms of DIF with the data of various rocks and rock-like materials from numerous references as shown in Figure 3.25, (a) based on strain rate, and (b) based on loading rate. The data covers the quasi-static rates up to the high-strain rates loading. In general, strength increases linearly at the lower rates and rises significantly at higher rates. Also, it is visible that the data in the ISR range is limited.



(a)

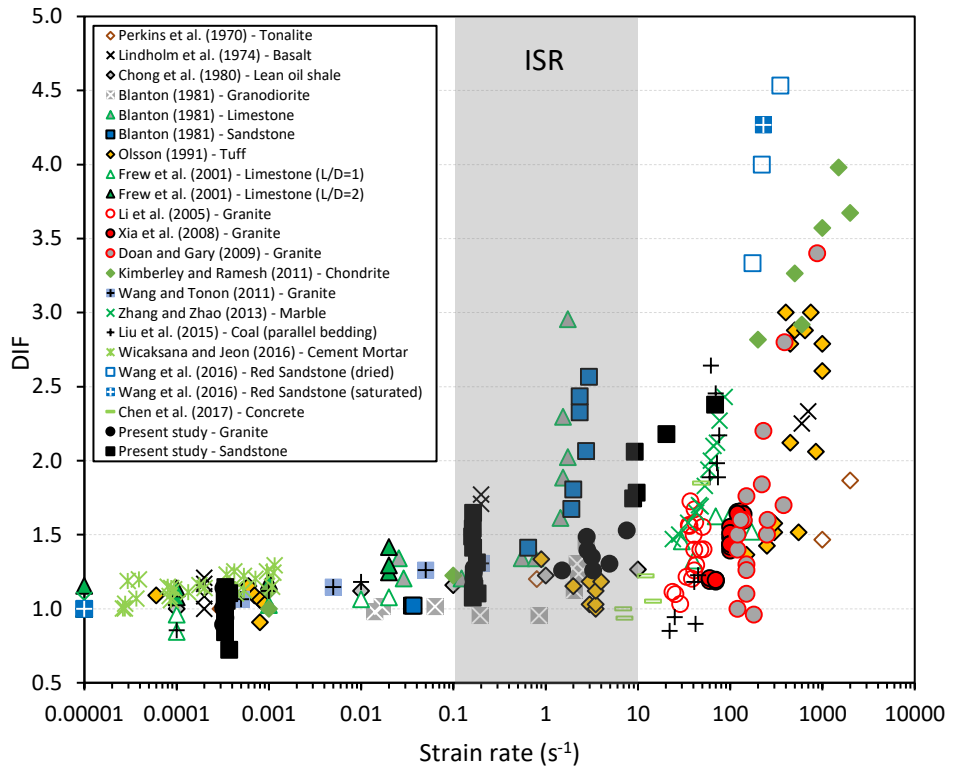


(b)

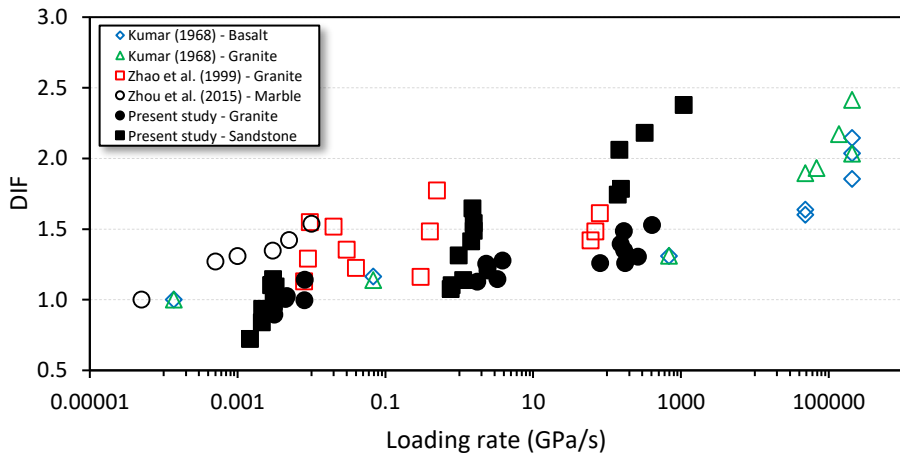


(c)

Figure 3.24. Relationship between DIF of uniaxial compressive strength and strain/loading rate for (a)-(b) granite; and (c) sandstone



(a)



(b)

Figure 3.25. DIF of uniaxial compressive strength for various rock related to (a) strain rate, and (b) loading rate

One should be pointed out that from those few data in the ISR rates, the tendency is not clear (Figure 3.25(a)). On the one hand, investigators found an insignificant increase in strength, but some of them found that differently. Blanton (1981), who made an observation on Indiana limestone and Berea sandstone, observed that the compressive strength has a vivid increase in this range. A similar fact was also found by Lindholm et al. (1974), who studied the dynamic compressive strength of Dresser basalt. The dynamic strength of the basalt was 1.8 times higher than its static strength at the strain rate of  $2.4 \times 10^{-1} \text{ s}^{-1}$ . In this study, a significant increase at the ISR was found only for the Linyi sandstone, but it is not for the Hwangdeung granite. As previously stated that in Sandstone, the dynamic strength at the ISR range reached up to two times from the static strength.

### *3.6.2.2 Effect of Strain Rate on Tensile Strength*

In the tensile test, the strength for both granite and sandstone increases significantly with the increasing rate in the ISR range. The DIFs of them are about 2.89 and 2.56 for granite and sandstone, respectively. These phenomena are also found in the previous works of others. Cho et al. (2003) observed even higher DIFs within the ISR range for Inada granite, by having the DIF of 3.8 to 6.6 over the rates from 4/s to 12/s (Figure 3.26(a)). For sandstone, the dynamic strength of Kimachi sandstone is 3.2 to 4.7 times higher than the static strength within the rates from 14/s to 40/s (Kubota et al., 2008) (Figure 3.26(c)).

At the loading rate slightly above the ISR range, Huang et al. (2010b) found that the increased strength was significantly different for dried and saturated sandstone specimens (Figure 3.26(d)). The increase was

significantly higher in the case of saturated rock by showing the DIF values of 7.9 at the loading rate of about 50 GPa/s, while the DIF was only about 1.5 for the dried rock at the same loading rate. It is implied from the results that the sandstone was more sensitive to saturation at a quasi-static rate compared to the dynamic rate. At the quasi-static rate, about  $10^{-4}$  GPa/s, the tensile strength of the dried sandstone was 2.8 MPa while it was only 0.38 MPa for the saturated one. At the dynamic rate, there was not much difference between them, showing 4.1 MPa for dried sandstone, and 3 MPa for saturated one. Since the DIF is the ratio dynamic to static strengths, it resulted in much higher DIF in the saturated sandstone case.

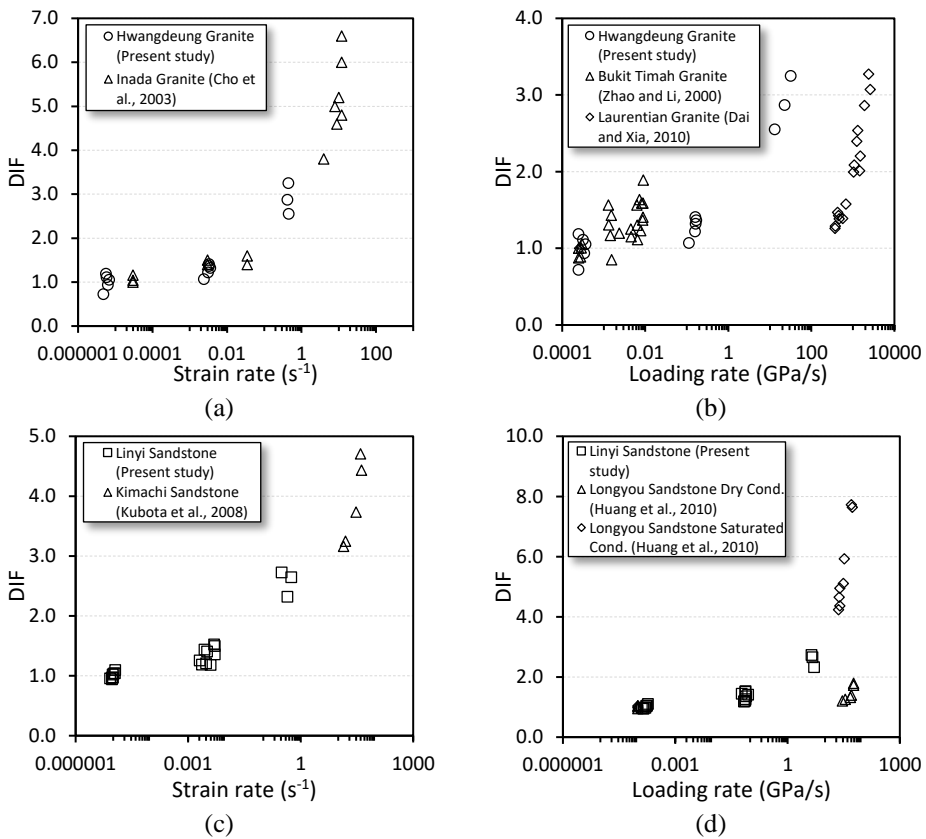


Figure 3.26. Relationship between DIF of tensile strength and strain/loading rate for (a)-(b) granite; and (c)-(d) sandstone

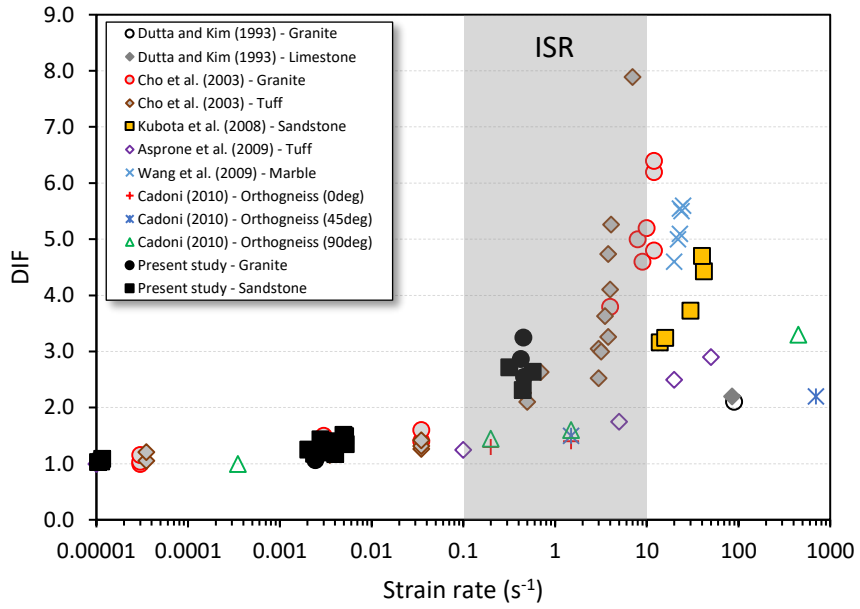
Similar to the compression strength, the tensile strength values from this study are also plotted with data of various rocks over a wide rate range from many references (Figure 3.27). Based on those limited data, it can be inferred that there are two tendencies in the strength increase at the ISR rate. As the apparent cases, Asprone et al. (2009) and Cadoni (2010) and found a slight increase of tensile strength for tuff and orthogneiss rocks, respectively, while Cho et al. (2003) and this study found a more sharp increase for granite, tuff, and sandstone rocks (see Figure 3.27(a) inside the shaded area).

### 3.6.2.3 *Effect of Strain Rate on Mode-I Fracture Toughness*

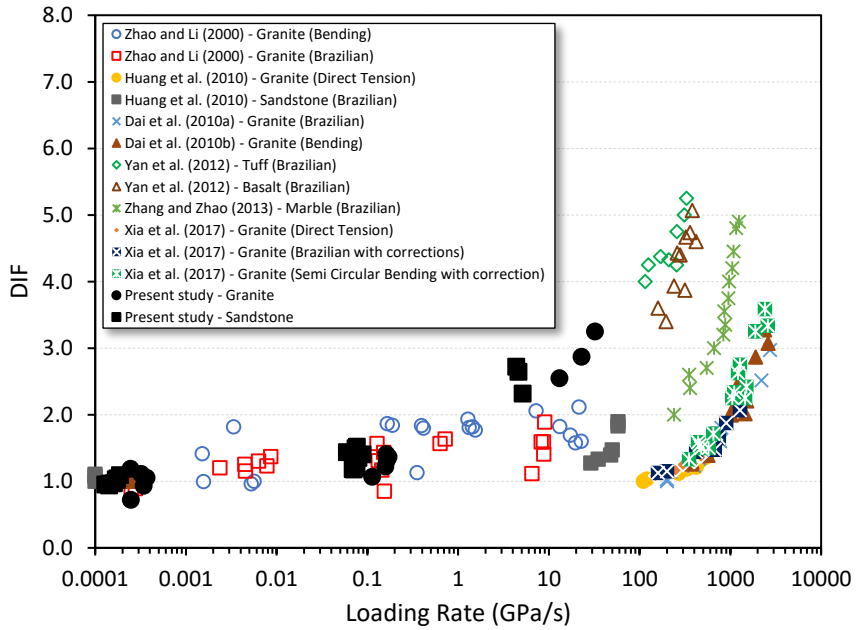
The results of granite and sandstone from this study are plotted in a chart with two of North American granites and a Chinese granite, and a Chinese sandstone (see Figure 3.28). Most of the references are at the high rates zone except for the Barre granite that was also tested at the rate of about  $10^{-4} \text{ GPa}\sqrt{\text{m}} \text{ s}^{-1}$ .

For granite at the high rates, the increasing trends of  $K_{IC}$  of this study match with the general trend from other references, even though there are some outliers. From the graph, the trend increase sharply above  $20 \text{ GPa}\sqrt{\text{m}} \text{ s}^{-1}$  at a higher rate end (Figure 3.28(a)). For Linyi sandstone, the  $K_{IC}$  values were plotted together with the results of Shuguang sandstone, which was also from China. At the higher rates, it seems there is a good agreement between them. However, no comparison can be made at the lower end.

Based on these limited data at the lower rates, it appears that  $K_{IC}$  increase with loading rate even though it is not as strong as at the higher loading rates overall.

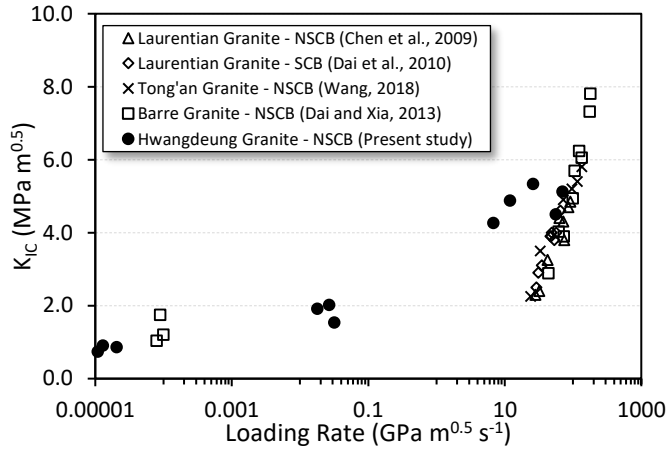


(a)

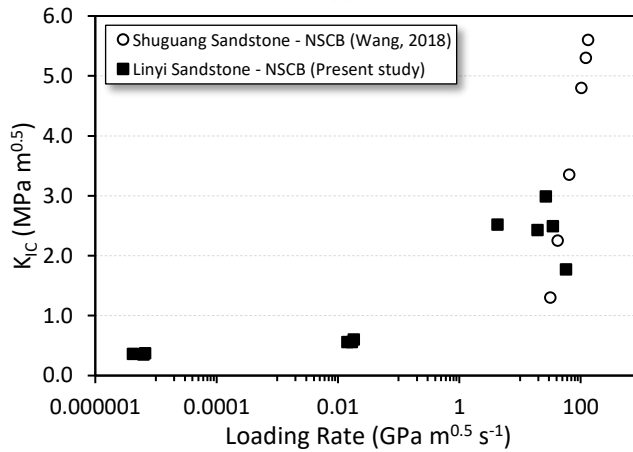


(b)

Figure 3.27. DIF of tensile strength for various rock related to (a) strain rate, and (b) loading rate



(a)



(b)

Figure 3.28. Relationship between  $K_{IC}$  and loading rate for (a) granite and (b) sandstone

### 3.6.2.4 Effect of Strain Rate on Shear Strength

There are few studies available performing dynamic punch shear experimentation. So, only a few data available to be integrated into this report. The results of this study are plotted together with the results of Min et al. (2016) for a Korean granite, and Huang et al. (2011) for a Longyou sandstone from China, as shown in Figure 3.29. Both of them

performed the punch shear test under fast loading using a split-Hopkinson pressure bar system.

The graph shows that at the higher rates above 10 GPa/s, the DIFs of shear strength are significantly higher than the DIFs at static ranges in all rocks. The data vary; however, the other two references show a more apparent trend compared to the results from this study at the higher end. At the lower end, the DIFs increase for about 1.5 times. Unfortunately, there is no literature review data to be compared with them at the lower regime.

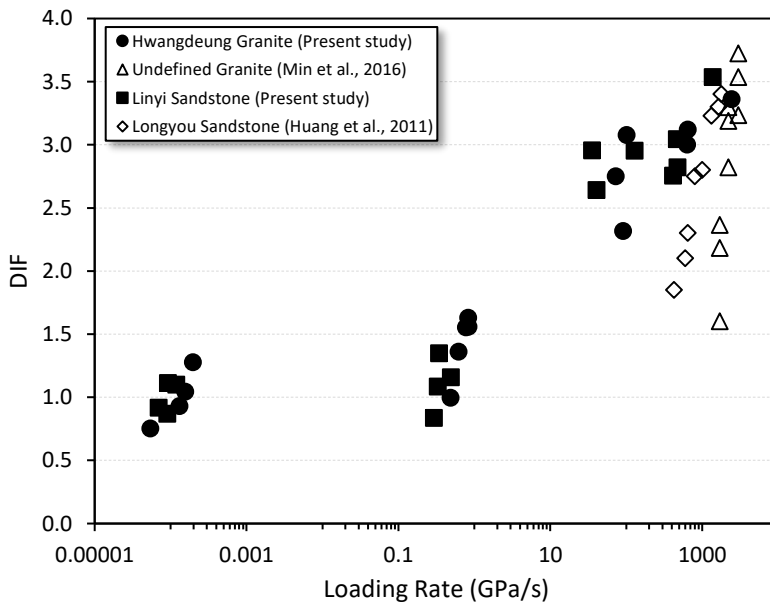


Figure 3.29. Relationship between DIF of shear strength and loading rate for granite and sandstone

### 3.6.2.5 The Trend of Rate Dependency

On the lower side of the ISR range, the effect of strain rate on rock strength is not dramatic. The strength is either constant or slightly increasing with increasing strain rate (Blanton, 1981). Some studies reported that the constant rate of increasing trend continues at higher strain rates (Green & Perkins, 1968; Lindholm et al., 1974; Shockey et al., 1974). However, other studies showed a significant increase in the trend at the higher strain rates, starting from somewhere between  $10^{-1}$  and  $10^3 \text{ s}^{-1}$ , depending on the study (Blanton, 1981; Kobayashi, 1970) (Figure 3.30). The latter case is also found in this study.

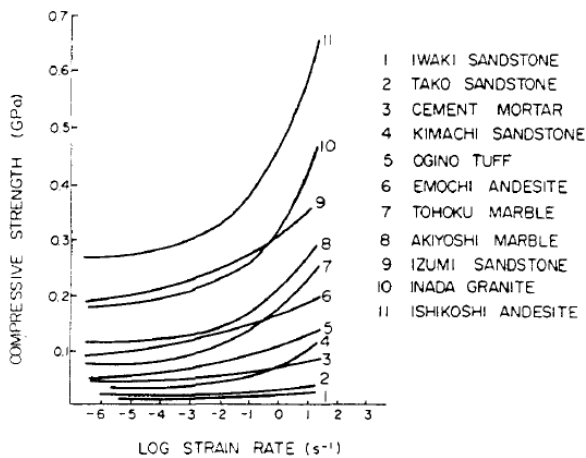


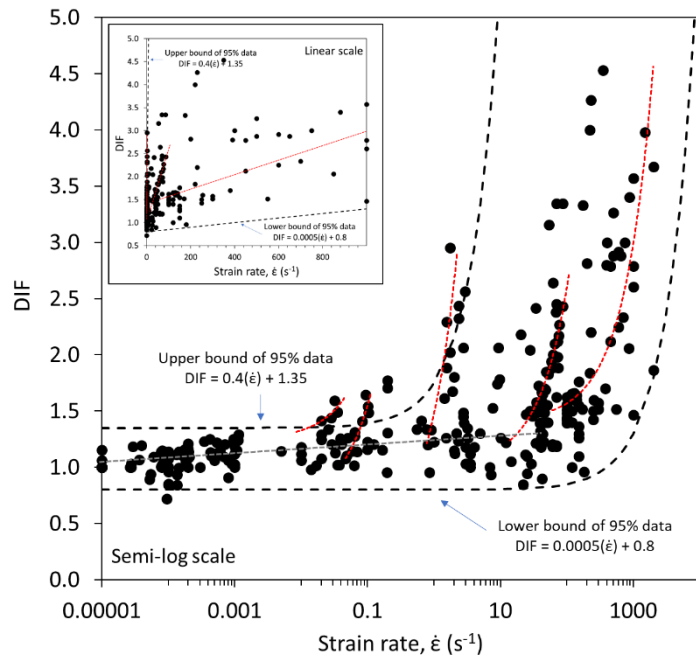
Figure 3.30. Experimental variation of compressive strength with strain rate from Kobayashi (1970) (after Blanton (1981))

Figure 3.31 presents the difference in the rate dependency trend under the compressive and tensile fracture mechanism for various rocks collected from multiple references. Within 95% of the data population, the transition from the lower to higher rates is uncertain. There are

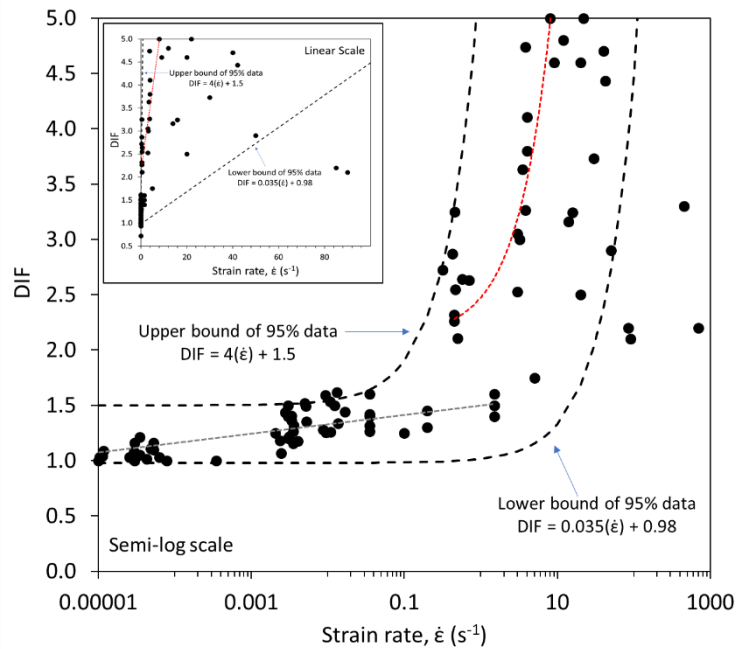
multiple rises on the main trend (see Figure 3.31(a)). On the other hand, in tensile mode, the transition from the lower to the higher rates is rather smooth (see Figure 3.31(b)).

One possible reason for those phenomena is that the failure mechanism of compressive loading is much more complicated than that is for tensile loading. According to Gramberg (1989), in tensile loading by the Brazilian test, the tensile stress is induced by compressive loading in an indirect way and, as a result, only one fracture will occur. The tensile stress divides the rocks into two parts, and secondary fractures will not develop. In compressive loading, however, both primary and secondary fracturing will occur. At gradually increasing of uniaxial pressure, the primary phenomenon will occur that is usually vertical cracks parallel to the loading direction. During the increasing of the pressure, the axial cracking will repeat, and multiple parallel cracks will grow and connect. Subsequently, the secondary failure process will also take place that is accompanied by the shearing phenomenon.

From the above explanation, it can be inferred that the chance of getting variation in the compression test is higher than in indirect tension due to its failure mechanism complexity. The complexity is even getting higher in the dynamic test where time is short, and the degree of fragmentation is high.



(a)



(b)

Figure 3.31. The trend of rate dependency under (a) compressive and (b) tensile fracture mechanisms

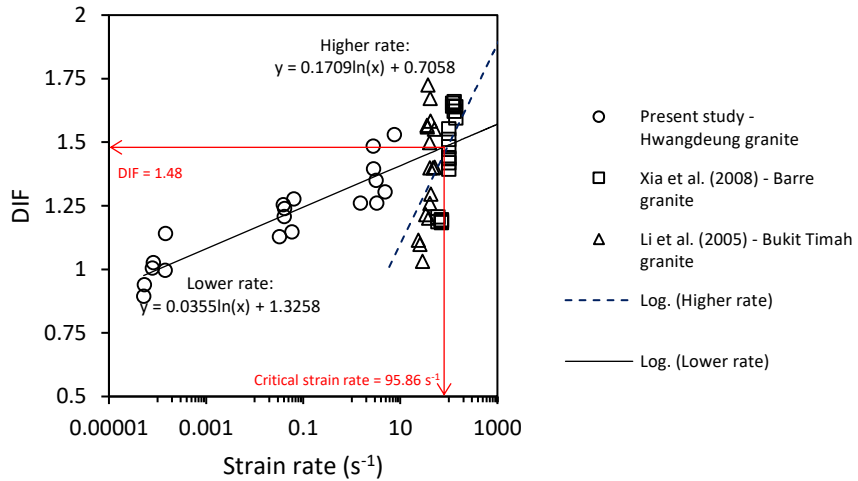
### 3.6.3 Critical Strain Rate

As previously explained within a full range of strain rates, basically, there are two distinct trends, i.e., a linear trend at the low strain rate region and an exponential trend at the high strain rate region. The strain rate value bridging those two regions is recognized as the critical strain rate ( $\dot{\epsilon}^*$ ).

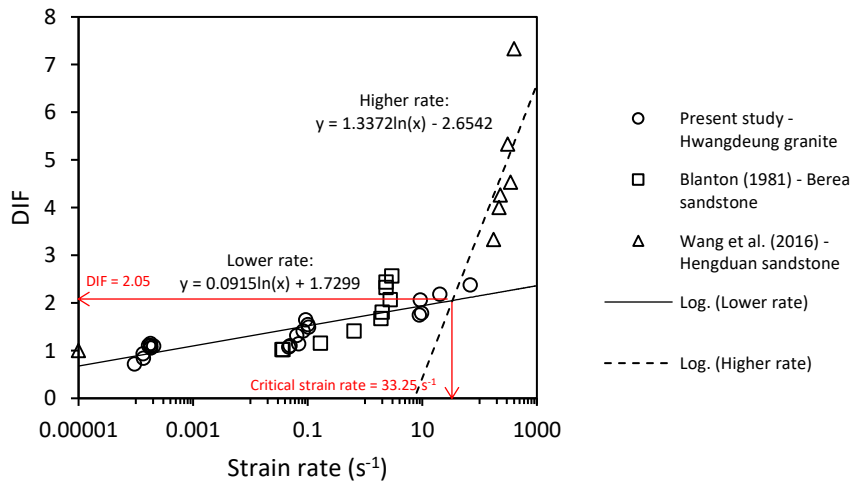
Green and Perkins (1968) found that the critical strain rate for Solenhofen limestone under uniaxial compression is  $10^2$  per second ( $\dot{\epsilon}^* = 10^2 \text{ s}^{-1}$ ), while Blanton (1981) stated that it is  $10^0$  per second ( $\dot{\epsilon}^* = 10^0 \text{ s}^{-1}$ ) for Charcoal granodiorite, Berea sandstone, and Indiana sandstone. Work by Olsson (1991) on tuff material stated that 76 per second is the estimated critical strain rate ( $\dot{\epsilon}^* = 76 \text{ s}^{-1}$ ). Over the range from  $10^{-6}$  to  $76 \text{ s}^{-1}$ , the strength is a weak function of strain rate, and it is proportional to the strain rate raised to the power 0.007 ( $\dot{\epsilon} < \dot{\epsilon}^*, \sigma \propto \dot{\epsilon}^{0.007}$ ). Above  $76 \text{ s}^{-1}$ , the relationship increases up to raised to the power 0.35 ( $\dot{\epsilon} > \dot{\epsilon}^*, \sigma \propto \dot{\epsilon}^{0.35}$ ). Moreover, over the range of  $10^{-6}$  to  $10^2$  per second, the critical strain rate of Lac du Bonnet granite is found to be 10 per second ( $\dot{\epsilon}^* = 10^1 \text{ s}^{-1}$ ) (Wang & Tonon, 2011).

This study does not cover the range beyond the ISR range. Thus, additional data at the higher strain rate regime should be combined with a respected rock type. It is found that, in uniaxial compression mode,  $\dot{\epsilon}^* = 95.86 \text{ s}^{-1}$  (corresponding DIF = 1.48) for granite, and  $\dot{\epsilon}^* = 33.25 \text{ s}^{-1}$  (corresponding DIF = 2.05) for sandstone, as shown in Figure 3.32. In other words, taking the sandstone case, the strength dependency is less prominent at  $\dot{\epsilon} < 33.25 \text{ s}^{-1}$  and starts to rise significantly at  $\dot{\epsilon} > 33.25 \text{ s}^{-1}$ , from 2 up to 7 times its static strength (see Figure 3.32(b)).

For tensile strength, the critical strain rate falls at the strain rate of 2.2 per second ( $\dot{\epsilon}^* = 2.2 \text{ s}^{-1}$ ) for the Neapolitan yellow tuff that was tested under direct uniaxial tension test (Asprone et al., 2009). In this study,  $\dot{\epsilon}^* = 0.09 \text{ s}^{-1}$  (corresponding DIF = 1.53) for granite, and  $\dot{\epsilon}^* = 9 \text{ s}^{-1}$  (corresponding DIF = 2.52) for sandstone (Figure 3.33).

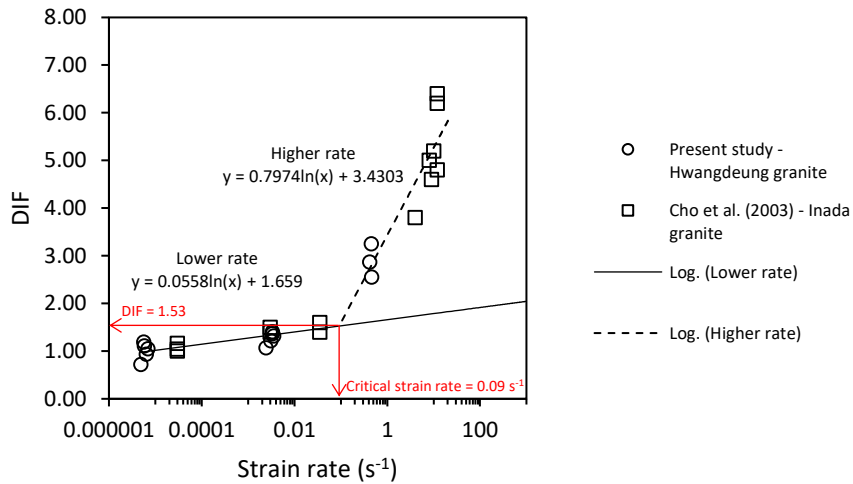


(a)

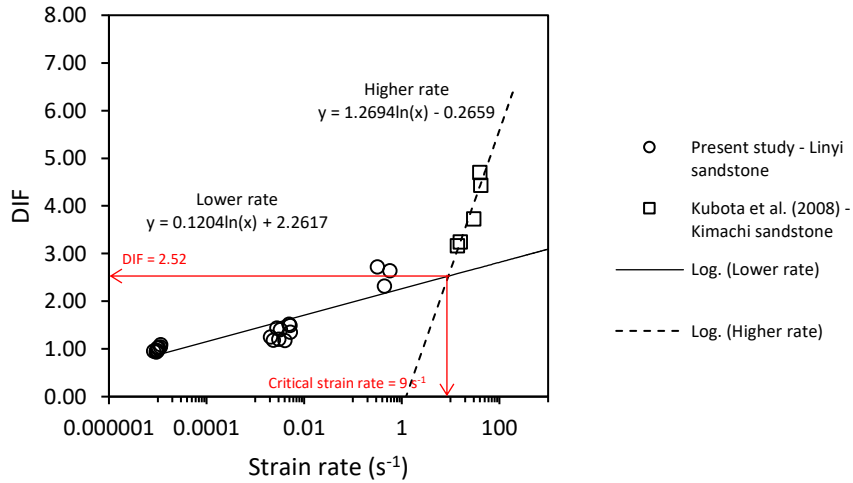


(b)

Figure 3.32. The critical strain rate of uniaxial compressive strength for (a) granite and (b) sandstone



(a)



(b)

Figure 3.33. The critical strain rate of tensile strength for (a) granite and (b) sandstone

### 3.6.4 Effect of Strain Rate on Elastic Properties

In this study, the elastic properties of the tested rocks were not obtained. During the dynamic test, the author attempted to attached strain gauges on the sample surface and collected strain data from them. However, due

to some technical limitations on the data acquisition of the dynamic loading system, the strain history during the test was not recorded.

Despite that, elastic properties, i.e., Young's modulus and Poisson's ratio, have been observed by many investigators. It has been reported that the change of Young's modulus is either very small or unaffected by strain rate increasing (Li et al., 2005; Wang & Tonon, 2011; Zhao et al., 1999). However, some of them revealed differently by having Young's modulus increases by increasing the strain rate (Kimberley & Ramesh, 2011; Zhou et al., 2015).

The possible reasons for Young's modulus increase are the deformation of granular material and the number of closed internal cracks (Kimberley & Ramesh, 2011). At the higher rate, the grains have less time to reorganize themselves, resulting in a stiffer response. Additionally, more of the internal cracks will be closed by applied higher applied stress. In quasi-static loading rates, only large optimally oriented cracks tend to initiate and grow at relatively low-stress levels leaving the more significant number of flaws open. At higher rate cases, the optimally oriented cracks initiate first, but the load quickly continues to increase before the associated wing cracks grow large enough to cause failure. This higher load possibly closes more cracks, resulting in a stiffer response (Kimberley & Ramesh, 2011).

At the intermediate strain rate, it has been reported that Poisson's ratio seems to increase slightly with the strain rate increasing (Zhao et al., 1999). At a higher strain rate, additional cracks and more continuous fracture fabric are generated. The expansion from axial crack growing may result in more significant lateral displacement compared to the axial displacement and cause an increased Poisson's ratio. Limited references

can be found on the effect of strain rate on Poisson's ratio, especially in the intermediate strain rate range.

## **4. ROCK CUTTING TEST**

### **4.1 Introduction to Rock Cutting Test**

The purpose of this chapter is to discuss the application of the dynamic rock properties, discussed in Chapter 3, to the rock excavation practice. A laboratory linear cutting test was adopted in this study since it is probably the most reliable way to observe the tool-rock interaction and to measure the forces acting on a tool. First, a set of laboratory linear cutting test was conducted to a sandstone rock. Second, numerical modeling was also performed for some of the laboratory cases using two different input parameters, namely, quasi-static and dynamic property sets. Third, the results of those simulations were compared to the laboratory cases. Fourth, several cutting force prediction models were developed, considering the dynamic properties of rock. Finally, several attempts were made to estimate the strain rate level in the rock excavation process.

### **4.2 Small-Scale Linear Cutting Machine**

A small-scaled linear cutting machine (SLCM) was used for experimental works. The machine has a 20-ton of normal load capacity and a capability to support its stiffness during cutting simulation work. The machine consists of a 4-column frame, two electric motor units for vertical and horizontal movements, a three-dimensional load cell, a cutter/tool mounting, a sample box, a control panel, and a data acquisition (DAQ) system that is connected to a personal computer. The load cell and the tool mounting are paired with a vertical electric motor

that can be moved vertically to control penetration depth. The rock specimen box can be moved in two ways: by electric motor horizontally in cutting direction and by a manual handle in sideways direction to set the cut spacing. The maximum cutting speed that can be applied by the horizontal electric motor is 1.4 mm/s. Electric motor movement is controlled by the control panel, while tool local coordinate information is also displayed on the panel. The load cell is capable of measuring working forces in three directions: cutting, normal, and side forces. The forces data are continuously recorded and acquired by the DAQ system and then stored in the personal computer for further analysis. The detailed picture of the machine and its parts are depicted in Figure 4.1.

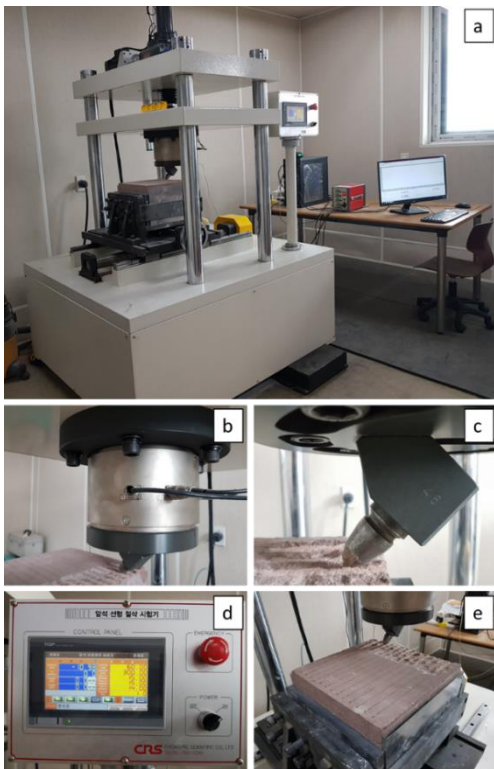


Figure 4.1. Small-scale linear cutting machine. a) the whole SLCM system; b) 3D load cell; c) cutting tool and its holder; d) control panel; and e) sample box

The cutting tool used in this study is a conical pick cutter manufactured by Vermeer Cooperation. According to the product specification of the cutter, it has a primary tip angle of  $70^\circ$ , tip diameter of 12 mm, gauge diameter of 40 mm, flange diameter of 30 mm, shank diameter of 18.5 mm, and a total length of 85 mm. The schematic and real picture of the conical pick cutter is shown in Figure 4.2.

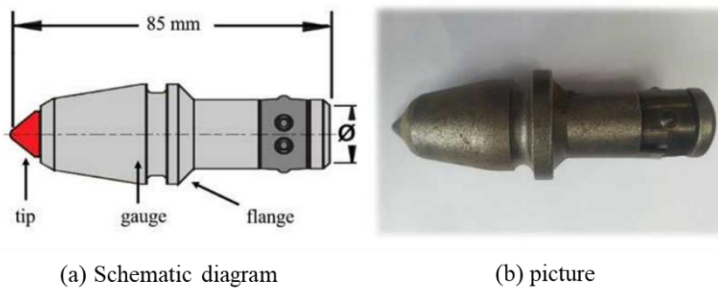


Figure 4.2. Schematic diagram and picture of the conical pick cutter (Jeong, 2017)

### 4.3 Linear Cutting Test

#### 4.3.1 Test Specimen for Linear Cutting Test

The rock specimen used in the experiment was Linyi sandstone from China, the same kind as the one that was used for dynamic rock tests. The rock was cut to the dimension of 300 mm x 300 mm x 200 mm in order to fit the sample box in the SLCM system (See Figure 4.3(a)). The sandstone was regarded as homogeneous, continuous, and appeared to have a less remarkable or negligible degree of anisotropy (Kim, 2017). So, the consideration of discontinuity and anisotropy during the test could be omitted.

### 4.3.2 Procedure of Linear Cutting Test

Prior to the test, the rock sample was subjected to initial cutting, i.e., preconditioning. Preconditioning is essential to ensure that the surface of the tested rock has reached a similar degree of steady-state on the cutting surface. Preconditioning was done with 3 mm penetration depth, and 10 mm cut spacing for a dedicated cutting surface, as shown in Figure 4.3(b).

The cutting test condition considered in this study is mentioned below:

- Penetration depth ( $p$ ) : 5 mm, 7 mm, 9 mm, and 11 mm
- Cut spacing ( $s$ ) : varied with penetration depth
- Attack angle ( $\alpha$ ) :  $45^\circ$
- Skew angle ( $\theta$ ) :  $0^\circ$

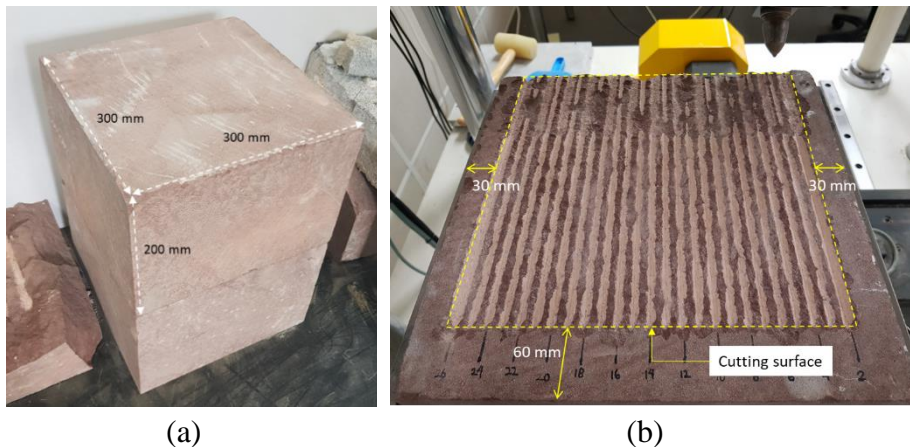


Figure 4.3. Rock sample (a) Typical rock block; (b) rock surface after preconditioning

The cutting length was maintained to be 240 mm out of 300 mm of total length to prevent edge breakage at the end of the specimen. At the side edges of the specimen, a 30 mm barrier for each of the sides was also

excluded from working face to avoid side breakage. The specimen was confined to a certain degree to ensure its stability during the cutting process.

Cutter forces from the load cell, i.e., cutting, normal, and side forces, were acquired by the data acquisition system with a sampling rate of 20 Hz. Cutting speed was a constant variable with 10 mm/s for all cases. The test for each of the cut spacing cases was repeated three to five times, depending on a given cutting condition. Bilgin et al. (2014) have suggested that at least three cutting lines should be made for each cut spacing scenario.

After finishing each case, the cut rock (debris) was manually collected with a brush and weighed. Given the information of rock density, the cut rock volume could be calculated. Cut rock volume information was used as an input parameter to calculate the specific energy.

It should be mentioned that the experiment in this study is an expansion work of the one which was performed earlier by Jeong (2017), for the same rock type, with the same apparatus. Some of the results of Jeong (2017), specifically in the case of  $\alpha = 45^\circ$  and  $\theta = 0^\circ$ , would be integrated into this report.

### **4.3.3 Results of Linear Cutting Test**

The results of the linear cutting test were obtained from the cutting condition of an attack angle of  $45^\circ$  and a skew angle of  $0^\circ$ . Cut spacing ( $s$ ) is varied depending on the penetration depth ( $p$ ) and is represented as the ratio between them ( $s/p$  ratio). The test results are summarized in Table 4.1.

Table 4.1. Linear cutting test results

$P$ (mm)	$s$ (mm)	$s/p$	Mean Cutter Force			$SE$ (MJ/m <sup>3</sup> )
			Side, $F_{S\_mean}$	Cutting, $F_{C\_mean}$	Normal, $F_{N\_mean}$	
5	5	1	0.81	3.22	3.61	82.96
	10	2	0.13	4.25	4.39	77.65
	15	3	0.17	5.22	5.29	77.86
	20	4	0.53	5.82	5.87	67.57
	25	5	0.27	6.36	6.44	85.81
	30	6	1.19	7.75	9.64	92.80
7	7	1	0.47	3.48	3.51	54.74
	14	2	0.55	5.09	5.14	48.94
	21	3	0.61	6.08	6.85	42.17
	28	4	0.84	6.97	7.25	44.94
	35	5	0.72	6.39	8.55	44.00
	42	6	0.91	7.16	10.36	54.09
9	9	1	0.60	5.03	5.66	49.73
	13.5	1.5	0.51	6.15	7.21	45.66
	18	2	0.52	6.64	7.96	37.69
	22.5	2.5	0.38	8.30	9.19	36.50
	27	3	0.52	7.60	9.40	33.12
	31.5	3.5	0.75	7.62	10.06	35.84
	36	4	0.78	8.31	10.96	39.70
11	45	5	0.75	7.90	10.85	53.88
	11	1	0.26	6.98	7.30	46.30
	22	2	0.63	7.94	8.40	34.23
	27.5	2.5	0.93	6.69	9.65	23.08
	33	3	1.28	8.91	9.65	31.10
	38.5	3.5	0.64	9.83	11.71	24.65
44	4	1.30	10.03	12.98	32.71	

#### 4.3.3.1 Cutter Force

Figure 4.4 shows a typical three orthogonal cutter forces obtained from the linear cutting test. The force values were represented by the mean forces that are the average values of the forces during the cutting test.

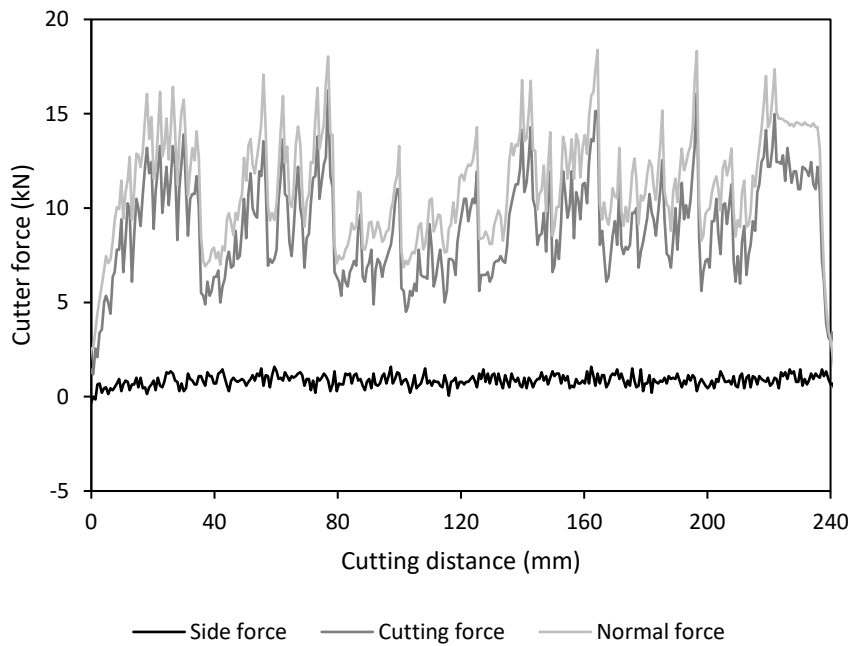


Figure 4.4. Typical of three orthogonal cutter forces history from a single linear cutting test (example: the case of  $p = 5$  mm,  $s = 30$  mm, 1<sup>st</sup> line)

Figure 4.5 presents the mean cutting force ( $F_{C\_mean}$ ) associated with the  $s/p$  ratio for all penetration depth cases. It shows that  $F_{C\_mean}$  increased with cut spacing and also with penetration depth. Although there were some unexpected results in the case of  $p = 9$  mm,  $s/p = 2.5$ ; and  $p = 11$  mm,  $s/p = 2.5$ , the tendency still showed an increase trend.

Figure 4.6 exhibits the mean normal force ( $F_{N\_mean}$ ) related to the  $s/p$  ratio for all penetration depth cases. Similar to the cutting force, the figure also shows that  $F_{N\_mean}$  increased with cut spacing and penetration depth.

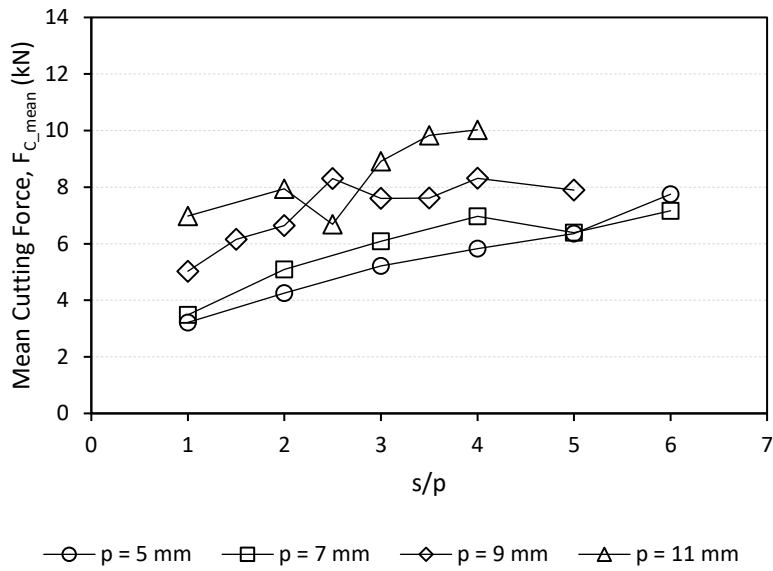


Figure 4.5. Mean cutting force associated with  $s/p$  ratio for all cutting conditions

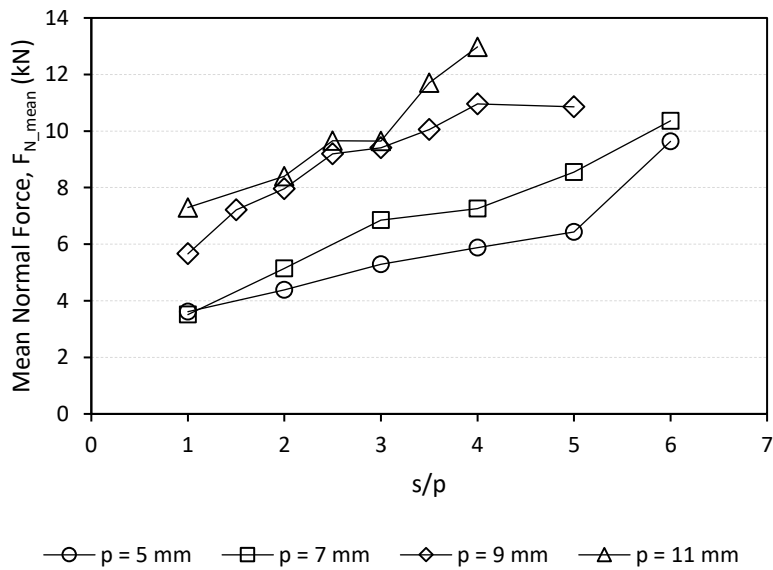


Figure 4.6. Mean normal force associated with  $s/p$  ratio for all cutting conditions

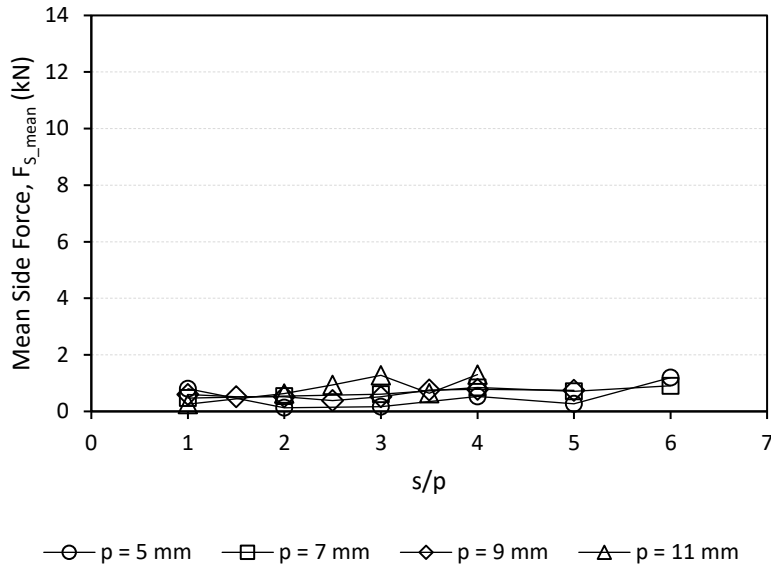


Figure 4.7. Mean side force associated with  $s/p$  ratio for all cutting conditions

Figure 4.7 shows the relationship between the mean side force ( $F_{S\_mean}$ ) and the  $s/p$  ratio for all penetration depth cases. It shows that there was no relationship between them. The side force was significantly smaller compared to the other two forces and was only fluctuating slightly above zero value during the entire cutting process, as shown in Figure 4.4.

#### 4.3.3.2 Specific Energy

Specific energy is defined as the required work to cut a unit volume of rock. Specific energy is commonly used as a representative number to estimate cutting efficiency and can be calculated by Eq. 4.1.

$$SE = \frac{F_{C\_mean} \times l}{V} \quad (4.1)$$

where  $SE$  is the specific energy ( $\text{MJ}/\text{m}^3$ ),  $F_{C\_mean}$  is the mean cutting force (kN),  $l$  is the cutting distance (mm), and  $V$  is the volume of cut rock ( $\text{m}^3$ ).

Figure 4.8 shows the relationship between the specific energy and  $s/p$  ratio for all penetration depth cases. The graph exhibits an optimum  $s/p$  ratio for all penetration depth cases by showing the minimum  $SE$  value in a specific  $s/p$  ratio. The optimum  $s/p$  ratio in each of the cases are  $s/p = 4$  for  $p = 5$  mm,  $s/p = 3$  for  $p = 7$  mm,  $s/p = 3$  for  $p = 9$  mm, and  $s/p = 2.5$  for  $p = 11$  mm. The optimum condition in each case is marked with dark symbols in the graph.

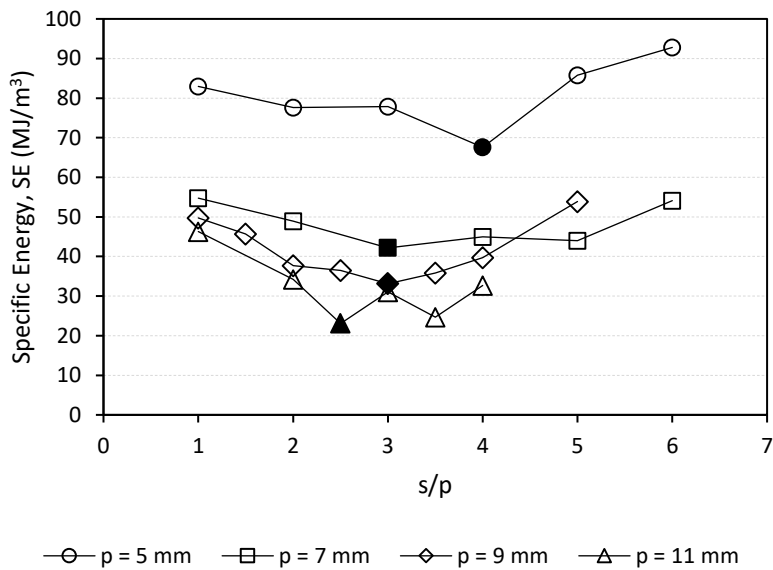


Figure 4.8. Specific energy with  $s/p$  ratio for all cutting conditions

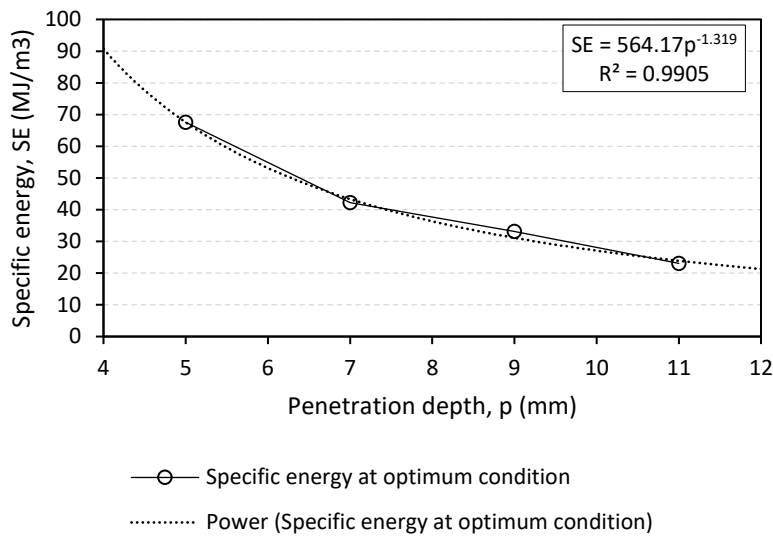


Figure 4.9. The relationship between specific energy and penetration depth at the optimum cutting condition

Figure 4.9 shows the relationship between specific energy and penetration depth at the optimum  $s/p$  ratio. The graph shows that the specific energy decreased exponentially with penetration depth. The graph could have determined the optimum penetration depth. In order to get the optimum penetration depth, the graph should exhibit a concave upward curve, having minimum specific energy at a certain penetration depth (Cho et al., 2010). To potentially have a concave upward curve, the  $SE$  value at the  $p$  deeper than 11 mm is needed. However, the cutting condition was limited to 11 mm of penetration depth in this study.

The best possible attempt to obtain optimum penetration depth was by using the equation in Figure 4.9. From the equation, the penetration depth was monotonously decreasing, and the optimum penetration depth might be at  $p \geq 11$  mm. This statement was also mentioned by Jeong (2017) since this study used the same penetration depth scenarios with that work.

#### **4.4 Numerical Modeling of Linear Cutting Test**

One of the most efficient ways to predict mechanical cutting efficiency is a numerical simulation. Numerous numerical studies have been done to simulate rock cutting process by different simulation tools: finite element method (FEM) (Cho et al., 2013; Geng et al., 2017; Menezes et al., 2014), discrete element method (DEM) (Rojek et al., 2011; Su & Akcin, 2011), and smooth particle hydrodynamics (SPH) (Jeong et al., 2013), etc. Among them, FEM appears to be the most popular method due to its simplicity compared to the others; DEM requires preliminary works to determine the micro properties of the materials for numerical modeling, and the applicability of the SPH method in rock cutting model still has room for improvement. The focus of numerical simulation in this study is to investigate the difference of numerical results between using quasi-static material input parameters and the dynamic ones. Therefore, FEM is seen to be the most direct way to be implemented.

##### **4.4.1 Material Model of Linear Cutting Test**

Rock model was considered homogeneous and isotropic. An approximation to Hooke's law represents the initial elastic behavior of the model (ANSYS, 2010). The properties of the model were defined as a linear equation of state. Bulk and shear modulus were derived based on elasticity theory, and the default room temperature was set to the room temperature of 20° Celsius.

Several strength models have been applied to simulate the rock cutting process. The function for yield stress is determined by the strength model in the program. The Drucker Prager yield criterion was found to be suitable for elastoplastic material such as rock (Tham, 2005). The yield

points under uniaxial compression and tension were assumed to be 90% of  $\sigma_c$  and  $\sigma_t$ , respectively (Jeong, 2017).

The software provides several failure model options according to the equation of state and strength model of the material. In the simulation, the principal stress/strain-based model was used to simulate the fragmentation or cracking behavior of rock. Fracture energy value was calculated from the  $K_{IC}$  value that was obtained from the mode-I fracture toughness test. The input parameters used in the simulation are provided in Table 4.2.

Table 4.2. Input parameters for Drucker Prager strength criterion in AUTODYN® simulation

Input Parameter	Unit	Value	
		Quasi-static	Dynamic
Density	gr/cm <sup>3</sup>	2.75	2.75
Bulk modulus	MPa	7.55 x 10 <sup>3</sup>	7.55 x 10 <sup>3</sup>
Reference temperature	°C	20	20
Strength model	-	Drucker Prager	Drucker Prager
Shear modulus	GPa	6.89	6.89
Yield stress in tensile uniaxial strain	MPa	3.20	8.19
Yield stress in compression uniaxial strain	MPa	45.68	92.71
Failure model	-	Principal stress/strain	Principal stress/strain
Principal tensile failure stress	MPa	4.00	10.23
Max. principal stress difference / 2	MPa	28.55	57.95
Principal tensile failure strain	-	0.0003	0.0006
Max. principal strain difference / 2	-	0.0018	0.0037
Fracture energy	J/m <sup>2</sup>	8.30	375.52

#### **4.4.2 Geometry and Boundary Conditions of Linear Cutting Test Model**

In this simulation, the rock model was built as a block with a dimension of 100 mm x 100 mm x 30 mm. The element size of the model was set to 1 mm in all axes, and the total number of elements was about 300,000 finite elements. The bottom surface of the rock model was restrained from moving in all directions as a fixed boundary. Side surfaces of the rock model were constrained as roller boundary that allows no movement to the lateral direction ( $z$ -direction in Figure 4.10). The pick cutter model was set to move steadily to the cutting direction. Two cutters, with attack angle ( $\alpha$ ) of  $45^\circ$ , were sequentially moved to cut the rock model. This type of simulation allowed us to observe the interaction between two adjacent pick cutters. The first cutter cuts the rock model first and followed by the second cutter after a 35-mm-cut of the first cutter. Penetration depth ( $p$ ) was set to be 5 mm with some combinations of cut spacing ( $s$ ) from 5 mm to 30 mm at 5 mm interval. The linear cutting test model is presented in Figure 4.10.

#### **4.4.3 Results of Linear Cutting Test Modeling**

The magnitude of cutter forces acting on the pick and the cut rock volume are essential parameters to estimate the cutting efficiency of a pick cutter. The contact force between the cutting tool and rock model (namely, external contact force) is automatically calculated and saved in each simulation cycle. The external contact force includes forces in three orthogonal directions. Therefore, the three-dimensional cutter forces acting on the pick can be obtained by measuring contact forces between pick cutter and rock models. The cutter forces reported in the simulation

result were the averaged values of the mean cutter forces acting on both cutter No.1 and cutter No.2. Figure 4.11 shows the representative cutter forces resulted from the FEM simulation.

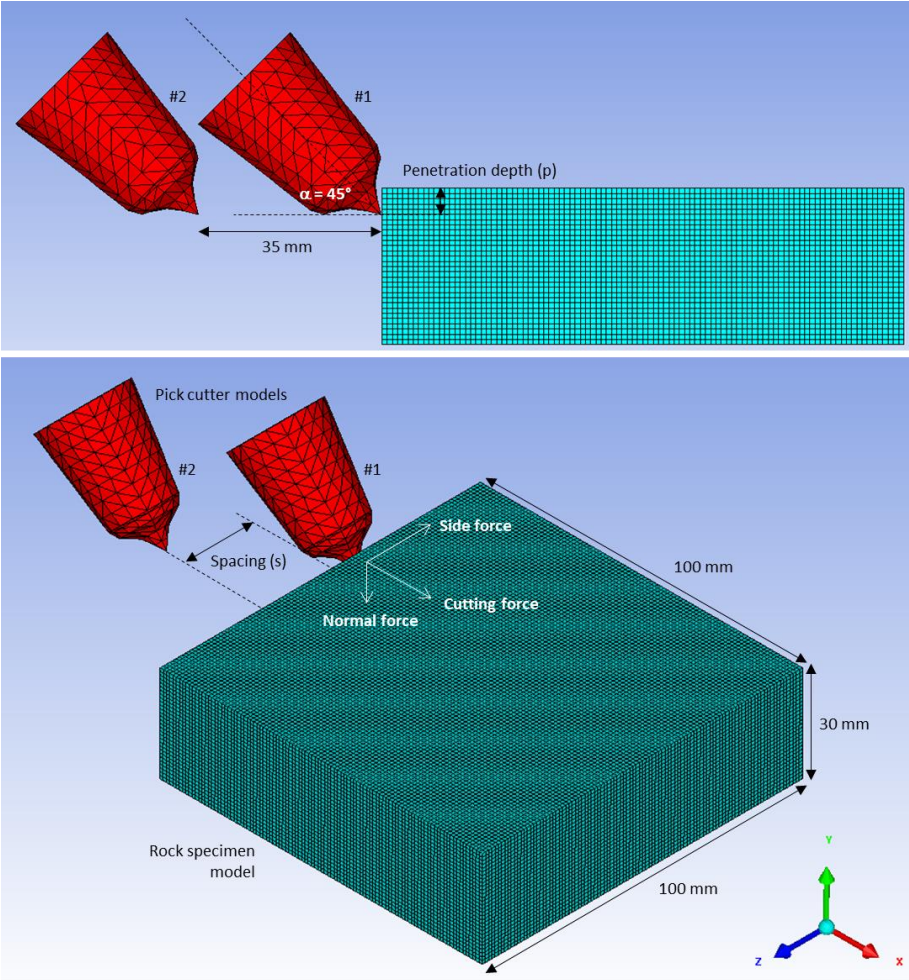


Figure 4.10. Numerical modeling of linear cutting test

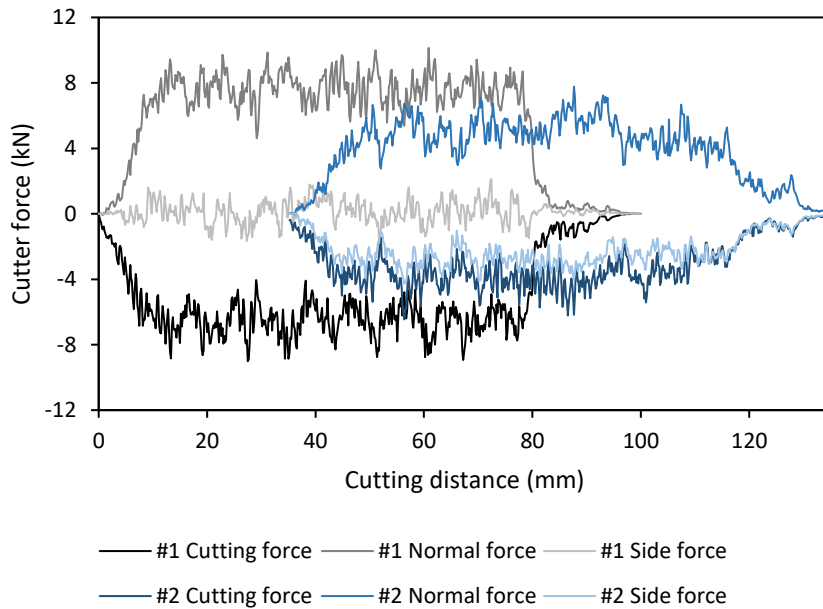


Figure 4.11. Representative cutter forces graph of the two-pick cutter model

In this simulation, the volume of cut rock was calculated by counting the fragmented particles, which reached the maximum damage after the cutting process finished. The volume of cut rock is one of the parameters that determine specific energy in a cutting process. Specific energy is defined as the required work to cut a unit volume of rock.

Figure 4.12 presents the volume reduction graph of the rock model over the cutting distance, implying that the volume of the rock model would be the difference between the initial and the final stage of the cutting process.

The results of the simulation, both using quasi-static and dynamic, are presented in Table 4.3. The final rock models that show cutting grooves resulted from each *s/p* scenario are shown in Figure 4.13.

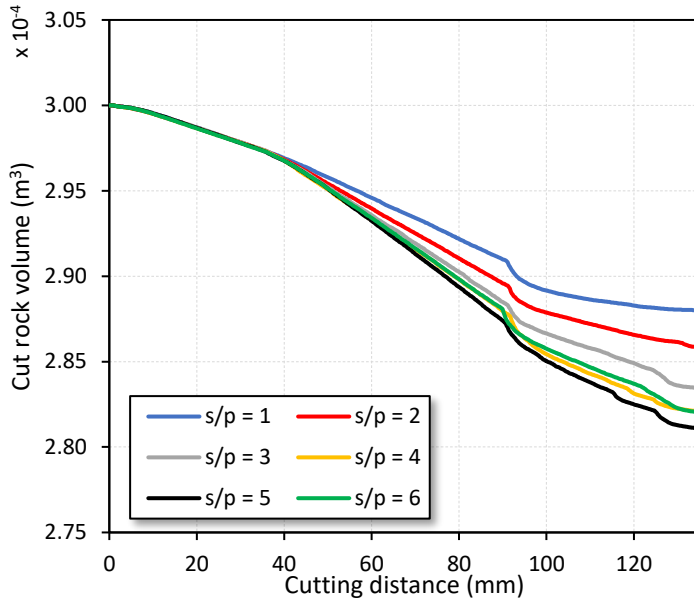


Figure 4.12. The cut volume of the rock model over the cutting process

Table 4.3. Results FEM linear cutting simulation with quasi-static and dynamic strength input properties

$p$ (mm)	$s/p$	$F_{C\_mean}$ (kN)		$F_{N\_mean}$ (kN)		$F_{S\_mean}$ (kN)		$SE$ (MJ/m <sup>3</sup> )	
		Q-stat.	Dyn.	Q-stat.	Dyn.	Q-stat.	Dyn.	Q-stat.	Dyn.
5	1	2.36	3.57	2.97	4.39	0.74	0.96	39.64	65.46
	2	2.88	4.36	3.81	5.63	1.11	1.78	40.86	61.86
	3	2.98	4.53	3.44	5.40	0.97	1.50	36.12	54.91
	4	2.84	4.83	3.74	6.21	0.81	1.60	31.81	54.10
	5	3.27	5.35	3.74	6.06	0.47	1.10	34.70	56.78
	6	3.74	5.74	4.88	7.25	0.50	0.80	41.79	64.14

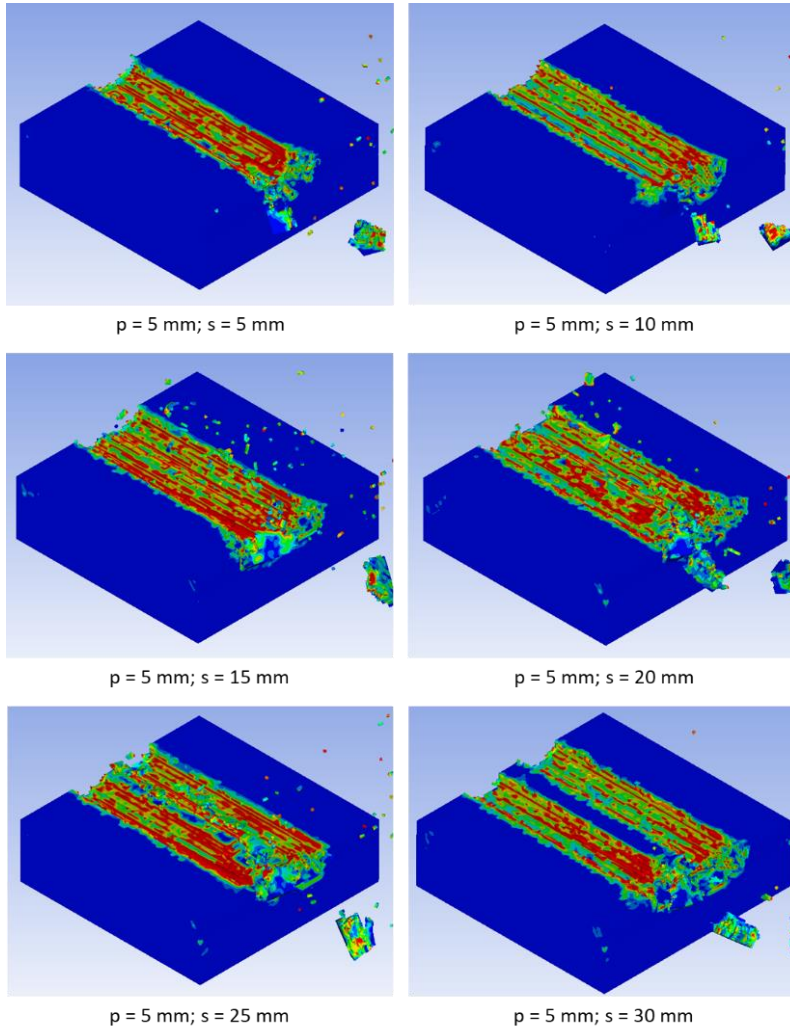


Figure 4.13. Cutting groove pattern of rock specimen at various cut spacing cases

#### 4.5 Discussion on the Linear Cutting Test: Laboratory vs. FEM Simulation

In all cases of laboratory experiment and numerical simulation,  $F_{C\_mean}$  and  $F_{N\_mean}$  tend to have a positive relationship with the  $s/p$  ratio. The  $F_{C\_mean}$  and  $F_{N\_mean}$  increase as the  $s/p$  ratio increases (see Figures 4.14

and 4.15). The  $s/p$  ratio determines the interconnection of the cracks between two adjacent cutting grooves or, in other words, it controls the damage level between grooves. In lower  $s/p$  ratio, some part of the rock surface has been chipped by the first cutter, so the second cutter only needs relatively smaller force to cut the rest of the surface. Whereas, in a higher  $s/p$  ratio, the second cutter needs more force to cut the rock surface since the damaging effect from the previous cutter is minimum.

On the other hand,  $F_{S\_mean}$  of LCM test and FEM simulation do not seem to have a good relationship between each other and are significantly small compared to cutting and normal forces (see Figure 4.16). Since this study does not involve skew angle as a variable (set as  $0^\circ$ ), where the side force may take effect on the cutting efficiency (Jeong & Jeon, 2018), the side force is discounted for further discussion.

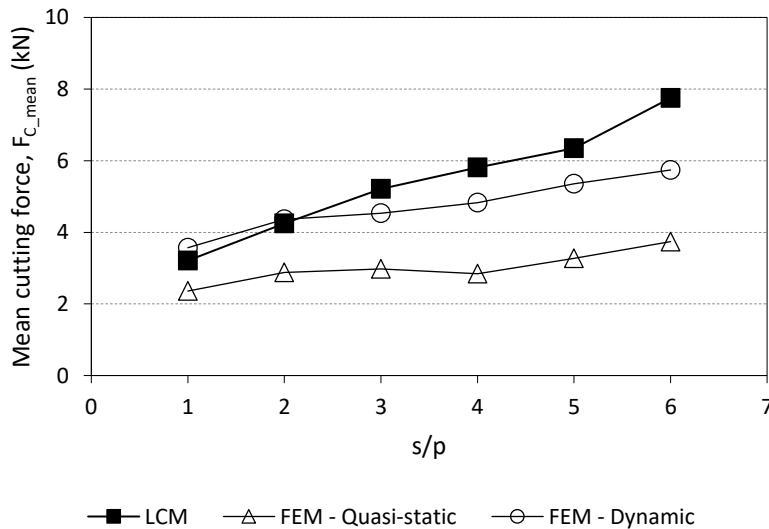


Figure 4.14. Mean cutting force comparison between experimental test and numerical simulation

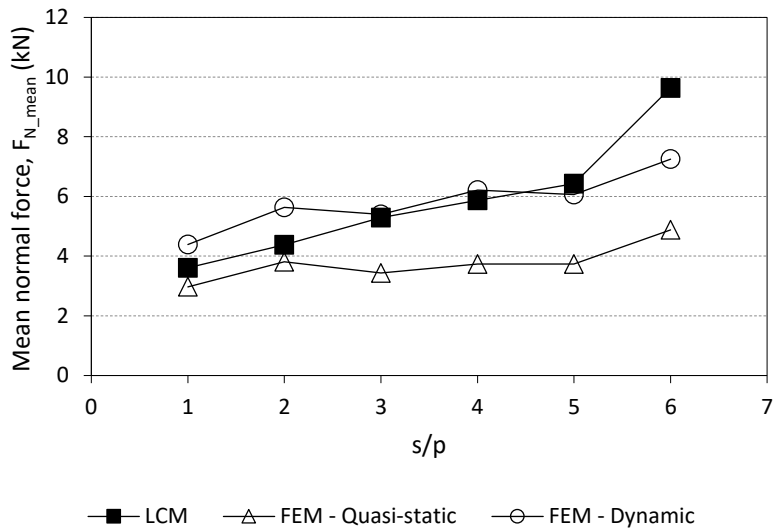


Figure 4.15. Mean normal force comparison between experimental test and numerical simulation

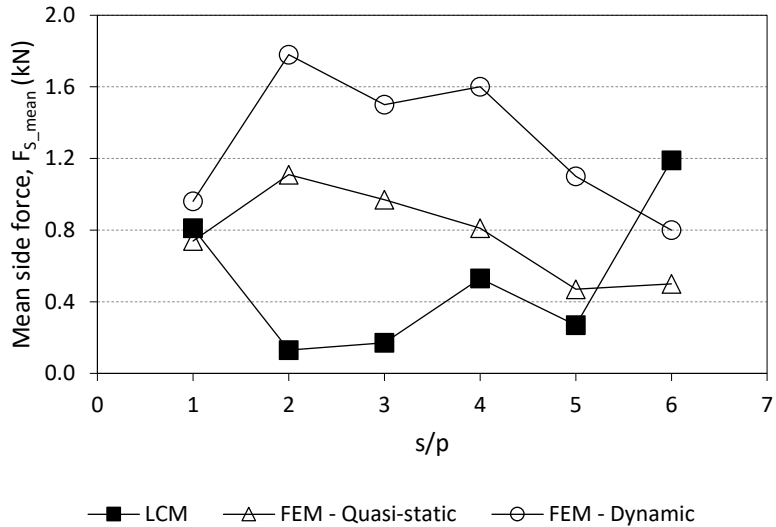


Figure 4.16. Mean side force comparison between experimental test and numerical simulation

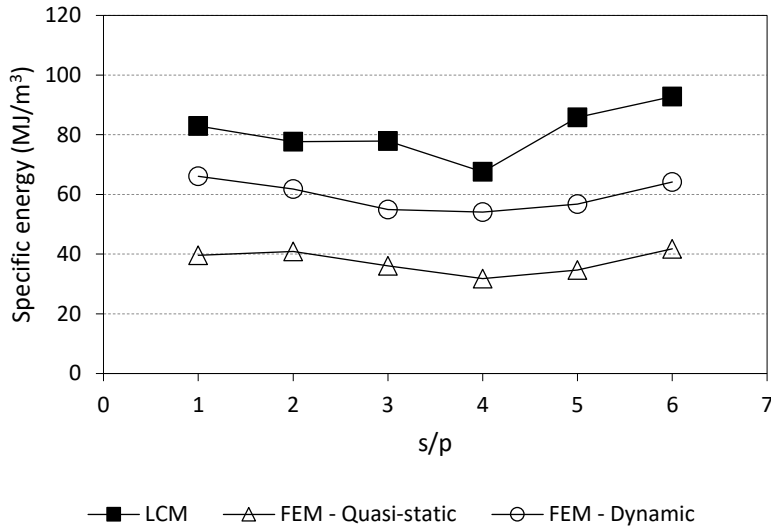


Figure 4.17. Specific energy comparison between experimental test and numerical simulation

Figures 4.14, 4.15, and 4.17 show that the FEM cases simulated from dynamic input parameters have a better fit with the results obtained from the laboratory test compared to the one simulated from quasi-static parameters. The mean absolute error (MAE) was used to quantify the difference between laboratory experiments with numerical simulation results, as shown in Eq. 4.2.

$$MAE = \frac{1}{n} \sum_{i=1}^n \frac{|x_{LCM_i} - x_{FEM_i}|}{x_{LCM_i}} \times 100 \quad (4.2)$$

The cases were consistent for  $F_{C\_mean}$ ,  $F_{N\_mean}$ , and  $SE$ . Compared to the FEM simulation using quasi-static properties, the FEM simulation using dynamic rock properties produces a relatively smaller error to the laboratory experiment. By using dynamic rock properties, the mean

absolute error reduces from 42% to 14% for  $F_{C\_mean}$ , 32% to 14% for  $F_{N\_mean}$ , and 53% to 26% for  $SE$  (see Table 4.4).

Table 4.4. The results of FEM simulation with quasi-static and dynamic strength input properties compared to laboratory LCM test with their mean absolute errors

	$s/p$	$F_{C\_mean}$ (kN)			Abs. Error (%)		MAE (%)	
		LCM	FEM <sub>QS</sub>	FEM <sub>D</sub>	FEM <sub>QS</sub>	FEM <sub>D</sub>	FEM <sub>QS</sub>	FEM <sub>D</sub>
Cutting Force	1	3.21	2.36	3.57	26.48	11.21	42.15	14.23
	2	4.25	2.88	4.36	32.24	2.59		
	3	5.21	2.98	4.53	42.8	13.05		
	4	5.81	2.84	4.83	51.12	16.87		
	5	6.35	3.27	5.35	48.50	15.75		
	6	7.75	3.74	5.74	51.74	25.94		
	$s/p$	$F_{N\_mean}$ (kN)			Abs. Error (%)		MAE (%)	
		LCM	FEM <sub>QS</sub>	FEM <sub>D</sub>	FEM <sub>QS</sub>	FEM <sub>D</sub>	FEM <sub>QS</sub>	FEM <sub>D</sub>
Normal Force	1	3.61	2.97	4.39	17.73	21.61	32.20	14.76
	2	4.38	3.81	5.63	13.01	28.54		
	3	5.29	3.44	5.4	34.97	2.08		
	4	5.87	3.74	6.21	36.29	5.79		
	5	6.43	3.74	6.06	41.84	5.75		
	6	9.64	4.88	7.25	49.35	24.75		
	$s/p$	$SE$ (MJ/m <sup>3</sup> )			Abs. Error (%)		MAE (%)	
		LCM	FEM <sub>QS</sub>	FEM <sub>D</sub>	FEM <sub>QS</sub>	FEM <sub>D</sub>	FEM <sub>QS</sub>	FEM <sub>D</sub>
Specific Energy	1	82.96	39.64	66.09	52.22	20.33	53.44	25.80
	2	77.65	40.86	61.86	47.38	20.33		
	3	77.86	36.12	54.91	53.6	29.47		
	4	67.57	31.81	54.1	52.93	19.94		
	5	85.81	34.7	56.78	59.56	33.83		
	6	92.80	41.79	64.14	54.97	30.88		

Note:

$s/p$ : the ratio of cut spacing to the penetration depth

LCM: laboratory linear cutting test by small-scale LCM

FEM<sub>QS</sub>: finite element analysis using quasi-static input parameters

FEM<sub>D</sub>: finite element analysis using dynamic input parameters

MAE: Mean absolute error (%)

Even though the use of dynamic rock properties decreases the mean absolute error between the numerical and experimental cases in the *SE* calculation, but it appears that the error is still significant, showing that *SE* from the numerical simulation is smaller than that of the LCM test in all cases. The reason is that the numerical cutting test was done in ideal conditions meaning that all the energy was only consumed to fragment the rock. In the laboratory LCM test, on the other hand, the cutting energy was not only consumed by rock fragmentation, but also by vibration and deformation related to the stiffness of the testing machine such as cutter holder, load cell, and loading frame. Therefore, the numerical cutting test is likely to provide more efficient results than the LCM test.

Although the *SE* calculation from FEM simulation does not match well with the LCM test, yet it gives us correct information to predict the optimum cutting condition. The optimum cutting condition can be defined as a point where *SE* gives the minimum value in its relationship with the *s/p* ratio. The results indicate that the optimum configuration to excavate the rock is by applying *s/p* ratio of about 4 (see Figure 4.17).

The previous studies have reported that cutting speed, within all practical ranges, does not affect cutter forces and specific energy (Bilgin et al., 2014). Knowing that speed does not affect forces and cutting efficiency improves with penetration depth, with a given capacity of the machine, a slow and deep cutting will cut more volume than a faster and proportionally shallower depth (Hood & Roxborough, 1992).

Roxborough and Phillips (1975) conducted a series of linear disc cutting tests on sandstone material with a cutting speed of 76 to 178 mm/s. The experiment showed that, in that laboratory range, thrust and rolling

forces, yield, and specific energy were not affected by cutting speed. However, it should be noted that the variation of speed that Roxborough applied in the experiment was relatively low, meaning that the ratio of the maximum cutting speed to its minimum applied in the experiment was only 2.3 times (ratio between 178 mm/s and 76 mm/s). Also, the cutting speed was far slower than the actual linear speed of the TBM cutter head on working conditions that is from about 1.6 to 5.5 rpm (from about 0.5 to 2 m/s with the diameter of 6.5 m to 14.5 m) (Bilgin et al., 2014).

On the other hand, if we examine from strain rate point of view, the range of strain rate under dynamic loading, specifically the ISR loading range in this study, is remarkably higher than the strain rate under quasi-static loading regime. A rock, under ISR loading, experiences load approximately in the order of  $10^0 \text{ s}^{-1}$ , while in quasi-static loading, the rock is subjected to a load in the range of only around  $10^{-5} \text{ s}^{-1}$ . The strain rate range, that rock experiences under ISR loading, is about 10,000 times higher than quasi-static loading. As the consequences of the higher strain rate, the rock would respond differently by exhibiting a higher strength, as discussed in the entire Chapter 3. Therefore, analyzing the rock cutting process using the strength under the ISR loading state in which rock experiences in real practice is considered more realistic, and predicting it using quasi-static strength might give underestimate results.

In addition, in the laboratory cutting experiment using small-scale LCM, it was observed that the pick is bumping due to irregularities of the rock surface. The bumping effect causes dynamic events. It can be seen from the force history graph during cutting when the force fluctuates rapidly during the whole process (see Figure 4.11). The fluctuation indicates that the rock is subjected to rapid load changes with a significantly high

loading rate. This phenomenon might not be related to any rock test under quasi-static loading condition. Thus, it is reasonable to see the mechanical rock cutting from a dynamic perspective, particularly the ISR loading condition.

## **4.6 Cutting Force Prediction Model**

### **4.6.1 Database and the Conversion to Dynamic Strength of Rock**

Cutting force prediction models considering the dynamic strength of rock were developed. The dynamic uniaxial compressive strength (UCS) and Brazilian tensile strength (BTS) at the ISR loading were obtained from the database for various rocks, as presented in Chapter 3. The DIFs of both strength properties were averaged only within the ISR range that is  $10^{-1}$  to  $10^1$   $s^{-1}$ , as shown in Figure 4.18. The average  $DIF_{UCS}$  and  $DIF_{BTS}$  were 1.48 and 3.09, respectively. Thus, the  $DIF_{UCS}$  and  $DIF_{BTS}$  can be applied to convert the quasi-static to the dynamic strength under ISR loading. It should be noted that we assumed that the  $DIFs$  would represent various kinds of rocks since they were derived from a collection of data from numerous rocks.

A literature review was done to collect data sets of conical picks cutting that include UCS, BTS, mean cutting force, peak cutting force, and some cutting configurations such as tip angle of the cutter and depth of cut ( $p$ ). The cutting force was limited only on the unrelieved force, meaning that the force has no influence from the cut spacing. The reason was that the prediction models from this study would be compared with some theoretical models that are based on a single cut without any parameters considering cut spacing. The data sets were taken from various Turkish

rocks (Bilgin et al., 2006; Copur et al., 2003) and some Chinese sandstones (Wang et al., 2018). The quasi-static UCS and BTS ( $\sigma_{c\_stat}$  and  $\sigma_{t\_stat}$ ) from the references were then converted to the dynamic strength ( $\sigma_{c\_dyn}$  and  $\sigma_{t\_dyn}$ ) using the  $DIF_{UCS}$  and  $DIF_{BTS}$ , respectively.

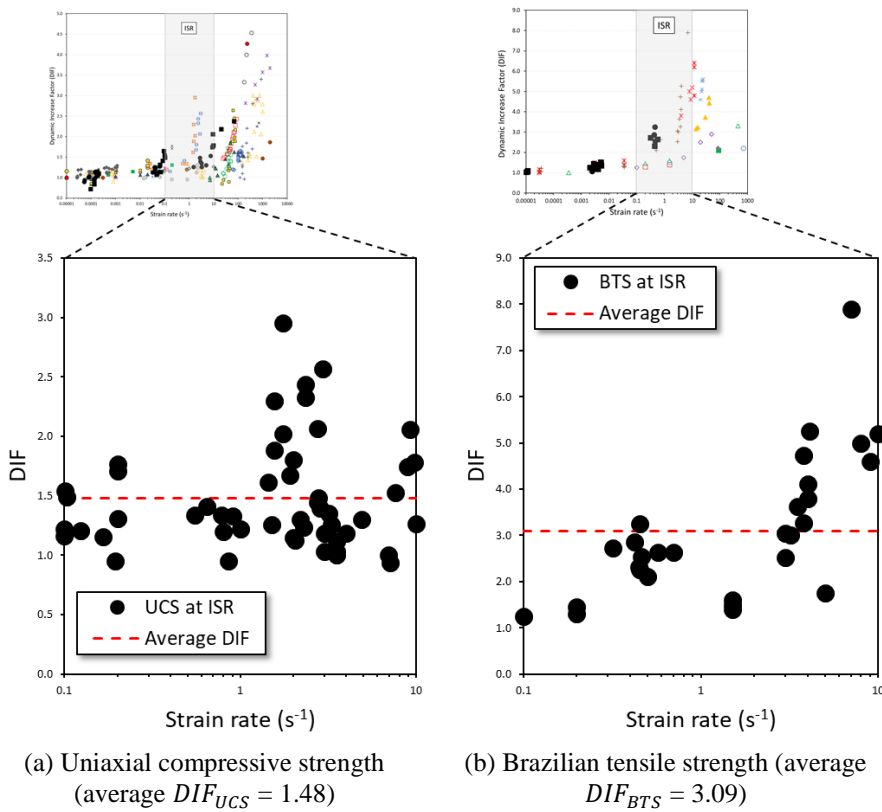


Figure 4.18. Dynamic increase factor (DIF) of UCS and BTS within the intermediate strain rate loading range and their representative averaged values

#### 4.6.2 Multiple Linear Regression Analysis

Multiple linear regression (MLR) analyses were carried out to predict mean cutting force and peak cutting force ( $F_{c\_mean}$  and  $F_{c\_peak}$ ) at the

confidence interval of 95% ( $\alpha = 0.05$ ). There were three possible variables from the database to be used as the independent variables, namely, dynamic UCS ( $\sigma_{c\_dyn}$ ), dynamic BTS ( $\sigma_{t\_dyn}$ ), and depth of cut ( $p$ ). In the MLR analysis, as the first approach, all three variables were included in the regression model as the independent variables. The summary of the MLR analysis of three independent variables resulted from SPSS statistical program is presented in Table 4.5.

Table 4.5. Summary of the selected results of the MLR analysis in predicting mean and peak cutting forces from three independent variables from the SPSS statistical program

<b>Dependent variable: <math>F_{c\_mean}</math></b>			<b>Dependent variable: <math>F_{c\_peak}</math></b>		
R Square		0.692	R Square		0.721
Adjusted R Square		0.679	Adjusted R Square		0.703
Observations		75	Observations		50
Degree of freedom		71	Degree of freedom		46
Significance F		$3.82 \times 10^{-18}$	Significance F		$8.39 \times 10^{-13}$
<b>Variables</b>	<b>Coefficients</b>	<b>p-value</b>	<b>Variables</b>	<b>Coefficients</b>	<b>p-value</b>
Intercept	-3.511	$1.16 \times 10^{-6}$	Intercept	-14.761	$7.45 \times 10^{-6}$
$\sigma_{c\_dyn}$	-0.004	<b><math>6.03 \times 10^{-1}</math></b>	$\sigma_{c\_dyn}$	0.033	<b><math>3.18 \times 10^{-1}</math></b>
$\sigma_{t\_dyn}$	0.333	$1.57 \times 10^{-6}$	$\sigma_{t\_dyn}$	0.618	$2.02 \times 10^{-2}$
$p$	0.494	$3.54 \times 10^{-12}$	$p$	2.440	$4.62 \times 10^{-9}$

Overall, the entire model consisting of those three independent variables is significant to the dependent variables for both cases by showing the significance F values of each model are less than the significance level of 0.05 (Montgomery & Runger, 2010). Subsequently, the significance test for each independent variable was conducted. One of the most common tests to decide whether one independent variable is significant to the dependent variable or not is by assessing the corresponding p-value. The p-value will decide whether the null hypothesis should be

rejected or not. The null hypothesis states that the independent variable does not affect the dependent variable. In the confidence interval of 95% ( $\alpha = 0.05$ ), if the p-value is greater than  $\alpha$ , then we fail to reject the null hypothesis. On the other hand, if the p-value is less than  $\alpha$ , we shall reject the hypothesis (Frost, 2013). In other words, if the p-value is greater than  $\alpha$ , the corresponding independent variable is not significant to the dependent variable and can be eliminated from the combination.

Table 4.5 shows that only  $\sigma_{t\_dyn}$  and  $p$  were significant to each of dependent variable  $F_{c\_mean}$  and  $F_{c\_peak}$ , given the value of p-values less than  $\alpha$ . For  $\sigma_{c\_dyn}$ , it is not significant to the dependent variables in all cases, given the p-value greater than  $\alpha$ . From this test, it can be concluded that  $\sigma_{c\_dyn}$  should be removed from the independent variable list.

The above explanation shows that predicting using three independent variables was not give any good results; then, the MLR analysis should be done by using two independent variables to predict each of the dependent variables. The possible pairs of independent variables are:  $\sigma_{c\_dyn}$  and  $p$  (regarded as Model 1 and Model 2),  $\sigma_{t\_dyn}$  and  $p$  (regarded as Model 3 and Model 4),  $\sigma_{c\_dyn}$  and  $\sigma_{t\_dyn}$  (regarded as Model 5 and Model 6). The MLR analyses were performed to those combinations, and the results are shown in Table 4.6.

Table 4.6. Summary of the selected results of the MLR analysis in predicting mean and peak cutting forces from two independent variables from the SPSS statistical program (DV: dependent variable and IV: independent variable)

<b>Model 1</b> (DV: $F_{c\_mean}$ , IV: $\sigma_{c\_dyn}$ and $p$ )			<b>Model 2</b> (DV: $F_{c\_peak}$ , IV: $\sigma_{c\_dyn}$ and $p$ )		
R Square		0.573	R Square		0.686
Adjusted R Square		0.561	Adjusted R Square		0.672
Observations		75	Observations		50
Degree of freedom		72	Degree of freedom		47
Significance F		$4.83 \times 10^{-14}$	Significance F		$1.53 \times 10^{-12}$
Variables	Coefficients	p-value	Variables	Coefficients	p-value
Intercept	-1.92545	$6.44 \times 10^{-3}$	Intercept	-12.1208	$9.69 \times 10^{-5}$
$\sigma_{c\_dyn}$	0.03345	$5.16 \times 10^{-12}$	$\sigma_{c\_dyn}$	0.10709	$2.35 \times 10^{-11}$
$p$	0.44611	$7.77 \times 10^{-9}$	$p$	2.44636	$1.27 \times 10^{-8}$
<b>Model 3</b> (DV: $F_{c\_mean}$ , IV: $\sigma_{t\_dyn}$ and $p$ )			<b>Model 4</b> (DV: $F_{c\_peak}$ , IV: $\sigma_{t\_dyn}$ and $p$ )		
R Square		0.691	R Square		0.715
Adjusted R Square		0.683	Adjusted R Square		0.703
Observations		75	Observations		50
Degree of freedom		72	Degree of freedom		47
Significance F		$4.28 \times 10^{-19}$	Significance F		$1.58 \times 10^{-13}$
Variables	Coefficients	p-value	Variables	Coefficients	p-value
Intercept	-3.44832	$1.04 \times 10^{-6}$	Intercept	-15.2853	$2.90 \times 10^{-6}$
$\sigma_{t\_dyn}$	0.30269	$4.04 \times 10^{-17}$	$\sigma_{t\_dyn}$	0.85992	$2.36 \times 10^{-12}$
$p$	0.49167	$2.86 \times 10^{-12}$	$p$	2.41241	$5.06 \times 10^{-9}$
<b>Model 5</b> (DV: $F_{c\_mean}$ , IV: $\sigma_{c\_dyn}$ and $\sigma_{t\_dyn}$ )			<b>Model 6</b> (DV: $F_{c\_peak}$ , IV: $\sigma_{c\_dyn}$ and $\sigma_{t\_dyn}$ )		
R Square		0.389	R Square		0.407
Adjusted R Square		0.372	Adjusted R Square		0.381
Observations		75	Observations		50
Degree of freedom		72	Degree of freedom		47
Significance F		$1.96 \times 10^{-8}$	Significance F		$4.70 \times 10^{-6}$
Variables	Coefficients	p-value	Variables	Coefficients	p-value
Intercept	0.82288	0.155	Intercept	2.70066	0.257
$\sigma_{c\_dyn}$	0.00115	<b>0.944</b>	$\sigma_{c\_dyn}$	0.02074	<b>0.768</b>
$\sigma_{t\_dyn}$	0.77407	0.006	$\sigma_{t\_dyn}$	1.95322	<b>0.095</b>

Table 4.6 shows that, as a whole model, all models were significant to predict both  $F_{c\_mean}$  and  $F_{c\_peak}$ , showing that the significance F of them were lower than 0.05. However, from the significance test of each independent variable, the coefficients of the variables used in Model 5 and Model 6 were not significant to the response variables, showing the p-value greater than 0.05. Thus, those models were eliminated from further consideration.

To summarize, four models were built considering the combination of  $\sigma_{c\_dyn}$  and  $p$ ; and the combination  $\sigma_{t\_dyn}$  and  $p$ . Model 1 and 3 predicted  $F_{c\_mean}$  and Model 2 and Model 4 predicted  $F_{c\_peak}$ . The equations of suggested models are presented in Eqs. 4.3 – 4.6. It should be noted that the  $F'_{c\_mean}$  and  $F'_{c\_peak}$  (with primes) indicate the predicted cutting forces resulted from the suggested prediction models.

**Model 1** (Eq. 4.3):

$$F'_{c\_mean} = a + b \times [\sigma_{c\_dyn}] + c \times [p]$$

$$\begin{aligned} F'_{c\_mean} &= -1.92545 + 0.033454 \times [\sigma_{c\_dyn}] + 0.446114 \times [p] \\ &= -1.92545 + 0.033454 \times [DIF_{UCS} \times \sigma_{c\_stat}] + 0.446114 \times [p] \\ &= -1.92545 + 0.033454 \times [1.48 \times \sigma_{c\_stat}] + 0.446114 \times [p] \\ &= -1.92545 + 0.049512 \times [\sigma_{c\_stat}] + 0.446114 \times [p] \end{aligned}$$

**Model 2** (Eq. 4.4):

$$F'_{c\_peak} = a + b \times [\sigma_{c\_dyn}] + c \times [p]$$

$$\begin{aligned} F'_{c\_peak} &= -12.1208 + 0.107093 \times [\sigma_{c\_dyn}] + 2.446356 \times [p] \\ &= -12.1208 + 0.107093 \times [DIF_{UCS} \times \sigma_{c\_stat}] + 2.446356 \times [p] \\ &= -12.1208 + 0.107093 \times [1.48 \times \sigma_{c\_stat}] + 2.446356 \times [p] \\ &= -12.1208 + 0.158498 \times [\sigma_{c\_stat}] + 2.446356 \times [p] \end{aligned}$$

**Model 3** (Eq. 4.5):

$$F'_{c\_mean} = a + b \times [\sigma_{t\_dyn}] + c \times [p]$$

$$\begin{aligned} F'_{c\_mean} &= -3.44832 + 0.302693 \times [\sigma_{t\_dyn}] + 0.491673 \times [p] \\ &= -3.44832 + 0.302693 \times [DIF_{UTS} \times \sigma_{t\_stat}] + 0.491673 \times [p] \\ &= -3.44832 + 0.302693 \times [3.09 \times \sigma_{t\_stat}] + 0.491673 \times [p] \\ &= -3.44832 + 0.935321 \times [\sigma_{t\_stat}] + 0.491673 \times [p] \end{aligned}$$

**Model 4** (Eq. 4.6):

$$F'_{c\_peak} = a + b \times [\sigma_{t\_dyn}] + c \times [p]$$

$$\begin{aligned} F'_{c\_peak} &= -15.2853 + 0.859924 \times [\sigma_{t\_dyn}] + 2.412407 \times [p] \\ &= -15.2853 + 0.859924 \times [DIF_{UTS} \times \sigma_{t\_stat}] + 2.412407 \times [p] \\ &= -15.2853 + 0.859924 \times [3.09 \times \sigma_{t\_stat}] + 2.412407 \times [p] \\ &= -3.44832 + 2.657165 \times [\sigma_{t\_stat}] + 2.412407 \times [p] \end{aligned}$$

### 4.6.3 Performance of the Proposed Prediction Models

The performance of the proposed four models developed in this study was compared against Evans' model (Evans, 1984a, 1984b), Goktan's model (Goktan, 1997), and Roxborough and Liu's model (Roxborough & Liu, 1995). Evans suggested that UCS and BTS are the most dominant factor governing the cutting force of a conical pick. Goktan and Roxborough & Liu modified Evans' theory and suggested that the friction angle between the cutting tool and rock should be included in the model. These cutting theories are valid for estimating the cutting force of conical cutter in unrelieved cutting mode (Bilgin et al., 2014). The theoretical models are presented in Eq. 4.7-4.9.

Evans' model:

$$FC = \frac{16. \pi. \sigma_t^2. p^2}{\cos^2\left(\frac{\phi}{2}\right). \sigma_c} \quad (4.7)$$

Goktan's model:

$$FC = \frac{4. \pi. p^2. \sigma_t. \sin^2\left(\frac{\phi}{2} + \psi\right)}{\cos\left(\frac{\phi}{2} + \psi\right)} \quad (4.8)$$

Roxborough and Liu's model:

$$FC = \frac{16. \pi. d^2. \sigma_t^2. \sigma_c}{\left[2. \sigma_t + \left(\sigma_c. \cos\left(\frac{\phi}{2}\right)\right) \left(\frac{1 + \tan\psi}{\tan(\phi/2)}\right)\right]^2} \quad (4.9)$$

where,  $\sigma_c$  is quasi-static UCS,  $\sigma_t$  is quasi-static BTS,  $p$  is the depth of cut,  $\phi$  is tip angle, and  $\psi$  is tool-rock friction angle. It should be noted that  $\phi$  is  $80^\circ$  for all case in the database, and  $\psi$  is  $16^\circ$ , as suggested by Roxborough and Liu (1995).

The database used in this study, including quasi-static strength, converted dynamic strength, laboratory cutting force from references, cutting force estimation from theoretical models, and cutting force estimation from the built models, are presented in Table 4.7. Based on the database presented in Table 4.7, the correlations between measured and predicted mean and peak cutting forces by different models were derived.

To further investigate the correlation between measured and predicted cutting forces, student's t-test is carried out to estimate whether a model is statistically significant to the measured data. At the 95% confidence

interval ( $\alpha = 0.05$ ), if the significance F value of the suggested model is lower than  $\alpha$  or the calculated t-value is greater than the t-value obtained from the distribution table, then it can be concluded that the regression is statistically significant (Montgomery & Runger, 2010). Besides, the mean squared error (MSE) calculation of each model is also carried out to estimate the fitness of the models to the data population. The coefficient of determination ( $R^2$ ), MSE, t-value (calculated and tabulated), and significance F value of all models are listed in Table 4.8. Based on Table 4.8, the calculated t-values of all models are higher than the tabulated t-value of mean cutting force (1.99) and the peak force (2.01). Furthermore, the significance F values of them are very small, smaller than the significance level of 0.05. It means that all models are reliable as a predictor of the actual data.

Table 4.7. Summary of mechanical properties, cutting configuration, and cutting forces from various estimations

Rock Type	Rock Strength				p (mm)	Unrelieved Cutting Force (kN)		Theoretical Cutting Force (kN)			Prediction Model Cutting Force			
	UCS (MPa)		BTS (MPa)			$F_{C,mean}$	$F_{C,peak}$	Evan	Goktan	Roxborough & Liu	$F'_{c,mean}$		$F'_{c,peak}$	
	$\sigma_{C,stat}$	$\sigma_{C,dyn}^*$	$\sigma_{t,stat}$	$\sigma_{t,dyn}^*$							1	3	2	4
<sup>1</sup> Harzburgite	58.0	85.8	5.5	17.0	5	5.21	14.68	0.74	2.12	3.45	3.18	4.15	9.30	11.39
	58.0	85.8	5.5	17.0	9	9.04	26.39	2.40	6.88	11.18	4.96	6.12	19.09	21.04
<sup>1</sup> Serpentinite	38.0	56.2	5.7	17.6	5	2.89	7.70	1.22	2.20	4.84	2.19	4.34	6.13	11.92
	38.0	56.2	5.7	17.6	9	6.96	19.76	3.94	7.13	15.69	3.97	6.31	15.92	21.57
<sup>1</sup> Trona	30.0	44.4	2.2	6.8	5	1.36	3.80	0.23	0.85	1.14	1.79	1.07	4.87	2.62
	30.0	44.4	2.2	6.8	9	4.12	12.02	0.74	2.75	3.69	3.57	3.03	14.65	12.27
<sup>1</sup> Limestone	121.0	179.1	7.8	24.1	3	3.87	11.61	0.26	1.08	1.31	5.40	5.32	14.40	12.68
	121.0	179.1	7.8	24.1	5	7.32	21.09	0.72	3.01	3.64	6.30	6.31	19.29	17.50
	121.0	179.1	7.8	24.1	9	11.93	32.21	2.32	9.76	11.81	8.08	8.27	29.07	27.15
<sup>1</sup> Claystone	58.0	85.8	5.6	17.3	3	1.17	3.75	0.28	0.78	1.28	2.28	3.26	4.41	6.83
	58.0	85.8	5.6	17.3	5	2.95	8.80	0.77	2.16	3.56	3.18	4.25	9.30	11.66
	58.0	85.8	5.6	17.3	7	3.17	10.78	1.51	4.24	6.98	4.07	5.23	14.20	16.48
	58.0	85.8	5.6	17.3	9	5.25	16.59	2.49	7.01	11.53	4.96	6.21	19.09	21.31
<sup>1</sup> Sandstone 1	114.0	168.7	6.6	20.4	3	3.83	8.95	0.20	0.92	1.02	5.06	4.20	13.29	9.49
	114.0	168.7	6.6	20.4	5	7.43	19.31	0.54	2.55	2.83	5.95	5.18	18.18	14.31
	114.0	168.7	6.6	20.4	9	9.73	28.95	1.76	8.26	9.15	7.73	7.15	27.97	23.96
<sup>1</sup> Sandstone 2	174.0	257.5	11.6	35.8	3	4.02	9.02	0.40	1.61	2.00	8.03	8.88	22.80	22.78
	174.0	257.5	11.6	35.8	5	8.04	22.80	1.10	4.48	5.57	8.92	9.86	27.69	27.60
	174.0	257.5	11.6	35.8	9	16.53	47.17	3.56	14.51	18.03	10.70	11.83	37.47	37.25
<sup>1</sup> Siltstone	58.0	85.8	5.3	16.4	3	3.07	7.34	0.25	0.74	1.17	2.28	2.98	4.41	6.03
	58.0	85.8	5.3	16.4	5	7.27	22.59	0.69	2.05	3.24	3.18	3.97	9.30	10.86
	58.0	85.8	5.3	16.4	9	8.27	31.38	2.23	6.63	10.49	4.96	5.93	19.09	20.51
<sup>1</sup> High Grade Chromite	32.0	47.4	3.7	11.4	5	2.74	7.02	0.61	1.43	2.67	1.89	2.47	5.18	6.61
	32.0	47.4	3.7	11.4	9	5.20	14.54	1.97	4.63	8.64	3.67	4.44	14.97	16.26
<sup>1</sup> Medium Grade Chromite	47.0	69.6	4.5	13.9	5	3.40	10.01	0.61	1.74	2.84	2.63	3.22	7.56	8.73
	47.0	69.6	4.5	13.9	9	9.13	25.98	1.99	5.63	9.21	4.42	5.19	17.35	18.38

Rock Type	Rock Strength				p (mm)	Unrelieved Cutting Force (kN)		Theoretical Cutting Force (kN)			Prediction Model Cutting Force			
	UCS (MPa)		BTS (MPa)			$F_{C,mean}$	$F_{C,peak}$	Evan	Goktan	Roxborough & Liu	$F'_{C,mean}$		$F'_{C,peak}$	
	$\sigma_{C,stat}$	$\sigma_{C,dyn}^*$	$\sigma_{t,stat}$	$\sigma_{t,dyn}^*$							1	3	2	4
<sup>1</sup> Low Grade Chromite	46.0	68.1	3.7	11.4	5	3.13	8.54	0.42	1.43	2.05	2.58	2.47	7.40	6.61
	46.0	68.1	3.7	11.4	9	6.50	15.93	1.37	4.63	6.66	4.37	4.44	17.19	16.26
<sup>2</sup> Copper (Yellow)	33.0	48.8	3.4	10.5	5	1.67	4.31	0.50	1.31	2.26	1.94	2.19	5.34	5.81
	33.0	48.8	3.4	10.5	9	4.99	14.78	1.61	4.25	7.33	3.72	4.16	15.13	15.46
<sup>2</sup> Copper (Black)	41.0	60.7	5.7	17.6	5	2.65	7.19	1.13	2.20	4.62	2.34	4.34	6.61	11.92
	41.0	60.7	5.7	17.6	9	8.90	25.32	3.65	7.13	14.98	4.12	6.31	16.39	21.57
<sup>2</sup> Anhydrite	82.0	121.4	5.5	17.0	5	3.31	12.28	0.52	2.12	2.65	4.37	4.15	13.11	11.39
	82.0	121.4	5.5	17.0	9	5.09	15.98	1.70	6.88	8.59	6.15	6.12	22.89	21.04
<sup>2</sup> Selestite	29.0	42.9	4.0	12.4	5	1.47	4.65	0.78	1.54	3.23	1.74	2.75	4.71	7.41
	29.0	42.9	4.0	12.4	9	3.36	8.89	2.54	5.00	10.46	3.53	4.72	14.49	17.06
<sup>2</sup> Jips	33.0	48.8	3.0	9.3	5	3.93	8.55	0.39	1.16	1.83	1.94	1.82	5.34	4.75
	33.0	48.8	3.0	9.3	9	3.31	6.40	1.26	3.75	5.91	3.72	3.78	15.13	14.40
<sup>2</sup> Tuff 1	10.0	14.8	0.9	2.8	5	0.73	2.01	0.12	0.35	0.54	0.80	-0.15	1.70	-0.83
	10.0	14.8	0.9	2.8	9	1.58	3.94	0.37	1.13	1.76	2.58	1.82	11.48	8.82
<sup>2</sup> Tuff 2	11.0	16.3	1.2	3.7	5	1.92	6.94	0.19	0.46	0.83	0.85	0.13	1.85	-0.03
	11.0	16.3	1.2	3.7	9	3.80	11.61	0.60	1.50	2.69	2.63	2.10	11.64	9.61
<sup>2</sup> Tuff 3	27.0	40.0	2.6	8.0	5	1.23	3.70	0.36	1.00	1.65	1.64	1.44	4.39	3.69
	27.0	40.0	2.6	8.0	9	2.69	7.08	1.15	3.25	5.34	3.43	3.41	14.18	13.33
<sup>2</sup> Tuff 4	14.0	20.7	1.5	4.6	5	0.91	2.78	0.23	0.58	1.03	1.00	0.41	2.33	0.76
	14.0	20.7	1.5	4.6	9	2.43	7.16	0.74	1.88	3.32	2.78	2.38	12.12	10.41
<sup>2</sup> Tuff 5	19.0	28.1	2.3	7.1	5	1.34	3.37	0.40	0.89	1.71	1.25	1.16	3.12	2.89
	19.0	28.1	2.3	7.1	9	2.93	7.21	1.28	2.88	5.53	3.03	3.13	12.91	12.54
<sup>2</sup> Tuff 6	6.0	8.9	0.2	0.6	5	0.46	1.30	0.01	0.08	0.05	0.60	-0.80	1.06	-2.69
	6.0	8.9	0.2	0.6	9	1.02	2.14	0.03	0.25	0.17	2.39	1.16	10.85	6.96
<sup>3</sup> Sandstone 1	17.9	26.5	1.6	5.1	3	0.55	-	0.08	0.23	0.36	0.30	-0.44	-	-
	17.9	26.5	1.6	5.1	6	1.26	-	0.31	0.91	1.44	1.64	1.04	-	-
	17.9	26.5	1.6	5.1	9	2.03	-	0.69	2.05	3.25	2.98	2.51	-	-
	17.9	26.5	1.6	5.1	12	2.74	-	1.23	3.65	5.78	4.31	3.99	-	-

Rock Type	Rock Strength				p (mm)	Unrelieved Cutting Force (kN)		Theoretical Cutting Force (kN)			Prediction Model Cutting Force			
	UCS (MPa)		BTS (MPa)			$F_{C,mean}$	$F_{C,peak}$	Evan	Goktan	Roxborough & Liu	$F'_{C,mean}$		$F'_{C,peak}$	
	$\sigma_{C,stat}$	$\sigma_{C,dyn}^*$	$\sigma_{t,stat}$	$\sigma_{t,dyn}^*$							1	3	2	4
<sup>3</sup> Sandstone 2	17.9	26.5	1.6	5.1	15	3.42	-	1.92	5.70	9.03	5.65	5.46	-	-
	17.9	26.5	1.6	5.1	18	4.33	-	2.77	8.21	13.00	6.99	6.94	-	-
	79.2	117.2	5.0	15.4	3	1.41	-	0.16	0.69	0.82	3.33	2.68	-	-
	79.2	117.2	5.0	15.4	6	2.66	-	0.64	2.76	3.27	4.67	4.15	-	-
	79.2	117.2	5.0	15.4	9	4.11	-	1.44	6.22	7.36	6.01	5.63	-	-
	79.2	117.2	5.0	15.4	12	6.60	-	2.55	11.05	13.09	7.35	7.10	-	-
	79.2	117.2	5.0	15.4	15	8.25	-	3.99	17.27	20.45	8.69	8.58	-	-
<sup>3</sup> Sandstone 3	79.2	117.2	5.0	15.4	18	-	-	5.75	24.87	29.44	10.03	10.05	-	-
	53.0	78.4	3.7	11.3	3	0.93	-	0.13	0.51	0.65	2.04	1.46	-	-
	53.0	78.4	3.7	11.3	6	1.61	-	0.52	2.04	2.61	3.37	2.93	-	-
	53.0	78.4	3.7	11.3	9	3.00	-	1.17	4.59	5.88	4.71	4.41	-	-
	53.0	78.4	3.7	11.3	12	4.60	-	2.08	8.16	10.45	6.05	5.88	-	-
	53.0	78.4	3.7	11.3	15	6.22	-	3.25	12.75	16.34	7.39	7.36	-	-
<sup>3</sup> Sandstone 4	53.0	78.4	3.7	11.3	18	-	-	4.69	18.37	23.52	8.73	8.83	-	-
	59.8	88.5	3.9	12.1	3	0.93	-	0.13	0.55	0.67	2.37	1.70	-	-
	59.8	88.5	3.9	12.1	6	2.37	-	0.53	2.19	2.68	3.71	3.18	-	-
	59.8	88.5	3.9	12.1	9	3.71	-	1.19	4.92	6.04	5.05	4.65	-	-
	59.8	88.5	3.9	12.1	12	5.71	-	2.12	8.74	10.74	6.39	6.13	-	-
	59.8	88.5	3.9	12.1	15	8.18	-	3.31	13.66	16.78	7.73	7.60	-	-
<sup>3</sup> Sandstone 5	59.8	88.5	3.9	12.1	18	-	-	4.76	19.67	24.16	9.07	9.08	-	-
	86.0	127.3	3.7	11.4	3	1.35	-	0.08	0.51	0.44	3.67	1.48	-	-
	86.0	127.3	3.7	11.4	6	2.22	-	0.32	2.05	1.77	5.01	2.95	-	-
	86.0	127.3	3.7	11.4	9	3.27	-	0.73	4.62	3.98	6.35	4.43	-	-
	86.0	127.3	3.7	11.4	12	5.58	-	1.30	8.21	7.07	7.68	5.90	-	-
	86.0	127.3	3.7	11.4	15	-	-	2.03	12.82	11.05	9.02	7.38	-	-
	86.0	127.3	3.7	11.4	18	-	-	2.92	18.47	15.91	10.36	8.85	-	-

<sup>1</sup> taken from Copur et al. (2003), <sup>2</sup> taken from Bilgin et al. (2006), <sup>3</sup> taken from Wang et al. (2018), \* converted using DIF

Table 4.8. Statistical analysis of the theoretical and prediction models

Data	Model	R <sup>2</sup>	MSE	Calculated t-value	Tabulated t-value (df*)	Significance F
(F <sub>C_mean</sub> )	Evans	0.522	14.4	9.01	1.99 (df=73)	1.8x10 <sup>-13</sup>
	Goktan	0.577	28.5	9.99	1.99 (df=73)	2.7x10 <sup>-15</sup>
	Roxborough & Liu	0.564	41.7	9.72	1.99 (df=73)	8.3x10 <sup>-15</sup>
	Model 1	0.363	9.1	9.90	1.99 (df=73)	3.8x10 <sup>-15</sup>
	Model 3	0.600	7.4	12.78	1.99 (df=73)	2.6x10 <sup>-20</sup>
(F <sub>C_peak</sub> )	Evans	0.507	213.0	7.18	2.01 (df=48)	3.8x10 <sup>-9</sup>
	Goktan	0.769	140.8	12.67	2.01 (df=48)	6.4x10 <sup>-17</sup>
	Roxborough & Liu	0.614	117.9	8.73	2.01 (df=48)	1.8x10 <sup>-11</sup>
	Model 2	0.593	28.3	10.24	2.01 (df=48)	1.2x10 <sup>-13</sup>
	Model 4	0.642	25.7	10.97	2.01 (df=48)	1.1x10 <sup>-14</sup>

\*df: the degree of freedom

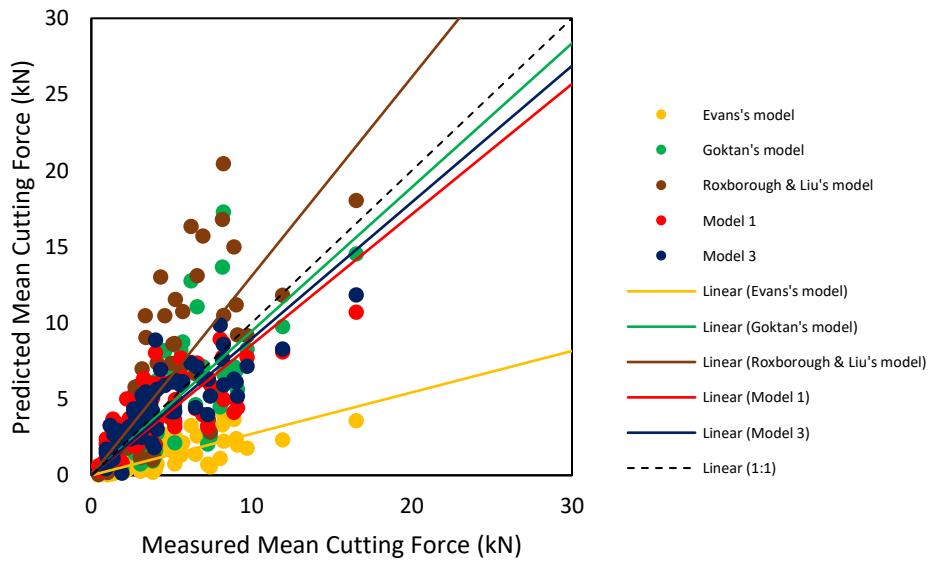


Figure 4.19. Relationship between measured and predicted mean cutting force of different models

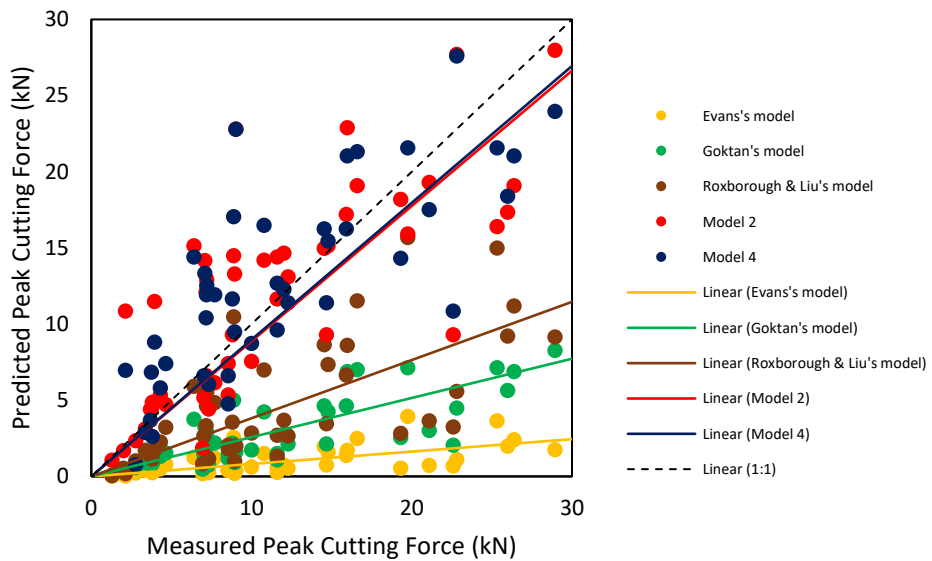


Figure 4.20. Relationship between measured and predicted peak cutting force of different models

Figure 4.19 shows the relationship between measured and predicted mean cutting forces of different models. Evan's model is underestimating the actual mean cutting force, while Roxborough & Liu's model is overestimating it. Among those models, it is seen that Goktan's model is the closest one to the 1:1 fitted line, followed by Model 3 and Model 1. However, according to the MSE calculation, Model 3 gives the lowest MSE compared to others (see Table 4.8). It implies that Model 3 has better fitness with the given database.

Figure 4.20 presents the relationship between measured and predicted peak cutting force of different models. Only two models proposed in this study are close to the 1:1 fitted line, while the other models give a lower force prediction of the actual peak cutting force. Model 4 results in a lower MSE value compared to Model 2 (see Table 4.8). Thus, it can be

implied that Model 4 performs better to predict the actual peak cutting force.

It should be noted that the proposed models were developed from various rocks with the UCS ranging from 6 - 174 MPa, and BTS ranging from 0.2 – 12 MPa. So, it is suggested that the proposed models are only reliable for predicting cutting forces within those given ranges.

#### **4.7 Strain Rate Determination During Cutting Process**

To estimate the strain rate during the cutting process, three attempts were made: (1) calculation from the technical data sheet, (2) direct measurement from laboratory linear cutting test, and (3) numerical simulation of the linear cutting test.

##### **4.7.1 Calculation from the Technical Data Sheet of the Machine**

The first attempt to begin the strain rate estimation in the cutting process was by using the technical data specification combined with a simple laboratory test. In this approach, some specifications or rock cutter machines were accessed, precisely their cutter head speed information. The speed of the cutter head is physically related to the speed of a cutter when the cutter attacks the excavated rock. In other words, it can be implied that the cutter head speed is physically related to the speed of the loading piston of the uniaxial compression test in a scaled-down laboratory case.

In that regard, a relationship between loading speed and strain rate occurred on the sandstone specimen surface under the uniaxial compression test was made, as shown in Figure 4.21. The test was

performed by a hydraulic servo-controlled loading machine on 13 sandstone specimens with the various loading speed from 0.25 to 30 mm/s (see Figure 4.21(a)). The strain rate was calculated from the axial strain history plot, as shown in Figure 4.21(b).

Taking from some machine technical specification sheets, the typical cutter head speed of a roadheader is calculated to be 1.4 m/s (Sandvik MH620, Sandvik MT720, and Voest-Alpine AHM105) and can reach up to 2.3 m/s (Wirth T3.20). By inputting the linear speed to the equation provided in Figure 4.21(a), the strain rate can be obtained in the range of  $0.76 - 1.03 \text{ s}^{-1}$ .

For the TBM case, the rotational speed of the 6.57 m diameter of TBM used in Kozyatagi-Kadikoy Metro Tunnel in Istanbul Turkey was 1.6 – 5.5 rpm and that of the 14.4 m TBM diameter used in Waterview Tunnel in Auckland New Zealand was 1.9 rpm (Bilgin et al., 2014). Concerning their diameters (outer diametral cutter position), the linear speed of the cutter head can be calculated as 0.55 – 1.89 m/s for the Turkey case and 1.43 m/s for the New Zealand case. Again, referring the relationship in Figure 4.21(a), the strain rate in these TBM case range would be about  $0.43 - 0.91 \text{ s}^{-1}$ . The recap of the calculation is presented in Table 4.9. The results of this simple approach indicate that the rock cutting process might belong to the ISR range, which was hypothetically expected.

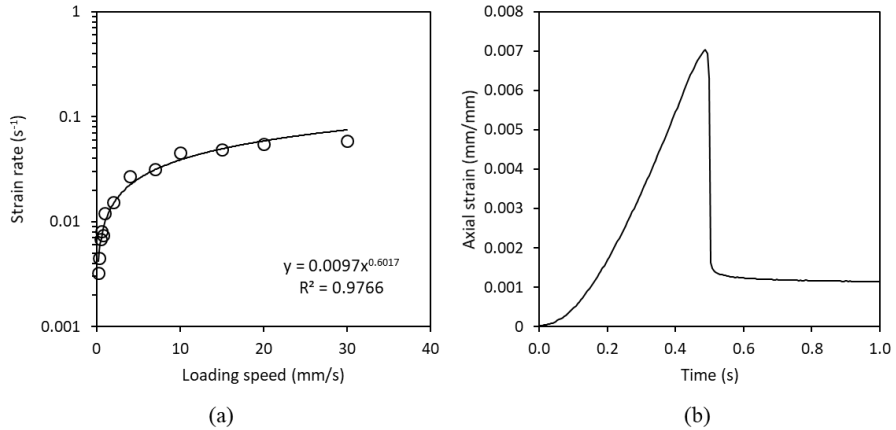


Figure 4.21. (a) Relationship between strain rates occurred on the sandstone surface and loading speed of the piston in uniaxial compression test, (b) the typical axial strain history plot

Table 4.9. Strain rate estimation from operational data of several cutting machines

No	Cutting Machine	Linear cutting Speed	Strain Rate	Classification
1	Sandvik Roadheader Hardrock MH620	1.4 m/s	0.76 s <sup>-1</sup>	ISR
2	Sandvik Roadheader Tunnelling MT720	1.4 m/s	0.76 s <sup>-1</sup>	ISR
3	Voest-Alpine Hard Rock Miner AHM 105	1.4 m/s	0.76 s <sup>-1</sup>	ISR
4	Wirth Roadheader T3.20	1.15-2.32 m/s	0.67-1.03 s <sup>-1</sup>	ISR
5	TBM (Kozyatagi-Kadikoy Metro Tunnel Project, Turkey)	1.6-5.5 rpm / 0.55-1.89 m/s (Ø=6.57 m)	0.43-0.91 s <sup>-1</sup>	ISR
6	TBM (Waterview Tunnel, Owairaka, New Zealand)	1.9 rpm / 1.43 m/s (Ø=14.4 m)	0.77 s <sup>-1</sup>	ISR

#### 4.7.2 Direct Measurement from Linear Cutting Test

To follow up on the evidence from the earlier sub-chapter, a set of linear cutting tests were prepared to estimate the strain rate level that occurs

during the cutting process. The estimation would give us information to investigate in what dynamic level the cutting process is. Three scenarios were conducted in this experiment: disc cutter on a granite, pick cutter on a sandstone, and disc cutter on a mixed ground material.

#### *4.7.2.1 Disc Cutter on Granite*

Disc cutter predominantly attacks rock surface by indentation that allows the normal/thrust force to initiate the rock breakage. A new portion of a cutting tool will always indent a new portion of the rock surface in a rapid condition, which is a dynamic process. In a non-ideal condition, the surface roughness of the rock may create undulation on the rolling disc that also leads to a series of dynamic events. Moreover, based on observation, even in a flat and smooth rock surface, a series of noticeable dynamic events still occur, especially when some portion of the rock is chipped.

In that regard, strain rate estimation during the cutting process by disc cutter was conducted on a granite rock sample. A small-scale disc cutter with a diameter of 0.1 m was used. Before the cutting, two biaxial strain gauges were placed next to the potential cutting groove: 1 cm on the side at the halfway of the groove and 1 cm at the end of the groove (see Figure 4.22). Since the strain gauge used is a biaxial type, the strain was measured parallel and perpendicular to the cutting line. The test was repeated four times in the same cutting line with the penetration depth of 0.5 mm in each cut. The linear cutting speed was set to 14 mm/s (equal to 2.7 rpm at the diameter of 0.1 m), which is the maximum speed available on the SLCM system. Strain value was continuously recorded

by the DAQ system and stored on a personal computer. The setting of the test is depicted in Figure 4.22.

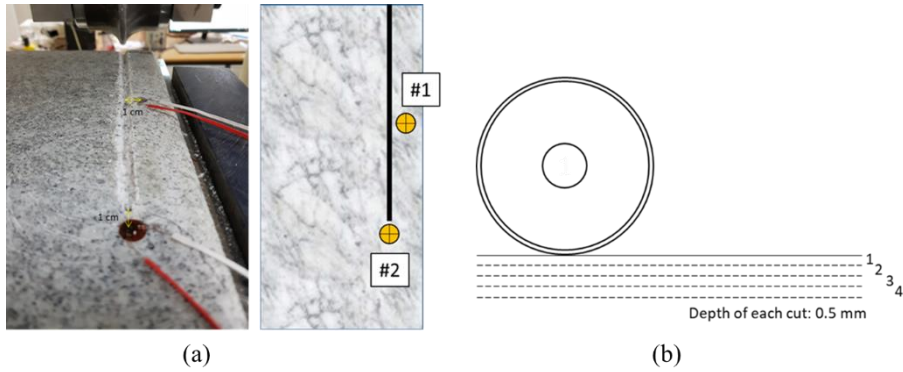


Figure 4.22. Strain rate determination during cutting by a disc cutter on a granitic rock. (a) strain gauge position, and (b) penetration depth scenarios

The strain rate was estimated from the strain-time plot. It is calculated from the slope of the first sudden change of the strain over time for each strain gauge (see Figure 4.23). The results of strain rate estimation in each cut are shown in Table 4.10. The results show that the obtained strain rate ranged from  $2.4 \times 10^{-5}$  to  $2.1 \times 10^{-2} \text{ s}^{-1}$ .

Table 4.10. Results of strain rate estimation of disc cutting on granite rock

Strain gauge location	Cut 1	Cut 2	Cut 3	Cut 4	
#1	Parallel	$4.2 \times 10^{-4}$	$6.7 \times 10^{-4}$	$1.1 \times 10^{-3}$	$2.7 \times 10^{-3}$
	Perpendicular	$1.2 \times 10^{-3}$	$1.8 \times 10^{-3}$	$8.5 \times 10^{-4}$	$2.6 \times 10^{-3}$
#2	Parallel	$2.4 \times 10^{-5}$	$7.3 \times 10^{-4}$	$1.9 \times 10^{-3}$	$2.1 \times 10^{-2}$
	Perpendicular	$1.7 \times 10^{-4}$	$2.6 \times 10^{-4}$	$1.0 \times 10^{-3}$	$4.5 \times 10^{-3}$

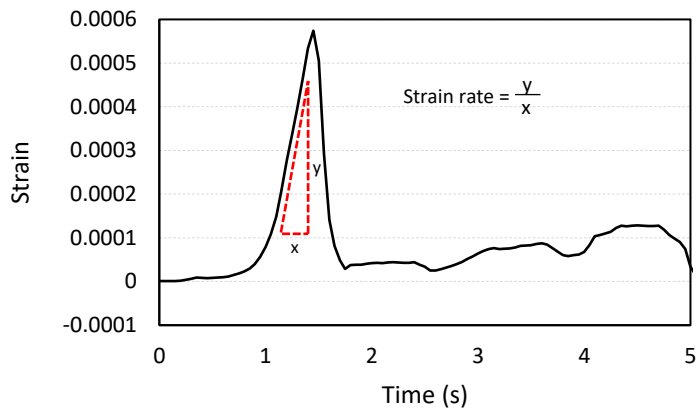


Figure 4.23. Example of strain rate calculation (cut 3, strain gauge #1, parallel to the cutting line)

#### 4.7.2.2 Pick Cutter on Sandstone

The second experiment was by performing pick cutting on a sandstone material. In mechanical excavation practice, a high rotational speed of the cutter head, where the picks are attached, will create an impact when they attack a rock surface. The interaction between the pick and the rock surface is physically a dynamic event. Moreover, the dynamic events might be intensified in case of attacking rough rock surface or coarse-grained material that has a high strength contrast between matrix and its fragment.

A sandstone block was placed inside the specimen box. Thirteen lines were drawn on the surface of the rock. Two biaxial strain gauges were attached on the front surface (#1) and the top surface (#2) of the rock (see Figure 4.24). However, to observe strain rate level during impact events, only strain gauge #1 was reported because gauge #1 was glued on the same face with the impact interaction between tool and rock (the initial cut). The lines on the top surface were numbered based on the

distance between lines and the strain gauge (from 2 cm to 26 cm with 2 cm interval). The cutting condition for the test was: 100 mm cutting distance, 10 mm penetration depth, and 14 mm/s cutting speed. The cutting test started from the farthest to the nearest lines from the monitoring point. The strain was continuously recorded for each cut.

The strain rate was calculated from the strain history plot, in the same manner with the procedure described in the previous sub-chapter. The typical strain history plot during cutting can be seen in Figure 4.25(a). The strain rate values for each test were plotted against the monitoring distance. Since the strain gauge type is a biaxial gauge, and it is glued on the front surface; thus, from the front view, the strain component is divided into a vertical and horizontal direction.

Figure 4.25(b) shows that the strain rate value increases as the distance from the monitoring point decreases. The maximum strain rate obtained was  $8.48 \times 10^{-4} \text{ s}^{-1}$  monitored at 2 cm away from the impact cutting point.

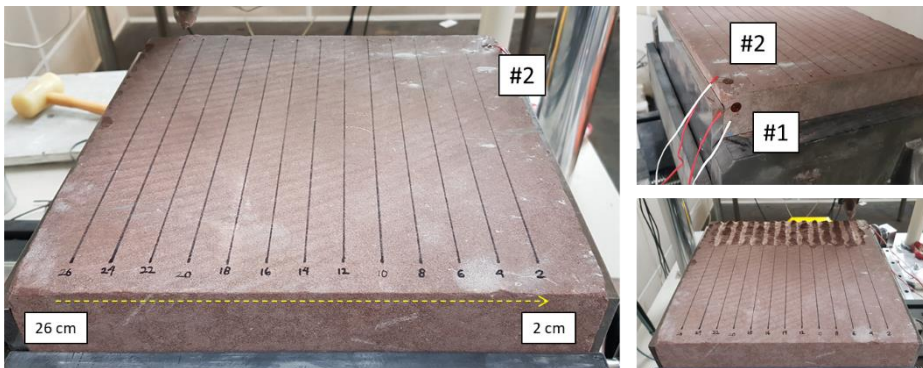
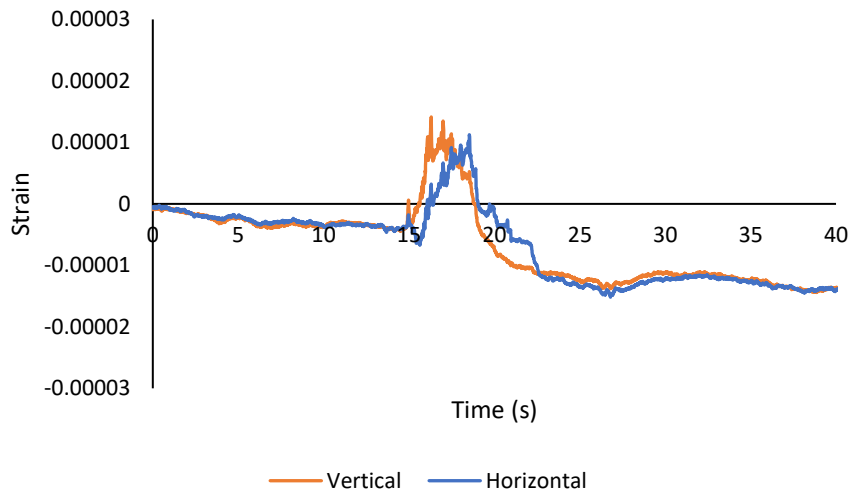
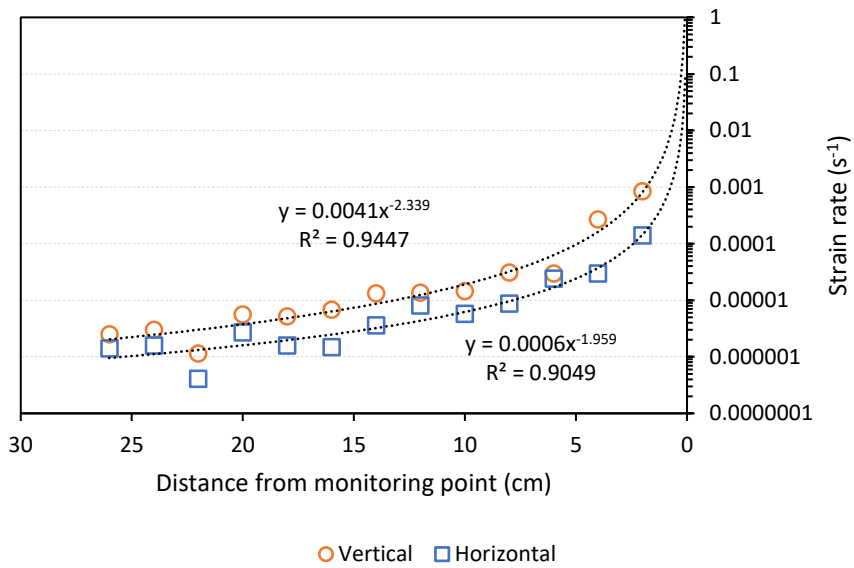


Figure 4.24. Strain rate determination in cutting by a pick cutter on a sandstone rock



(a)



(b)

Figure 4.25. (a) Typical strain history plot; (b) the relationship between strain rate and monitoring distance during cutting by a pick cutter on a sandstone

#### *4.7.2.3 Disc Cutter on Mixed Ground Material*

For the third experiment, the cutting test was done by performing disc cutting on a mixed ground surface. In mechanical excavation practices, the appearance of the mixed ground surface is likely to be dealt with. The main feature of this type of surface is the property contrast between the matrix and its fragments, i.e., strength contrast, as the most obvious one. The strength contrast on the surface might create bounces during rock-tool interaction. The bounces transfer the constant thrust load into a series of dynamic loads throughout the cutting process.

A mixed ground block was made from a mixture of 4:1 cement to water ratio with an arrangement of gravel material on its surface. At first, the gravel fragments were arranged at the bottom of a steel molding box before the mixture cement was poured into it. The mixed ground block was taken away from the molding box after it cured. The block was then placed at the specimen box of the SLCM upside down, so the arranged gravels were on the upper surface of the block.

A biaxial strain gauge was carefully glued on the gravel surface. The distance of the strain gauge to the anticipated cutting line was 1 cm. The cutting test was performed with a 5 mm penetration depth and 14 mm/s cutting speed (the maximum speed of the machine). The strain rate was calculated from the strain history plot, in the same manner with the procedure described in the two previous experiments.

The test is depicted in Figure 4.26. The strain rate obtained from this cutting test was  $3.6 \times 10^{-3}$  and  $7.8 \times 10^{-3} \text{ s}^{-1}$  for parallel and perpendicular directions to the cutting line, respectively.

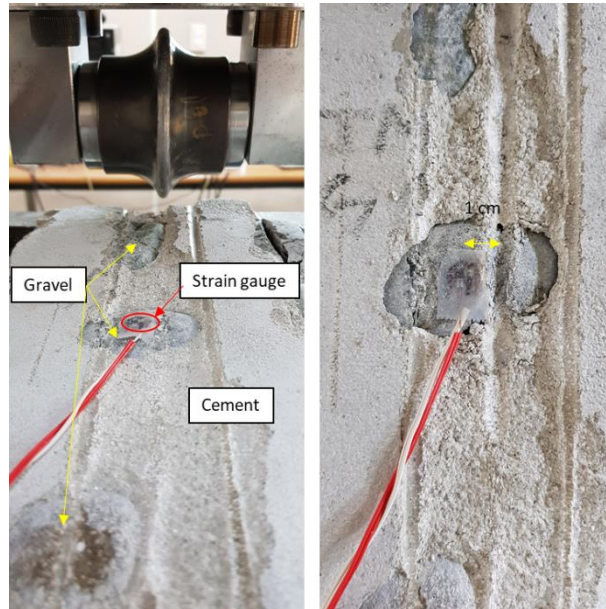


Figure 4.26. Strain rate determination in cutting by a disc cutter on a cement-gravel mixed ground

#### 4.7.2.4 Results and Limitations of the Tests

From those three experiments based on laboratory linear cutting tests, it showed that the result failed to reach the expected strain rate target to be happening during the cutting process. All the results were found to be below  $10^{-1} \text{ s}^{-1}$ , the lower limit of the ISR range.

It should be noted that the tests had some limitations to represent what happens during the cutting process. First, we could not obtain an averaged value from multiple strain gauges during cutting. The number of strain gauges used in the tests was limited to a maximum of two biaxial strain gauges (four outputs) due to the limited input channel of the data acquisition system by having only four channels available for strain measurement. However, based on a trial test conducted before the actual

test with two strain gauges attached linearly, the strain rate obtained from a cutting test shows a relatively close value.

Second, the monitored points where strain gauges were attached had some distances from the actual tool-rock interaction zone. The closest monitoring point where the strain gauges were attached was 1 cm from the cutting line, and they were glued on the surface of the rock, not in the vicinity of the tool-rock interaction region. The hypothesis is, beneath the tool-rock interaction zone, the strain rate would be significantly higher than on the surfaces aside from the cutting line. Direct measurement beneath the cutter, however, is technically not possible.

Third, the test was done at a relatively slow speed, with only 14 mm/s. This speed is far lower than the one performed by cutting head in the field practice. For example, the Sandvik Roadheader Hardrock MH620 has a linear cutting speed of 1.4 m/s (Sandvik). Such speed levels cannot be accommodated by the SLCM in the lab.

These limitations mentioned above would be accommodated by a numerical simulation approach, which is explained in the following section.

### **4.7.3 Numerical Modeling of Linear Cutting Test**

To overcome the limitations of strain rate estimation during the cutting process addressed in the previous sub-chapter, an FEM based numerical model was built. By using FEM numerical simulation, the actual cutting speed and intended monitoring gauge location for detecting strain rate levels can be simulated.

Prior to the simulation, a numerical calibration was performed. The case of pick cutter cutting on sandstone (sub-chapter 4.7.2.2) was selected. The strain rate values at the distance of 2 cm and 4 cm from the impact interaction between the cutting tool and the rock (front surface) were compared. The calibration process is depicted in Figure 4.27, and the calibration result is presented in Table 4.11. The results show that the strain rates obtained from the laboratory test and FEM simulation are comparable, showing the values are relatively at the same order.

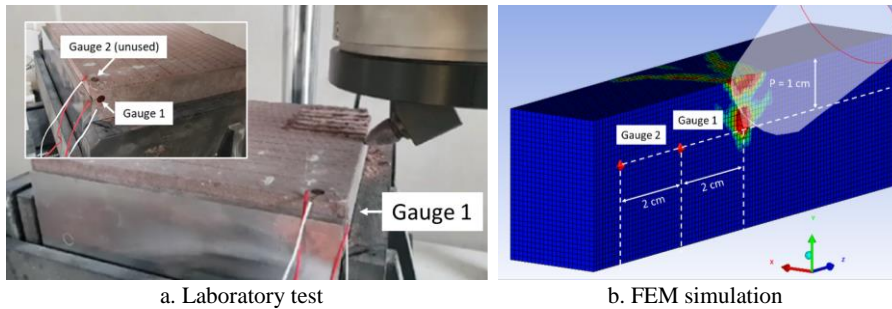


Figure 4.27. Configuration of the strain rate measurement calibration process between laboratory and FEM simulation

Table 4.11. Strain rate measured at 2 cm and 4 cm from the cutting line resulted by laboratory LCM test and FEM simulation

Distance from cutting line	Strain direction	Laboratory LCM	FEM simulation
2	Vertical	$8.48 \times 10^{-4}$	$9.90 \times 10^{-4}$
2	Horizontal	$1.40 \times 10^{-4}$	$1.02 \times 10^{-3}$
4	Vertical	$2.67 \times 10^{-4}$	$7.63 \times 10^{-4}$
4	Horizontal	$2.96 \times 10^{-5}$	$8.93 \times 10^{-4}$

After calibration, strain rate measurement during a cutting process was performed. Fifty virtual gauges were pointed in the rock model in the

position relatively underneath the moving pick cutter. Five various vertical distances were set from 0 mm to 4 mm (interval 1 mm) below the cutter tip level. The pick cutter was moved to attack the rock with a penetration depth of 5 mm and a constant speed of 1.4 m/s (representing the actual linear speed) (see Figure 4.28).

The gauges recorded strain rate value in x (cutting), y (normal), and z (side) directions. All the strain gauge values were averaged based on strain direction and their vertical distance from the tip of the pick cutter. During the cutting process, the gauges No. 1 to 10 were destroyed and displaced from their original position. In consequence, the strain rate values obtained from them were considered invalid and discounted from the calculation.

The simulation shows that the strain rate value is inversely correlated with the distance of the gauges from the cutting groove in all directions. The strain rate values range from  $1.44 \text{ s}^{-1}$  to  $24.10 \text{ s}^{-1}$  calculated from all strain gauges in all directions (see Table 4.12). The plot of the result shows, in Figure 4.29, that most of the strain rate values are captured inside the ISR range (shaded area). This simulation result appears to be one of the signs that the rock cutting process belongs to the ISR loading state.

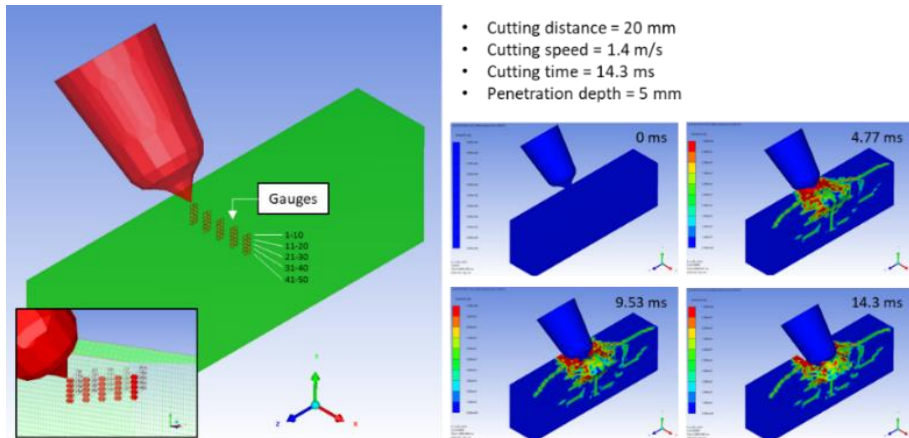


Figure 4.28. Model configuration for strain rate level detection during cutting

Table 4.12. Averaged strain rate from FEM cutting simulation

Gauge ID	Distance (mm)	Averaged strain rate (/s)		
		x-direction	y-direction	z-direction
1-10	0	<i>Excluded</i>		
11-20	1	17.6	24.1	15.9
21-30	2	13.5	6.8	3.9
31-40	3	8.6	9.4	2.3
41-50	4	7.6	4.5	1.4

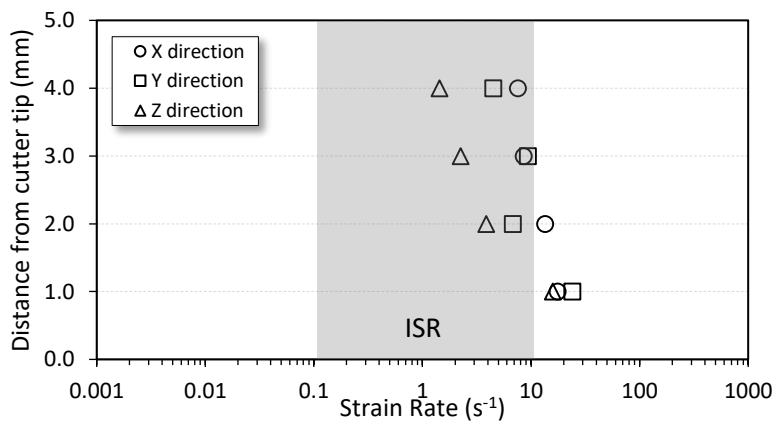


Figure 4.29. Averaged strain rates values recorded in various distance from cutting tip using FEM simulation

#### **4.7.4 Recapitulation of the Strain Rate Determination in Cutting Process**

Three attempts have been made to figure out the dynamic level in the cutting process: technical data sheet information, direct measurement in the laboratory, and numerical simulation. The results of those attempts can be summarized in Figure 4.30.

Based on the simple calculation from the technical data sheet, the results showed that the cutting process of typical roadheader and TBM belongs to the ISR range. It should be accepted that the attempt was rough, the fact that only the linear speed of the cutter head movement was considered in the calculation. However, it was still a piece of invaluable information to be reviewed.

From the laboratory linear cutting test, all three cases resulted in strain rate values below the target ISR range. This attempt had various limitations, so it could not thoroughly represent the field cutting condition. The cutting speed used in the experiment was slow compared to the actual machine speed. Indeed, higher speed cutter movement would result in more aggressive interaction between rock and cutting tools, thus deliver more dynamic phenomenon. Also, the strain rate would be much higher if there was a way to monitor the strain changes beneath the rock-tool interaction zone, which was almost impossible to be carried out in the laboratory linear cutting test.

Numerical simulation by the finite element method managed to deal with all the limitation occurred in the laboratory test. The cutting speed was significantly faster, referred to as the typical linear speed of the cutter head of a roadheader. Multiple virtual strain gauges were placed right underneath the cutting line to monitor the strain rate as close as possible

to the rock-tool interaction zone. By this approach, most of the strain rate values stretched in the ISR range, regardless of their directions.

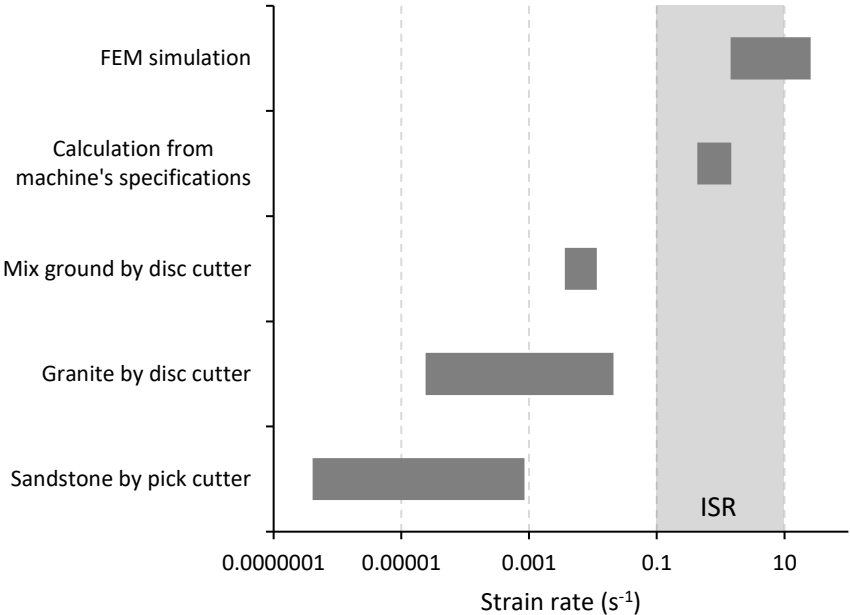


Figure 4.30. Determination of strain rate level in cutting process

## 5. ABRASIVENESS TEST

### 5.1 Introduction to Abrasiveness Test

Assessment of rock abrasiveness is crucial when dealing with mechanized excavation in various mining and civil works. The abrasiveness of excavated rocks controls the wear amount of cutting tools; therefore, it has a significant impact on the service life and efficiency of the tools. In practice, cutting tools are subjected to a dynamic load in which the tools interact with the rock at high-speed velocity and unpredictable angle of occurrence.

The most widely used and successful method to assess rock abrasiveness in civil and mining fields is the Cerchar abrasiveness test. The test has been discussed intensively elsewhere, covering the test methods, factors affecting the result, and some engineering applications (Hamzaban et al., 2014; Ko et al., 2016; Lee et al., 2013; Plinninger et al., 2004; Rostami et al., 2014). However, the Cerchar test is performed relatively in a static environment with a constant load, a short scratch length, and a slow linear pin movement. It is conceivable that the available procedure of the Cerchar abrasiveness test does not replicate the actual field condition with its dynamic attributes.

To address the issue mentioned above, this study discusses the other abrasiveness test that incorporates dynamic features introduced by Golovanevskiy and Bearman (2008). The test is called the Gouging abrasiveness test, and the quantifying property is called the Gouging abrasiveness index ( $G_i$ ). The method and testing apparatus allow the pin/stylus to interact with the rock surface in high-speed gouging/sliding

impact abrasiveness mode, which imitates the process that is experienced by cutting tools in the field.

A modification to an available impact testing machine was done to accommodate the standard procedure of the Gouging abrasiveness test. The original purpose of the impact testing machine is to perform Charpy impact test. The Charpy impact test is one of the standard tests in material engineering, mainly polymers, ceramics, and metal-based materials. The purpose of the test is to determine the amount of energy absorbed by a v-notched material during fracture under a high strain rate impact test. The main feature of the Gouging test is similar to the Charpy test except for the way that the tool mounted on the swinging pendulum interacts with the tested specimen. The Charpy produces a full impact on the specimen while the Gouging creates a sliding impact that allows a sharpened-pin to scratch the surface of the tested specimen. Before the modification of the machine for the Gouging test purpose, a preliminary work on the Charpy test was conducted to check the strain rate that occurred caused by the impact of the pendulum.

Two types of abrasiveness tests, i.e., Gouging and Cerchar, were performed to various rock types. The basic physical and mechanical properties of the rock samples were estimated, and the effects of them on the abrasiveness properties were evaluated.

## **5.2 Preparation of the Testing Apparatus**

### **5.2.1 Strain Rate Determination in the Charpy Test**

To test the possibility of the machine to be used for the high-rate scratch test, strain rate measurement in a standard Charpy test was performed.

The tests were subjected to two types of material: granite and polymethylmethacrylate (PMMA). Specimens were shaped according to ASTM standard by having 55 mm length, 10 mm width, 10 mm thickness, 2 mm v-notch depth, and 45° v-notch angle (ASTM, 2007).

A strain gauge was attached on the front surface, next to the area where the specimen would be impacted by the hammer (opposite side from where the v-notch was made). The strain gauge was connected to the data acquisition system, and the strain history curve of each test was recorded. The strain rate value was calculated from the strain history curve. Necessary information about the test is depicted in Figure 5.1.

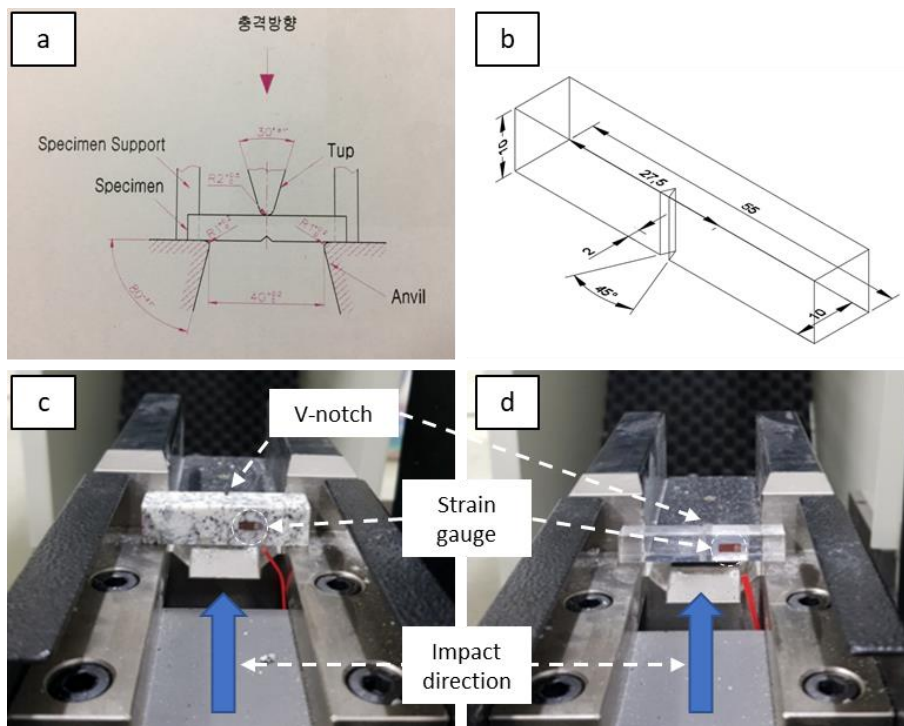


Figure 5.1. Charpy impact test. a) primary mechanism; b) specimen dimension; c) test on granite; and d) test on PMMA

Table 5.1 shows the results of repeated Charpy tests on PMMA and granite specimens. The energy was calculated from the energy potential principle, which was derived from the hammer height different before and after impacting the tested sample, as mentioned in Eq. 5.1.

$$E_{p1} - E_{p2} = m \times g \times h_1 - m \times g \times h_2 = \text{absorbed energy} \quad (5.1)$$

where  $m$  is the hammer mass (kg),  $g$  is gravity acceleration ( $\text{m/s}^2$ ), and  $h_1$  and  $h_2$  is the hammer height (m) before and after hitting the tested sample, respectively. The impact strength was calculated from the energy value divided by the actual cross-sectional area of the specimen.

Table 5.1. Charpy impact test results including strain rate information

Sample	No.	Energy (J)	Impact strength ( $\text{kJ/m}^2$ )	Strain rate ( $\text{s}^{-1}$ )
PMMA	1	0.426	5.32	0.69
	2	0.426	5.32	6.27
	3	0.426	5.32	3.21
	4	0.426	5.32	0.99
	5	0.426	5.32	7.14
Granite	1	3.013	19.81	0.57
	2	1.713	11.12	7.89
	3	0.639	4.18	0.54
	4	2.578	16.97	7.66
	5	3.013	19.41	6.9
	6	3.013	19.41	6.01

The strain rate value, which was calculated from the strain history plot, is also shown in Table 5.1. The strain rate values measured adjacent to the impact zone for PMMA and granite samples range from  $0.69 - 7.14 \text{ s}^{-1}$  and  $0.54 - 7.89 \text{ s}^{-1}$ , respectively. The results imply that the strain rate level under Charpy impact testing might be included in the ISR range

( $10^{-1} - 10^1 \text{ s}^{-1}$ ). Thus, this information was used as a foundation to use the apparatus for the dynamic scratch test. This result is quite similar to Costin (1981), who investigate the fracture toughness of an oil shale using a Charpy impact machine at the ISR loading (Zhang & Zhao, 2014a).

### **5.2.2 Impact Testing Machine Modification**

The impact testing machine available in the laboratory was used initially to perform the Charpy test. The apparatus consists of a pendulum hammer with defined mass and length that is swung from a known height to impact the tested specimen. The pendulum hammer weight is about 20.6 kgf with a typical striking velocity of 5.3 m/s when it is impacting to the specimen from  $154.6^\circ$  pendulum angle from the vertical.

Having known that strain rate tested by the machine matched the target, the machine was modified for a dynamic scratch test purpose, namely, Gouging abrasiveness test. The basic concept of the modification followed the original reference that was explained by Golovanevskiy and Bearman (2008). There were two parts of the machine that needed to be redesigned from the current impact testing machine, i.e., sample holder and pendulum hammer.

The main features of the new sample holder are a rock sample fastener and a spring-loaded system (Figure 5.2). The specimen can be locked in position by a pair of bolts. The spring-loaded system allows the specimen to move aside when the moving pendulum hits the locking bolt. The side movement prevents the sample from scratch when the pendulum swings back after reaching the highest point. Thus, secondary scratching can be avoided. The pendulum part was modified to be able to hold the pin

securely. Since the pin is replaced for every test, the design of the pin holder allows the pin to be attached and detached easily.

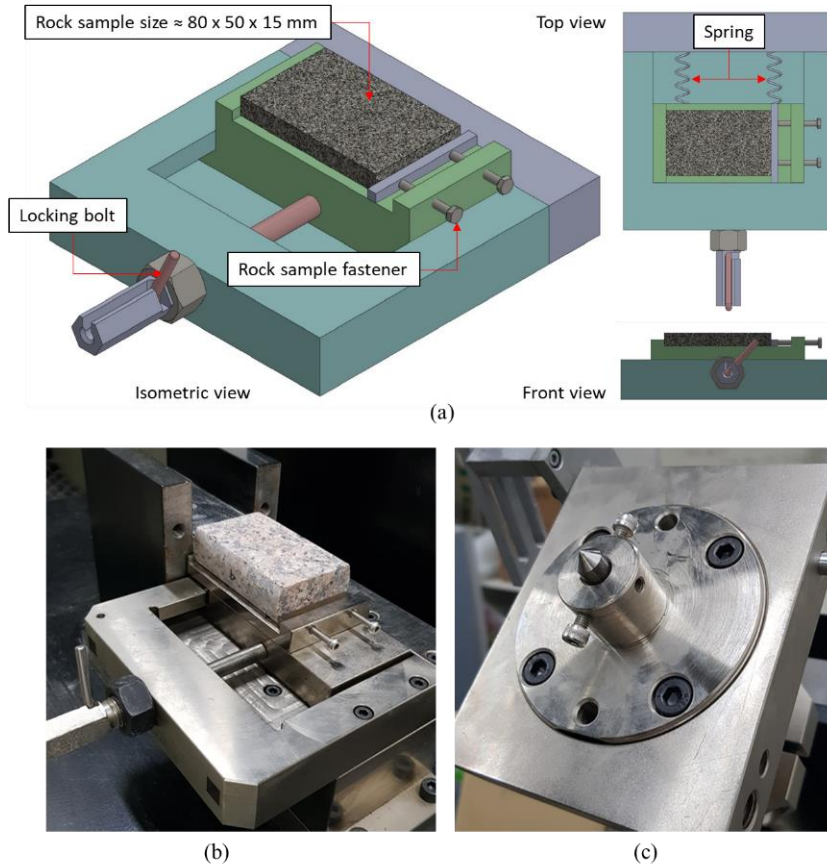


Figure 5.2. Machine modification. (a) schematic design of sample holder; the real picture of (b) sample holder; and (c) pin holder

### 5.3 Rock Sample

The tests were subjected to fourteen rock samples, mostly from Korea except for one sandstone from China. The rock types include granite, limestone, sandstone, diorite, gabbro, granodiorite, dolomite, and shale. Before the scratch test, physical and mechanical properties were

examined to obtain the basic properties of the rock. Also, the rock samples were subjected to x-ray diffraction (XRD) analysis to quantify the mineral composition of the rocks. The information on the rock type, location, and mineral composition is provided in Table 5.2.

Table 5.2. Type, location, and mineral composition of rock samples used in the Gouging and Cerchar abrasiveness tests

No	Rock Type	Location	Mineral composition	Appearance
1	Granite 1	Korea Jeollabuk-do Hwangdeung	Quartz: 35.4 % Albite: 34.9 % Microcline: 20.8 % Biotite: 8.9 % Magnetite: 0 %	
2	Granite 2	Korea Jeollabuk-do Jinan	Quartz: 37.6 % Albite: 35.4 % Microcline: 17.8 % Biotite: 7.1 % Magnetite: 2 %	
3	Granite 3	Korea Gyeonggi-do Pocheon	Quartz: 31 % Albite: 30.2 % Microcline: 27.9 % Orthoclase: 10.9 % Biotite: 0 %	
4	Granite 4	Korea Gyeongsangbuk-do Sangju	Microcline: 35.7 % Albite: 34.8 % Quartz: 29.5 % Biotite: 0 % Chlorite: 0 %	
5	Granodiorite porphyry	Unknown	Albite: 44.2 % Quartz: 29.4 % Orthoclase: 13.9 % Biotite: 6.8 % Hornblende: 5.1 % Magnetite: 0.7 %	
6	Diorite	Korea Jeollanam-do Goheung	Albite: 49.3 % Orthoclase: 21.6 % Hornblende: 11.4 % Quartz: 7.5 % Biotite: 5.3 % Magnetite: 4.9 %	

No	Rock Type	Location	Mineral composition	Appearance
7	Gabbro	Korea Gyeongsangnam- do Hamyang	Albite: 53.4 % Diopside: 25.4 % Biotite: 14.3 % Magnetite: 4.6 % Quartz: 2.4 %	
8	Limestone 1	Korea Chungcheongnam -do Geumsan	Calcite: 100%	
9	Limestone 2	Korea Chungcheongnam -do Geumsan	Calcite: 99.4 % Quartz: 0.6 %	
10	Limestone 3	Korea Chungcheongnam -do Geumsan	Calcite: 92.7 % Dolomite: 7.3 %	
11	Sandstone 1	China Linyi	Albite: 42.2 % Quartz: 38.3 % Orthoclase: 10.7 % Hematite: 3.3 % Laumonite: 3 % Calcite: 1.7 % Montmorillonite: 0.7 %	
12	Sandstone 2	Korea Chungcheongnam -do Boryeong	Quartz: 52.8 % Muscovite: 23.6 % Albite: 19.7 % Orthoclase: 2.6 % Calcite: 1.3 %	
13	Shale	Korea Chungcheongnam -do Boryeong	Muscovite: 46.4 % Quartz: 41 % Chlorite/Clinochlore: 12.6 %	
14	Dolomite	Unknown	Dolomite: 86.8 % Hornblende: 7.9 % Calcite: 5.3 %	

To fit with the sample holder in the impact scratch machine, a brick-shaped specimen with a dimension of about 80 mm x 50 mm x 15 mm was required. It was cut from an NX size core sample (diameter of 54 mm), which was carefully ground on four of its sides to form a rectangular-shaped and so that the specimen was also polished. For the Cerchar test, the sample was core shaped specimen with 54 mm of diameter and about 60-80 mm of height. The top and bottom surfaces of the core were ground to ensure the surface smoothness and flatness during the test. The typical specimens for both tests are shown in Figure 5.3.



(a)



(b)

Figure 5.3. Representative specimen for (a) Gouging and (b) Cerchar abrasiveness tests

## 5.4 Wear Tool (Pin)

Wear tool, often called as a pin, has a diameter of 10 mm with a 90° tip angle in one of its ends. The pin was made of hardened steel with specific Rockwell Hardness of HRC 55, as suggested by the ISRM standard for the Cerchar test (Alber et al., 2014).

The pin was checked under a microscope to ensure that the point of the stylus was undamaged before the use. In practice, some pin might be in a slightly imperfect condition, so any pin showing damage greater than 5  $\mu\text{m}$  was rejected, as recommended by Al-Ameen and Waller (1994). The standard pin used in this study is shown in Figure 5.4.

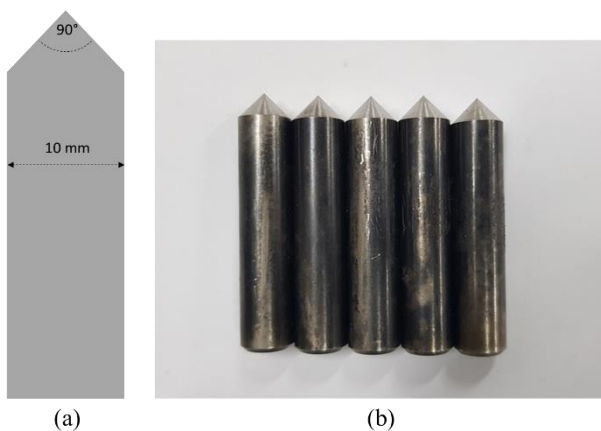


Figure 5.4. The wear tool (Pin); (a) schematic design and (b) real picture

## 5.5 Test Procedure

### 5.5.1 Gouging Abrasiveness Test

The necessary procedure of the test followed the one proposed by Golovanevskiy and Bearman (2008). However, some modifications to

the original were made to fit with laboratory conditions. For example, in the reference, height adjustment was set by vertical transmission screw, while in this study, a dedicated thin plate with a predetermined thickness was used in sample height adjustment.

The complete procedure of the Gouging abrasiveness test is mentioned below.

- The specimen is clamped securely in the holder.
- The pin is fixed in its holder when the pendulum arm is in vertically neutral position (ensure there is no contact between sample and pin at this moment).
- The pin holder is loosened up to allow the pin to make gentle contact with the sample, and then tighten up again.
- Pendulum arm is raised to the initial position and ensured that it is locked.
- A 1-mm thin plate is placed under the specimen, so the specimen is raised by 1 mm. The test is ready at this moment.
- The pendulum is released, and the conical tip of the pin scratches the rock sample surface.
- The pendulum will continue to travel past the rock sample and swinging back after reaching the highest point.
- Immediately after the pin disengages from contact with rock surface, the sample holder is quickly moved horizontally (perpendicular to the swinging path) by the spring-loaded mechanism to ensure no secondary contact due to return swing.
- Pendulum arm is stopped, and the pin is taken out for inspection

- Rock sample position is adjusted to provide a fresh surface for the next scratch, and the sample holder is reinstalled in its working position.
- The scratching is conducted three times for each rock type with a new and sharpened wear tool in each of the scratch.

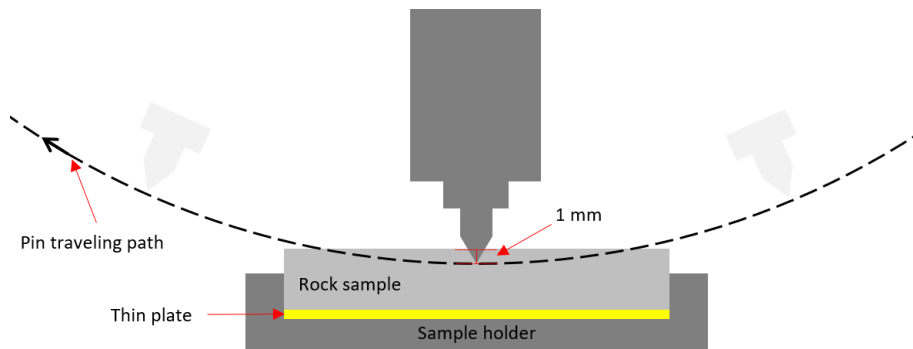


Figure 5.5. Testing procedure showing rock and pin interaction during scratching

In practice, a minimum of three scratch tests should be done on a single rock sample (Golovanevskiy & Bearman, 2008). Each of the tests used a new pin and a new wear surface. Wear flat diameter was measured under a microscope with an accuracy of  $0.01 \mu\text{m}$  (see Figure 5.6). The wear flat diameter for a pin was measured twice in an orthogonal direction. It should be noted that the calibration process was carefully performed before the measurement (see Figure 5.7).

Gouging abrasiveness index ( $G_i$ ) is calculated as the average mean of the wear flat diameter of the pin (in millimeter) multiplied by a factor of 10, as presented in Eq. 5.2.

$$Gi = \frac{1}{n} \sum_{i=1}^n d_i \times 10 \quad (5.2)$$

where  $d_i$  and  $i$  denote as the individual diameter of wear flat and the number of wear flat measurement, respectively.

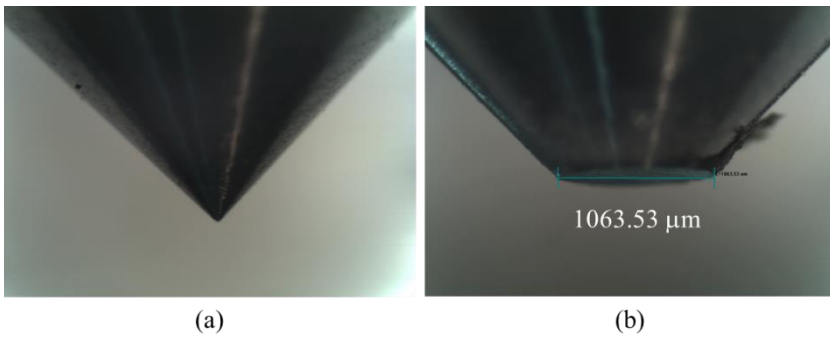


Figure 5.6. The pin under the microscope; (a) before, and (b) after the Gouging abrasiveness test



Figure 5.7. (a) Calibration ruler, and (b) calibration process under microscope

### 5.5.2 Cerchar Abrasiveness Test

There are two distinct mechanisms in the Cerchar test; the original Cerchar developed by Valantin (1973) and the modified design updated

by West (1989). The apparatus used in this study adopted the West mechanism, as the rock sample moved slowly by screw feed beneath a fixed pin (See Figure 5.8(a)).

The rock sample was clamped firmly in the sample jig. The specification of the pin was similar to the pin used in the Gouging test. The pin was attached to the pin holder and was carefully lowered onto the rock surface to avoid initial damage at the tip of the pin. The length of the scratch was precisely 10 mm per line, with the test duration about 10 seconds per line. After each test, the pin was carefully lifted from the rock surface for examination under a microscope. A new pin was used for the next test. A minimum of five lines per sample was made with two lines scratched perpendicularly to the other three lines. So, five new pins were used for each rock type.

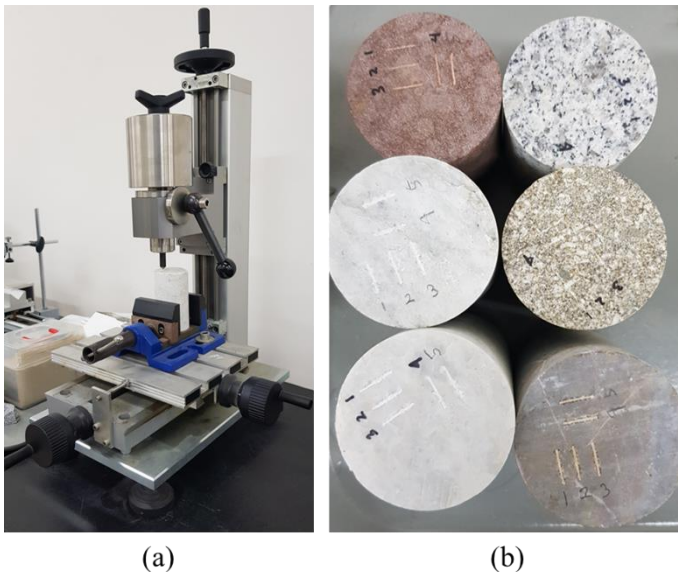


Figure 5.8. Cerchar abrasiveness test; (a) testing apparatus, and (b) typical rock specimen

The Cerchar abrasiveness index (CAI) is defined as the average value of wear flat diameter. The wear flat diameter for a pin was measured twice, parallel, and perpendicular to the scratching direction. Typical wear flat diameter measurement of the Cerchar test under a microscope can be seen in Figure 5.9. The CAI can be calculated from Eq. 5.3.

$$CAI = \frac{1}{n} \sum_{i=1}^n d_i \times 10 \quad (5.3)$$

where  $d_i$  and  $i$  denote as the individual diameter of wear flat and the number of wear flat measurement, respectively.

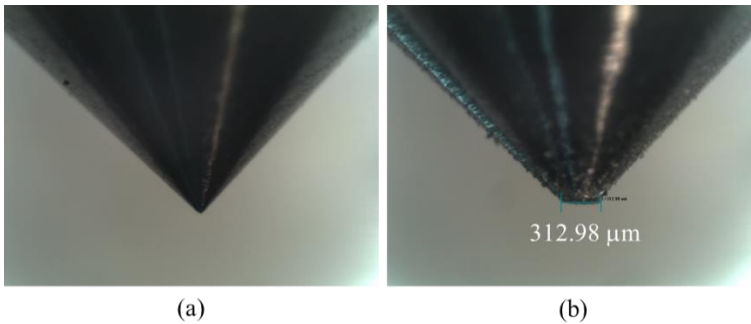


Figure 5.9. The pin under the microscope; (a) before, and (b) after the Cerchar abrasiveness test

## 5.6 Results and Discussion

### 5.6.1 Equivalent Quartz Content

Previous studies showed that the CAI had a good correlation with the abrasive mineral content of the rock (Lee et al., 2013; West, 1986). Among all minerals of the rock, quartz is found to be the most common abrasive minerals that contribute to the wearing of the tool. Although it

might be less significant, the contribution of minerals other than quartz is still counted. To incorporate all minerals of the rock, an equivalent value to the hardness of the quartz mineral was determined, regarded as equivalent quartz content (EQC).

The EQC was calculated by multiplying the amount of each mineral with its Rosiwal hardness to quartz, as mentioned in Eq. 5.4:

$$EQC = \sum_{i=1}^n A_i \times \frac{H_{Ros_i}}{H_{RosQ}} \quad (5.4)$$

where EQC is the equivalent quartz content,  $A_i$  is each mineral quantity,  $H_{Ros_i}$  is Rosiwal hardness of each mineral, and  $H_{RosQ}$  is Rosiwal hardness of quartz. The Rosiwal hardness of each mineral is converted from the Mohs hardness using the relationship shown in Figure 5.10 (Thuro & Plinninger, 2003), while the reference Mohs hardness of all minerals were cited from (Mottana et al., 1978). The results of the EQC of all rocks are summarized in Table 5.3.

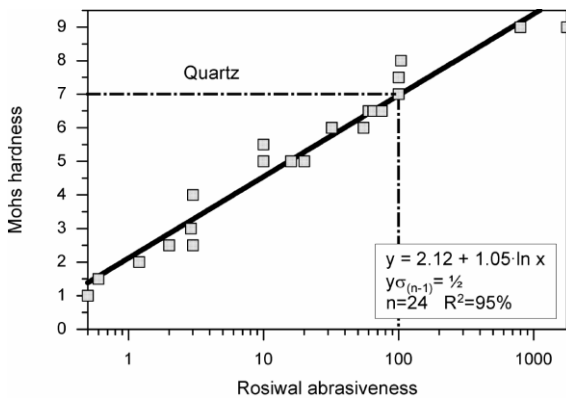


Figure 5.10. Relationship between Mohs hardness and Rosiwal hardness (Thuro & Plinninger, 2003)

Table 5.3. Mineral composition and its equivalent quartz content

No	Rock Type	Mineral	Percentage (%)	Mohs hardness	Rosival hardness	EQC (%)
1	Granite 1	Quartz	35.4	7	104.29	62.82
		Albite	34.9	6.25	51.06	
		Microcline	20.8	6.25	51.06	
		Biotite	8.9	2.75	1.82	
		Magnetite	0	6	40.24	
2	Granite 2	Quartz	37.6	7	104.29	64.54
		Albite	35.4	6.25	51.06	
		Microcline	17.8	6.25	51.06	
		Biotite	7.1	2.75	1.82	
		Magnetite	2	6	40.24	
3	Granite 3	Quartz	31	7	104.29	63.65
		Albite	30.2	6.25	51.06	
		Microcline	27.9	6.25	51.06	
		Orthoclase	10.9	6	40.24	
		Biotite	0	2.75	1.82	
4	Granite 4	Microcline	35.7	6.25	51.06	64.01
		Albite	34.8	6.25	51.06	
		Quartz	29.5	7	104.29	
		Biotite	0	2.75	1.82	
		Chlorite	0	6.5	64.78	
5	Granodiorite porphyry	Albite	44.2	6.25	51.06	58.01
		Quartz	29.4	7	104.29	
		Orthoclase	13.9	6	40.24	
		Biotite	6.8	2.75	1.82	
		Hornblende	5.1	5.5	25.00	
6	Diorite	Magnetite	0.7	6	40.24	44.68
		Albite	49.3	6.25	51.06	
		Orthoclase	21.6	6	40.24	
		Hornblende	11.4	5.5	25.00	
		Quartz	7.5	7	104.29	
7	Gabbro	Biotite	5.3	2.75	1.82	36.65
		Magnetite	4.9	6	40.24	
		Albite	53.4	6.25	51.06	
		Diopside	25.4	5.5	25.00	
		Biotite	14.3	2.75	1.82	
		Magnetite	4.6	6	40.24	

No	Rock Type	Mineral	Percentage (%)	Mohs hardness	Rosiwal hardness	EQC (%)
		Quartz	2.4	7	104.29	
8	Limestone 1	Calcite	100.0	3	2.31	2.22
9	Limestone 2	Calcite	99.4	3	2.31	2.80
		Quartz	0.6	7	104.29	
10	Limestone 3	Calcite	92.7	3	2.31	2.39
		Dolomite	7.3	3.75	4.72	
11	Sandstone 1	Albite	42.2	6.25	51.06	64.54
		Quartz	38.3	7	104.29	
		Orthoclase	10.7	6	40.24	
		Hematite	3.3	6	40.24	
		Laumontite	3.0	3.75	4.72	
		Calcite	1.7	3	2.31	
		Montmorillonite	0.7	1	0.34	
		Quartz	52.8	7	104.29	
12	Sandstone 2	Muscovite	23.6	2.125	1.00	63.70
		Albite	19.7	6.25	51.06	
		Orthoclase	2.6	6	40.24	
		Calcite	1.3	3	2.31	
		Muscovite	46.4	2.125	1.00	
13	Shale	Quartz	41.0	7	104.29	47.61
		Chlorite	12.6	6.25	51.06	
14	Dolomite	Dolomite	86.8	3.75	4.72	5.94
		Hornblende	7.9	5.5	25.00	
		Calcite	5.3	3	2.31	

Table 5.4. The result of CAI, Gi, and physical and mechanical properties of tested rocks

No	Rock Type	Location	$\rho$ (gr/cm <sup>3</sup> )	$n$ (%)	$E$ (GPa)	$\nu$	$\sigma_c$ (MPa)	$\sigma_t$ (MPa)	$H_s$	$HS$	QC (%)	EQC (%)	CAI	Gi
1	Granite 1	Hwangdeung	2.63	0.70	55.21	0.29	168.8	15.0	68.8	52.6	25.80	62.82	2.75	11.74
2	Granite 2	Jinan	2.67	0.44	72.00	0.23	178.0	8.0	81.3	53.3	37.60	64.54	3.00	9.64
3	Granite 3	Pocheon	2.62	0.96	43.00	0.29	177.0	8.0	82.6	52.7	31.00	63.65	3.06	10.95
4	Granite 4	Sangju	2.56	0.94	64.00	0.27	151.0	10.0	84.3	51.6	29.50	64.01	2.41	10.77
5	Granodiorite porphyry	Unknown	2.48	6.37	2.76	0.45	31.3	1.9	39.5	25.4	29.40	58.01	2.09	10.96
6	Diorite	Goheung	2.80	0.49	57.00	0.28	235.0	15.0	83.6	52.9	7.50	44.68	2.68	10.77
7	Gabbro	Hamyang	2.85	0.45	74.00	0.20	110.0	8.0	71.2	52.4	2.40	36.65	2.63	10.85
8	Limestone 1	Geumsan	2.71	0.28	72.88	0.11	65.4	4.5	44.0	40.7	0.00	2.22	1.01	8.23
9	Limestone 2	Geumsan	2.68	0.53	43.27	0.22	80.7	4.3	39.0	42.6	0.60	2.80	0.91	8.44
10	Limestone 3	Geumsan	2.69	0.42	55.60	0.28	86.2	10.7	51.2	45.1	0.00	2.39	1.02	7.81
11	Sandstone 1	Linyi (China)	2.43	10.00	15.00	0.30	64.0	4.2	45.1	40.7	38.30	64.54	1.24	10.95
12	Sandstone 2	Boryeong	2.71	0.46	58.32	0.35	292.2	24.5	69.5	44.4	52.80	63.70	3.50	10.70
13	Shale	Boryeong	2.78	0.35	50.21	0.37	192.7	15.6	48.5	48.4	41.00	47.61	0.82	8.83
14	Dolomite	Unknown	2.84	0.34	68.00	0.31	124.0	9.0	46.4	40.9	0.00	5.64	0.98	8.79

Note:

$\rho$ : Rock density

$n$ : Porosity

$E$ : Young's Modulus

$\nu$ : Poisson's ratio

$\sigma_c$ : Uniaxial compressive strength

$\sigma_t$ : Tensile strength

$H_s$ : Shore hardness

$HS$ : Schmidt hammer rebound

QC: Quartz content

EQC: Equivalent quartz content

CAI: Cerchar abrasiveness index

Gi: Gouging abrasiveness index

### 5.6.2 Effect of Geomechanical Properties of Rock

Table 5.4 summarizes the geomechanical properties of the rocks, including the results of the Gouging and Cerchar abrasiveness tests. The properties include: density ( $\rho$ ), porosity ( $n$ ), Young's modulus ( $E$ ), Poisson's ratio ( $\nu$ ), uniaxial compressive strength ( $\sigma_c$ ), tensile strength ( $\sigma_t$ ), shore hardness ( $H_s$ ), Schmidt hammer rebound ( $SH$ ), and equivalent quartz content ( $EQC$ ). The relationships between each of those properties and the abrasiveness indexes are presented in Figures 5.11-5.20.

The properties of rock, regarded as independent variables, are subjected to a statistical significance test using p-value. The p-value is used to verify the validity of the null hypothesis. The null hypothesis in this test shows that the predictor does not contribute to the prediction of the response variable. If the p-value is less than 0.05 (p-value<0.05), it indicates that the null hypothesis is rejected, meaning that the predictor is statistically significant (Frost, 2013). Thus, based on that criterion,  $H_s$  and  $EQC$  are significant to both CAI and Gi, while UCS is significant only to CAI (see Table 5.5). Therefore, the rest of the other properties are omitted for further analysis since they do not significantly affect the change of abrasiveness indexes.

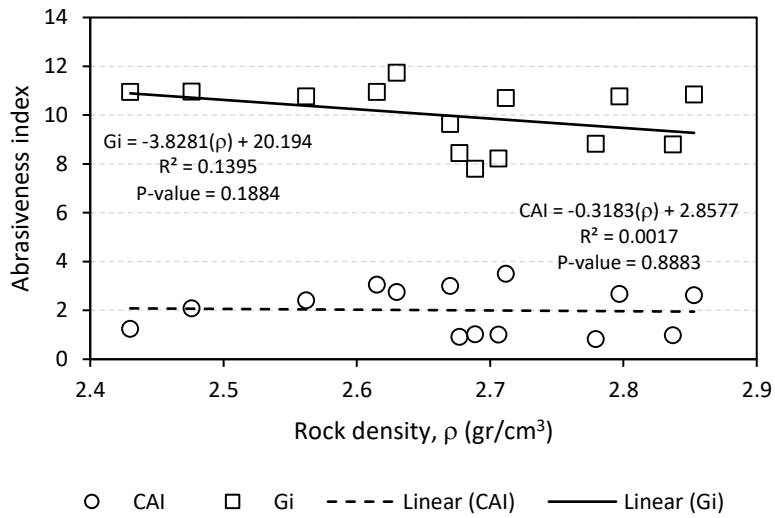


Figure 5.11. Relationship between the abrasiveness indexes and rock density

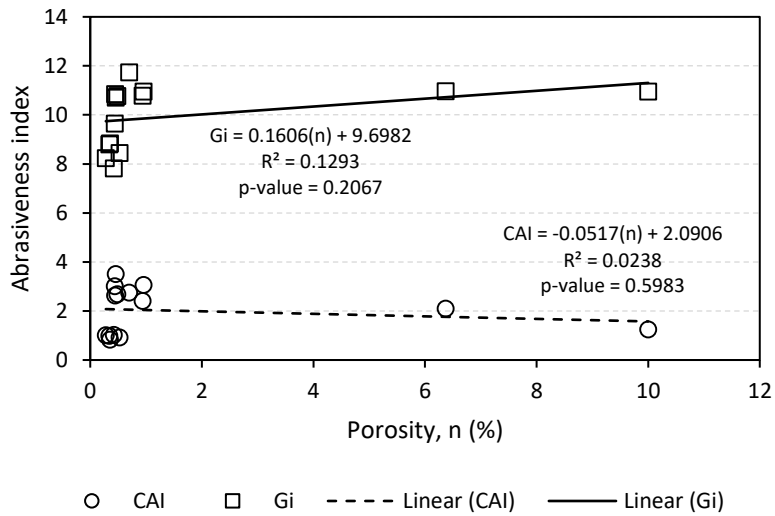


Figure 5.12. Relationship between the abrasiveness indexes and porosity

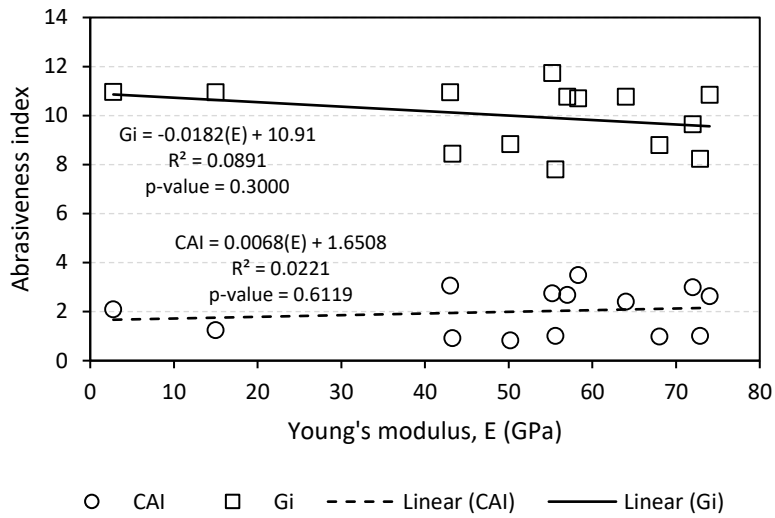


Figure 5.13. Relationship between the abrasiveness indexes and Young's modulus

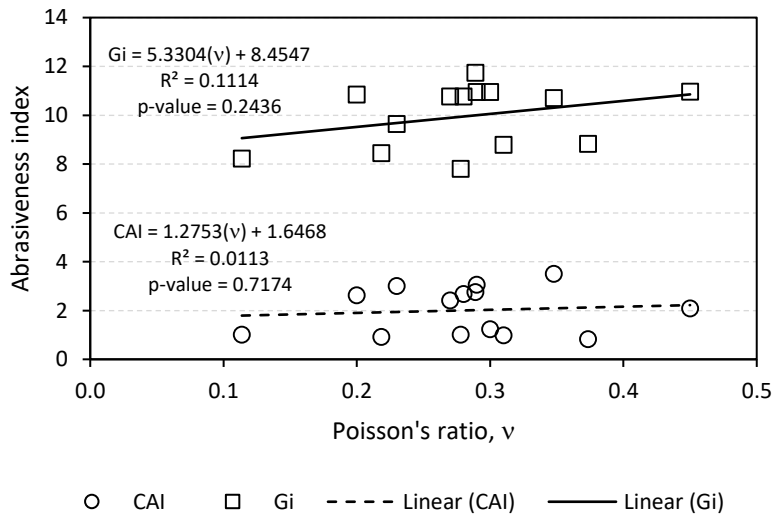


Figure 5.14. Relationship between the abrasiveness indexes and Poisson's ratio

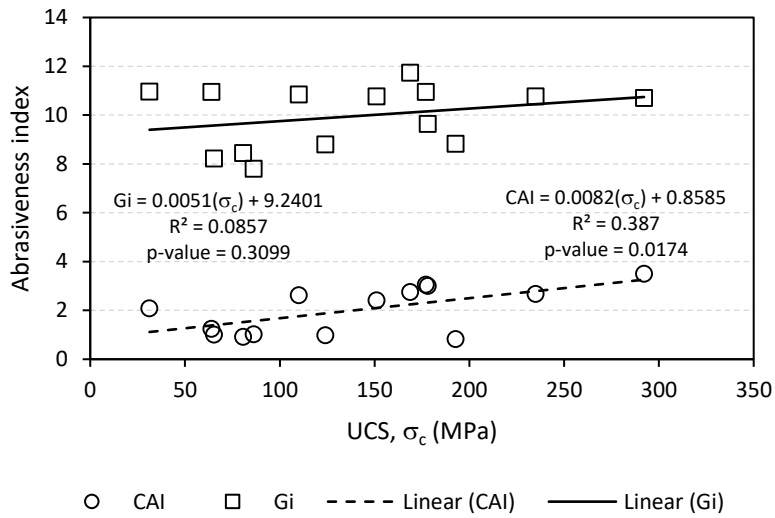


Figure 5.15. Relationship between the abrasiveness indexes and uniaxial compressive strength

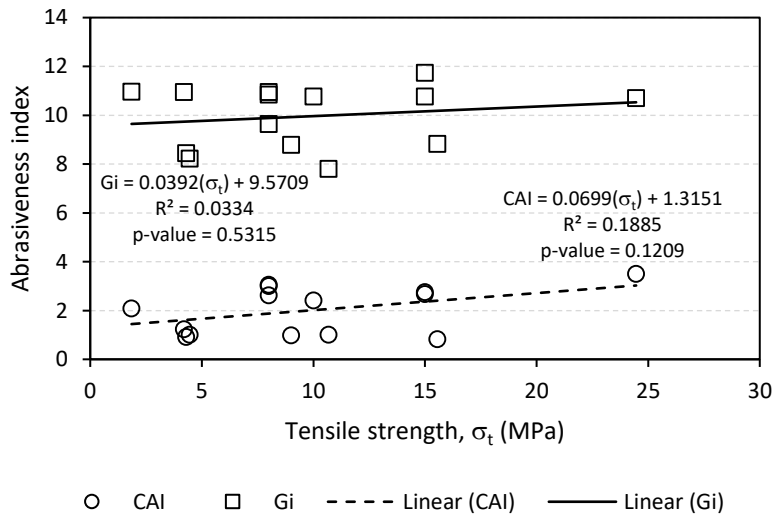


Figure 5.16. Relationship between the abrasiveness indexes and tensile strength

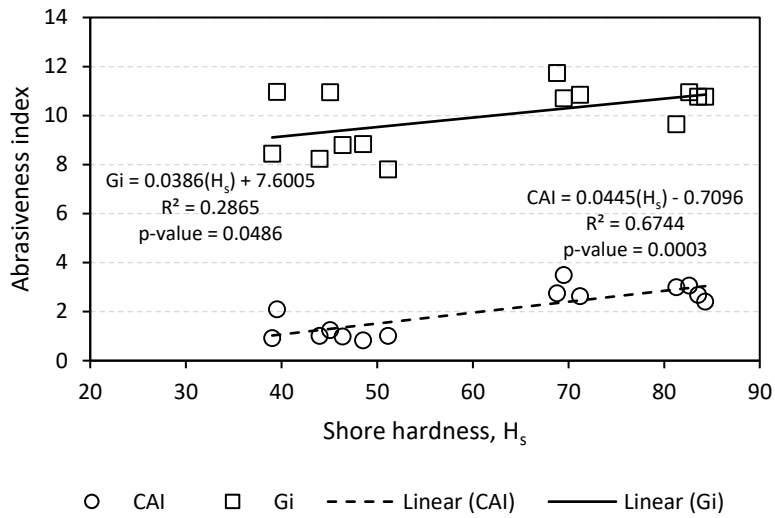


Figure 5.17. Relationship between the abrasiveness indexes and shore hardness

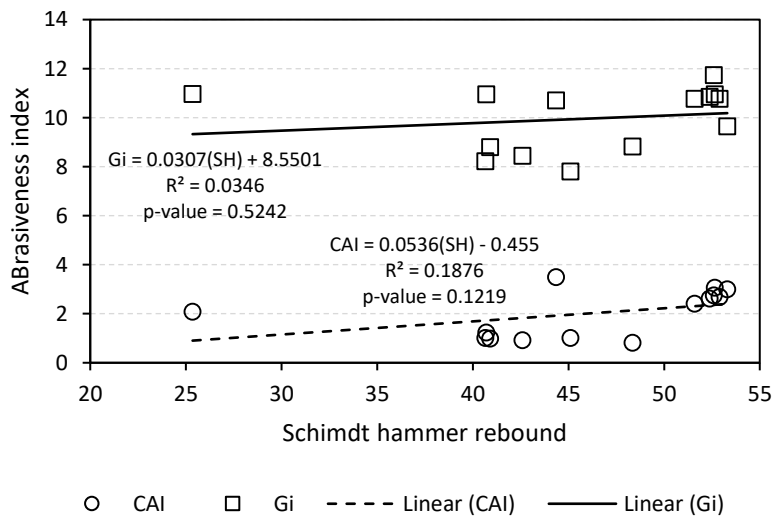


Figure 5.18. Relationship between the abrasiveness indexes and Schmidt hammer rebound value

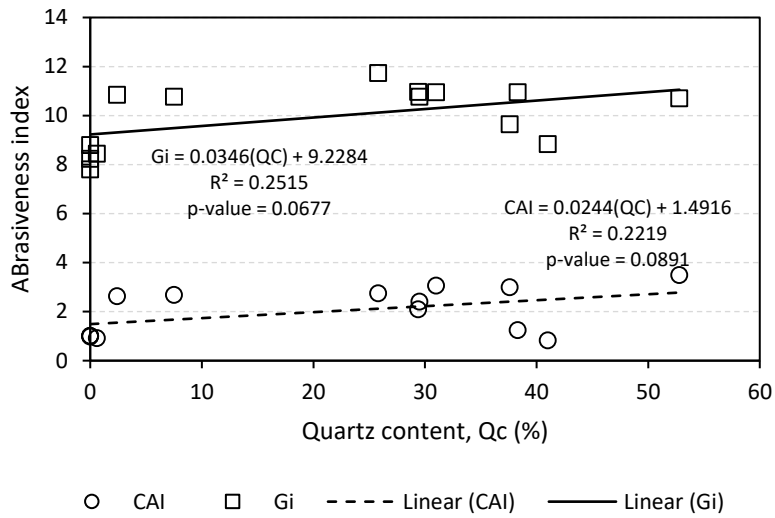


Figure 5.19. Relationship between the abrasiveness indexes and quartz content

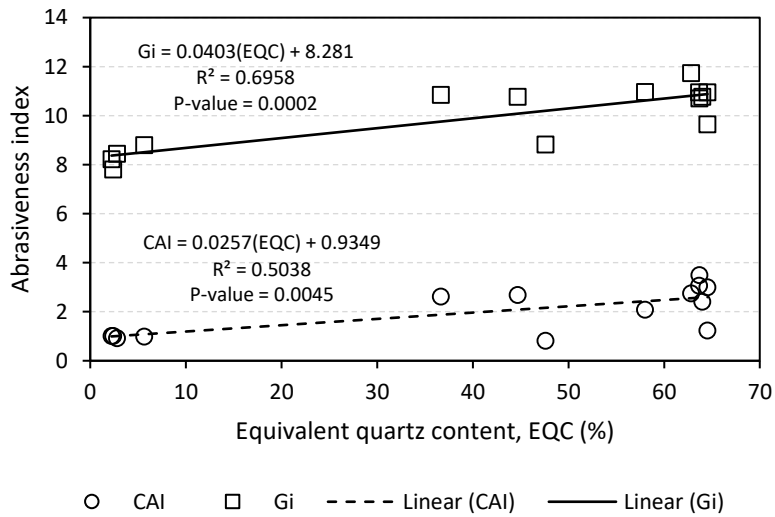


Figure 5.20. Relationship between the abrasiveness indexes and equivalent quartz content

Table 5.5. Recapitulation of coefficient of determination ( $R^2$ ) and p-value of all independent variables

Independent variable	CAI		Gi	
	$R^2$	p-value	$R^2$	p-value
Density, $\rho$	0.0017	0.8883	0.1395	0.1884
Porosity, $n$	0.0238	0.5983	0.1293	0.2067
Young's modulus, $E$	0.0221	0.6119	0.0891	0.3000
Poisson's ratio, $\nu$	0.0113	0.7174	0.1114	0.2436
UCS, $\sigma_c$	0.3878	<b>0.0174</b>	0.0857	0.3099
Tensile strength, $\sigma_t$	0.1885	0.1209	0.0334	0.5315
Shore hardness, $H_s$	0.6744	<b>0.0003</b>	0.2865	<b>0.0486</b>
Schmidt hammer rebound, $SH$	0.1876	0.1219	0.0346	0.5242
Quartz content, $QC$	0.2219	0.0891	0.2515	0.0677
Equivalent quartz content, $EQC$	0.5038	<b>0.0045</b>	0.6958	<b>0.0002</b>

To develop a prediction model of each abrasiveness indexes, single and multiple linear regression models are considered. The single linear regression includes only EQC that is statistically significant to both CAI and Gi. In the multiple linear regression model,  $\sigma_c$  is included since it is statistically significant to CAI and might affect Gi also after the regression. Shore hardness ( $H_s$ ) must be excluded from the combination even though it is statistically significant to the abrasiveness indexes. The reason is that  $H_s$  and EQC are not independent of each other, given the p-value of 0.035. In this case, EQC is chosen over  $H_s$  since it has a relatively higher coefficient of determination values in relationship with the CAI and Gi. The models are presented as follows:

Model 1:

$$CAI' = a_{CAI} + b_{CAI} \times [EQC]$$

$$Gi' = a_{Gi} + b_{Gi} \times [EQC]$$

Model 2:

$$CAI' = a_{CAI} + b_{CAI} \times [\sigma_c] + c_{CAI} \times [EQC]$$

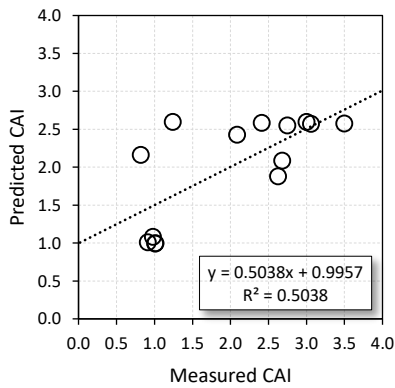
$$Gi' = a_{Gi} + b_{Gi} \times [\sigma_c] + c_{Gi} \times [EQC]$$

The results of the linear regression of both models are presented in Table 5.6. The results show that both models are statistically significant, given that the significance F is less than 0.05. However, model 2 results in a better fit than model 1 by showing the higher value of the coefficient of determination ( $R^2$  value).

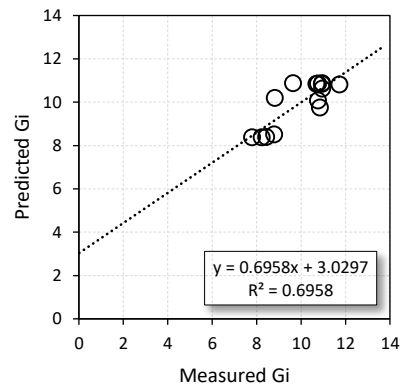
Figures 5.21 and 5.22 present the relationships between the measured index and predicted index based on model 1 and model 2, respectively.

Table 5.6. Results of multiple linear regression of model 1 and model 2

Index, $i$	Coefficient			$R^2$ value	Significance F
	$a_i$	$b_i$	$c_i$		
Model 1					
CAI	0.9349	0.0257	-	0.5038	0.0045
Gi	8.2809	0.0403	-	0.6958	0.0002
Model 2					
CAI	0.4782	0.0051	0.0196	0.6243	0.0046
Gi	8.4220	-0.0016	0.0422	0.7023	0.0013

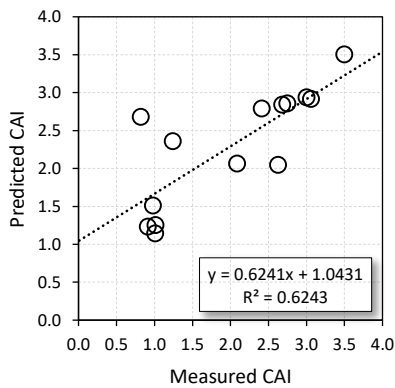


(a)

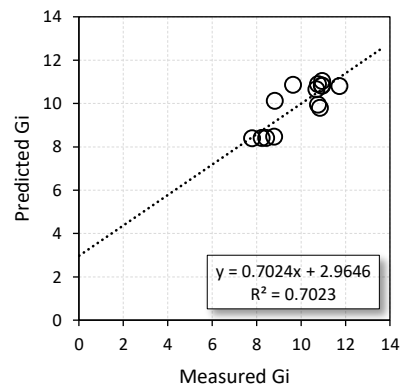


(b)

Figure 5.21. Relationship between the measured index and predicted index based on model 1: (a) CAI and (b) Gi



(a)



(b)

Figure 5.22. Relationship between the measured index and predicted index based on model 2: (a) CAI and (b) Gi

### 5.6.3 Relationship Between CAI and Gi

A direct comparison between Cerchar and Gouging tests is difficult. The main reason is that they have a distinct working principle. Cerchar works at a scratch on a constant length of 10 mm under a constant load of 70 N

while Gouging uses a constant predefined maximum penetration depth of 1 mm. However, it is interesting to see the performance of the Gouging test compared to the widely used method like the Cerchar test.

Generally,  $G_i$  agrees with the CAI at the lower abrasive rock. However, for higher abrasive rock, the  $G_i$  does not increase as CAI does.  $G_i$  tends to level out to a value between 10-12, as seen in Figure 5.23. From the physical point of view, in the higher abrasive rock, the pin seemed to be flattened entirely by the rock surface, and the pin wear was controlled purely by the penetration depth, not the rock abrasiveness. It implies that  $G_i$  does not work well in high abrasive rock.

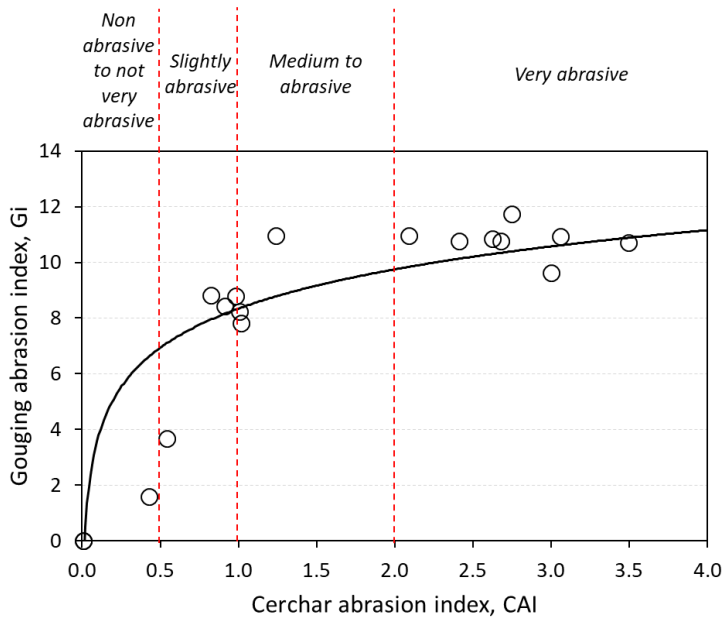


Figure 5.23. Relationship between CAI and  $G_i$  of tested rocks

In this study, the pin hardness used to perform the Gouging test was HRC 55, like the one recommended for the Cerchar test. The case would have

been much unfavorable if this study used HRC 44 pin hardness, which is recommended by the original requirement of the Gouging test (Golovanevskiy & Bearman, 2008). The pin with HRC 44 would not work better than the HRC 55 against a very abrasive rock. So, this study proposes to use a more robust pin for the Gouging test, at least harder than HRC 55.

#### **5.6.4 Groove Profile**

Considering the scratching mechanism of the Gouging test, it was expected to observe a full arc-shaped groove from the swing motion of the scratch tool. However, the expected shape is not detected in all cases. The reason is that most part of the pin is flattened due to the initial impact interaction between the pin and the rock surface. So, after the initial impact, the groove is produced by a relatively flatter and shorter pin, especially for the high abrasive rock.

In general, there are two distinct groove profiles in Gouging test:

- Low abrasive rock: noticeable groove along the scratch line with a short “pencil mark” part at the end of the line
- High abrasive rock: fair short groove at the beginning followed by a dominant “pencil mark” for the rest of the line

Figures 5.24 and 5.25 show the groove profile of the Gouging test for the low and the high abrasive rocks, respectively. In Figure 5.24, for the low abrasive rock, the maximum scratching depth is about 0.45 mm, and it occurs at the beginning of the scratch line. It indicates that most of the pin is destroyed at the beginning and does not reach to a potential

maximum depth of 1 mm, based on the predefined penetration depth before the test.

On the other hand, a discrete profile is observed for the high abrasive rock, as shown in Figure 5.25. The groove occurs at the very beginning of the line with only shallow depth. It means that the pin cannot bite the rock and destroyed immediately after the impact. Then, the scratching process leaves only a “pencil mark” on the rock surface for the rest of the line. This phenomenon also supports the previous statement that the Gouging test does not work effectively in a highly abrasive rock.

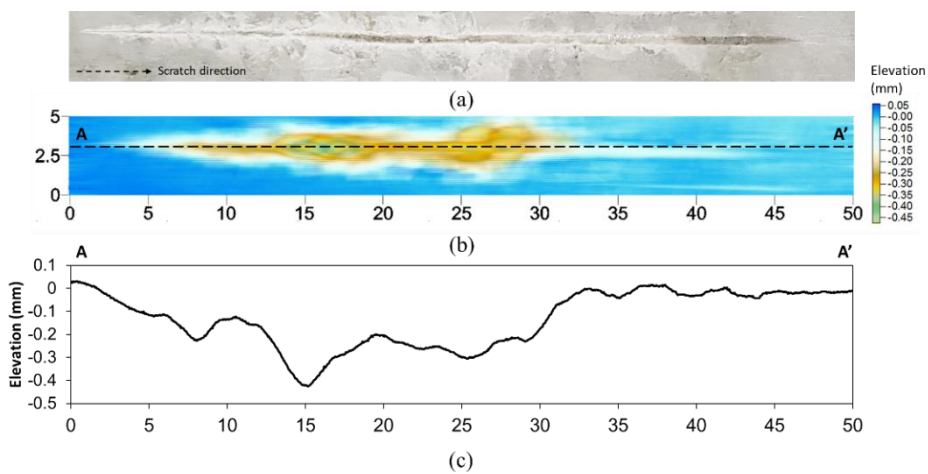


Figure 5.24. Groove profile of Gouging test for low abrasive rock. (a) picture; (b) color-contoured map; (c) representative (A-A') cross-sectional profile

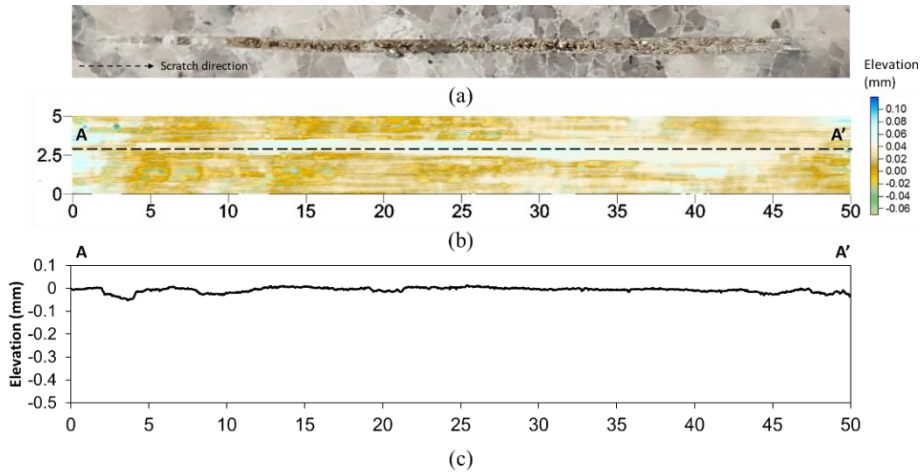


Figure 5.25. Groove profile of Gouging test for high abrasive rock. (a) picture; (b) color-contoured map; (c) representative (A-A') cross-sectional profile

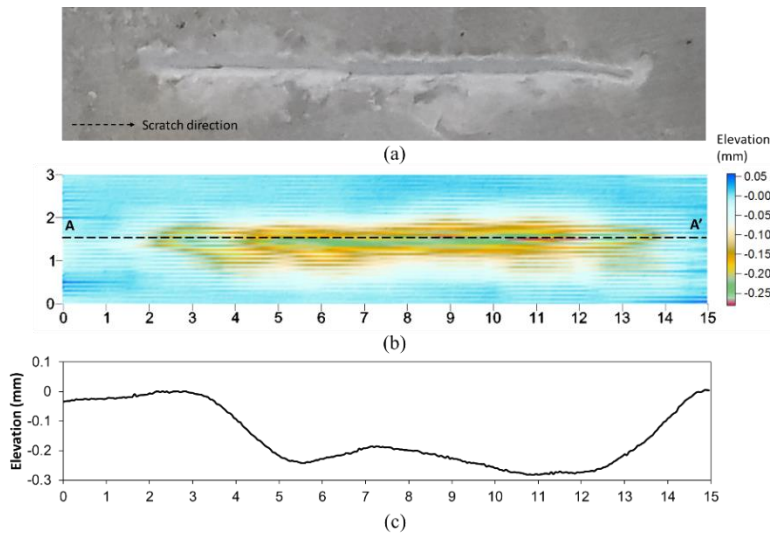


Figure 5.26. Groove profile of Cerchar test for low abrasive rock. (a) picture; (b) color-contoured map; (c) representative (A-A') cross-sectional profile

Figure 5.26 shows the groove profile of the Cerchar test for the low abrasive rock. The maximum penetration depth is about 0.3 mm and

appears to be consistent with a gentle undulation along the scratching line of 10 mm. This result is expected since the scratching process is done linearly, with a static load and a defined length.

Compared with the Cerchar test, the Gouging test groove appears to have a more complex groove profile as a result of a more complicated scratching mechanism.

### **5.6.5 Gouging and Cerchar Tests in an Identical Scratch Distance**

The scratch distance between Cerchar and Gouging tests is different. Cerchar adopts a constant scratch distance of 10 mm while the distance in Gouging varies depending on the abrasiveness of the tested rock. In Gouging, the constant parameter is the penetration depth ( $p = 1 \text{ mm}$ ), and scratch distance is dependent on the penetration depth by modifying the penetration depth; the scratching distance will also change.

In this section, a comparison between Gouging and Cerchar tests under similar scratch length for a high abrasive rock is discussed. Gouging tests were conducted ten times with ten different penetration depths from 0.2 mm to 2 mm with an increment of 0.2 mm. Scratch length is dependent on penetration depth in the Gouging test, so ten different scratch length measures were obtained. After that, Cerchar tests were also done ten times, referring to those scratch length measures resulted from the Gouging test. Then, the wear diameter of the pin was measured under a microscope, and the results between them were compared. The test procedure was illustrated in Figure 5.27, and the result is presented in Table 5.7.

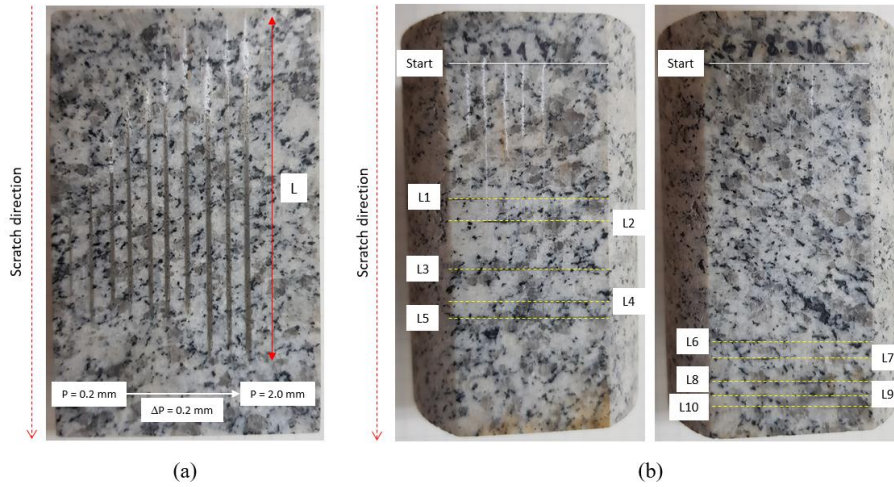


Figure 5.27. Scratch test under an identical scratch length. (a) Gouging test; (b) Cerchar test

Table 5.7. Results wear diameter of Gouging and Cerchar abrasiveness tests under an identical scratch length

No.	Gouging test				L (mm)	Cerchar test		
	P (mm)	D <sub>1</sub> (mm)	D <sub>2</sub> (mm)	D <sub>ave.</sub> (mm)		D <sub>1</sub> (mm)	D <sub>2</sub> (mm)	D <sub>ave.</sub> (mm)
1	0.2	0.57	0.64	0.60	25.15	0.33	0.32	0.33
2	0.4	0.82	0.85	0.84	29.75	0.44	0.31	0.37
3	0.6	0.92	0.95	0.93	38.75	0.37	0.41	0.39
4	0.8	0.94	0.99	0.96	45.00	0.42	0.43	0.42
5	1.0	1.00	1.00	1.00	47.90	0.40	0.41	0.41
6	1.2	1.08	1.12	1.10	51.70	0.46	0.46	0.46
7	1.4	1.06	1.10	1.08	55.10	0.39	0.42	0.40
8	1.6	1.20	1.24	1.22	60.25	0.43	0.49	0.46
9	1.8	1.07	1.11	1.09	63.70	0.44	0.43	0.44
10	2.0	1.24	1.28	1.26	65.40	0.43	0.45	0.44

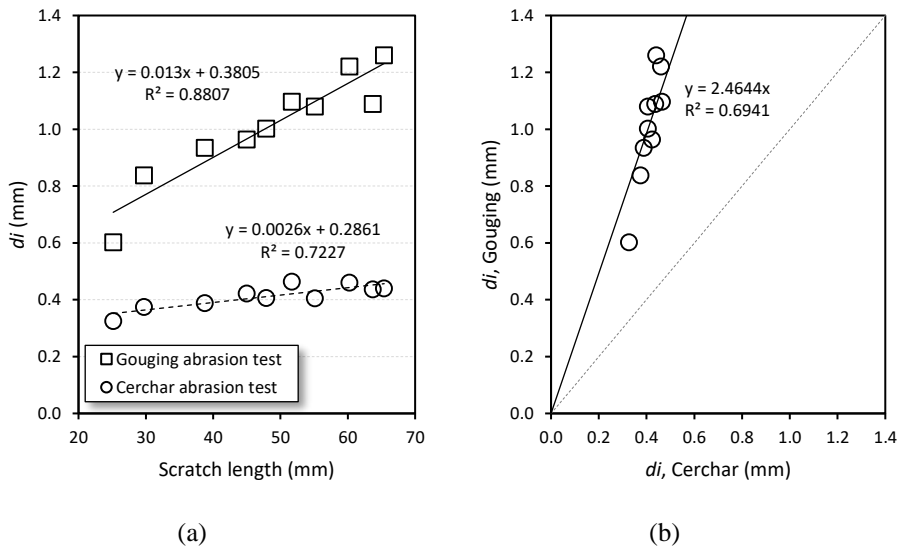


Figure 5.28. Comparison between the Gouging and Cerchar tests. (a) wear diameter vs. scratch length; (b) wear diameter of Gouging vs. Cerchar tests

Figure 5.28 shows a comparison between Gouging and Cerchar tests. In Gi, a longer scratch distance means a deeper penetration depth, and a greater part of the pin was impacted on the rock surface. So, there is no question that the wear amount of the pin tends to get larger over a longer scratch distance. In Cerchar, a longer distance does not proportionally relate to deeper penetration depth. In Figure 5.28(a), it is shown that the Cerchar test is less sensitive to the scratch length. It is supported by the previous study showing that 60-70% of the final Cerchar abrasiveness index (observed at a 20 mm scratch) is observed at the first 2 mm, 85-93% at 10 mm, and 99% at 15 mm of the scratch length (Yaralı & Duru, 2016).

Additionally, Figure 5.28(b) shows that, for the same scratch length, the wear amount of the Gouging abrasiveness test is approximately 2.5 times larger than the wear amount of the Cerchar abrasiveness test.

## 6. CONCLUSIONS

A review of rock response subjected to several test modes in dynamic loading, particularly in the intermediate strain rate (ISR) loading is presented. According to a literature, ISR loading ranges from  $10^{-1}$  to  $10^1$  per second. The techniques to produce such loading are commonly done by gas-operated machine, hydro-pneumatic machine, drop weight apparatus, and modified split-Hopkinson pressure bar. In this study, a new technique is proposed by using a loading apparatus driven by the reaction of a non-explosive powder called non-explosive rock cracker (NRC). It is proved that this apparatus can generate a loading rate in the ISR range.

Four testing modes, namely uniaxial compression, Brazilian tension, mode-I fracture toughness (notched semi-circular bending type), and punch shear, were carried out in both quasi-static and ISR loading regimes for Hwangdeung granite and Linyi sandstone. It is found that the rock strength increases in the ISR range, about 1.4 to 6.7 times its static strength depending on test mode and rock type. The rate dependency is usually associated with some micromechanical phenomena, such as thermal activation, inertial effect, fracture energy, and heterogeneity of rock material. Overall, the results agree with the general notion in rock dynamics that strain rate dependency of rock strength has two general trends, i.e., moderate increase at the lower rates, and significant rise at the higher rates. The idea is also confirmed by some comparisons with literature survey data, and numerical simulation works using an explicit dynamic finite element program.

Cutting in rock involves dynamic events in its process due to the fast-moving cutter, irregularities of the rock surface, and some inherent rock characteristics. The dynamic level of the cutting process is presumed to be lower than that of blasting operation, which is commonly associated with high strain rate loading, but it has a rate higher than the quasi-static regime. Thus, considering rock mechanical properties under the ISR range seems to be reasonable. Several attempts have been made for estimating the actual strain rate during the cutting process based on literature surveys, laboratory linear cutting tests, and some numerical simulations. Despite its limitation, the results of those attempts indicate that the cutting process belongs to the ISR loading regime.

This study tries to apply the ISR strength of rock to rock mechanical excavation applications. Linear cutting test using a conical pick on a sandstone block was carried out with various ratios of spacing and depth of cut ( $s/p$ ), with an integration with some reference data for the identical rock type. A small-scale linear cutting machine was used for the works. The cutter forces, i.e., cutting, normal, and side forces, were estimated. Cutting specific energy was also investigated, and it varied depending on the cutting configurations. Besides, numerical modeling of the linear cutting test was also performed for the case of 5 mm cutting depth using two different sets of input property, i.e., static and dynamic property sets. The results show that the numerical modeling with dynamic properties fit better for predicting laboratory works by showing a relatively minimal error compared to the static one.

Some data from literature reviews were collected to develop a cutting force prediction model that accommodates the dynamic strength of rock under ISR. The data includes experimental unrelieved cutting forces (mean and peak), uniaxial compression strength (UCS), Brazilian tensile

strength (BTS), and other cutting configurations such as tip angle of the conical cutter and depth of cut. The quasi-static values of UCS and BTS were then converted to the dynamic values by using the averaged dynamic increase factor (DIF) within the ISR range for various rocks. Four prediction models were built using multiple linear regression and compared with some well-known theoretical cutting force models. The results show that model 2 and model 4 can perform better than other theoretical models for estimating mean and peak cutting force, respectively. Statistical analysis shows that the proposed models possess a lower value of mean squared error to the data population.

Assessment of rock abrasiveness is crucial when dealing with mechanized excavation in various mining and civil works. Cerchar abrasive index (CAI) is one of the most common indexes used for predicting rock abrasiveness, despite its static environment in the procedure. In this study, the other method is introduced called the Gouging abrasiveness test that resembles a high-speed impact experienced by cutting tools in the field. The effect of geomechanical properties to both abrasiveness indexes and the prediction models were derived using single and multiple linear regression. The relationships between abrasiveness indexes were discussed, including the groove profile resulted from them. It appears that the Gouging index is not suitable for higher abrasive rock, given that the values do not vary enough for the higher abrasive rock as CAIs do.

In conclusion, this study contributes to the field of rock engineering in viewing the rock cutting phenomenon from a dynamic perspective. The prediction models using static parameters may underestimate the actual cutting performance. It is seen from the results of cutting force from numerical simulation and some of the theoretical approaches. By using

dynamic parameters, the simulated and predicted cutting forces correspond to the measured cutting forces from the laboratory linear cutting tests.

It should be admitted that there are many limitations to this study. Further studies need to be addressed to understand more about what is happening during the cutting process. This study suggests that direct strain rate measurement on the cutter and the adjacent rock surface should be carried out in the actual mechanical excavation project; thus, the actual dynamic level could be precisely defined. Then, dynamic tests on the actual strain rate level could be performed on some typical rocks from the excavation project sites. Rock mass features and machine performance factors might also be included in the prediction model; thus, it would result in a more comprehensive and applicable output.

## REFERENCE

- Al-Ameen, S. I., & Waller, M. D. (1994). The influence of rock strength and abrasive mineral content on the Cerchar Abrasive Index. *Engineering Geology*, 36(3), 293-301.
- Alber, M., Yarali, O., Dahl, F., Bruland, A., Kasling, H., Michalakopoulos, T. N., Cardu, M., Hagan, P., Aydin, H., & Ozarslan, A. (2014). ISRM suggested method for determining the abrasivity of rock by the CERCHAR abrasivity test. *Rock Mechanics and Rock Engineering*, 47(1), 261-266.
- ANSYS. (2010). AUTODYN User's Manual Version 13. Canonsburg, PA: Century Dynamics.
- Asprone, D., Cadoni, E., Prota, A., & Manfredi, G. (2009). Dynamic behavior of a Mediterranean natural stone under tensile loading. *International Journal of Rock Mechanics and Mining Sciences*, 46(3), 514-520.
- ASTM. (2007). ASTM E23-18. In *Standard Test Methods for Notched Bar Impact Testing of Metallic Materials*. West Conshohocken, PA: ASTM International.
- Atkinson, T., Cassapi, V. B., & Singh, R. N. (1986). Assessment of abrasive wear resistance potential in rock excavation machinery. *International Journal of Mining and Geological Engineering*, 4(2), 151-163.
- Bilgin, N., Copur, H., & Balci, C. (2014). Mechanical excavation in mining and civil industries. CRC Press.
- Bilgin, N., Demircin, M. A., Copur, H., Balci, C., Tuncdemir, H., & Akcin, N. (2006). Dominant rock properties affecting the performance of conical picks and the comparison of some experimental and theoretical results. *International Journal of Rock Mechanics and Mining Sciences*, 43(1), 139-156.
- Blanton, T. L. (1981). Effect of strain rates from  $10^{-2}$  to  $10 \text{ sec}^{-1}$  in triaxial compression tests on three rocks. *International Journal of Rock Mechanics and Mining Sciences & Geomechanics Abstracts*, 18(1), 47-62.
- Blau, P. J. (1989). Friction and wear transitions of materials—break-in, run-in, wear-in. New Jersey, United States: Noyes Publications.

- Budinski, K. G. (1988). *Surface Engineering for Wear Resistance*. New Jersey, United States: Prentice-Hall Inc.
- Cadoni, E. (2010). Dynamic characterization of orthogneiss rock subjected to intermediate and high strain rates in tension. *Rock Mechanics and Rock Engineering*, 43(6), 667-676.
- Chen, X. D., Xu, L. Y., & Zhu, Q. (2017). Mechanical behavior and damage evolution for concrete subjected to multiple impact loading. *KSCE Journal of Civil Engineering*, 21(6), 2351-2359.
- Cho, J. W., Jeon, S., Jeong, H. Y., & Chang, S. H. (2013). Evaluation of cutting efficiency during TBM disc cutter excavation within a Korean granitic rock using linear-cutting-machine testing and photogrammetric measurement. *Tunnelling and Underground Space Technology*, 35, 37-54.
- Cho, J. W., Jeon, S., Yu, S., H., & Chang, S. H. (2010). Optimum spacing of TBM disc cutters: A numerical simulation using the three-dimensional dynamic fracturing method. *Tunnelling and Underground Space Technology*, 25(3), 230-244.
- Cho, S. H., Ogata, Y., & Kaneko, K. (2003). Strain-rate dependency of the dynamic tensile strength of rock. *International Journal of Rock Mechanics and Mining Sciences*, 40(5), 763-777.
- Chong, K. P., Hoyt, P. M., Smith, J. W., & Paulsen, B. Y. (1980). Effects of strain rate on oil-shale fracturing. *International Journal of Rock Mechanics and Mining Sciences*, 17(1), 35-43.
- Copur, H., Bilgin, N., Tuncdemir, H., & Balci, C. (2003). A set of indices based on indentation tests for assessment of rock cutting performance and rock properties. *Journal of the Southern African Institute of Mining and Metallurgy*, 103(9), 589-599.
- Costin, L. S. (1981). Static and dynamic fracture behavior of oil shale. In *Fracture mechanics for ceramics, rocks, and concrete*. ASTM International.
- Dai, F., Huang, S., Xia, K. W., & Tan, Z. Y. (2010a). Some fundamental issues in dynamic compression and tension tests of rocks using split hopkinson pressure bar. *Rock Mechanics and Rock Engineering*, 43(6), 657-666.
- Dai, F., & Xia, K. W. (2013). Laboratory measurements of the rate dependence of the fracture toughness anisotropy of Barre granite. *International Journal of Rock Mechanics and Mining Sciences*, 60, 57-65.

- Dai, F., Xia, K. W., & Tang, L. Z. (2010b). Rate dependence of the flexural tensile strength of Laurentian granite. *International Journal of Rock Mechanics and Mining Sciences*, 47(3), 469-475.
- Doan, M. L., & Gary, G. (2009). Rock pulverization at high strain rate near the San Andreas fault. *Nature Geoscience*, 2(10), 709-712.
- Dutta, P. K., & Kim, K. (1993). High-strain-rate tensile behavior of sedimentary and igneous rocks at low temperatures. No. CRREL-93-16. Cold Regions Research and Engineering Lab. Hanover.
- Dyno Nobel (n.d.). Dynamix technical information. Retrieved from <https://www.dynonobel.com> (accessed: June 22, 2019)
- Evans, I. (1962). A theory of the basic mechanics of coal ploughing. In *Mining Research*, 761-798. Pergamon
- Evans, I. (1965). The force required to cut coal with blunt wedges. *International Journal of Rock Mechanics and Mining Sciences & Geomechanics Abstracts*, 2(1), 1-12.
- Evans, I. (1972). Line spacing of picks for effective cutting. *International Journal of Rock Mechanics and Mining Sciences*, 9(3), 355-361.
- Evans, I. (1982). Optimum line spacing for cutting picks. *Mining Engineer*, 141, 433-434.
- Evans, I. (1984a). Basic mechanics of the point-attack pick. *Colliery Guardian*, 232(5), 189-193.
- Evans, I. (1984b). A theory of the cutting force for point-attack picks. *International Journal of Mining Engineering*, 2(1), 63-71.
- Fairhurst, C. E., & Hudson, J. A. (1999). ISRM suggested method for the complete stress-strain curve for intact rock in uniaxial compression. *International Journal of Rock Mechanics and Mining Sciences*, 36(3), 281-289.
- Fowell, R. J., Anderson, I., & Waggott, A. (1988). Investigations into the dynamic rock cutting characteristics of boom tunnelling machine. In *The 29th US Symposium on Rock Mechanics (USRMS)*. American Rock Mechanics Association.
- Frew, D. J., Forrestal, M. J., & Chen, W. (2001). A split Hopkinson pressure bar technique to determine compressive stress-strain data for rock materials. *Experimental Mechanics*, 41(1), 40-46.

- Frost, J. (2013). Regression analysis: How do I interpret R-squared and assess the goodness-of-fit? Retrieved from <http://blog.minitab.com/blog/adventures-in-statistics/regression-analysis-how-do-i-interpret-r-squared-and-assess-the-goodness-of-fit> (accessed: December 24, 2015)
- Geng, Q., Wei, Z., & Ren, J. (2017). New rock material definition strategy for FEM simulation of the rock cutting process by TBM disc cutters. *Tunnelling and Underground Space Technology*, 65, 179-186.
- Goktan, R. M. (1997). A suggested improvement on Evans' cutting theory for conical bits. In *the Proceedings of fourth symposium on mine mechanization automation*, vol. 1, 57-61
- Golovanevskiy, V. A., & Bearman, R. A. (2008). Gouging abrasion test for rock abrasiveness testing. *International Journal of Mineral Processing*, 85(4), 111-120.
- Grady, D. E., & Kipp, M. E. (1979). The micromechanics of impact fracture of rock. *International Journal of Rock Mechanics and Mining Sciences & Geomechanics Abstracts*, 16(5), 293-302.
- Grady, D. E., & Kipp, M. E. (1980). Continuum modeling of explosive fracture in oil-shale. *International Journal of Rock Mechanics and Mining Sciences*, 17(3), 147-157.
- Gramberg, J. (1989). A non-conventional view on rock mechanics and fracture mechanics. Rotterdam: Balkema.
- Green, S. J., & Perkins, R. D. (1968). Uniaxial compression tests at varying strain rates on three geologic materials. In *the 10<sup>th</sup> U.S. Symposium on Rock Mechanics (USRMS)*. American Rock Mechanics Association.
- Griffiths, G., & Thom, N. (2007). Concrete Pavement Design Guidance Notes. CRC Press.
- Hamzaban, M.-T., Memarian, H., & Rostami, J. (2014). Continuous monitoring of pin tip wear and penetration into rock surface using a new Cerchar abrasivity testing device. *Rock Mechanics and Rock Engineering*, 47(2), 689-701.
- Hogan, J. D., Rogers, R. J., Spray, J. G., & Boonsue, S. (2012). Dynamic fragmentation of granite for impact energies of 6-28 J. *Engineering Fracture Mechanics*, 79, 103-125.

- Hood, M., & Roxborough, F. F. (1992). Rock breakage: mechanical. In *SME mining engineering handbook, 1*, 680-721.
- Hood, M., Roxborough, F. F., & Salamon, M. D. G. (1989). A review of non-explosive rock breaking. HDRK Mining Research Ltd. Calgary.
- Huang, S., Chen, R., & Xia, K. W. (2010a). Quantification of dynamic tensile parameters of rocks using a modified Kolsky tension bar apparatus. *Journal of Rock Mechanics and Geotechnical Engineering*, 2(2), 162-168.
- Huang, S., Feng, X. T., & Xia, K. (2011). A dynamic punch method to quantify the dynamic shear strength of brittle solids. *Review of Scientific Instruments*, 82(5), 053901
- Huang, S., Xia, K. W., Yan, F., & Feng, X. T. (2010b). An experimental study of the rate dependence of tensile strength softening of Longyou sandstone. *Rock Mechanics and Rock Engineering*, 43(6), 677-683.
- Islam, M. T., & Bindiganavile, V. (2012). Stress rate sensitivity of Paskapoo sandstone under flexure. *Canadian Journal of Civil Engineering*, 39(11), 1184-1192.
- Jeong, H. Y. (2017). *Assessment of rock cutting efficiency of pick cutters for the optimal design of a mechanical excavator*. Doctoral dissertation. Seoul National University, Korea.
- Jeong, H. Y., & Jeon, S. (2018). Characteristic of size distribution of rock chip produced by rock cutting with a pick cutter. *Geomechanics and Engineering*, 15(3), 811-822.
- Jeong, H. Y., Jeon, S., & Cho, J. W. (2013). A numerical study on rock cutting by a TBM disc cutter using SPH code. *Journal of Korean Tunnelling and Underground Space Association*, 15(3), 345-356. (in Korean).
- KAIA. (2010). Strategic Report for Mechanized and Automatic Tunnel Construction through Development of TBM Technology. Korea Agency for Infrastructure Technology Advancement. (in Korean)
- Kim, H., Hwang, G. H., & Choi, K. H. (2002). 부산지하철 230 공구 썰드터널 시공사례. *Journal of the Korean Society of Civil Engineers*, 50(2), 85-90. (in Korean)

- Kim, T. H. (2017). *Shear characteristics of a rock discontinuity under various thermal, hydraulic and mechanical conditions*. Doctoral dissertation. Seoul National University, Korea.
- Kimberley, J., & Ramesh, K. T. (2011). The dynamic strength of an ordinary chondrite. *Meteoritics & Planetary Science*, 46(11), 1653-1669.
- Ko, T. Y., Kim, T. K., Son, Y., & Jeon, S. (2016). Effect of geomechanical properties on Cerchar Abrasivity Index (CAI) and its application to TBM tunnelling. *Tunnelling and Underground Space Technology*, 57, 99-111.
- Kobayashi, R. (1970). On mechanical behaviours of rocks under various loading rates. *Rock Mechanics Japan*, vol. 1, 56-58.
- Kubota, S., Ogata, Y., Wada, Y., Simangunsong, G., Shimada, H., & Matsui, K. (2008). Estimation of dynamic tensile strength of sandstone. *International Journal of Rock Mechanics and Mining Sciences*, 45(3), 397-406.
- Kumar, A. (1968). The effect of stress rate and temperature on the strength of basalt and granite. *Geophysics*, 33(3), 501-510.
- Kuruppu, M. D., Obara, Y., Ayatollahi, M. R., Chong, K. P., & Funatsu, T. (2014). ISRM suggested method for determining the mode I static fracture toughness using semi-circular bend specimen. *Rock Mechanics and Rock Engineering*, 47(1), 267-274.
- Lankford, J. (1976). Dynamic strength of oil shale. *Society of Petroleum Engineers Journal*, 16(1), 17-22.
- Lankford, J. (1981). Mechanisms responsible for strain-rate-dependent compressive strength in ceramic materials. *Journal of the American Ceramic Society*, 64(2), C33-C34.
- Lankford, J. (1982). Inertia as a factor in the dynamic strength of brittle materials. *Journal of the American Ceramic Society*, 65(8), C122-C122.
- Lee, S., Jeong, H. Y., & Jeon, S. (2013). Assessment of TBM cutter wear using Cerchar abrasiveness test. In *the Proceedings of world tunneling conference (WTC)*. Geneva, Switzerland.
- Li, X. B., Lok, T. S., & Zhao, J. (2005). Dynamic characteristics of granite subjected to intermediate loading rate. *Rock Mechanics and Rock Engineering*, 38(1), 21-39.

- Lindholm, U. S., Yeakley, L. M., & Nagy, A. (1974). The dynamic strength and fracture properties of dresser basalt. *International Journal of Rock Mechanics and Mining Sciences & Geomechanics Abstracts*, 11(5), 181-191.
- Liu, X. H., Dai, F., Zhang, R., & Liu, J. F. (2015). Static and dynamic uniaxial compression tests on coal rock considering the bedding directivity. *Environmental Earth Sciences*, 73(10), 5933-5949.
- Logan, J. M., & Handin, J. (1970). Triaxial compression testing at intermediate strain rates. In *the 12<sup>th</sup> US Symposium on Rock Mechanics (USRMS)*. American Rock Mechanics Association.
- Lundberg, B. (1976). A split Hopkinson bar study of energy absorption in dynamic rock fragmentation. *International Journal of Rock Mechanics and Mining Sciences & Geomechanics Abstracts*, 13(6), 187-197.
- Menezes, P. L., Lovell, M. R., Avdeev, I. V., & Higgs III, C. F. (2014). Studies on the formation of discontinuous rock fragments during cutting operation. *International Journal of Rock Mechanics and Mining Sciences*, 71, 131-142.
- Merchant, M. E. (1944). Basic mechanics of the metal-cutting process. *Journal of Applied Mechanics*, 11, A168-A175.
- Min, G. J., Oh, S. W., Kim, M. S., Yoon, J. J., Cho, S. H., & Park, L. J. (2016). Determination of the dynamic strength of granite under confined pressure. In *Rock Dynamic: From Research to Engineering*. London: CRC Press.
- Min, G. J., Oh, S. W., Wicaksana, Y., Jeon, S., & Cho, S. H. (2017). Development of the strain measurement-based impact force sensor and its application to the dynamic Brazilian tension test of the rock. *Explosives and Blasting*, 35(3), 15-20. (in Korean)
- Mishnaevsky, L. L. (1995). Physical mechanisms of hard rock fragmentation under mechanical loading: a review. *International Journal of Rock Mechanics and Mining Sciences and Geomechanics Abstracts*, 32(8), 763.
- Montgomery, D. C., & Runger, G. C. (2010). *Applied statistics and probability for engineers*: John Wiley & Sons
- Mottana, A., Crespi, R., Liborio, G., Prinz, M., Harlow, G. E., & Peters, J. (1978). *Simon and Schuster's guide to rocks and minerals*. Simon and Schuster.

- Nakamura, Y., Cho, S. H., Kaneko, K., Kajiki, S., & Kiritani, Y. (2012). Dynamic fracture experiments of mortar using a high-speed loading apparatus driven by explosives. *Science and Technology of Energetic Materials*, 73(5-6), 136-141.
- Nilsen, B., Dahl, F., Holzhäuser, J., & Raleigh, P. (2006). Abrasivity testing for rock and soils. *Tunnels and Tunnelling International*, 47-49.
- Nishimatsu, Y. (1972). The mechanics of rock cutting. *International Journal of Rock Mechanics and Mining Sciences & Geomechanics Abstracts*, 9(2), 261-270.
- Olsson, W. A. (1991). The compressive strength of tuff as a function of strain rate from  $10^{-6}$  to  $10^3$ /Sec. *International Journal of Rock Mechanics and Mining Sciences*, 28(1), 115-118.
- Park, D., & Jeon, S. (2010). Reduction of blast-induced vibration in the direction of tunneling using an air-deck at the bottom of a blasthole. *International Journal of Rock Mechanics and Mining Sciences*, 47(5), 752-761.
- Paul, B., & Sikarskie, D. L. (1965). A preliminary model for wedge penetration in brittle materials. *Transactions of the American Institute of Mining Engineers*, 232, 373-383.
- Perkins, R. D., Green, S. J., & Friedman, M. (1970). Uniaxial stress behavior of porphyritic tonalite at strain rates to  $10^3$ /second. *International Journal of Rock Mechanics and Mining Sciences*, 7(5), 527-535.
- Plinninger, R. J., Kasling, H., & Thuro, K. (2004). Wear prediction in hardrock excavation using the CERCHAR abrasiveness index (CAI). In *the EUROCK 2004 & 53<sup>rd</sup> Geomechanics Colloquium*.
- Potts, E. L. J., & Shuttleworth, P. (1958). A study of ploughability of coal with special reference to the effects of blade shape, direction of planning to the cleat, planning speed and influence of water infusion. *Transactions of the American Institute of Mining Engineers*, 117, 519-553.
- Powerking. (n.d.). NRC technical specification. Retrieved from <http://www.powerkingmc.com> (accessed: June 22, 2019)
- Reddish, D. J., Stace, L. R., Vanichkobchinda, P., & Whittles, D. N. (2005). Numerical simulation of the dynamic impact breakage

- testing of rock. *International Journal of Rock Mechanics and Mining Sciences*, 42(2), 167-176.
- Reichmuth, D. R. (1963). *Correlation of force-displacement data with physical properties of rock for percussive drilling systems*. Master thesis. University of Minnesota, United States.
- Riedel, W., Thoma, K., Hiermaier, S., & Schmolinske, E. (1999). Penetration of reinforced concrete by BETA-B-500 numerical analysis using a new macroscopic concrete model for hydrocodes. In the *Proceedings of the 9<sup>th</sup> International Symposium on the Effects of Munitions with Structures*, vol. 315. Berlin-Strausberg Germany.
- Rojek, J., Onate, E., Labra, C., & Kargl, H. (2011). Discrete element simulation of rock cutting. *International Journal of Rock Mechanics and Mining Sciences*, 48(6), 996-1010.
- Rostami, J., Ghasemi, A., Gharahbagh, E. A., Dogruoz, C., & Dahl, F. (2014). Study of dominant factors affecting Cerchar abrasivity index. *Rock Mechanics and Rock Engineering*, 47(5), 1905-1919.
- Rostami, J., & Ozdemir, L. (1993). A new model for performance prediction of hard rock TBMs. In *the Proceedings of Rapid Excavation and Tunneling Conference*.
- Roxborough, F., & Liu, Z. (1995). Theoretical considerations on pick shape in rock and coal cutting. In *the Proceedings of the sixth underground operator's conference*, 189-193. Kalgoorlie, Australia.
- Roxborough, F., & Phillips, H. (1975). Rock excavation by disc cutter. *International Journal of Rock Mechanics and Mining Sciences & Geomechanics Abstracts*, 12(12), 361-366
- Sandvik. Mining and Rock Excavation Products and Equipment. Retrieved from <https://mining.sandvik.com> (accessed: September 24, 2018)
- Shockey, D. A., Curran, D. R., Seaman, L., Rosenberg, J. T., & Petersen, C. F. (1974). Fragmentation of rock under dynamic loads. *International Journal of Rock Mechanics and Mining Sciences & Geomechanics Abstracts*, 11(8), 303-317.
- Su, O., & Akcin, N. A. (2011). Numerical simulation of rock cutting using the discrete element method. *International Journal of Rock Mechanics and Mining Sciences*, 48(3), 434-442.

- Swan, G., Cook, J., Bruce, S., & Meehan, R. (1989). Strain Rate Effects in Kimmeridge Bay Shale. *International Journal of Rock Mechanics and Mining Sciences & Geomechanics Abstracts*, 26(2), 135-149.
- Tarigopula, V., Albertini, C., Langseth, M., Hopperstad, O. S., & Clausen, A. H. (2009). A hydro-pneumatic machine for intermediate strain-rates: Set-up, tests and numerical simulations. In *DYMAT - International Conference on the Mechanical and Physical Behaviour of Materials under Dynamic Loading*, vol. 1, 381 - 387. Brussels, Belgium.
- Tham, C. Y. (2005). Reinforced concrete perforation and penetration simulation using AUTODYN-3D. *Finite Elements in Analysis and Design*, 41(14), 1401-1410.
- Thuro, K., & Plinninger, R. J. (2003). Hard rock tunnel boring, cutting, drilling and blasting: rock parameters for excavatability. In *the 10<sup>th</sup> ISRM Congress*. International Society for Rock Mechanics and Rock Engineering.
- Valantin, A. (1973). Test CERCHAR pour la mesure de la dureté et de l'abrasivité des roches. *Annexe de l'exposée présenté aux Journées d'Information*.
- Vanichkobchinda, P. (2005). *Numerical simulation of the dynamic impact breakage testing of rock*. Doctoral dissertation. University of Nottingham, United Kingdom.
- Vogt, D. (2016). A review of rock cutting for underground mining: past, present, and future. *Journal of the Southern African Institute of Mining and Metallurgy*, 116(11), 1011-1026.
- Wang, P., Xu, J. Y., Liu, S., Wang, H. Y., & Liu, S. H. (2016). Static and dynamic mechanical properties of sedimentary rock after freeze-thaw or thermal shock weathering. *Engineering Geology*, 210, 148-157.
- Wang, Q. Z., Li, W., & Xie, H. P. (2009). Dynamic split tensile test of flattened Brazilian disc of rock with SHPB setup. *Mechanics of Materials*, 41(3), 252-260.
- Wang, X., Wang, Q.-F., Liang, Y.-P., Su, O., & Yang, L. (2018). Dominant cutting parameters affecting the specific energy of selected sandstones when using conical picks and the development of empirical prediction models. *Rock Mechanics and Rock Engineering*, 51(10), 3111-3128.

- Wang, Y. N., & Tonon, F. (2011). Dynamic validation of a discrete element code in modeling rock fragmentation. *International Journal of Rock Mechanics and Mining Sciences*, 48(4), 535-545.
- West, G. (1986). A relation between abrasiveness and quartz content for some coal measures sediments. *Geotechnical and Geological Engineering*, 4(1), 73-78.
- West, G. (1989). Rock abrasiveness testing for tunnelling. *International Journal of Rock Mechanics and Mining Sciences & Geomechanics Abstracts*, 26(2), 151-160.
- Whittles, D. N., Kingman, S., Lowndes, I., & Jackson, K. (2006). Laboratory and numerical investigation into the characteristics of rock fragmentation. *Minerals Engineering*, 19(14), 1418-1429.
- Wicaksana, Y., & Jeon, S. (2016). Strain rate effect on the crack initiation stress level under uniaxial compression. In *the Proceedings of the 9<sup>th</sup> Asian Rock Mechanics Symposium*. Bali, Indonesia.
- Wicaksana, Y., Jeon, S., Min, G. J., & Cho, S. H. (2018a). Tensile behavior of rock under intermediate dynamic loading for Hwangdeung granite and Linyi sandstone. In *the Proceedings of the 2018 European Rock Mechanics Symposium, Geomechanics and Geodynamics of Rock Masses*, vol. 1. Saint Petersburg, Russia.
- Wicaksana, Y., Jeon, S., Min, G. J., Cho, S. H., & Lee, S. (2018b). Mode-I Fracture Toughness Under Intermediate Level Dynamic Loading for Granite and Sandstone. In *the Proceeding of the 10<sup>th</sup> Asian Rock Mechanics Symposium*. Singapore.
- Xia, K. W., Nasser, M. H. B., Mohanty, B., Lu, F., Chen, R., & Luo, S. N. (2008). Effects of microstructures on dynamic compression of Barre granite. *International Journal of Rock Mechanics and Mining Sciences*, 45(6), 879-887.
- Xia, K. W., Yao, W., & Wu, B. B. (2017). Dynamic rock tensile strengths of Laurentian granite: Experimental observation and micromechanical model. *Journal of Rock Mechanics and Geotechnical Engineering*, 9(1), 116-124.
- Yan, F., Feng, X. T., Chen, R., Xia, K. W., & Jin, C. Y. (2012). Dynamic Tensile Failure of the Rock Interface Between Tuff

- and Basalt. *Rock Mechanics and Rock Engineering*, 45(3), 341-348.
- Yaralı, O., & Duru, H. (2016). Investigation into effect of scratch length and surface condition on Cerchar abrasivity index. *Tunnelling and Underground Space Technology*, 60, 111-120.
- Yilmaz, N. G., Yurdakul, M., & Goktan, R. (2007). Prediction of radial bit cutting force in high-strength rocks using multiple linear regression analysis. *International Journal of Rock Mechanics and Mining Sciences*, 6(44), 962-970.
- Zhang, Q. B., & Zhao, J. (2013). Determination of mechanical properties and full-field strain measurements of rock material under dynamic loads. *International Journal of Rock Mechanics and Mining Sciences*, 60, 423-439.
- Zhang, Q. B., & Zhao, J. (2014a). Quasi-static and dynamic fracture behaviour of rock materials: phenomena and mechanisms. *International Journal of Fracture*, 189(1), 1-32.
- Zhang, Q. B., & Zhao, J. (2014b). A review of dynamic experimental techniques and mechanical behaviour of rock materials. *Rock Mechanics and Rock Engineering*, 47(4), 1411-1478.
- Zhao, J., & Li, H. B. (2000). Experimental determination of dynamic tensile properties of a granite. *International Journal of Rock Mechanics and Mining Sciences*, 37(5), 861-866.
- Zhao, J., Li, H. B., Wu, M. B., & Li, T. J. (1999). Dynamic uniaxial compression tests on a granite. *International Journal of Rock Mechanics and Mining Sciences*, 36(2), 273-277.
- Zhou, H., Yang, Y. S., Zhang, C. Q., & Hu, D. W. (2015). Experimental investigations on loading-rate dependency of compressive and tensile mechanical behaviour of hard rocks. *European Journal of Environmental and Civil Engineering*, 19, S70-S82.
- Zhu, W. C. (2008). Numerical Modelling of the Effect of Rock Heterogeneity on Dynamic Tensile Strength. *Rock Mechanics and Rock Engineering*, 41(5), 771-779.
- Zhu, W. C., Niu, L. L., Li, S. H., & Xu, Z. H. (2015). Dynamic Brazilian test of rock under intermediate strain rate: Pendulum hammer-driven SHPB test and numerical simulation. *Rock Mechanics and Rock Engineering*, 48(5), 1867-1881.

Zum Gahr, K.-H. (1987). Microstructure and wear of materials. vol. 10.  
Elsevier.

## 초록

기계식 굴착공법은 다양한 토목, 자원개발 공사에서 사용되고 있다. 기계식 굴착공법은 발파공법과 비교하여 굴착공사의 연결성, 안정성, 안전성, 환경피해 측면에서 장점을 가진다. 또한 안전과 환경피해에 대한 관심이 커짐에 따라 도심지 터널공사를 중심으로 기계식 굴착공법의 수요는 지속적으로 증가하고 있다.

암석의 기계굴착에서는 굴착도구를 통해 암석에 동적인 하중을 가하기 때문에 암석의 동적거동이 고려되어야 한다. 또한 많은 선행연구들에서는 암석의 동적인 하중하에서의 강도는 정적 하중에 비해 높게 나타남을 보고하고 있다. 그러나 현재까지 암석의 굴착효율을 평가하기 위한 예측모델에서는 암석의 동적물성을 고려하지 않고 있다. 이것은 잠재적으로 장비의 굴착 효율을 평가하거나 장비를 선정하는데 있어 잘못된 정보를 도출 할 수 있다.

본 연구에서는 암석의 동적 거동측면에서의 암석의 절삭 문제를 고찰하였다. 먼저 기계굴착에서의 암석의 변형 속도는 준정적 변형률 속도와 높은 변형률 속도의 중간에 해당하는 중간변형률속도에 속하는 것을 알 수 있었다. 그리하여 비폭발성 분말을 이용한 하중재하장치를 이용하여 중간변형률 속도의 하중을 모사하고 중간변형률에서의 암석의 다양한 물성을 획득하였다. 또한 중간변형률 속도에서 획득된 암석의 동적물성에 대하여 고찰하였다.

다양한 절삭조건하에서 선형절삭시험을 수행하였다. 또한 암석의 정적인 물성과 동적인 물성을 적용한 유한요소 해석기법을 통하여 수치해석적으로 암석의 절삭과정을 모사하였다. 수치해석으로부터 획득한 커터작용력과 비에너지를 선형절삭시험결과를 통해 검증하였다. 수치해석결과는 준정적인 하중 하에서 획득된 암석의 물성을 사용하는 것 보다 동적인 물성을 사용하는 것이 실험결과와 더 일치하는 결과를 보였다. 또한 암석의 동적물성을 이용하여 암석의 절삭성능을 예측하기 위한 예측모델을 도출하였다. 도출된 예측 모델은 선행연구들로부터 획득한 데이터를 활용하여 검증하였고, 일련의 이론모델보다 향상된 예측결과를 보였다.

마지막으로 동적인 조건에서 암석의 마모시험 (가우징 마모시험) 을 수행하였다. 이 시험법은 금속핀을 암석표면에 접촉시켜 빠른 속도로 긁는 시험으로, 절삭도구가 실제 현장에서 굴착하는 환경을 모사할 수 있다. 가우징 마모시험 으로부터 획득한 결과를 세르샤 마모시험 결과와 비교하여 고찰하였고, 두 시험결과 사이의 상관관계를 암석의 역학적 물성과 마모시험 으로부터 생성된 암석의 표면정보 등을 통하여 분석하였다.

핵심어: 암석절삭성능, 동적 물성, 중간변형률 속도, 비 폭발성 반응 기반 하중장치, 선형절삭시험, 유한요소해석, 가우징 마모시험

## ACKNOWLEDGMENT

First and foremost, I would like to express my deepest gratitude to my advisor, Prof. Seokwon Jeon, who has given me everything he could since the first day I arrived in Korea. Without his consistent guidance, encouragement, and support, I would not have been able to reach this far. He guided me throughout the research process, supported me financially, and actively involved in every detail of it. He always put an effort to expose me to the rock mechanics society not only in Korea but also in international scope. His remarkable knowledge, personality, and work ethics would be the perfect example of being a well-respected scholar.

I would like to extend my gratitude to the faculty member of the Rock Mechanics and Rock Engineering Laboratory, Prof. Jae-Joon Song and Prof. Ki-Bok Min. Their courses, discussions, and comments have advanced my knowledge in various aspects of rock mechanics. Also, I would like to express my sincere appreciation to Professor Emeritus Chung-In Lee, who always gives motivation and encouragement to the young scholars in the SNU rock mechanics group through his remarkable experiences.

I would like to convey my sincere appreciation to the external committee members of the thesis defense, Prof. Sangho Cho from Chonbuk National University and Dr. Tae Young Ko from SK Engineering & Construction Company. Their expertise, critical comments and constructive discussions have helped me to improve this thesis significantly.

I would like to show my appreciation to my laboratory colleagues I have been with over the years, Dr. Byungkyu Jeon, Dr. Nan Zhang, Jae-

Woong Jung, Dr. Taehyun Kim, Dr. Ho-Young Jeong, Dr. Seung-Bum Choi, Su-Deuk Lee, Dr. Sunghoon Ryu, Dr. Linmao Xie, Dr. Hanna Kim, Dr. Bona Park, Dr. Chae-Soon Choi, Dr. Sayedalireza Fereshtenejad, Yong-Ki Lee, Dong-Ho Yoon, Sehyeok Park, Kwang-Il Kim, Saeha Kwon, Il-Seok Kang, Hoon Byun, Hwa-Jung Yoo, Yim Juhyi, Shahabedin Hojjati, Ali Mehrabifard, Yeongmin Yoon, Seungki Lee, Moonjoo Kim, Wonhee Lee, Suyeon Hong, Yongjune Sohn, and other lab members that are not mentioned here. Thank you for always being kind and supportive since the first day I arrived in Seoul. Special appreciation goes to Dr. Ho-Young Jeong, Su-Deuk Lee, and Shahabedin Hojjati for their valuable insights and contributions to the thesis.

I would like to extend my special gratitude to my life role models and former advisors at Institut Teknologi Bandung (ITB), Dr. Suseno Kramadibrata and Prof. Ridho Kresna Wattimena. They brought me to the field of rock mechanics, armed me with fundamental knowledge, trained me through practical experiences, and encourage me to pursue a Ph.D. degree at Seoul National University. Without their support, I would not have been able to be at this moment. Special acknowledgment also goes to Prof. Made Astawa Rai, Prof. Irwandy Arif, Prof. Budi Sulistianto, Dr. Ganda Marihot Simangunsong, Dr. Nuhindro Priagung Widodo, Dr. Simon Heru Prassetyo, Dr. Ginting Jalu Kusuma and all members of Rock Mechanics and Mine Equipment Laboratory of ITB.

To my parents, Rachmat Sambas and Eka Astusti Handayani, my brothers, Dwiki Budhitama and Muhammad Pandu Perwira, thank you for allowing me to travel this far for years to pursue my dream. Your unconditional support and prayers have brought me to reach this precious moment. To my wife, Dwi Pangestu Ramadhani (soon to be a doctor, too), and my daughter, Ilmaira Ayudya Anjani, your unconditional love

through comfort and pain have shaped me to be a better person every single day. I am in debt to you two in so many ways. Also, special appreciation to my parents and sister in law who always supported us endlessly. Most importantly, my deepest gratitude to Allah SWT, who always leads the way whenever I go and whatever I do. Without this spiritual guidance, it would be impossible for me to overcome all the challenges in life.

Lastly, I would like to express my immense appreciation to the Indonesia Endowment Fund for Education (LPDP) under the Ministry of Finance, the Republic of Indonesia, for the generous financial support for the first four years of my study. Without this scholarship program, this academic journey would not have happened.